INTEGRATING STRUCTURE AND CONTROL DESIGN USING TENSEGRITY PARADIGM

A Dissertation

by

RAMAN GOYAL

Submitted to the Office of Graduate and Professional Studies of
Texas A&M University
in partial fulfillment of the requirements for the degree of

DOCTOR OF PHILOSOPHY

Chair of Committee,	Robert Skelton
Committee Members,	Manoranjan Majji
	Raktim Bhattacharya
	Dileep Kalathil
Head of Department,	Rodney Bowersox

August 2020

Major Subject: Aerospace Engineering

ABSTRACT

For centuries researchers have been pushing the boundaries of their respective technical domains, but it is only a few decades ago that research started taking its dig on system design theory. A system design theory encapsulates all individual components design and their simultaneous optimization, i.e., it provides a complete framework to design the structure. The approach behind this research is to make small steps in structure design, dynamic models, information architecture, and control design with some free parameters and then finally optimize those free parameters in a wholesome design approach to meet some specified performance. The author uses tensegrity design models to integrate structure and control design due to the various advantages mentioned further. This dissertation first makes three contributions to the study of tensegrity structures and then provides a system design theory to integrate structure and control design using the tensegrity paradigm.

The first part of the dissertation provides a detailed study of the minimum mass tensegrity structures designed to take compressive loads, namely, D-bar and T-bar structures. These design studies consider both local and global failures in designing the optimal configuration (optimal complexity, angle, and cross-sectional area) for both D-bar and T-bar structures. The formulation developed here provides a general methodology to avoid global buckling failures for any class-k tensegrity structures. The proposed research provides different approaches to design a structure based on optimizing mass, stiffness, or mechanical energy stored in a tensegrity structure.

The second part of this research work provides accurate dynamic models of axially loaded members forming any general tensegrity structure. The formulation develops a second-order matrix differential equation to perform dynamic simulation of tensegrity structures with massive strings and rigid bars. The dynamics models for novel gyroscopic tensegrity systems are also developed, which adds an extra degree of freedom to the control of the structure. A Matlab based tensegrity dynamics simulator is another outcome of this research.

The third section of the dissertation discusses a model-based approach to control the shape of any general tensegrity structure. A reduced-order model of tensegrity dynamics is used to design non-linear output feedback regulation, which derives error in position, velocity, and acceleration to zero yielding a linear programming problem as the final equation to solve. The shape control of gyroscopic tensegrity system is also discussed to show the increase in reachable 3-dimensional space. A Linear Matrix Inequality (LMI) framework is further used to calculate control gains to bound errors for five different types of control problems for given disturbance profile. All the examples for this part are performed on a $T_n D_1$ tensegrity robotic arm.

The last fragment of the dissertation starts with the derivation of the minimal-order linear model by linearizing the system about an equilibrium point and removing the modes which causes the length of the bars to change. The liner control theory is further applied to reject the disturbances using $\mathcal{H}_\infty$, generalized $\mathcal{H}_2$ and covariance bound controller. The chapter further provides a methodology to integrate structure and control design where some parameter of the structure in the linearized dynamic model, control law and the information about the system architecture (actuator/sensor) is simultaneously optimized to achieve some desired performance for a covariance control problem. The developed Linear Matrix Inequality (LMI) framework is general enough for any linear model with linear structure parameters to bound the output covariance for given disturbance intensity. The force density in the strings (prestress) is used as the optimization variable for the structure, which appears affinely in the system matrices of the linearized tensegrity dynamics. The sub-optimal solution of this non-convex system design problem is found by iterating over an approximated convex problem through the use of a convexifying potential function, which enables convergence to a local minimum.

DEDICATION

To Baba, Mummy, Papa, Govind and V.

ACKNOWLEDGMENTS

I would like to thank my advisor Prof. Robert E. Skelton for his guidance, support, and for giving me the opportunity to work for him. He accepted me with my limited knowledge of controls and no knowledge of tensegrity structures and taught me everything. I feel honored to have them as my advisor. He taught me how to think critically and scientifically during our various research discussions throughout the years. His perspective and passion for research has inspired me and will shape my career in years to come. I am also grateful to Judy Ma'am for making me feel like a family.

I would also like to thank Dr. Manoranjan Majji for all the helpful discussions and for having a positive and friendly attitude towards every research topic we discussed. This dissertation could not have been successfully completed without his guidance and help over the years. I would also like to thank Dr. Raktim Bhattacharya and Dr. Dileep Kalathil for their valuable time and for serving on my doctoral committee. Dr. Bhattacharya taught me a lot about convex optimization during our many helpful discussions and his course on robust control was very helpful for the last two chapters of my dissertation.

My sincere gratitude goes to my good friend and colleague Dr. Edwin Peraza Hernandez for teaching me to be meticulous and succinct in technical writing. I also would like to thank him for giving me intricate details of the academic world along with many helpful suggestions. Dr. Maziar Izadi and Dr. Utku Boz also have been great friends and colleagues to work with during their stay at Texas A&M.

I would also like to thank my friends Ms. Vishala, Mr. Utkarsh Ranjan Mishra, Dr. Atanu Halder, and Mr. Rajan Kapoor for their company, friendship, and for our deep discussions on life and beyond. Finally, a thank you to the staff of the Department of Aerospace Engineering at Texas A&M University for all the help and support throughout the years. Ms. Nicole Parker and Ms. Gail Rowe made my life so much easier during my time here.

CONTRIBUTORS AND FUNDING SOURCES

Contributors

This work was supported by a dissertation committee consisting of Professor Robert E. Skelton (advisor), Professors Manoranjan Majji and Raktim Bhattacharya of the Department of Aerospace Engineering and Professor Dileep Kalathil of the Department of Electrical Engineering.

All other work conducted for the dissertation was completed by the student independently.

Funding Sources

This work was made possible in part by the NASA Innovative Advanced Concepts (NIAC) Program Phase II grant.

Its contents are solely the responsibility of the author and do not necessarily represent the official views of NASA.

TABLE OF CONTENTS

Page

LIST OF FIGURES

FIGURE Page

LIST OF TABLES

TABLE Page

1. INTRODUCTION

1.1 Literature Review

Tensegrity is a name coined by Buckminister Fuller [3]. The word is conjugated from “tension” and “integrity”, and was originally used for art and architectural applications by Ioganson (1921) and Kenneth Snelson [4]. Tensegrity is a network of compressive and tensile members, where the compressive members (bars, struts) are connected together by tension members (strings, cables, tendons) forming a stable system [5]. These structures are also described as a structurally stable network of axially loaded pre-stressable members [6]. Skelton describes “Class-1" tensegrity when no compressive members touch each other, and a “Class-k" when k compressive members join at a node [6]. For class-k structures, bars are connected by frictionless ball joints, or their mathematical equivalents, to constraint all members to be “axially loaded" only. For both class of structures, as all the strings are connected to the node center of the bars, there would be no torque along the axis of the bar and, therefore, no rotation along the bar axis.

Tensegrity allows for the development of structures with optimal properties or responses by methodically arranging networks of one-dimensional elements [6, 7, 8]. Since tensegrity structures are comprised exclusively of axially loaded members, elegant and accurate structural models and design approaches have been developed to respectively simulate and optimize their responses; see, for example [9, 10, 11]. Reviews of models and analyses of stability, statics, and dynamics of tensegrity structures are found in [12, 13, 14, 15, 16]. Tensegrity provides a unique method in which shape change can be achieved without a change in stiffness of the structure, and stiffness can also be changed without changing the shape of the structure. This is achievable as structure morphs from one equilibrium configuration to another on the control surface [6, 17] as shown in figure 1.1. This morphing from one equilibrium position to another equilibrium position also results in minimal control energy requirement for shape change [18]. In addition to the accurate dynamic models, tensegrity structures of several topologies have been mathematically proven to

optimally (i.e., with minimum mass) sustain different loads when compared to their continuum counterparts.

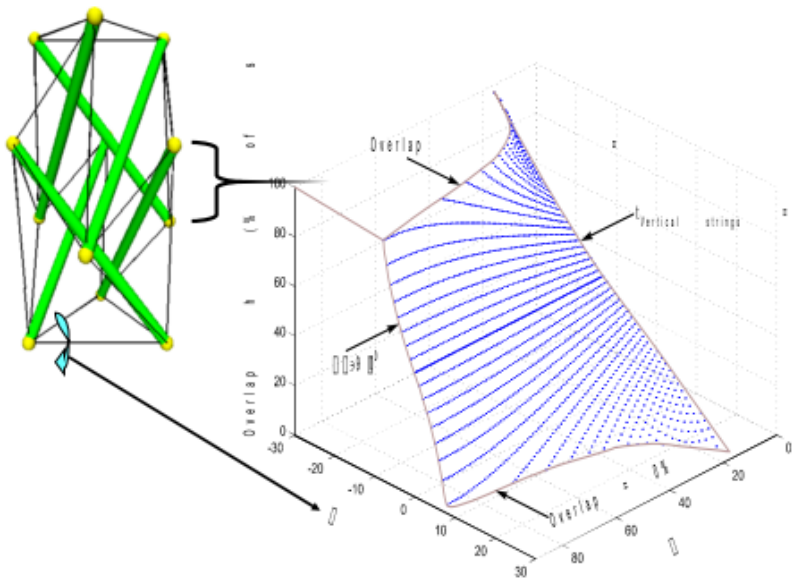

Figure 1.1: Multiple equilibrium paths that can be optimized for desired performance/weight/shape a lower cost of control energy. Reprinted with permission from [6]: "Tensegrity Systems", by Robert E. Skelton, Mauricio C. de Oliveira, 2009, Springer Nature, Boston, MA. Coyright [2009] Springer-Verlag US.

Tensegrity structures have been shown to provide a minimal mass solution to five different kinds of problems in engineering mechanics: 1. Tensile loading, 2. Compressive loading, 3. Cantilever loading, 4. Simple-supported loading, and 5. Torsional loading [6, 19, 20]. The minimal mass solution to compressive loading is provided by a T-bar structure assuming no global buckling [6] (a 3D T-bar structure is installed outside Frick Chemistry Lab in Princeton). Tensegrity D-bar structure has also been shown to require less mass than a simple continuum bar to take the same load. Moreover, the tensegrity D-bar structure has also shown significant potential in robotics due to its minimum mass and easy deployability, which also makes them suitable for space applications [21, 18]. Research has also shown D-bar structures to be efficient as sensors/actuators and impact landers [21, 22]. Michell truss is proven to provide the minimum mass solution for cantilevered

bending loads [6].

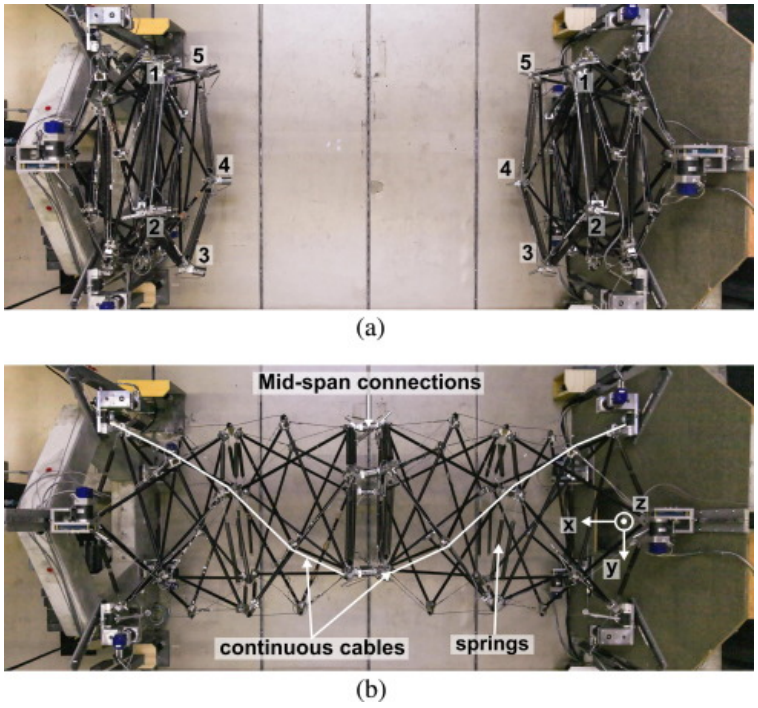

Figure 1.2: Active Deployable Tensegrity Footbridge System (EPFL 2012-2018). Reprinted with permission from [1].

Researchers are using tensegrity approaches to provide minimum mass solutions to many static structural problems such as civil engineering bridges [23, 24] and composite membrane design [25, 26]. “Tensegrity Ball" has been extensively studied for its use as a lander [2, 27], and various impact structures [21]. All the above-mentioned properties of tensegrity structures have found their use in various applications ranging from deployable bridges (see Fig. 1.2) [23, 28] to compliant soft robotics applications [29, 30, 31], to Light-weight and deployable space structure [32], tunable meta-materials [33], and artificial gravity space habitats [34, 35] in aerospace engineering. These applications can be attributed to the fact that several fundamental problems in engineering mechanics are solved by various structural topologies of tensegrity structures. Various tensegrity architecture also appears in many biological systems, ranging from bone and muscle networks to fibrous structural components in living cells [36] and to the molecular structure of spider fiber.

See also tensegrity models for the Bio-mechanics of the animal skeletal [37, 38] (see Fig. 1.3). Tensegrity structures can also be used in the design of human prosthetics or as augmentative devices (orthotics) due to their lightweight and efficient control energy requirements [39]. Multiple redundant control strings make the system robust avoiding failure in case of any string loss.

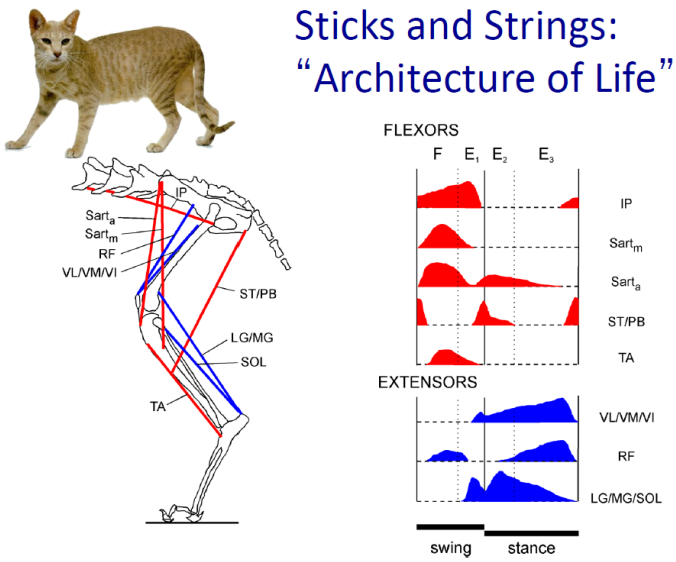

Figure 1.3: Muscular activation shown for a cat during normal walking. Reprinted with permission from [6]: "Tensegrity Systems", by Robert E. Skelton, Mauricio C. de Oliveira, 2009, Springer Nature, Boston, MA. Coyright [2009] Springer-Verlag US.

1.2 Motivation

The idea of system design theory has received a lot of attention in the last few decades. A system design theory encapsulates all individual components design and their simultaneous optimization to provide a complete framework to design the structure. The system design theory provides all the information about structure (mass, stiffness, dimensions, material, etc.), information architecture (which actuator/sensor, actuator/sensor location, actuator/sensor precision, etc.), control law (linear, non-linear, state feedback, output feedback), and most importantly which model to use (order or complexity of model). Moreover, these design choices

are not separate and should be optimized together, not individually. A systematic study of system design approach is much needed for solving various engineering problems ranging from basic sciences (maths, physics, chemistry) to basic engineering (mechanical, aerospace, civil) fields. The philosophy behind this research is to make small steps in structure design, dynamic model and its order, information architecture, and control design with some free parameters and then finally optimize those free parameters in a wholesome design approach to meet some specified performance.

The author believes that tensegrity structures are best suited to integrate structure and control design due to its very accurate models of axially loaded members [6]. An accurate model of the system dynamics will yield precise control. Moreover, as tensegrity provides good efficiency for both structural and control avenue, it would be an ideal choice for various adaptive structures where structure and control parameters should be optimized simultaneously [6]. All the above-mentioned advantages make tensegrity systems an obvious choice to showcase this idea of system thinking. Some elementary results are provided to guide the way toward the choice of elementary building blocks to build more complex structures.

2. DESIGN OF TENSEGRITY BASED MASS-EFFICIENT ENERGY ABSORPTION ELEMENTS*

[1] This chapter studies tensegrity structures known as “D-bar" systems for applications as lightweight components for mechanical energy absorption. A D-bar system of *complexity* 1 (a *D-bar unit*) is generated by replacing a compressive structural member with $2p$ bars emanating from its end-points towards the vertices of a centered p-sided polygon formed by strings ($p = 3$ in Fig. 1(b) in the manuscript). Aerospace structures such as planetary landers, designed to absorb energy from large impact loads while requiring minimal mass, would benefit from such components. Previous studies showed that D-bar systems support compressive loads with minimal mass compared to continuum options such as single columns. In this work, analytical equations for the mechanical (elastic) energy stored in D-bar systems of any complexity (a quantity proportional to the number of strings/bars in the system) are derived. The energy stored in D-bar systems is compared with that of bent buckled beams used in “flexible-bar tensegrity" concepts, which were proposed in the literature as energy absorption components for planetary landers. Comparisons are made between D-bar systems and bent buckled beams as isolated components subject to a compressive load and as part of a larger tensegrity planetary landers. In all comparisons, the results show that D-bar systems of low complexity allow for higher energy storage *and* lower mass than bent buckled beams. Thus, it is concluded that D-bar systems can enhance the design of planetary landers and other applications that need lightweight mechanical energy absorption components.

2.1 Introduction

Objectives: This work presents a study on lightweight components for mechanical energy absorption based on a special tensegrity topology known as *D-bar* system [6]. The study was motivated by aerospace structures such as planetary landers that need lightweight components

[1]*Portions of this section are reprinted or adapted from [21] : Raman Goyal, Edwin A. Peraza Hernandez, and Robert E. Skelton, "Analytical Study of Tensegrity Lattices for Mass-Efficient Mechanical Energy Absorption", International Journal of Space Structures, 34(2), 3-21, 2019, DOI: 10.1177/0956059919845330. Copyright © 2019, © SAGE Publications. Reproduced with permission.

to absorb energy from large impact loads (to protect their interior systems and payload) while requiring low mass. Recent examples of planetary lander designs include those proposed by SunSpiral and coworkers [2], who developed ball-like tensegrity robots for planetary exploration and landing that can safely absorb impact loads. Rimoli [27] extended the approach of [2] by proposing bent buckled beams used in “flexible-bar tensegrity" concepts for energy absorption components in planetary landers. Here, conversely, the proposed approach is to store energy from external loads as mechanical (elastic) energy in the strings and bars of D-bar systems without triggering local structural instabilities such as buckling and thereby allowing for more reliable structures. In this chapter, the analytical equations for the mechanical energy stored in D-bar systems of any complexity are derived for the first time. The energy stored in D-bar systems is compared with that of bent buckled beams (Fig. 2.1(a)) used in flexible-bar tensegrity concepts, which have been proposed in the literature as energy absorption components for planetary landers [27]. Comparisons between the energy stored in D-bar systems and bent beams at the single component level and as parts of a tensegrity lander structure are presented.

Tensegrity systems are structurally stable networks of axially loaded one-dimensional members [6, 7, 8, 40, 13]. The one-dimensional elements are defined to be loaded and deformed only along their longitudinal direction. As illustrated in Fig. 2.1, a D-bar system of *complexity* 1 (a *D-bar unit*) is generated by replacing a compressive structural member with $2p$ bars emanating from its end-points towards the vertices of a centered p-sided polygon formed by strings ($p = 3$ in Fig. 2.1(b)). A D-bar system of complexity q is generated by replacing each bar in a D-bar system of complexity $q - 1$ with a D-bar unit. It is worth mentioning that increasing the complexity of a D-bar system results in a higher number of joints and members which increases manufacturing costs and makes scalability more difficult. Therefore, D-bar systems of low complexity are more convenient for practical applications.

Previous studies showed that D-bar systems can support compressive loads with minimal mass considering buckling and material yielding constraints as compared to single columns [6]; however, their mechanical energy storage properties have not been explored so far. It should be noted that

the conventional D-bar structures studied in [6] include strings connecting the end-points of each D-bar unit in the D-bar systems, which are not present in this work (see Fig. 2.1(b)). These strings are necessary only to ensure self-equilibrium in the absence of an external compressive force or to actuate/deploy the D-bar systems. Such strings are omitted in this work as the D-bar systems considered herein are strictly designed to be in the presence of a compressive load, and our focus is solely on the compressive load-bearing and energy storage functionalities of D-bar systems. For applications of D-bar systems where external compressive loads are absent or actuation/deployment is needed, the strings connecting the end points of each D-bar unit must be included. These applications of D-bar tensegrity systems include its use as sensors and actuators [22] and as lightweight energy absorption components in advanced materials formed by tensegrity lattices [41, 42, 23].

The remainder of the chapter is organized as follows: Section 2.2 summarizes the assumptions made in the analytical derivations, Section 2.3 presents the analysis of the energy stored and minimal mass of bent buckled beams subject to compressive loads, Section 2.4 addresses the analysis of the energy stored and minimal mass of D-bar systems, and Section 2.5 presents the comparisons in energy stored and minimal mass between D-bar systems and bent buckled beams. Concluding remarks are provided in Section 2.6.

2.2 Summary of Assumptions

The assumptions made in the analysis of bent buckled beams (Section 2.3) are as follows:

- Deflections are small and thus captured by Euler-Bernoulli beam theory
- The beam is long and slender such that Euler theory of buckling applies
- The beam is subject to a single axial compressive load applied at its end-points (no moments or transverse loads are applied)
- The beam has uniform circular full cross-section and is comprised of a homogeneous and isotropic linear elastic material

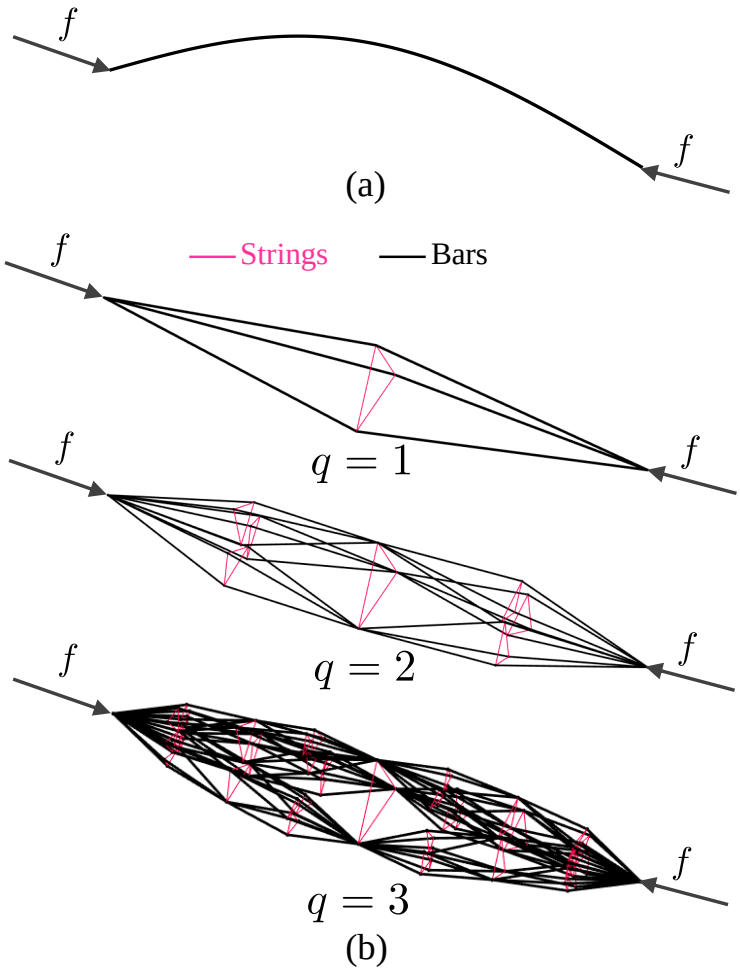

Figure 2.1: (a) A buckled beam subject to a compressive force of magnitude f. (b) D-bar systems of different complexity q subject to a compressive force of magnitude f.

- The beam is in a post-buckled state under the applied force. Therefore, failure occurs when stress reaches the material yield stress at any point in the beam during post-buckling
- The maximum energy stored in the beam is that exhibited at the onset of failure (yielding at any point of the beam) during post-buckling

The assumptions made in the analysis of D-bar systems (Section 2.4) are as follows:

- The D-bar system is subject to a single axial compressive load applied at its end points

- The studied D-bar topology is stable only under compressive loading since strings connecting the end-points of each D-bar unit in the D-bar systems are not present in this work
- The strings and bars are connected through frictionless ball joints such that no moments are transmitted among them
- The strings and bars are subject only to tensile and compressive axial loads, respectively. Hence, strings can be replaced by bars.
- The strings and bars have uniform circular full cross-sections and are comprised of homogeneous and isotropic linear elastic materials
- All the strings are comprised of the same material. All the bars are comprised of the same material
- Mass of the joints is neglected
- Failure at any string occurs when the stress reaches its material yield stress
- Failure at any bar occurs when the compressive force reaches its critical buckling force
- Linearized (small) strain assumptions are used for the strings and bars as the strain is expected to remain within the small deformation domain
- The minimal mass of the D-bar system is determined by finding the minimum radii of strings and bars, which corresponds to the radii for which all the members are at the onset of failure under the applied force
- The maximum energy stored in the D-bar system is that exhibited at the onset of failure in the strings and bars

The assumptions made in the analysis of planetary landers with bent buckled beams and D-bar systems (Section 2.5.2) are as follows:

- The bent buckled beams and D-bar systems in the lander follow the aforesaid assumptions made in Sections 2.3 and 2.4
- The geometry of the tensegrity lander developed in [2] is assumed
- The static loads for the analysis are assumed to be the maximum (peak) load on the structure during the landing operation
- The total force F on top three nodes of the lander is assumed to be equally distributed and the force is assumed to be $F = 15000$N

2.3 Bent Beam Analysis

The goal in this section is to derive analytical formulas for the *mechanical (elastic) energy stored* (V_B) and the *minimal mass* (m_B) of a bent buckled beam subjected to an axial compressive force of magnitude f; refer to Fig. 2.1(a). Such an axial compressive force is assumed in order to simulate impact loading conditions. The results presented in this section are based on Euler-Bernoulli beam theory and Euler theory of buckling [43, 44]. Since the beam is subjected to a single axial compressive load, it is assumed that the beam is in a post-buckled state. It is assumed that the beam is subjected to an axial force. Moreover, the beam is assumed to be in a state of controlled buckling with no exceedance of the yield stress in the most bent section.

The beam has length l and is initially aligned with the x-axis. It is subject only to a compressive force of magnitude f applied at its end points and aligned with the x-axis as indicated in Fig. 2.2. It is assumed that the beam is composed of a homogeneous and isotropic material with Young's modulus E_b, yield stress σ_b, and mass density ρ_b. The beam has a uniform cross-section with minimum area moment of inertia I. It is assumed that the beam has a circular full cross-section of radius r.

To determine the mechanical energy stored and minimal mass of the bent beam in a post-buckled state, the formulas for its deflection w and magnitude of the critical buckling load f must be first provided. It is a known result from Euler theory of buckling [43, 44] that the critical buckling load of a beam of full circular section is given as:

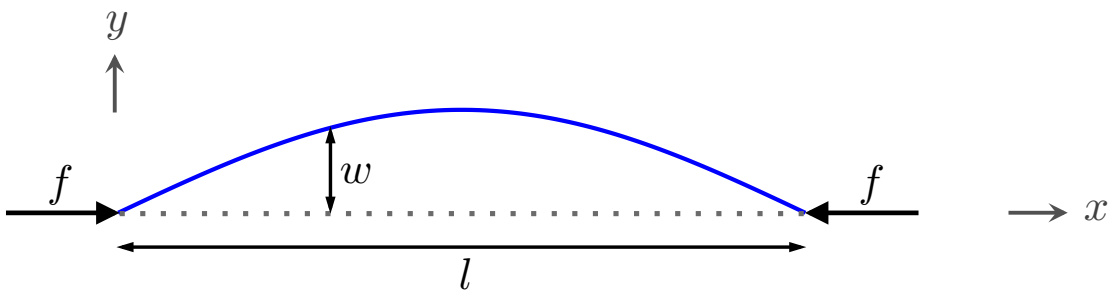

Figure 2.2: Geometry of a buckled beam subject to an axial compressive load f. The deflection w along the y-axis is indicated.

$$f = \frac{n^2\pi^3 E_b r^4}{4l^2}, \qquad n = 1,\, 2,\, 3,\, \ldots, \tag{2.1}$$

where n indicates the buckling mode. Furthermore, the deflection w in its buckled configuration is given as:

$$w = w_{max} \sin\left(\tfrac{n\pi x}{l}\right), \tag{2.2}$$

where w_{max} is the maximum deflection of the beam and $0 \leq x \leq l$.

To calculate the highest mechanical energy stored in the bent beam, it is assumed that the beam is loaded up to the onset of failure. In the post-buckled state of the beam studied here, failure occurs when the stress anywhere in the bent beam reaches the material yield stress. Using the expression for deflection field w in Eq. (2.2), formulas for w_{max} at material yield and the associated axial strain field are derived.

Lemma 2.3.1. *Consider a beam of length l and deflection field w given by Eq. (2.2). Suppose that the beam is composed of a homogeneous and isotropic material with Young's modulus E_b and yield stress σ_b and has a uniform circular cross-section of radius r. Then, the maximum allowable deflection of the beam w_{max} that occurs at the onset of material yield is given by:*

$$w_{max} = \frac{\sigma_b}{rE_b}\left(\frac{l}{n\pi}\right)^2, \tag{2.3}$$

and the axial strain of the beam at such a maximum deflection (i.e., the maximum allowable axial strain) is given as:

$$\varepsilon = y\frac{\sigma_b}{rE_b}\sin\left(\tfrac{n\pi x}{l}\right), \tag{2.4}$$

where $0 \leq x \leq l$ *and* $-r \leq y \leq r$.

The proof is given in Appendix C.1.

The mechanical energy stored in the bent beam V_B at post-buckling is obtained by integrating the strain energy density $\frac{1}{2}\sigma\varepsilon$ over the entire volume of the beam:

$$V_B = \int_{vol} \frac{1}{2}\sigma\varepsilon \, \mathrm{d}v. \tag{2.5}$$

The following theorem provides the final expressions for V_B and the minimal mass m_b of the bent beam.

Theorem 2.3.1. *Consider a beam of length* l *subject to a compressive force of magnitude* f. *Suppose that the beam is composed of a homogeneous and isotropic material having Young's modulus* E_b*, yield stress* σ_b*, and mass density* ρ_b*. Furthermore, the maximum allowable strain of the beam at the onset of material yield is given by Eq. (2.4). Then, the mechanical energy stored in the bent beam* V_B *is given as:*

$$V_B = \frac{l^2\sigma_b^2}{8}\left(\frac{f}{\pi E_b^3}\right)^{\frac{1}{2}}, \tag{2.6}$$

and the associated mass of the beam m_B *for a given beam length* l*, in terms of the applied compressive force* f*, is given as:*

$$m_B = 2l^2\rho_b\left(\frac{f}{\pi E_b}\right)^{\frac{1}{2}}. \tag{2.7}$$

Proof. For a material with Young's modulus E_b, the stress σ is given by $\sigma = E_b\varepsilon$. Substituting this into Eq. (2.5), the following is obtained:

$$V_B = \int_{vol} \frac{1}{2} E_b \varepsilon^2 \, \mathrm{d}v. \tag{2.8}$$

The highest energy stored in the buckled beam V_B is determined by substituting the maximum allowable strain from Eq. (2.4) into Eq. (2.8):

$$V_B = \int_{vol} \frac{1}{2} y^2 \frac{\sigma_b^2}{r^2 E_b} \sin^2\left(\tfrac{n\pi x}{l}\right) \, \mathrm{d}v. \tag{2.9}$$

The previous volume integral is evaluated as an integral over the length of the beam along the x-axis and an integral over the cross-section area of the beam:

$$V_B \;=\; \frac{1}{2} \frac{\sigma_b^2}{r^2 E_b} \int_0^l \int_{area} y^2 \sin^2\left(\tfrac{n\pi x}{l}\right) \, \mathrm{d}a \, \mathrm{d}x \;=\; \frac{l I \sigma_b^2}{4 r^2 E_b}, \tag{2.10}$$

where I is the area moment of inertia. For a beam having a circular cross-section, $I = \frac{\pi r^4}{4}$:

$$V_B = \frac{\pi l r^2 \sigma_b^2}{16 E_b}. \tag{2.11}$$

To determine an expression of V_B as a function of the magnitude of the compressive force f, a formula for r as a function of f from Eq. (2.1) is first determined:

$$r = \left(\frac{4 l^2 f}{n^2 \pi^3 E_b} \right)^{\frac{1}{4}}, \tag{2.12}$$

and then it is substituted into Eq. (2.11):

$$V_B = \frac{l^2 \sigma_b^2}{8n} \left(\frac{f}{\pi E_b^3} \right)^{\frac{1}{2}}. \tag{2.13}$$

From Eq. (2.13), it is clear that the first beam buckling mode ($n = 1$) results in the highest stored mechanical energy V_B in comparison to higher buckling modes ($n > 1$). Therefore, the first buckling mode is assumed for all subsequent calculations and the energy stored in the beam is given by Eq. (2.6). The mass of the beam m_B is obtained by multiplying ρ_b by its total volume:

$$m_B = \rho_b \pi l r^2. \tag{2.14}$$

The expression for the radius r as a function of f from Eq. (2.12) is substituted into Eq. (2.14) to obtain the formula for the minimal mass of the beam m_B in terms of f stated in Eq. (2.7). □

2.4 D-bar Tensegrity System Analysis

The goal in this section is to derive analytical formulas for the *mechanical (elastic) energy stored* (V_D) and *minimal mass* (m_D) of a D-bar system subject to an axial compressive force; refer to Fig. 2.1(b). The boundary condition assumed for the D-bar system is identical to that assumed for the bent beam in Section 2.3, where a single compressive force of magnitude f is applied at the end points of the D-bar. The strings and the bars of the D-bar system are composed of homogeneous, isotropic, linear elastic materials. The geometry of D-bar systems of complexity $q = 1, 2$ is illustrated in Fig. 2.3. The total length of the D-bar system is denoted by l. The angle between the line connecting the end points of each D-bar unit and the line along any of its associated bars is denoted by α. The number of strings in each D-bar unit is denoted as p, where $p \geq 3$. Figure 2.4 shows D-bar tensegrity systems of complexities $q = 1, 2$ with parameter $p = 3, 4, 5$.

The length of *all* the bars in a D-bar system of complexity q is denoted by l_q. The number of bars in a D-bar system is denoted by n_b. It can be verified that:

$$l_q = \frac{l}{(2\cos(\alpha))^q}, \tag{2.15}$$

$$n_b = (2p)^q. \tag{2.16}$$

The length of the strings introduced in each self-similar iteration is denoted as l_{si}, $i = 1, \ldots, q$. The number of strings introduced in each self-similar iteration is denoted as n_{si}, $i = 1, \ldots, q$. It can be shown that:

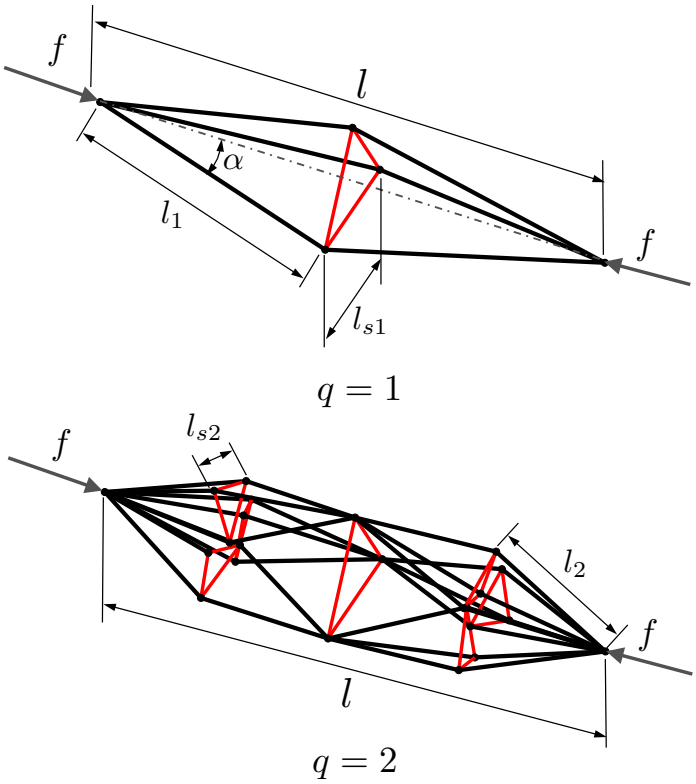

Figure 2.3: Geometric parameters of D-bar tensegrity systems of complexities $q = 1, 2$.

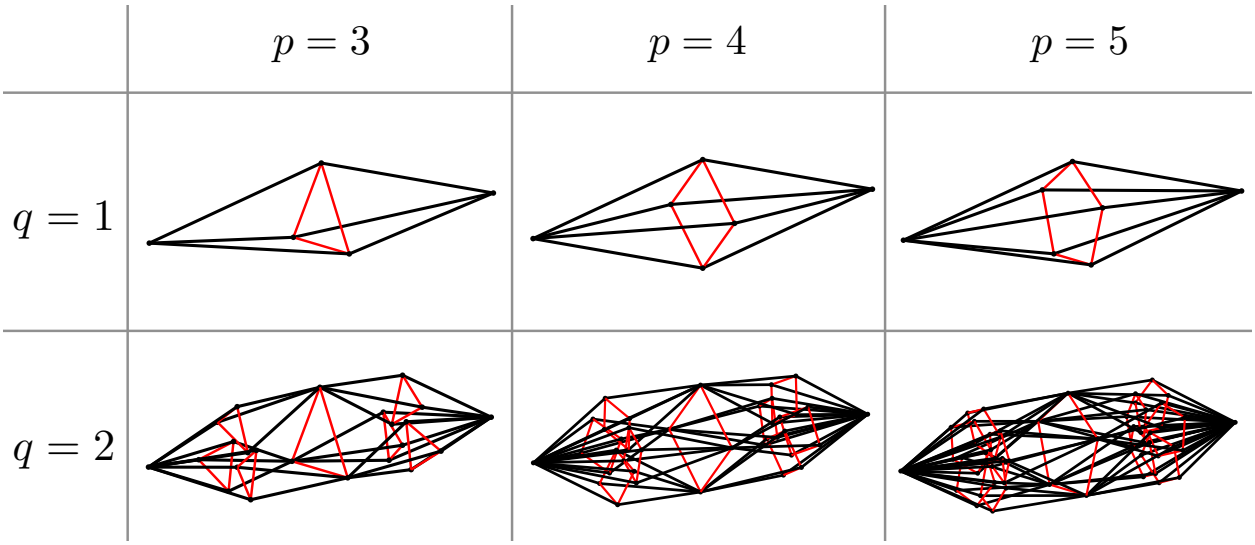

Figure 2.4: D-bar tensegrity systems of complexities $q = 1, 2$ with parameter $p = 3, 4, 5$.

$$l_{si} = 2l_i \sin\left(\frac{\pi}{p}\right) \sin(\alpha) \qquad\qquad i = 1, \ldots, q, \tag{2.17}$$

$$n_{si} \;=\; p(2p)^{i-1} \;=\; 2^{i-1}p^i \qquad\qquad i = 1, \ldots, q. \tag{2.18}$$

The formula for l_q from Eq. (2.15) is then substituted into Eq. (2.17) to obtain an expression for l_{si} in terms of l and α:

$$l_{si} \;=\; \frac{2l \sin\left(\frac{\pi}{p}\right) \sin(\alpha)}{(2\cos(\alpha))^i} \;=\; \frac{l \sin\left(\frac{\pi}{p}\right) \tan(\alpha)}{2^{i-1}\cos^{i-1}(\alpha)} \qquad\qquad i = 1, \ldots, q. \tag{2.19}$$

The total number of strings, denoted by n_s, is given as follows:

$$n_s \;=\; \sum_{i=1}^{q} n_{si} \;=\; \sum_{i=1}^{q} 2^{i-1}p^i. \tag{2.20}$$

It is shown in Chapter 3 of [6] that the magnitude of the compressive force in *all* the bars of the D-bar system, denoted by f_q, is given as follows:

$$f_q = \frac{f}{(p\cos(\alpha))^q}, \tag{2.21}$$

and the magnitude of the tensile force in the strings introduced in each self-similar iteration, denoted by t_i, $i = 1, \ldots, q$, is given as:

$$t_i = \frac{f \tan(\alpha)}{p^i \sin\left(\frac{\pi}{p}\right) \cos^{i-1}(\alpha)} \qquad\qquad i = 1, \ldots, q. \tag{2.22}$$

After presenting the geometry and force distribution of D-bar systems with arbitrary complexity, we then determine their energy stored and minimal mass under material yield and buckling constraints. To determine the highest energy stored in the D-bar system, we assume that all the strings and bars are loaded up to the onset of failure corresponding to reaching the material yield stress of the strings and the critical buckling force of the bars. Given these assumptions, the

strain in the strings and bars is expected to remain within the small deformation domain. Therefore, linearized strain assumptions, such as those used in the beam calculations of Section 2.3, are also assumed here.

The aforesaid assumption that all the strings and bars are loaded up to the onset of failure is critical in this study. It allows us to determine the values for the mininum radii, and thereby the minimum mass, of the strings and bars[2]. The validity of such an assumption is *enforced* by calculating and employing the radii of the strings and bars corresponding to those for which the members are loaded exactly to the onset of failure (yield for strings and buckling for bars) under their calculated forces from Eqs. (2.22) and (2.21). Sizing the minimum radii of the strings and bars with respect to their member force is a feasible procedure in this study as the member forces in Eqs. (2.22) and (2.21) are independent from their cross-sectional area. Once the minimum radii of the strings and bars are determined (in terms of the applied force f, D-bar geometric parameters l, α, q and p, and material properties), the minimal mass and the energy stored of the D-bar system can be analytically assessed.

Theorem 2.4.1. *Consider a D-bar system of complexity q, angle parameter α, length l, and p strings per D-bar unit subject to a compressive force of magnitude f. Suppose that all the strings and bars are loaded up to the onset of failure corresponding to reaching the critical buckling force of the bars and the material yield stress of the strings. The material comprising the strings has Young's modulus E_s and yield stress σ_s, and the material comprising the bars has Young's modulus E_b. Then, the total mechanical energy stored in the D-bar system V_D is given as:*

$$V_D = \frac{2^{q-2}}{p^{\frac{q}{2}} \cos^{\frac{3q}{2}}(\alpha)} \left(\frac{\pi f^3}{E_b}\right)^{\frac{1}{2}} + \frac{l f \sigma_s (\sec^{2q}(\alpha) - 1)}{2E_s}. \tag{2.23}$$

Proof. We start by determining the total mechanical energy stored in the bars. The magnitude of the compressive force f_q of each bar in a D-bar system of complexity q provided in Eq. (2.21) can also be expressed in terms of their extensional stiffness k_q, current length l_q, and rest length l_{q0}:

[2]Using the radii for which the members are l to the onset of failure corresponds in practice to using a factor of safety of one, which is the case when structures are designed for minimum mass (minimum resources). A larger factor of safety can be readily introduced in the calculations based on specific application requirements.

$$f_q = k_q(l_q - l_{q0}), \tag{2.24}$$

where k_q is given as:

$$k_q = \frac{E_b A_q}{l_q}, \tag{2.25}$$

and A_q is the cross-sectional area of the bars. Assuming failure by buckling at the bars of the D-bar system, the maximum value of force allowed for each bar corresponds to the critical buckling force, obtained from Euler theory of buckling [43, 44] (cf. Eq. (2.1)):

$$f_q \;=\; \frac{\pi^3 E_b r_q^4}{4l_q^2} \;=\; \frac{\pi E_b A_q^2}{4l_q^2}. \tag{2.26}$$

where r_q is the radius of each bar (assumed to have circular cross-sections). Equation (2.26) is solved for A_q:

$$A_q = 2l_q \left(\frac{f_q}{\pi E_b}\right)^{\frac{1}{2}}, \tag{2.27}$$

and the previous expression for A_q is substituted in Eq. (2.25) to obtain an expression for k_q in terms of the compressive force f_q:

$$k_q = 2\left(\frac{f_q E_b}{\pi}\right)^{\frac{1}{2}}. \tag{2.28}$$

The elastic energy stored in each bar of a D-bar system of complexity q is denoted as V_q and is given as follows:

$$V_q \;=\; \frac{1}{2} k_q (l_q - l_{q0})^2. \tag{2.29}$$

We now proceed to determine an expression for V_q in terms of f, q, p, α, and material parameters. First, Eq. (2.24) is substituted into Eq. (2.29) and the following expression for V_q

is determined:

$$V_q = \frac{f_q^2}{2k_q}. \tag{2.30}$$

The expression for k_q from Eq. (2.28) is substituted into Eq. (2.30):

$$V_q = \frac{1}{4}\left(\frac{\pi f_q^3}{E_b}\right)^{\frac{1}{2}}. \tag{2.31}$$

The expression for f_q from Eq. (2.21) is substituted into Eq. (2.31) to obtain the mechanical energy stored of each bar in terms of f, q, p, α, and material parameters:

$$V_q \;=\; \frac{1}{4}\left(\frac{\pi f^3}{E_b(p\cos(\alpha))^{3q}}\right)^{\frac{1}{2}} \;=\; \frac{1}{4p^{\frac{3q}{2}}}\left(\frac{\pi f^3}{E_b\cos^{3q}(\alpha)}\right)^{\frac{1}{2}}. \tag{2.32}$$

The total mechanical energy in the bars of the D-bar system is obtained by adding the energy stored in each bar:

$$V_b \;=\; n_b V_q \;=\; \frac{2^{q-2}}{p^{\frac{q}{2}}}\left(\frac{\pi f^3}{E_b\cos^{3q}(\alpha)}\right)^{\frac{1}{2}}. \tag{2.33}$$

After determining the total mechanical energy in the bars of the D-bar system, we continue by determining the total mechanical energy stored in the strings. First, the magnitude of the tensile force t_i of every elastic string introduced in each self-similar iteration provided in Eq. (2.22) can also be expressed in terms of their extensional stiffness k_{si}, current length l_{si}, and rest length l_{si0}:

$$t_i = k_{si}(l_{si} - l_{si0}) \qquad\qquad i = 1, \ldots, q, \tag{2.34}$$

where k_{si} is given as:

$$k_{si} = \frac{E_s A_{si}}{l_{si}} \qquad\qquad i = 1, \ldots, q, \tag{2.35}$$

and A_{si} is the cross-sectional area of the strings. Assuming that failure occurs by material yielding

at the strings and that the tensile force of the strings reaches the onset of yielding, A_{si} is determined as follows:

$$t_i = \sigma_s A_{si} \qquad \rightarrow \qquad A_{si} = \frac{t_i}{\sigma_s}. \tag{2.36}$$

where σ_s is the yield stress of the material comprising the strings. Substituting the expression for A_{si} from Eq. (2.36) into Eq. (2.35), the following is obtained:

$$k_{si} = \frac{E_s t_i}{\sigma_s l_{si}}. \tag{2.37}$$

The expressions for t_i and l_{si} from Eqs. (2.22) and (2.19), respectively, are substituted into Eq. (2.37) and the following is obtained:

$$k_{si} \;=\; \frac{E_s}{\sigma_s}\frac{f\tan(\alpha)}{p^i \sin\left(\frac{\pi}{p}\right)\cos^{i-1}(\alpha)}\frac{2^{i-1}\cos^{i-1}(\alpha)}{l\sin\left(\frac{\pi}{p}\right)\tan(\alpha)} \;=\; \frac{2^{i-1} f E_s}{p^i \sin^2\left(\frac{\pi}{p}\right) l\sigma_s}. \tag{2.38}$$

The elastic energy stored in each string introduced at every self-similar iteration is denoted as V_{si} and is given as follows:

$$V_{si} \;=\; \frac{1}{2}k_{si}(l_{si} - l_{si0})^2 \qquad\qquad i = 1, \ldots, q. \tag{2.39}$$

We now proceed to determine an expression for V_{si} in terms of f, l, p, α, and material parameters. First, Eq. (2.34) is substituted into Eq. (2.39) and the following expression for V_{si} is determined:

$$V_{si} = \frac{t_i^2}{2k_{si}} \qquad\qquad i = 1, \ldots, q, \tag{2.40}$$

and the expression for k_{si} from Eq. (2.38) is substituted into Eq. (2.40) to obtain the following:

$$V_{si} = \frac{p^i \sin^2\left(\frac{\pi}{p}\right) l\sigma_s t_i^2}{2^i f E_s} \qquad\qquad i = 1, \ldots, q. \tag{2.41}$$

By substitution of the expression for t_i from Eq. (2.22) into Eq. (2.41), the following expression for V_{si} in terms of f, l, p, α, and material parameters is obtained:

$$V_{si} = \frac{lf\sigma_s \tan^2(\alpha)}{(2p)^i E_s \cos^{2i-2}(\alpha)} \qquad\qquad i = 1, \ldots, q. \tag{2.42}$$

The total mechanical energy stored in the strings of a D-bar system of complexity q, denoted as V_s, is determined as the sum of the energy stored in each of its strings as follows:

$$V_s = \sum_{i=1}^{q} n_{si} V_{si}. \tag{2.43}$$

Substituting Eqs. (2.18) and (2.42) into the previous equation, the following is obtained:

$$V_s \;=\; \sum_{i=1}^{q} p^i 2^{i-1} \frac{lf\sigma_s \tan^2(\alpha)}{(2p)^i E_s \cos^{2i-2}(\alpha)} \;=\; \frac{lf\sigma_s \tan^2(\alpha)}{2E_s} \sum_{i=1}^{q} \frac{1}{\cos^{2i-2}(\alpha)}. \tag{2.44}$$

To simplify the formula for the energy stored in a D-bar system in Eq. (2.44), we consider the following trigonometric identity that can be verified by the reader:

$$\tan^2(\alpha) \sum_{i=1}^{q} \frac{1}{\cos^{2i-2}(\alpha)} = \sec^{2q}(\alpha) - 1. \tag{2.45}$$

Substituting the previous identity into Eq. (2.44), we obtain the following formula for the mechanical energy stored in the strings of the D-bar system:

$$V_s = \frac{lf\sigma_s(\sec^{2q}(\alpha) - 1)}{2E_s}. \tag{2.46}$$

The total mechanical energy in the D-bar system, denoted as V_D, is obtained by adding the energy stored in the bars V_b and the energy stored in the strings V_s:

$$V_D = V_b + V_s. \tag{2.47}$$

By substitution of V_b from Eq. (2.33) and V_s from Eq. (2.46) into Eq. (2.47), the final expression

for V_D stated in Eq. (2.23) is obtained. □ □

We now proceed to provide a formula for the *minimal mass* m_D of the D-bar system in terms of the magnitude of the applied compressive force f.

Theorem 2.4.2. *Consider a D-bar system of length l, complexity q, angle parameter α, and p strings per D-bar unit subject to a compressive force of magnitude f. Suppose that the material comprising the bars has Young's modulus E_b and mass density ρ_b while the material comprising the strings has yield stress σ_s and mass density ρ_s. Then, the mass associated with the D-bar system, m_D is given as:*

$$m_D = \frac{p^{\frac{q}{2}}\rho_b l^2}{2^{q-1}\cos^{\frac{5q}{2}}(\alpha)}\left(\frac{f}{\pi E_b}\right)^{\frac{1}{2}} + \frac{lf\rho_s(\sec^{2q}(\alpha)-1)}{\sigma_s}. \tag{2.48}$$

The proof is given in Appendix C.2. Chapter 3 of [6] has a formula for mass m_D that includes additional strings connecting the end nodes of each D-bar unit, which are not required in a minimal mass design for a D-bar. From Eqs. (2.23) and (2.48), it is clear that a D-bar system stores more energy and requires less mass for lower values of the number of strings in each D-bar unit (p). Therefore, the minimum value of p, corresponding to 3, is assumed for the remainder of the chapter.

2.5 Comparison of Energy Stored and Mass of a D-bar System and a Bent Beam

2.5.1 Single Component Assessment

To compare D-bar systems with bent buckled beams at the single component level, the ratio of energy stored in a D-bar to that of a bent beam (V_D/V_B) and the ratio of the mass of a D-bar to that of a bent beam (m_D/m_B) are determined. The compressive force f and length l of the bent buckled beam and the D-bar system are assumed equal. The ratio V_D/V_B is determined by dividing V_D from Eq. (2.23) by V_B from Eq. (2.6):

$$\frac{V_D}{V_B} = \frac{2^{q+1}}{3^{\frac{q}{2}}\cos^{\frac{3q}{2}}(\alpha)}\left(\frac{\pi E_b}{\sigma_b^2}\right)\left(\frac{f^{\frac{1}{2}}}{l}\right)^2 + \frac{4\sigma_s(\sec^{2q}(\alpha)-1)(\pi E_b^3)^{\frac{1}{2}}}{E_s\sigma_b^2}\left(\frac{f^{\frac{1}{2}}}{l}\right). \tag{2.49}$$

For given values of α, f, l, and material parameters, the ratio V_D/V_B in Eq. (2.49) monotonically increases as q increases. Moreover, the limit of V_D/V_B as q approaches infinity is infinity. Therefore, there always exist D-bar systems that store more energy than a buckled beam (i.e., for which $V_D/V_B > 1$). The minimum value of q for such D-bar systems can be determined by increasing q until the value of $\frac{V_D}{V_B}$ becomes greater than 1. In order to further comparatively assess the feasibility of D-bar systems against buckled beams, their mass ratio must also be evaluated. The ratio m_D/m_B is determined by dividing m_D from Eq. (2.48) by m_B from Eq. (2.7):

$$\frac{m_D}{m_B} = \frac{3^{\frac{q}{2}}}{2^q \cos^{\frac{5q}{2}}(\alpha)} + \frac{\rho_s(\sec^{2q}(\alpha) - 1)(\pi E_b)^{\frac{1}{2}}}{2\sigma_s \rho_b} \left(\frac{f^{\frac{1}{2}}}{l}\right). \tag{2.50}$$

It is noted that the length l and applied force magnitude f appear only in the parameter $f^{\frac{1}{2}}/l$ in Eqs. (2.49) and (2.50). This parameter can be used as a scaling factor to evaluate D-bar energy storage components across scales.

We now proceed to provide quantitative comparisons between D-bar systems and bent buckled beams using the stored energy and mass ratios provided in Eqs. (2.49) and (2.50). Conventional material parameters of aluminum are assumed for the beam, bars, and strings ($E_b = E_s = 60$ GPa, $\sigma_b = \sigma_s = 110$ MPa, $\rho_b = \rho_s = 2700$ kg/m^3). These values are used to generate the contour plots of V_D/V_B shown in Fig. 2.5 for $f^{\frac{1}{2}}/l = 100$ N$^{\frac{1}{2}}$/m, 150 N$^{\frac{1}{2}}$/m, and 200 N$^{\frac{1}{2}}$/m. The axes of the contour plots correspond to the D-bar system complexity q and angle α (refer to Fig. 2.3). As indicated in Fig. 2.5, as the value of $f^{\frac{1}{2}}/l$ increases, there exist D-bar systems of lower complexity q and lower α that store more energy than that of bent buckled beams (i.e., for which $V_D/V_B > 1$). D-bars of low q are desirable as they require fewer members/joints and are easier to manufacture while D-bars of low α occupy smaller volumes. It is also noted that even though the results show that increasing complexity would generate D-bar systems of higher energy storing capabilities, manufacturing and scaling issues would prevent the synthesis of D-bar systems of very high complexity.

Contours of the ratio for the mass of the D-bar system to the bent beam (m_D/m_B) are shown in Fig. 2.6. The design space of D-bar systems that have lower mass than bent beams (i.e., for which

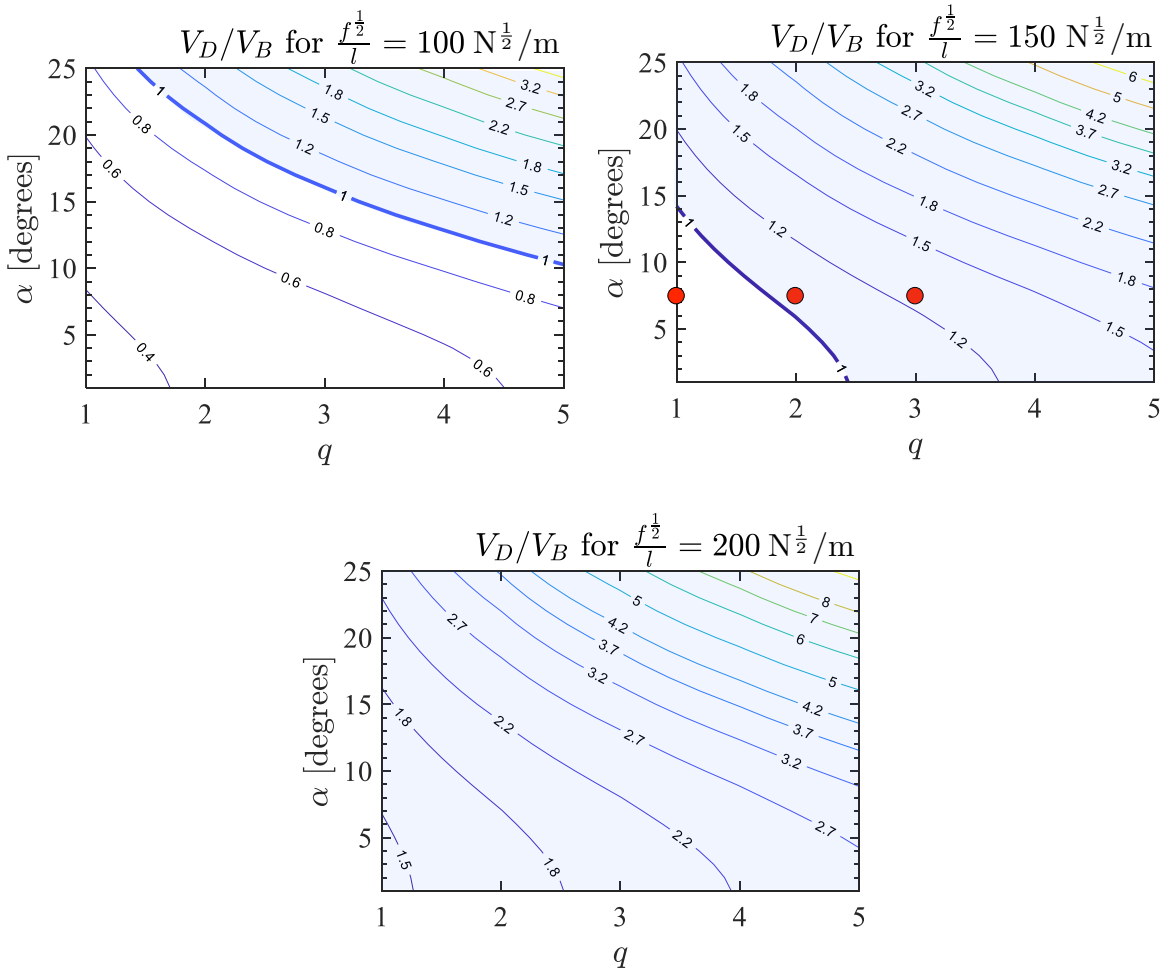

Figure 2.5: Contours of ratio of mechanical energy stored for the D-bar system to the bent beam (V_D/V_B). The shaded areas show the regions for which $V_D/V_B > 1$. Material parameters of aluminum are assumed for the beam, bars, and strings. D-bar structures for the red dots corresponding to complexities $q = 1, 2, 3$ and $\alpha = 7.5°$ are shown in Fig. 2.9.

$m_D/m_B < 1$) is shown in the shaded regions. It is observed that there are D-bar systems of any of the shown complexities for which $m_D/m_B < 1$ provided that α is lower than approximately 17°.

A favorable D-bar system stores more energy while requiring less mass to take the same compressive load than a bent buckled beam. The design space of D-bar systems that meet such requirements corresponds to the intersection of the regions where $V_D/V_B > 1$ and $m_D/m_B < 1$. Based on Figs. 2.5 and 2.6, Fig. 2.7 shows the regions where D-bar systems are favorable in terms of having lower mass and higher energy storage. The trends in Fig. 2.7 show that D-bar systems

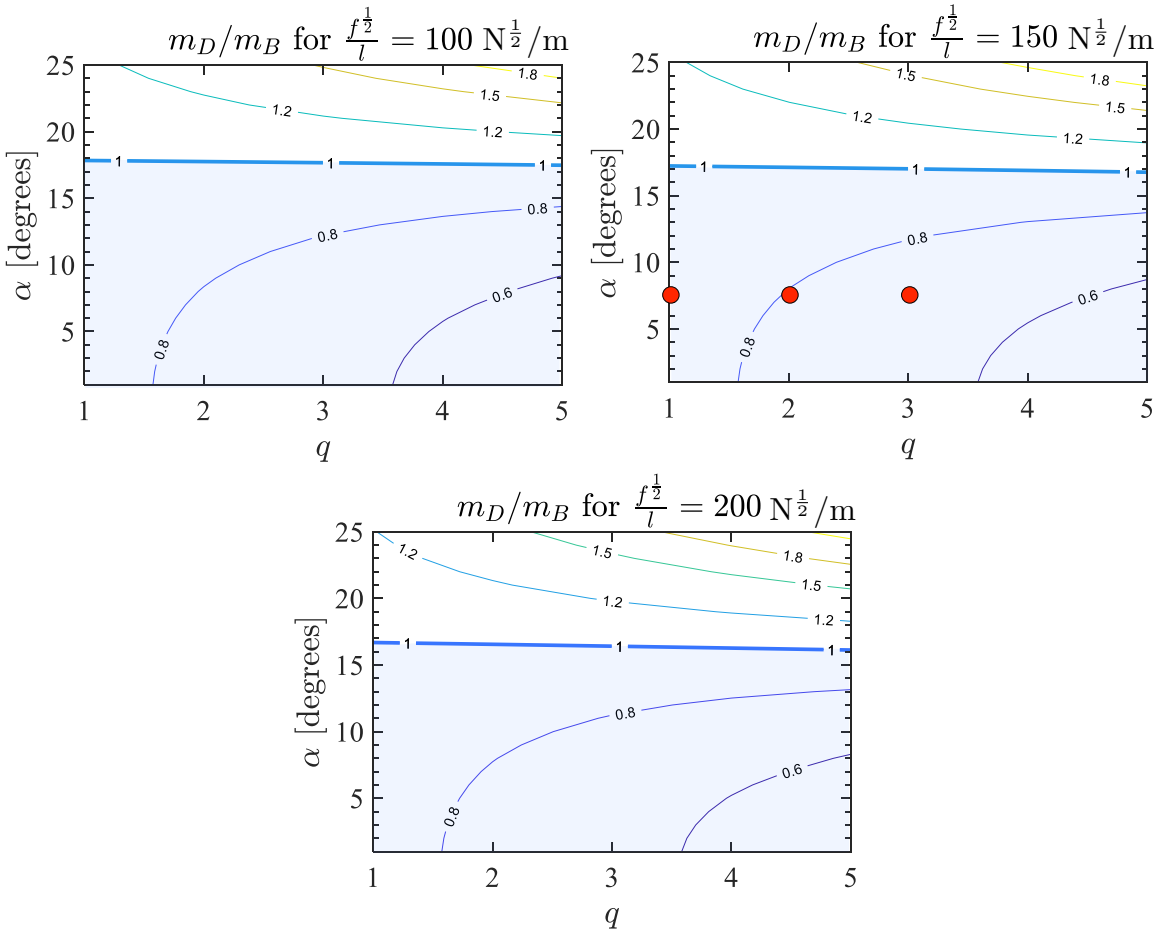

Figure 2.6: Contours of ratio of mass for the D-bar system to the bent beam (m_D/m_B). The shaded areas show the regions for which $m_D/m_B < 1$. Material parameters of aluminum are assumed for the beam, bars, and strings. D-bar structures for the red dots corresponding to complexities $q = 1, 2, 3$ and $\alpha = 7.5°$ are shown in Fig. 2.9.

with lower values of q and α have better performance than bent beams for higher values of $f^{\frac{1}{2}}/l$, which correspond to higher values of compressive force f and/or lower values of length l. This is observed as the design region for which $V_D/V_B > 1$ and $m_D/m_B < 1$ expands towards lower values of q and α as $f^{\frac{1}{2}}/l$ is increased in Fig. 2.7. These trends indicate that D-bar systems are more favorable as mass-efficient energy absorption components in systems subject to high impact loads (large values of f) and having limited volumes (low values of l).

A new parameter corresponding to the *mechanical energy stored per unit mass* for the bent beam is given as:

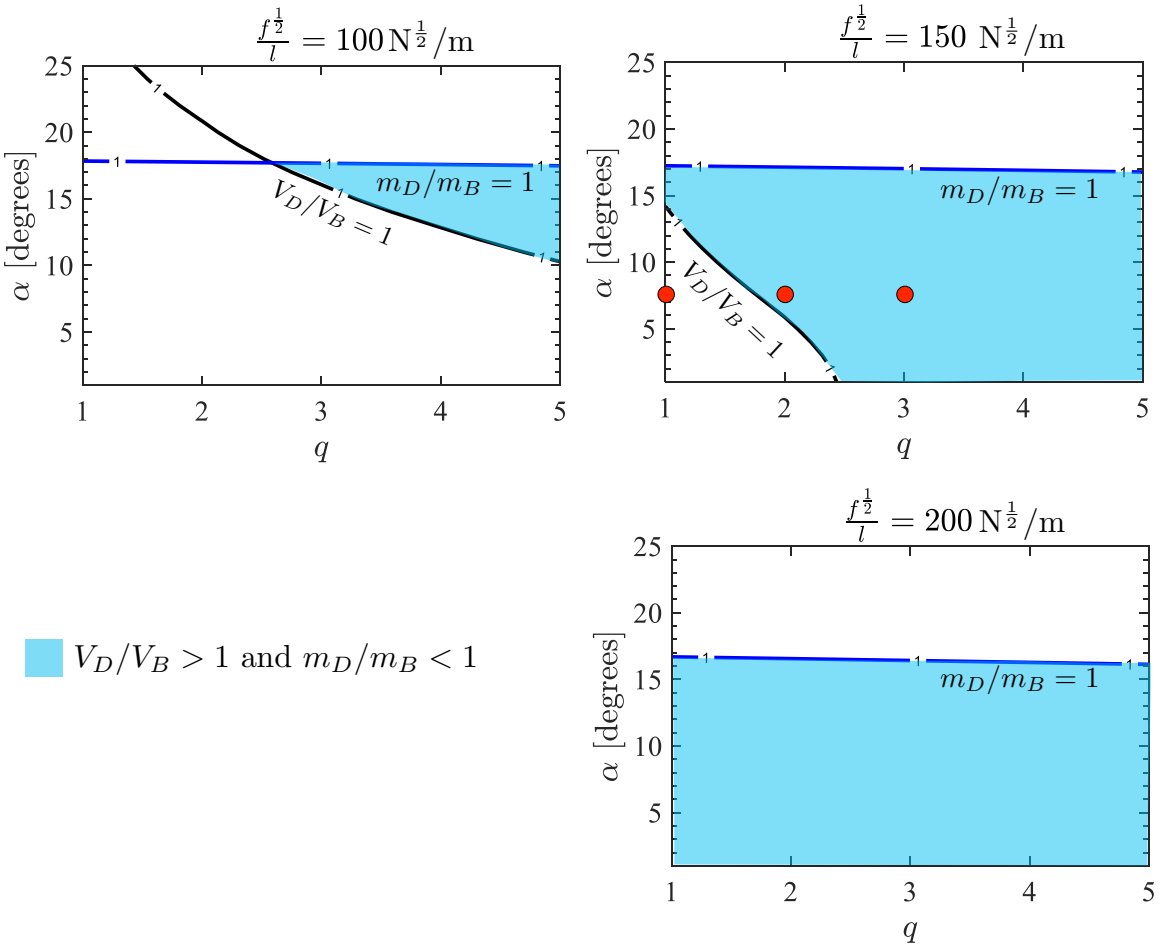

Figure 2.7: Regions showing the design space of D-bar systems for which $V_D/V_B > 1$ and $m_D/m_B < 1$.

$$\mu_B := \frac{V_B}{m_B} = \frac{\sigma_b^2}{16\rho_b E_b}, \tag{2.51}$$

which can be calculated by substituting for the mechanical energy stored in the bent beam V_B, given by Eq. (2.6) and the associated mass m_B, given by Eq. (2.7). Notice that the ratio μ_B is independent of the beam length l and applied force magnitude f.

The ratio of V_D to m_D, denoted as μ_D, corresponds to the *mechanical energy stored per unit mass* for the D-bar system:

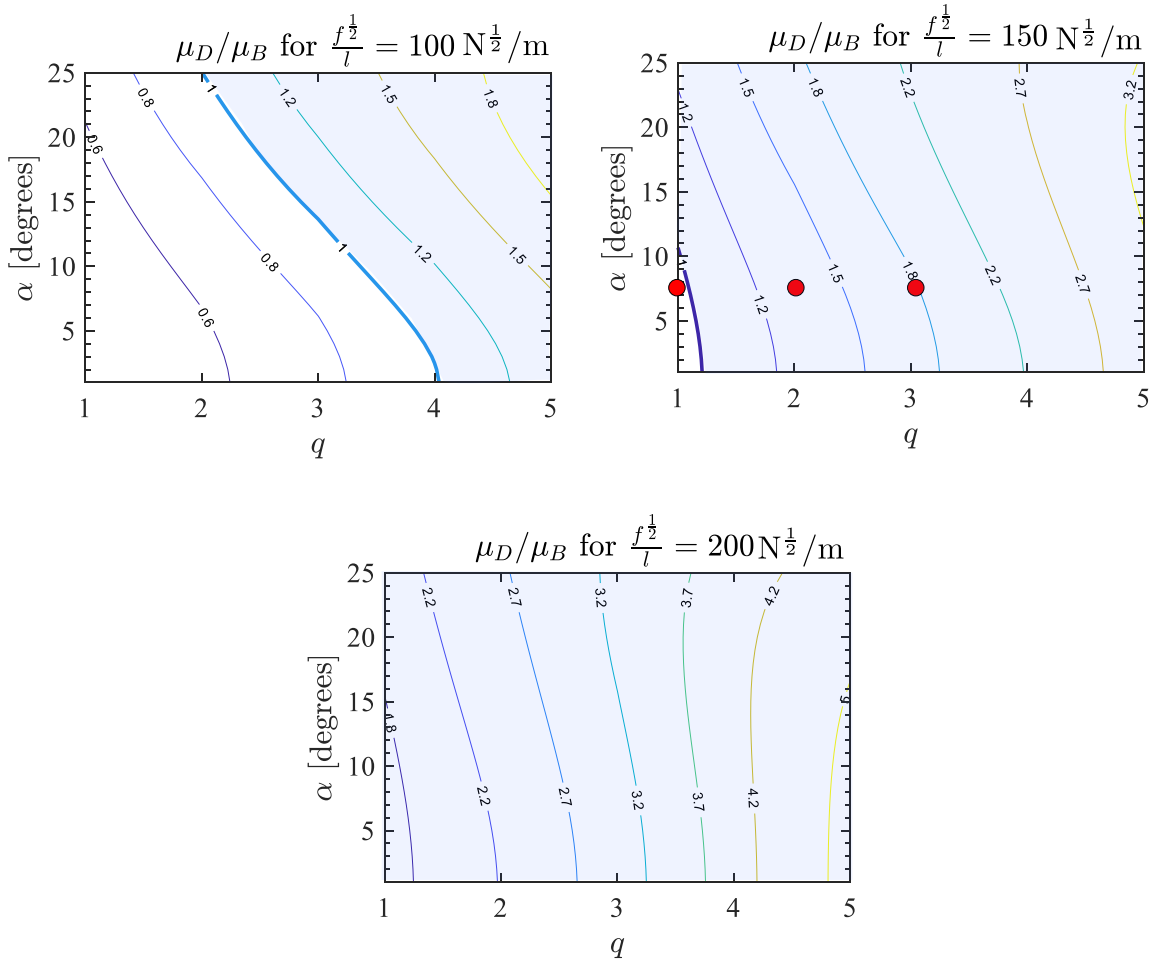

Figure 2.8: Contours of ratio of V_D/m_D for the D-bar system to the bent beam V_B/m_B. The shaded areas show the regions for which $\mu_D/\mu_B > 1$. Material parameters of aluminum are assumed for the beam, bars, and strings. D-bar structures for the red dots corresponding to complexities $q = 1, 2, 3$ and $\alpha = 7.5°$ are shown in Fig. 2.9.

$$\mu_D := \frac{V_D}{m_D} = \frac{V_b + V_s}{m_b + m_s}, \tag{2.52}$$

which can also be written as:

$$\mu_D = \frac{\dfrac{2^{q-2}}{p^{\frac{q}{2}}\cos^{\frac{3q}{2}}(\alpha)}\left(\dfrac{\pi}{E_b}\right)^{\frac{1}{2}}\left(\dfrac{f^{\frac{1}{2}}}{l}\right) + \dfrac{\sigma_s(\sec^{2q}(\alpha)-1)}{2E_s}}{\dfrac{p^{\frac{q}{2}}\rho_b}{2^{q-1}\cos^{\frac{5q}{2}}(\alpha)}\left(\dfrac{1}{\pi E_b}\right)^{\frac{1}{2}}\left(\dfrac{f^{\frac{1}{2}}}{l}\right)^{-1} + \dfrac{\rho_s(\sec^{2q}(\alpha)-1)}{\sigma_s}}. \tag{2.53}$$

The previous expression for μ_D is determined by substitution of V_D and m_D from Eqs. (2.23) and (2.48), respectively, into Eq. (2.52). Notice that D-bar length l and applied force magnitude f again only appear in the parameter $f^{\frac{1}{2}}/l$ in Eq. (2.53).

The shaded region in the Fig. 2.8 provides the design region for $\mu_D/\mu_B > 1$ for a single component analysis. The shaded area corresponds to the design region where mechanical energy stored per unit mass for the D-bar system is higher than the mechanical energy stored per unit mass for the bent beam. Fig. 2.8 shows that D-bar system have better performance than bent beams for higher values of $f^{\frac{1}{2}}/l$.

A single beam (in its initial configuration) and D-bar systems of complexities $q = 1, 2, 3$ indicated with red dots in Figs. 2.5–2.7 are illustrated in Fig. 2.9. The calculated radii of the beam (Eq. (2.12)), bars (Eq. (C.13)), and strings (Eq. (C.18)) are considered in such figures. It is worth noting that the radii of the bars of the D-bar system decrease by increasing the complexity q. Also notice that $q = 3$ stores 25% more energy and saves 30% mass compared to a beam. This is a good gain for space applications. No intersection between any bar and string was observed for all complexities in Fig. 2.9.

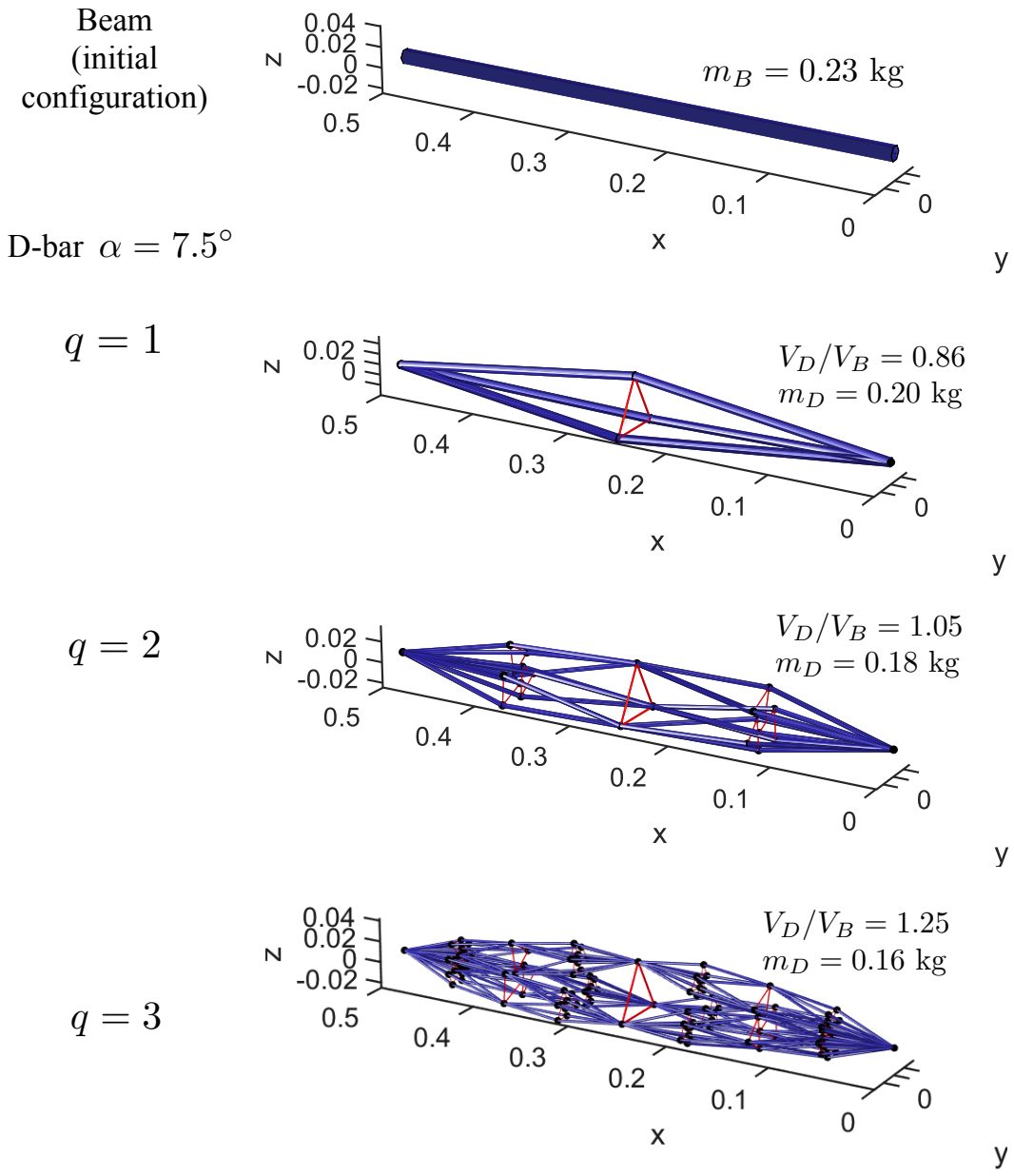

Figure 2.9: Schematics of a beam (initial configuration prior to buckling) and D-bars of different complexities. The axes units are in meters. Values of $\alpha = 7.5^\circ$, $l = 0.5$ m, $f^{\frac{1}{2}}/l = 150$ N$^{\frac{1}{2}}$/m, and material parameters of aluminum for the beam, bars, and strings are assumed. The calculated radii of the beam, bars, and strings are considered in the schematics.

2.5.2 Assembly-level Assessment

Having compared the energy stored and mass for single D-bar systems and bent beams, this section considers an example of a planetary lander to compare D-bar systems and bent buckled beams as part of a larger tensegrity structure. The geometry and boundary conditions of the tensegrity lander are first described. Then, the equilibrium equations used to calculate the forces in each member are provided. Finally, the energy stored and the total mass of a lander with bent beams are compared against those of a lander with D-bar systems replacing the beams.

The geometry of the tensegrity lander developed in [2] for planetary exploration is considered for this assessment. The lander has 6 compressive members of length L and 24 tensile members of length $(3/8)^{\frac{1}{2}}L$. As illustrated in Fig. 2.10(a), vertical compressive forces are applied to the top three nodes of the structure and the bottom three nodes are kept fixed to simulate the impact conditions. The total force applied to the top surface is denoted as F.

To calculate the forces in each member, the equilibrium equations for tensegrity systems developed in [16] are used. First, let $n_i \in \mathbb{R}^3$ be the position vector of the i^{th} node and N be the matrix containing the node position vectors $N = [n_1\ n_2\ \cdots]$. Also, let $w_i \in \mathbb{R}^3$ be the vector of external forces applied at the i^{th} node and W be the matrix containing such vectors $W = [w_1\ w_2\ \cdots]$. The magnitude of the tensile force per unit length at the i^{th} string is denoted γ_i and the magnitude of the compressive force per unit length at the j^{th} bar is denoted λ_j. Define the vectors $\gamma = [\gamma_1\ \gamma_2\ \cdots]^\top$ and $\lambda = [\lambda_1\ \lambda_2\ \cdots]^\top$. Denote $\hat{\gamma}$ and $\hat{\lambda}$ as the square matrices whose diagonal components correspond to the elements of γ and λ. The equilibrium equations are then written as follows [16]:

$$N(C_s^\top \hat{\gamma} C_s - C_b^\top \hat{\lambda} C_b) = W, \tag{2.54}$$

where C_b and C_s are connectivity matrices for bars and strings, respectively [16]. The node positions for the geometry shown in Fig. 2.10 are given by:

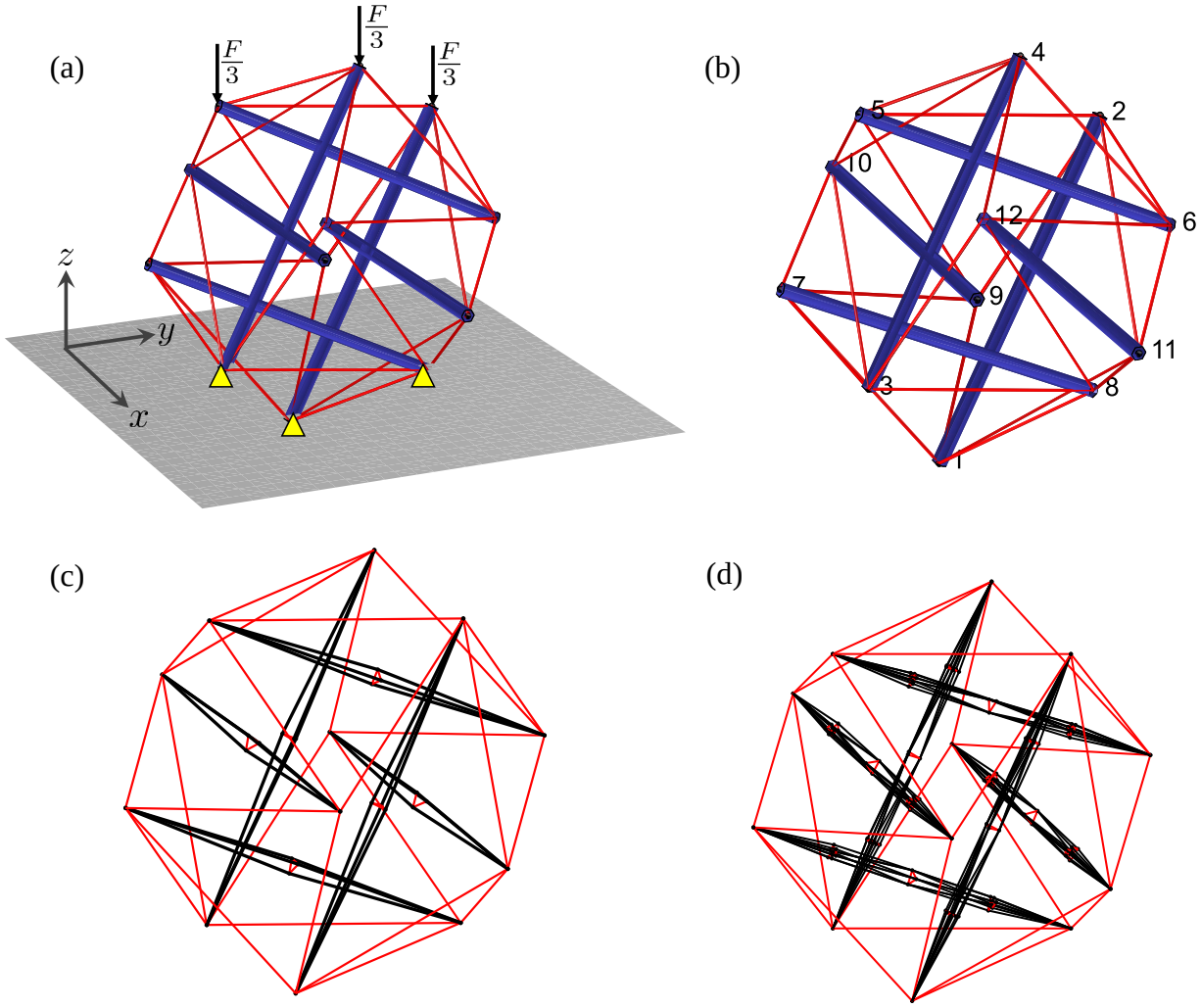

Figure 2.10: (a) Geometry and boundary conditions of a tensegrity lander [2]. The strings are shown in red and have length $\left(\frac{3}{8}\right)^{\frac{1}{2}} L$ and the beams are shown in blue and have length L. The yellow triangles indicate the nodes that are fixed. (b) Node labels (see Eq. (2.55)). (c) Tensegrity lander obtained by replacing the beams with D-bar systems of complexity $q = 1$. (d) Tensegrity lander obtained by replacing the beams with D-bar systems of complexity $q = 2$.

$$N = \begin{bmatrix} \frac{L}{4} & \frac{L}{4} & -\frac{L}{4} & -\frac{L}{4} & 0 & 0 & 0 & 0 & \frac{L}{2} & -\frac{L}{2} & \frac{L}{2} & -\frac{L}{2} \\ 0 & \frac{L}{\sqrt{5}} & 0 & \frac{L}{\sqrt{5}} & -\frac{L}{4\sqrt{5}} & \frac{7L}{4\sqrt{5}} & -\frac{3L}{4\sqrt{5}} & \frac{\sqrt{5}L}{4} & 0 & 0 & \frac{L}{\sqrt{5}} & \frac{L}{\sqrt{5}} \\ 0 & \frac{2L}{\sqrt{5}} & 0 & \frac{2L}{\sqrt{5}} & \frac{2L}{\sqrt{5}} & \frac{L}{\sqrt{5}} & \frac{L}{\sqrt{5}} & 0 & \frac{\sqrt{5}L}{4} & \frac{\sqrt{5}L}{4} & \frac{3L}{4\sqrt{5}} & \frac{3L}{4\sqrt{5}} \end{bmatrix}, \qquad (2.55)$$

and the external forces are given by:

$$w_2 = w_4 = w_5 = \begin{bmatrix} 0 & 0 & -\frac{F}{3} \end{bmatrix}^\top. \tag{2.56}$$

The reaction forces w_1, w_3, and w_8 at the fixed nodes can be calculated in a subsequent step after determining the loading of each tensile and compressive member. Equation (2.54) can also be written as:

$$\begin{bmatrix} (C_s^\top \otimes I_3)\hat{S} & -(C_b^\top \otimes I_3)\hat{B} \end{bmatrix} \begin{bmatrix} \gamma \\ \lambda \end{bmatrix} = w, \tag{2.57}$$

where $[b_1\ b_2\ \cdots] = NC_b^\top$ and $[s_1\ s_2\ \cdots] = NC_s^\top$ are respectively the vectors along the length of each bar and each string, $\hat{B} = \text{b.d.}(b_1, b_2, \cdots)$, $\hat{S} = \text{b.d.}(s_1, s_2, \cdots)$, $w^\top = [w_1^\top\ w_2^\top\ \cdots]$, b.d. is the block diagonal operator, and $\otimes$ is the Kronecker product.

The rows of Eq. (2.57) associated with the fixed nodes (nodes 1, 3, and 8 in this example) are removed. Subsequently, such an equation is solved numerically to find γ and λ such that the total sum of forces in all members is minimized with a constraint of γ and λ being positive, i.e., all the strings in the structure are in tension and all the bars are in compression. We calculate the compressive forces in the bars and the tensile forces in the strings under different landing configurations that correspond to different boundary conditions, i.e., as if the structure touched the ground at nodes $\{1, 3, 8\}$ (shown in Fig. 2.10), $\{3, 7, 10\}$, $\{2, 4, 5\}$, $\{2, 6, 11\}$, etc. Among different boundary conditions, the maximum load in each bar and each string is employed to design each individual element. From the symmetry of the structure, all the bars will have the same maximum compressive load, denoted as f, and all the strings will have the same maximum tensile load, denoted by t, among all the different landing configurations.

Proposition 2.5.1. *Consider the tensegrity lander whose geometry is illustrated in Fig. 2.10. The compressive members of the lander take a maximum load f and are comprised of a material with Young's modulus E_b, and mass density ρ_b. The strings take a maximum tensile load t and are*

comprised of a material with Young's modulus E_s, yield stress σ_s, and mass density ρ_s. In a minimum mass design, if the compressive members of the lander are beams that undergo buckling, its stored energy V_{SB} and mass m_{SB} are given as:

$$V_{SB} = (24)\left(\frac{3}{8}\right)^{\frac{1}{2}} \frac{\sigma_s L t}{2E_s} + (6)\frac{L^2\sigma_b^2}{8}\left(\frac{f}{\pi E_b^3}\right)^{\frac{1}{2}}, \tag{2.58}$$

$$m_{SB} = (24)\left(\frac{3}{8}\right)^{\frac{1}{2}} \frac{\rho_s L t}{\sigma_s} + (6)2L^2\rho_b\left(\frac{f}{\pi E_b}\right)^{\frac{1}{2}}. \tag{2.59}$$

Furthermore, if the compressive members of the lander are D-bar systems, its stored energy V_{SD} and mass m_{SD} are given as:

$$\begin{aligned} V_{SD} &= (24)\left(\tfrac{3}{8}\right)^{\frac{1}{2}} \frac{\sigma_s L t}{2E_s} \\ &\quad +(6)\left(\frac{2^{q-2}}{3^{\frac{q}{2}}\cos^{\frac{3q}{2}}(\alpha)}\left(\frac{\pi f^3}{E_b}\right)^{\frac{1}{2}} + \frac{Lf\sigma_s(\sec^{2q}(\alpha)-1)}{2E_s}\right), \end{aligned} \tag{2.60}$$

$$\begin{aligned} m_{SD} &= (24)\left(\tfrac{3}{8}\right)^{\frac{1}{2}} \frac{\rho_s L t}{\sigma_s} \\ &\quad +(6)\left(\frac{3^{\frac{q}{2}}\rho_b L^2}{2^{q-1}\cos^{\frac{5q}{2}}(\alpha)}\left(\frac{f}{\pi E_b}\right)^{\frac{1}{2}} + \frac{Lf\rho_s(\sec^{2q}(\alpha)-1)}{\sigma_s}\right). \end{aligned} \tag{2.61}$$

Proof. The energy stored in each of the strings is determined using the procedure followed in Eqs. (2.34)–(2.41). This energy stored is denoted V_S and is given as:

$$V_S = \left(\frac{3}{8}\right)^{\frac{1}{2}} \frac{\sigma_s L t}{2E_s}. \tag{2.62}$$

The mass of each string is denoted m_S and is found using the approach described in Eqs. (C.15) and (C.16). The expression for m_S is given as follows:

$$m_S = \left(\frac{3}{8}\right)^{\frac{1}{2}} \frac{\rho_s L t}{\sigma_s}. \tag{2.63}$$

If the compressive members are beams that undergo buckling, their energy stored (V_B) and

mass (m_B) as functions of their length L and compressive force f are given by Eqs. (2.6) and (2.7), respectively. Conversely, if the compressive members are D-bar systems, their energy stored (V_D) and mass (m_D) as functions of L and f are given by Eqs. (2.23) and (2.48), respectively.

The energy stored (V_{SB}) and mass (m_{SB}) of a lander with beams that undergo buckling are given as:

$$V_{SB} = 24V_S + 6V_B, \tag{2.64}$$

$$m_{SB} = 24m_S + 6m_B. \tag{2.65}$$

Substituting Eqs. (2.62) and (2.6) into Eq. (2.64), the expression for V_{SB} of Eq. (2.58) is obtained. Substituting Eqs. (2.63) and (2.7) into Eq. (2.65), the expression for m_{SB} of Eq. (2.59) is obtained.

Similarly, the energy stored (V_{SD}) and mass (m_{SD}) of a lander with D-bar systems as its compressive members are given as:

$$V_{SD} = 24V_S + 6V_D, \tag{2.66}$$

$$m_{SD} = 24m_S + 6m_D. \tag{2.67}$$

Substituting Eqs. (2.62) and (2.23) into Eq. (2.66), the expression for V_{SD} of Eq. (2.60) is obtained. Substituting Eqs. (2.63) and (2.48) into Eq. (2.67), the expression for m_{SD} of Eq. (2.61) is obtained. This concludes the proof. □ □

Having determined the mechanical energy stored and the total mass of tensegrity landers whose compressive members are beams that undergo buckling or D-bar systems, the two designs are now compared. Conventional material parameters of aluminum are assumed for the beams, bars, and strings are assumed ($E_b = E_s = 60$ GPa, $\sigma_b = \sigma_s = 110$ MPa, $\rho_b = \rho_s = 2700$ kg/m^3). Values

of $F = 15000$ N and $L = 1$ m are also assumed. These values of F and L resulted in maximum member forces $f = 22360$ N and $t = 9128$ N. Contours for the ratios of mechanical energy stored and total mass for the two designs are provided in Fig. 2.11. In the m_{SD}/m_{SB} contour, it is observed that landers with D-bar systems have lower mass than landers with bent beams for the entire studied domain of q, provided that α is below approximately $17°$.

The values of ratio are $m_{SD}/m_{SB} = 0.92$, $m_{SD}/m_{SB} = 0.85$, and $m_{SD}/m_{SB} = 0.78$ for $q = 1, 2,$ and 3, respectively. These values are corresponding to the three red circles in Fig. 2.11 for $\alpha = 10°$, showing a significant saving in the mass of the lander. The design region of landers with D-bar systems that store more energy ($V_{SD}/V_{SB} > 1$) and require less mass ($m_{SD}/m_{SB} < 1$) than landers with bent buckled beams is also shown in Fig. 2.11. The values corresponding to the three red dots in Fig. 2.11 for V_{SD}/V_{SB} contour plots are: $V_{SD}/V_{SB} = 0.96$, $V_{SD}/V_{SB} = 1.05$, and $V_{SD}/V_{SB} = 1.11$ for $q = 1, 2,$ and 3, respectively. Fig. 2.11 also shows the contour plot corresponding to $\mu_{SD}/\mu_{SB} > 1$. The values corresponding to the three red dots in Fig. 2.11 for μ_{SD}/μ_{SB} contour plots are: $\mu_{SD}/\mu_{SB} = 1.04$, $\mu_{SD}/\mu_{SB} = 1.23$, and $\mu_{SD}/\mu_{SB} = 1.42$. Such a design region spans the entire studied domain of q, with lower values of α feasible by increasing q. At $q = 3$, any value of α below approximately $17°$ generates a favorable D-bar design in terms of energy stored and mass. Overall, the results in Fig. 2.11 indicate that designs of tensegrity landers can be significantly enhanced if beams that undergo buckling during vehicle impact are replaced with D-bar systems of low complexities.

2.6 Conclusions

This chapter presented an analytical study of D-bar tensegrity systems for applications as lightweight components for mechanical energy absorption. This work was motivated by aerospace structures such as planetary landers that necessitate these lightweight components to absorb energy from large impact loads (to protect their interior systems and payload) while requiring minimal mass. Recent works proposed bent buckled beams used in “flexible-bar tensegrity" concepts as energy absorption components in planetary landers. Here, conversely, the approach was to absorb energy from external loads as mechanical (elastic) energy in the strings and bars of D-bar systems

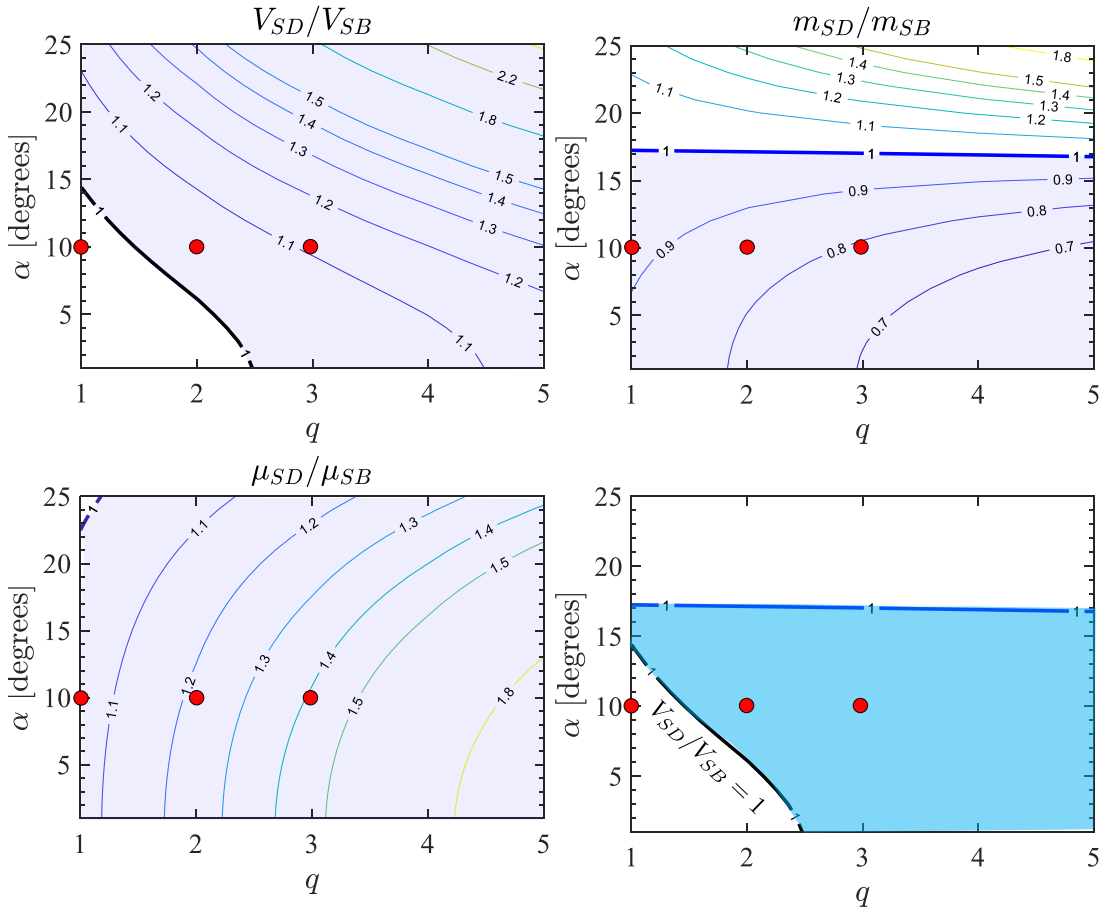

Figure 2.11: Contours of ratios of mechanical energy stored (V_{SD}/V_{SB}) and total mass (m_{SD}/m_{SB}) for tensegrity landers whose compressive members are D-bar systems or beams that undergo buckling. The design region with $V_{SD}/V_{SB} > 1$ and $m_{SD}/m_{SB} < 1$ is shown in 2nd row-2nd column plot. The shaded areas in 2nd row-1st column plot, show the regions for which $\mu_{SD}/\mu_{SB} > 1$. Material parameters of aluminum are assumed for the beams, bars, and strings.

without triggering local instabilities such as buckling (thereby enabling more reliable structures).

Previous studies have demonstrated that D-bar systems support compressive loads with minimal mass compared to continuum structures such as prismatic columns. This work adds to the body of knowledge of tensegrity structures by developing analytical formulas to describe the energy absorption properties of D-bar systems. The analytical equations are applicable to D-bar systems of any complexity, number of strings in each D-bar unit, elastic material properties, system length, and applied compressive force.

The energy stored in D-bar systems was compared with that of bent buckled beams. The comparisons were made between D-bar systems and bent buckled beams as isolated components subject to a compressive load and as the components of tensegrity planetary landers. The following was concluded from the comparative studies:

- For the component-level comparison, the results showed that D-bar system of low complexity allow for higher energy storage *and* lower mass than bent buckled beams. For $q = 2$ and $\alpha = 7.5°$, the mass saving was around 21% with 5% higher energy storage (Fig. 2.9)

- For the comparison as a part of larger tensegrity system, the results followed the same trend. For $q = 2$ and $\alpha = 10°$, the mass saving was around 15% with 4% higher energy storage (Fig. 2.11)

- D-bar systems of lower complexities had better performance (in terms of energy stored and mass) than bent beams for higher compressive force and lower system length. Notice the increase in design region as the value of $f^{\frac{1}{2}}/l$ increases in Fig. 2.5 or Fig. 2.7. These trends indicate that D-bar systems are more favorable as mass-efficient energy absorption components in structures subject to high impact loads and placed in small volumes (such as aerospace systems)

Therefore, it is finally concluded that D-bar systems can enhance the design of planetary landers and other applications that require lightweight mechanical energy absorption components.

3. DESIGN OF MINIMUM MASS TENSEGRITY T-BAR STRUCTURE*

[1] This work centers on the design of tensegrity-based lattices, known as “T-bar" structures, capable of supporting compressive loads with minimum mass. Previous mass studies of load-bearing tensegrity structures based their calculations only on local failure of the truss members without consideration of global buckling failure. In this work, analytical formulas for the calculation of the mass of these structures under externally applied forces and pre-stress are derived. These formulas account for local failure of the T-bar structures (material yielding and buckling of its individual members). The formulation to determine the critical global buckling loads and mode shapes of tensegrity structures with arbitrary shape and topology is used in conjunction with local failure constraints (member material failure and member buckling) to develop a holistic model for load-bearing tensegrity structures that accounts for both local and global failure modes. A numerical approach is introduced to assess the global stability of the structures under external forces and pre-stress and to account for global buckling in the design process. The mass of the structure is minimized by adjusting its shape and topology while global buckling is simultaneously prevented using two different design methods: *i)* optimizing the pre-stress distribution in the structure, and *ii)* optimizing the cross-section areas of the tensegrity members. Using either method, the results show that 2D and 3D T-bars possess a global minimum mass design for a given externally applied force and length. The computed results also show that designs obtained by optimizing the cross-section areas of the members have lower mass than those obtained by optimizing the pre-stress distribution.

3.1 Introduction

Tensegrity structures with double-pyramid shape known as T-bars and D-bars have been analytically shown to support compressive loads with minimum mass compared to continuum

[1]*Portions of this section are reprinted or adapted from [45] : Raman Goyal, Robert E. Skelton, and Edwin A. Peraza Hernandez, “Minimum Mass Tensegrity T-bar Structure with local and global stability”, Mechanics Research Communications, 103 (103477), 2020, DOI: 10.1016/j.mechrescom.2020.103477.

compressive columns [6]. The mass calculations of the tensegrities in the aforementioned studies are based on estimations of the minimal cross-section areas of their individual members considering their local failure modes such as material yielding and/or buckling. To obtain more accurate and reliable designs and assessments of the mass of load-bearing tensegrity structures, their global stability under the applied loads must also be considered. A formulation for global buckling specifically developed for two-dimensional T-bar compressive structures was derived in [46, 47]. De Tommasi and coworkers provided an analytical condition for global instability of two-dimensional T-bar tensegrity fractals based on the potential energy stored in the structures. They also provide the optimal topology that minimizes structural mass considering both local and global instabilities [48]. First, they define the tangent stiffness matrix to be Hessian of potential energy, which can be very difficult to obtain for even a simple tensegrity structure. Second, the generalized displacements required to calculate potential energy are chosen to be symmetric and anti-symmetric, which simplifies the analysis of positiveness but loses the more generalized displacements. In a later paper, De Tommasi and coworkers presented a morphological optimization study on three-dimensional T-bar tensegrities considering local and global failure modes using the same approach developed in their previous work [42].

The objective of this work is to design tensegrity lattices for the support of compressive loads with minimal mass. The focus is on a tensegrity topology known as the T-bar structure, previously studied and proposed for compressive constructions [47, 42]. Schematics of T-bar structures are shown in Fig. 3.1. These structures have double-pyramid shape and compressive forces applied at their end points. T-bars can be used as components of lightweight lattice materials as illustrated in Fig 3.1. A T-bar of complexity $q = 1$ is formed by a single *T-bar unit* that has two bars (compressive members) of equal length along the loading direction and p bars connecting the intersection of the longitudinal bars to the vertices of a centered p-sided regular polygon. Figure 3.1 shows T-bars of $p = 2$ (2D T-bars) and $p = 4$ (T-bars with a centered square). Strings (tensile members) form the sides of the central polygon and also connect the vertices of this polygon to the end points of the T-bar unit. A T-bar of complexity q is formed by replacing the longitudinal

bars of a T-bar of complexity $q-1$ with T-bar units (this is denoted as a self-similar iteration), as illustrated in Fig. 3.1 for T-bars of complexities $q=2$ and $q=3$. Previous studies have only considered T-bars of complexity $q=1$ [42] or are limited to 2D T-bars [47]. This work is the first to consider 2D and 3D T-bars of arbitrary complexity in structural design of compressive lattices. Local and global failure modes are also accounted for, and different methods to prevent global buckling of the T-bars while preserving minimal mass are explored. This paper also discusses the effects of changing pre-stress, area of the strings and area of all the members into the critical buckling force and the minimum mass required for the structure.

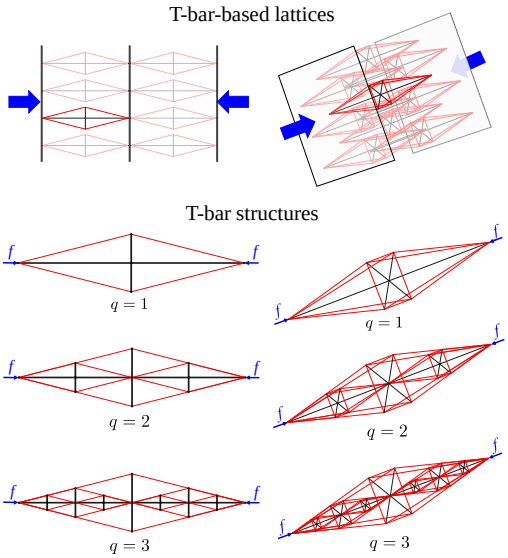

Figure 3.1: 2D and 3D T-bar structures of different complexity q. These structures can be integrated in larger assemblies to synthesize lattice compressive materials of minimal mass.

The contributions of this work are summarized as follows:

- This work is the first to provide a formulation to address structural design of compressive lattices using 2D and 3D T-bars of arbitrary complexity. Previous studies of compressive structures based on T-bar systems have only considered T-bars of complexity $q=1$ [42] or are limited to 2D T-bars [47].

- Equations for the member loads in T-bar systems are extended from previous works [6, 47] to account for arbitrary pre-stress loading scenarios.

- Local and global failure stability constraints are concurrently accounted for in the minimal mass design of T-bar systems. A novel algorithm that allows for the design of minimum mass 2D and 3D T-bars of any complexity is developed. Two approaches to prevent global instabilities, one based on optimizing the pre-stress distribution and the other based on optimizing the cross-section areas of the members, are implemented in the algorithm. The algorithm hierarchically determines minimal mass designs of the T-bar units introduced at each self-similar iteration and hence the final T-bar system is also of minimal mass.

The design of compressive T-bar members of minimal mass is relevant for the development of any general tensegrity structure where *lightweight properties* are critical. This is because monolithic compressive members (bars or struts) can be replaced with T-bars of optimal complexity to minimize the overall structural mass. Examples of recent practical tensegrity structures that would greatly benefit from the replacement of bars/struts by optimal T-bars include: metamaterials based on pentamode lattices studied by Fraternali, Amendola, and coworkers [49, 50]; ball-like robots for planetary exploration investigated by Sunspiral and coworkers [51, 52]; and minimal mass tensegrity bridges researched by Fraternali, Skelton, and coworkers [23, 24].

This chapter is organized as follows: Section 3.2 provides the analytical formulas for the mass of T-bar structures considering local failure criteria of the individual members. In Section 3.3, we formulate the global stiffness matrix of tensegrity structures via linearization of the equations of static equilibrium and provide the criteria for global stability of T-bar structures In Section 3.4, methods for determining minimum mass designs of T-bar structures are detailed and an algorithm for hierarchical design of minimal mass T-bar structures with arbitrary complexity is given. Results and discussion are provided in Section 3.5 to demonstrate the implementation of the given algorithm to design lightweight tensegrities under local and global failure constraints. Concluding remarks are provided in Section 3.6.

3.2 Minimum Mass under Local Failure Constraints

This section provides the analytical formulas for the mass of T-bar structures considering local failure criteria of the individual members. Figure 3.2 shows a 3D T-bar structure subjected to a compressive force f. The total length of the T-bar structure, is denoted by l. Each T-bar unit forming a T-bar structure has two kinds of bars: *longitudinal bars* that are aligned with the applied compressive force, and *radial bars* that connect the center of the unit to the vertices of the central polygon. A T-bar unit also has two kinds of strings: *planar strings* that form the sides of the central polygon and *diagonal strings* that connect the vertices of the central polygon to the end points of the unit. In each T-bar unit, the angle between the longitudinal bars and the diagonal strings is denoted as the aperture angle. The aperture angle of the T-bar units introduced at the i^{th} self-similar iteration is denoted by α_i, where $i = 1, 2, \ldots, q$ (see Fig. 3.2).

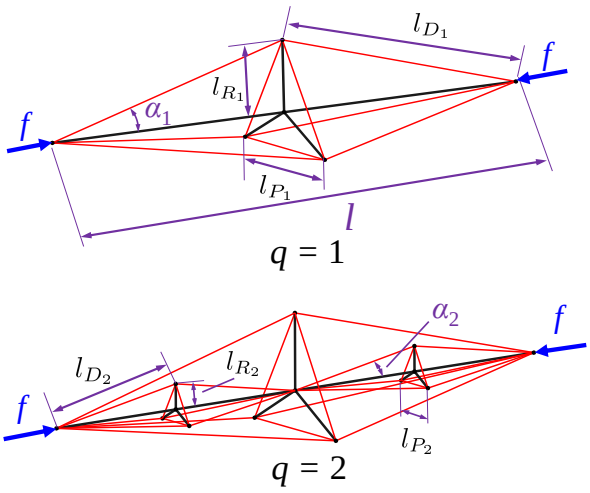

Figure 3.2: Geometric parameters of 3D tensegrity T-bar systems for complexities $q = 1, 2$.

The material properties of the bars and strings are assumed given, and therefore the calculation of the mass of the T-bar consists of finding the cross-section area (obtained through local failure constraints) and the length of the members. The length of the longitudinal bars, radial bars, diagonal strings, and planar strings are denoted by l_L, l_{R_i}, l_{D_i}, and l_{P_i}, respectively. Also, the

total number of longitudinal bars, radial bars, diagonal strings, and planar strings in the T-bar structure are denoted by n_L, n_{R_i}, n_{D_i}, and n_{P_i}, respectively, for $i = 1, \ldots, q$. These parameters are determined from geometry as follows:

$$n_L = 2^q, \quad l_L = \frac{l}{2^q}. \tag{3.1}$$

$$n_{R_i} = 2^{i-1}(p), \quad l_{R_i} = \frac{l}{2^i}\tan(\alpha_i), \quad \text{for} \quad i = 1, 2, \ldots, q, \tag{3.2}$$

$$n_{D_i} = 2^{i-1}(2p), \quad l_{D_i} = \frac{l}{2^i \cos(\alpha_i)}, \quad \text{for} \quad i = 1, 2, \ldots, q, \tag{3.3}$$

$$n_{P_i} = 2^{i-1}(p), \; l_{P_i} = \frac{2l \sin\left(\frac{\pi}{p}\right) \sin(\alpha_i)}{2^i \cos(\alpha_i)}, \; \text{for } i = 1, 2, \ldots, q. \tag{3.4}$$

The magnitude of compressive force in the radial bars introduced at each iteration is denoted by $f_{R_i}, i = 1, \ldots, q$, and the magnitude of the compressive force in the longitudinal bars is denoted by f_L. Using the static equilibrium condition that the sum of the member forces at each node is zero, the magnitude of compressive forces in all the bar members can be uniquely calculated from the given external force f and independent string pre-tensions t_{D_i} and t_{P_i}:

$$f_L = f + p\sum_{i=1}^{q} t_{D_i}\cos(\alpha_i), \quad f_{R_i} = 2t_{D_i}\sin(\alpha_i) + 2t_{P_i}\sin\left(\frac{\pi}{p}\right), \quad \text{for} \quad i = 1, 2, \ldots, q. \tag{3.5}$$

The term $2t_{P_i}\sin\left(\frac{\pi}{p}\right)$ in the formula for the compressive force of the radial bars f_{R_i} in Eq. (3.5) can be intuitively observed by analyzing the force balance of the central p-sided polygon of a T-bar unit. Examples for $p = 3$, $p = 4$, and any p are provided in Fig. 3.3. These schematics indicate that the radial bars must balance a force of $t_{P_i}\cos\left(\frac{\pi}{2} - \frac{\pi}{p}\right)$ for each of the two planar strings connected

at every polygon vertex, making the total force contribution of these strings into the compressive force of the radial bars $2t_{P_i}\cos\left(\frac{\pi}{2}-\frac{\pi}{p}\right)=2t_{P_i}\sin\left(\frac{\pi}{p}\right)$.

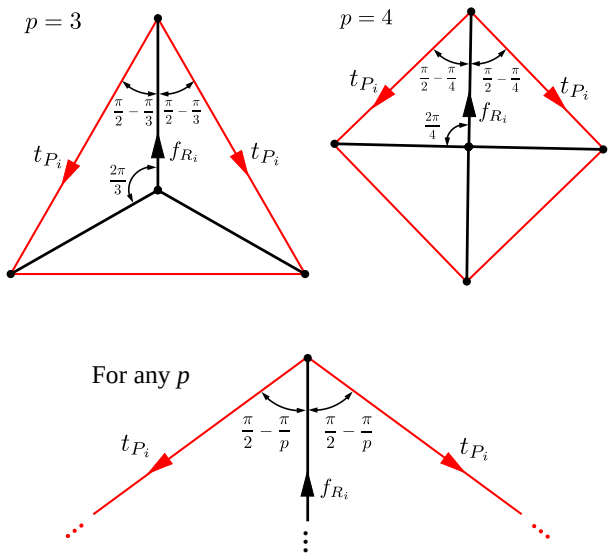

Figure 3.3: Force balance diagram for planar strings and radial bars. These schematics illustrate the central p-sided polygon of a T-bar unit.

Note that t_{D_i} and t_{P_i} are pre-tensions that can be arbitrarily selected to adjust the load distribution in a T-bar. Equation (3.5) is valid for any $p \geq 2$, $q \geq 1$, and $\alpha_i > 0$. Using Euler theory of buckling, the minimum mass of a compressive member of length $\hat{l}$ subjected to a force $\hat{f}$ that is designed to satisfy buckling constraints is given as [21]:

$$m_{bB} = 2\rho_b \hat{l}^2 \left(\frac{\hat{f}}{\pi E_b}\right)^{\frac{1}{2}}, \tag{3.6}$$

where ρ_b and E_b are the mass density and Young's modulus of the bar material, respectively. The minimum mass of a compressive member designed under yielding constraint is denoted by m_{bY} and the minimum mass of a tensile member also designed under yielding constraint is denoted by

m_{sY}. These are given by:

$$m_{bY} = \frac{\rho_b}{\sigma_b}\hat{l}\hat{f}, \;\; m_{sY} = \frac{\rho_s}{\sigma_s}\hat{l}\hat{f}, \tag{3.7}$$

where σ_b is the yield stress of the bar material and ρ_s and σ_s are the mass density and yield stress of the string material. The minimum mass of a compressive member is the maximum of the mass required for either yielding or buckling constraints, while a tensile member is only subjected to yield constraints. Accordingly, the mass of a string m_s and the mass of a bar m_b of a T-bar structure are:

$$m_b = \max(m_{bB}, m_{bY}), \;\; m_s = m_{sY}. \tag{3.8}$$

The minimum mass of the string and bar members in a T-bar structure are obtained by substituting the force and length values from Eqs. (3.2)-(3.5) into Eqs. (3.6)-(3.8). Then, the minimum total mass of a T-bar system subjected to a compressive force of magnitude f is obtained as the addition of the mass of all the members in the system as:

$$m_T \quad = \quad \max\left(m_{LB}, m_{LY}\right) \;+\; \sum_{i=1}^{q} \max\left(m_{RB_i}, m_{RY_i}\right) \;+\; \sum_{i=1}^{q} m_{P_i} \;+\; \sum_{i=1}^{q} m_{D_i}, \tag{3.9}$$

where the mass of the different kinds of members is:

$$m_{LB} = \frac{2\rho_b l^2}{\sqrt{\pi E_b}} \frac{\sqrt{f + p\sum_{i=1}^{q} t_{D_i}\cos(\alpha_i)}}{2^q}, \tag{3.10}$$

$$m_{LY} = \frac{\rho_b}{\sigma_b} l \left(f + p\sum_{i=1}^{q} t_{D_i}\cos(\alpha_i) \right), \tag{3.11}$$

$$m_{RB_i} = \frac{2\rho_b l^2}{\sqrt{\pi E_b}} \frac{p\tan^2(\alpha_i)\sqrt{2t_{D_i}\sin(\alpha_i) + 2t_{P_i}\sin\left(\frac{\pi}{p}\right)}}{2^{i+1}}, \tag{3.12}$$

$$m_{RY_i} = \frac{\rho_b}{\sigma_b} pl\tan(\alpha_i)\left(t_{D_i}\sin(\alpha_i) + t_{P_i}\sin\left(\frac{\pi}{p}\right)\right), \tag{3.13}$$

$$m_{P_i} = \frac{p\rho_s l\sin(\frac{\pi}{p})\sin(\alpha_i)}{\sigma_s\cos(\alpha_i)} t_{P_i}, \quad m_{D_i} = \frac{p\rho_s l}{\sigma_s\cos(\alpha_i)} t_{D_i}. \tag{3.14}$$

This section provided the minimum mass (Eq. (3.9)) for a T-bar structure for given pre-stress in the strings t_{P_i} and t_{D_i} and externally applied compressive force f. Only local failure modes of the individual members in the T-bar structure were considered. The next section provides the formulation employed to assess the global buckling properties of T-bar tensegrity structures to also account for such failure mode in the structural design.

3.3 Global Failure Criteria

As stated in the introduction, existing design studies of lightweight load-bearing tensegrity structures consider only local failure criteria or they develop global failure criteria limited to specific types of tensegrities. If a tensegrity structure is subjected to external compressive loads and/or pre-stress, the entire structure can buckle as a whole if the load is large enough, without necessarily reaching the member forces that would trigger local failure of its strings and bars (see Fig. 3.2). To determine the critical buckling forces, the global stiffness matrix of tensegrity structures is derived by linearizing the static equilibrium equation about a equilibrium configuration. The equations of static equilibrium of tensegrity structures with arbitrary node positions and member connectivity are written as follows [16]:

$$NK = W \quad \text{where} \quad K = C_s^\top \hat{\gamma} C_s - C_b^\top \hat{\lambda} C_b, \tag{3.15}$$

where C_s and C_b are the connectivity matrices for strings and bars, respectively and the vectors $\gamma = [\gamma_1 \ \gamma_2 \ \cdots \ \gamma_\tau]^\top \in \mathbb{R}^\tau$ and $\lambda = [\lambda_1 \ \lambda_2 \ \cdots \ \lambda_\beta]^\top \in \mathbb{R}^\beta$ contain the forces per unit length in the strings and bars, respectively. The matrices containing the string and bar vectors ($S \in \mathbb{R}^{3\times\tau}$ and $B \in \mathbb{R}^{3\times\beta}$, respectively) can then be determined as:

$$\begin{aligned} S &= NC_s^\top = [s_1 \ s_2 \ \cdots \ s_\tau], \\ B &= NC_b^\top = [b_1 \ b_2 \ \cdots \ b_\beta]. \end{aligned} \tag{3.16}$$

The tensile force vector $t_{s_j} \in \mathbb{R}^3$ of the j^{th} string is determined from γ_j and the compressive force vector $t_{b_k} \in \mathbb{R}^3$ of the k^{th} bar is written as:

$$\begin{aligned} \begin{bmatrix} t_{s_1} & t_{s_2} & \cdots & \cdots & t_{s_\tau} \end{bmatrix} &= S\hat{\gamma} \in \mathbb{R}^{3\times\tau}, \\ \begin{bmatrix} t_{b_1} & t_{b_2} & \cdots & \cdots & t_{b_\beta} \end{bmatrix} &= B\hat{\lambda} \in \mathbb{R}^{3\times\beta}. \end{aligned} \tag{3.17}$$

3.3.1 Global Stiffness Matrix

The global stiffness matrix of the entire T-bar structure is determined from the contributions of the stiffness matrices from all its individual members. The linearized global stiffness matrix can be obtained by linearizing the static equilibrium equation of tensegrity structures given as [16]:

$$S\hat{\gamma} C_s - B\hat{\lambda} C_b = W, \tag{3.18}$$

where $S = [s_1 \ s_2 \ \cdots \ s_\tau]$ and $B = [b_1 \ b_2 \ \cdots \ b_\beta]$ are the matrices containing the vectors along the lengths of the strings s_j and bars b_k, respectively. The total number of strings in the T-bar is denoted by τ and the total number of bars is denoted by β. The force density (magnitude of

the tensile force per unit length) in the j^{th} string is denoted by $\gamma_j \geq 0$ and the force density (the magnitude of the compressive force per unit length) in the k^{th} bar is denoted by $\lambda_k \geq 0$. The string connectivity matrix C_s and bar connectivity matrix C_b provide the information of the start and end nodes of each string and each bar, respectively [16]. The diagonal matrices $\hat{\gamma}$ and $\hat{\lambda}$ are written by arranging γ_j and λ_k in their diagonal elements, and the external force matrix $W = [w_1\ w_2\ \cdots\ w_\nu]$ contains the vector of external forces w_i applied to the i^{th} node. The number of nodes in the system is denoted by ν.

The non-linear static equilibrium Eq. (3.18) is linearized about an equilibrium configuration to obtain:

$$\mathbb{K}_L \mathrm{d}n = \mathrm{d}w, \tag{3.19}$$

where $\mathrm{d}n = [\mathrm{d}n_1^\top\ \mathrm{d}n_2^\top\ \cdots\ \mathrm{d}n_\nu^\top]^\top$ is a vector containing small variations of the node positions vectors, and $\mathrm{d}w = [\mathrm{d}w_1^\top\ \mathrm{d}w_2^\top\ \cdots\ \mathrm{d}w_\nu^\top]^\top$ is a vector containing small variations of external forces at all the nodes. The linearized global stiffness matrix $\mathbb{K}_L$ from Eq. (3.19) can be obtained as:

$$\mathbb{K}_L = (C_s^\top \otimes I_3)\text{b.d.}(\cdots, K_{s_j}, \cdots)(C_s \otimes I_3) - (C_b^\top \otimes I_3)\text{b.d.}(\cdots, K_{b_k}, \cdots)(C_b \otimes I_3). \tag{3.20}$$

The contributions of the j^{th} string and the k^{th} bar in the global stiffness matrix are denoted by K_{s_j} and K_{b_k}, respectively:

$$K_{s_j} \triangleq \gamma_j I_3 + E_{s_j} A_{s_j} \frac{s_j s_j^\top}{l_{s_j}^3}, \quad K_{b_k} \triangleq \lambda_k I_3 - E_{b_k} A_{b_k} \frac{b_k b_k^\top}{l_{b_k}^3}, \tag{3.21}$$

where E_{s_j} and A_{s_j} are the Young's modulus and the cross-section area of the j^{th} string, respectively. Similarly, E_{b_k} and A_{b_k} denote the Young's modulus and the cross-section area of the k^{th} bar member.

3.3.2 Criteria for Global Stability of T-bar structures

The string force density vector $\gamma = [\gamma_1\ \gamma_2\ \cdots\ \gamma_\tau]^\top$ and the bar force density vector $\lambda = [\lambda_1\ \lambda_2\ \cdots\ \lambda_\beta]^\top$ can be written as the sum of force densities due to pre-stress (γ_p, λ_p) and force densities due to the external force (γ_w, λ_w) as:

$$\gamma = \gamma_p + \gamma_w, \quad \lambda = \lambda_p + \lambda_w, \tag{3.22}$$

where the force densities due to pre-stress (self-equilibrated under zero external force) are solved using the static equilibrium equation (Eq. (3.18)) as:

$$(C_b^\top \otimes I_3)\hat{B}\lambda_p = (C_s^\top \otimes I_3)\hat{S}\gamma_p, \ \ \gamma_p \geq 0, \ \ \lambda_p \geq 0, \tag{3.23}$$

where I_3 is the identity matrix of dimension 3×3 and $\hat{S} = \text{b.d.}(s_1, s_2, \ldots, s_\tau)$ and $\hat{B} = \text{b.d.}(b_1, b_2, \ldots, b_\beta)$ are the body diagonal matrices formed by arranging the string vectors s_j and bar vectors b_k along their body diagonals, respectively. Equation (3.23) gives a unique solution for the force densities in the bars (λ_p) for given values of pre-stress in the strings (γ_p) because the coefficient matrix $(C_b^\top \otimes I_3)\hat{B}$ is a full column rank matrix for any T-bar structure. This can also be confirmed from the exact analytical solution given in Eq. (3.5).

The external force f on the T-bar structure only causes compressive loading in the longitudinal bars. This can be verified from Fig. 3.2 and Eq. (3.5):

$$\gamma_w = 0, \quad \lambda_{w_k} = \begin{cases} \frac{2^q f}{l}; & \text{For longitudinal bars} \\ 0; & \text{Otherwise} \end{cases}. \tag{3.24}$$

Using Eqs. (3.23) and (3.24), the linearized global stiffness matrix from Eq. (3.20) is updated

with:

$$K_{s_j} = \gamma_{p_j} I_3 + E_{s_j} A_{s_j} \frac{s_j s_j^\top}{l_{s_j}^3}, \tag{3.25}$$

$$K_{b_k} = (\lambda_{p_k} + \lambda_{w_k}) I_3 - E_{b_k} A_{b_k} \frac{b_k b_k^\top}{l_{b_k}^3}. \tag{3.26}$$

From Eq. (3.19), global instability is interpreted as non-trivial values of displacement in the structure ($\mathrm{d}n \neq 0$) under no changes in the values of the external forces ($\mathrm{d}w = 0$):

$$\mathbb{K}_L \mathrm{d}n = 0. \tag{3.27}$$

Equation (3.27) has non-trivial solutions for $\mathrm{d}n$, *if and only if*, the symmetric global stiffness matrix $\mathbb{K}_L$ is singular, or determinant of $\mathbb{K}_L$ is zero. Thus, to minimize mass of the T-bar structure under global instability constraints, the minimum values of pre-stress (γ_p) or cross-section areas of the members such that the matrix $\mathbb{K}_L$ reaches singularity (i.e., the onset of buckling failure) for the given external force f must be determined.

As stated in Eq. (3.27), global stability of the tensegrity structures is assessed by means of a linearized matrix, as in buckling analysis of beams and plates using the finite element method [53, 54]. This matrix is obtained by linearizing the non-linear equations of static equilibrium (Eq. (3.18)) about the current equilibrium configuration of the tensegrity structure. Some inaccuracy is introduced in the process as here the nominal (initial) coordinate positions of the nodes are employed instead of their deformed positions. However, such differences in node positions between initial and deformed configurations are small as the strings and bars are assumed to be comprised of a stiff material in this work (aluminum). Thus, changes in the length of the strings and bars, and consequently differences in node positions between initial and deformed configurations, are small compared to the dimensions of the tensegrity. Further research quantifying the effect of this assumption and non-linear buckling analysis of tensegrity structures are recommended for future studies.

The mass minimization of the structure considering global buckling alone is a convex problem (unique optimum solution) as all the design variables appear linearly in Eq. (3.27). However, the combined problem of minimizing the mass of the structure considering both local and global failure becomes a non-convex as the area of the bar members (A_{b_k}) is a non-linear function of the force densities in the bar λ_k, for local buckling constraints (cf. Eq. (3.6)). The next section discusses two design approaches to solve this non-convex problem.

3.4 Methods for Determining Minimum Mass Designs of T-bar Structures

This section describes two approaches to minimize the mass of T-bar structures based on the local and global failure criteria developed in the previous sections.

3.4.1 Pre-stress Method: Optimum Pre-stress for a T-bar Unit

A T-bar unit (equivalent to a T-bar of $q = 1$) has p planar strings and $2p$ number of diagonal strings that can be independently pre-stressed. The tension in these strings is scaled using two independent *pre-stress factors*: $\gamma_P \geq 0$ for planar strings and $\gamma_D \geq 0$ for diagonal strings,

$$\gamma_p = \begin{bmatrix} \gamma_P \, [1 \; 1 \; \cdots \; 1]^\top_{p\times 1} \\ \gamma_D \, [1 \; 1 \; \cdots \; 1]^\top_{2p\times 1} \end{bmatrix}. \tag{3.28}$$

The force density in the bars due to pre-stress (λ_p) can be uniquely calculated as a function of pre-stress factors γ_P and γ_D using Eq. (3.23). Equation (3.22) allows us to solve for the force density in each member and Eqs. (3.6) and (3.7) are used to calculate the area of each member. All the variables in Eq. (3.20) are now dependent on the pre-stress factors. The design problem to minimize the mass of the T-bar unit then consists of finding the minimum values of the pre-stress factors such that the stiffness matrix of the T-bar unit $\mathbb{K}_L$ reaches singularity, which physically represents the onset of global buckling.

3.4.2 Area Method: Optimum String Cross-section Areas for a T-bar Unit

Similar to the method discussed in Sect. 3.4.1, the cross-section areas of the planar strings and diagonal strings can be independently scaled to prevent global buckling. Let us define $\eta_P \geq 1$ and

$\eta_D \geq 1$ as the *area factors* that scale the cross-section areas of the planar strings A_P and diagonal strings A_D, respectively. The areas of the strings are then scaled as follows:

$$A_P \rightarrow \eta_P A_{Pb}, \quad A_D \rightarrow \eta_D A_{Db}, \tag{3.29}$$

where A_{Pb} and A_{Db} are the baseline member cross-section areas [6]. Pre-stress values of $\gamma_p = \lambda_p = 0$ are used in this method. The design problem for this method consists of finding the minimum values of the area factors such that the stiffness matrix of the T-bar unit $\mathbb{K}_L$ reaches singularity.

3.4.3 Hierarchical Design of T-bar Structures

For a T-bar structure of complexity q, there would be different T-bar units introduced at each self-similar iteration that may be subjected to global buckling. The minimum mass design of a T-bar is obtained when the T-bar units introduced at each self-similar iteration are designed such that they reach the onset of buckling. Algorithm 1 outlines the hierarchical design approach for minimal mass T-bar structures of arbitrary complexity, where the pre-stress or area factors of T-bar units are optimized sequentially for each self-similar iteration i, from $i = 1$ to $i = q$.

Algorithm 1: Hierarchical design of minimal mass T-bar structures with arbitrary complexity.

Step 1: Design a complexity $q = 1$ T-bar structure (equivalent to a T-bar unit) of length $l_1 = l$ and external force $f_1 = f$ by determining the minimum values of pre-stress or area factors for both planar and diagonal strings ($[\gamma_{P_1}, \gamma_{D_1}]$ or $[\eta_{P_1}, \eta_{D_1}]$) such that the stiffness matrix of the T-bar unit $\mathbb{K}_{L_1}$ reaches singularity.

Step 2: Design the T-bar units of the subsequent self-similar iteration $i + 1$ which have length $l_{i+1} = l/2^i$ and external force $f_{i+1} = f_i + p\,\gamma_{D_i}\,l_{D_i}\cos(\alpha_i)$ by calculating the minimum pre-stress or area factors ($[\gamma_{P_{i+1}}, \gamma_{D_{i+1}}]$ or $[\eta_{P_{i+1}}, \eta_{D_{i+1}}]$) such that the stiffness matrix of the T-bar units $\mathbb{K}_{L_{i+1}}$ reaches singularity.

Step 3: Repeat **Step 2** for each self-similar iteration.

3.5 Results and Discussion

Results of mass minimization for 2D and 3D T-bar structures using the approach developed in the previous section are presented herein. The *mass ratio* μ is used to compare the mass of the T-bar structures m_T with that of a compressive column of solid circular cross-section, m_{col}, as:

$$\mu = \frac{m_T}{m_{col}}, \quad \text{where } m_{col} = \max\left(\frac{2\rho_b l^2\sqrt{f}}{\sqrt{\pi E_b}}, \frac{\rho_b l f}{\sigma_b}\right). \tag{3.30}$$

If $\mu < 1$, the T-bar structure requires less mass than the compressive column to support a compressive force f. Note that both yielding and buckling failure modes are accounted for in the mass calculation of the solid column. The mass ratio is referred to as μ_{2D} for 2D T-bars and μ_{3D} for 3D T-bars.

The increase in pre-stress and cross-section area required to prevent global buckling of a T-bar system under compressive loading (obtained via the pre-stress and area methods, respectively) add mass to the structure. To quantify this additional mass, a parameter ϕ defined as the ratio of the mass of the T-bar designed considering global buckling m_T and the mass of the T-bar designed without considering global buckling $m_{T_{local}}$ is introduced:

$$\phi = \frac{m_T}{m_{T_{local}}}, \tag{3.31}$$

where $m_{T_{local}}$ is calculated using Eq. (3.9) with $t_{D_i} = t_{P_i} = 0$ to consider only local failure constraints. This parameter is referred to as ϕ_{2D} for 2D T-bars and ϕ_{3D} for 3D T-bars.

Material properties of aluminum are used for both string and bar members ($E_s = E_b = 60$ GPa, $\sigma_s = \sigma_b = 110$ MPa, and $\rho_s = \rho_b = 2700$ kg/m^3) and the analogous compressive column. For simplicity, it is assumed that the aperture angles of the T-bar units are equal among all the self-similar iterations: $\alpha_1 = \alpha_2 = \cdots = \alpha_q = \alpha$.

Figure 3.4 shows the initial configuration of a T-bar structure of length $l = 2$ m, complexity $q = 1$, and aperture angle $\alpha = 5°$. The first critical global buckling force and the corresponding two mode shapes for this first buckling mode are also shown in the figure. The critical buckling force for this structure $f = 20656.3$ N is larger than the externally applied force $f_0 = 10000$ N and hence the structure would not undergo global instability. A T-bar structure with $q = 2$, $l = 2$ m, and $\alpha = 5°$ is shown in Fig. 3.5. The first buckling eigenvalue and its corresponding four eigenmodes are also shown in the figure. The critical buckling force $f = 10319.6$ N is slightly higher than the nominal external force $f_0 = 10000$ N and thus global buckling would not occur. The critical buckling force f for this structure is almost half than that of the $q = 1$ structure.

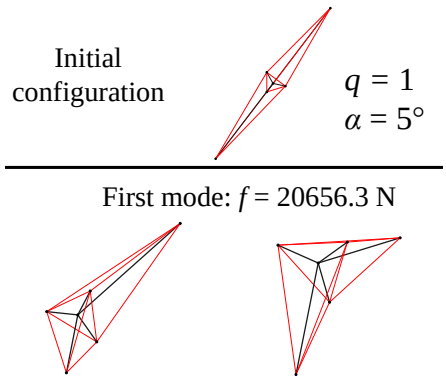

Figure 3.4: Eigenmodes for the first critical buckling force of a T-bar structure with parameters $l = 2$ m, $f_0 = 10000$ N, $q = 1$, and $\alpha = 5°$.

3.5.1 2D T-bar Structures

For 2D T-bar structures ($p = 2$), there are no planar strings and thus the only optimization variables are the pre-stress factor (γ_D) and the area factor (η_D). Figure 3.6(a) provides the contour plots of the mass ratio μ_{2D} for a 2D T-bar structure for pre-stress factor γ_D obtained using Algorithm 1. The lighter shaded area in the contour plot corresponds to the region where the mass of the T-bar structure is lower than the mass of a compressive column designed for buckling $m_T < m_{col}$. As observed in the figure, T-bar structures provide lower mass solutions for

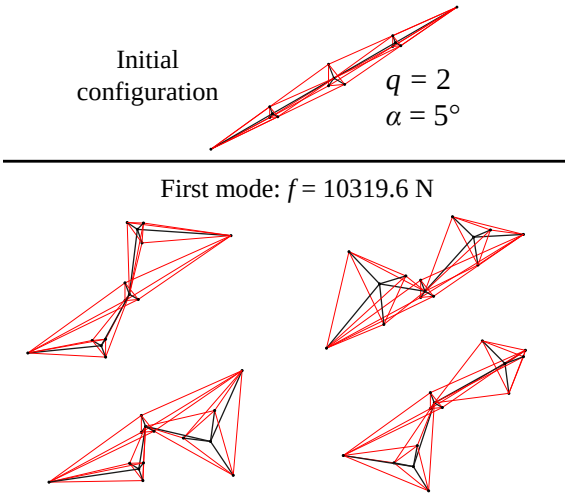

Figure 3.5: Eigenmodes for the first critical buckling force of a T-bar structure with parameters $l = 2$ m, $f_0 = 10000$ N, $q = 2$, and $\alpha = 5°$.

compressive loads for a large range of aperture angles and throughout the entire studied complexity range ($q = 1, \ldots, 5$). The darker shaded region in the contour plot represents the complexity and angle set (q, α) where global buckling cannot be prevented for any value of pre-stress in the strings. This can be explained as T-bar structures of low aperture angles have a large “length-to-width" ratio and thus have low critical buckling forces. Figure 3.6(a) also shows that there is a global optimum design for the given force f and length l, which was found to be $\mu_{2D} = 0.2246$ for $q = 3$ and $\alpha = 24°$ (marked with an ‘$\times$’ in the contour plot). Figure 3.6(b) shows the optimum configuration of the T-bar structure displaying the calculated member cross-sections.

The contour plots of mass ratio μ_{2D} for optimized area factor η_D are shown in Fig. 3.7(a) and the global optimum configuration ($q = 3, \alpha = 31°, \mu_{2D} = 0.2068$) is shown in Fig. 3.7(b). Notice that the method of optimizing area factor (η_D) provides a solution with lower mass than that obtained by optimizing the pre-stress factor (γ_D). The same trend is observed for different values of f and l as shown in Table 3.1.

Table 3.1 also provides optimum complexity q and angle α for different combinations of force f and length l. The first column in the table represents a force per unit area parameter f/l^2. For a small value of this parameter, the compressive column is more prone to buckling failure and thus

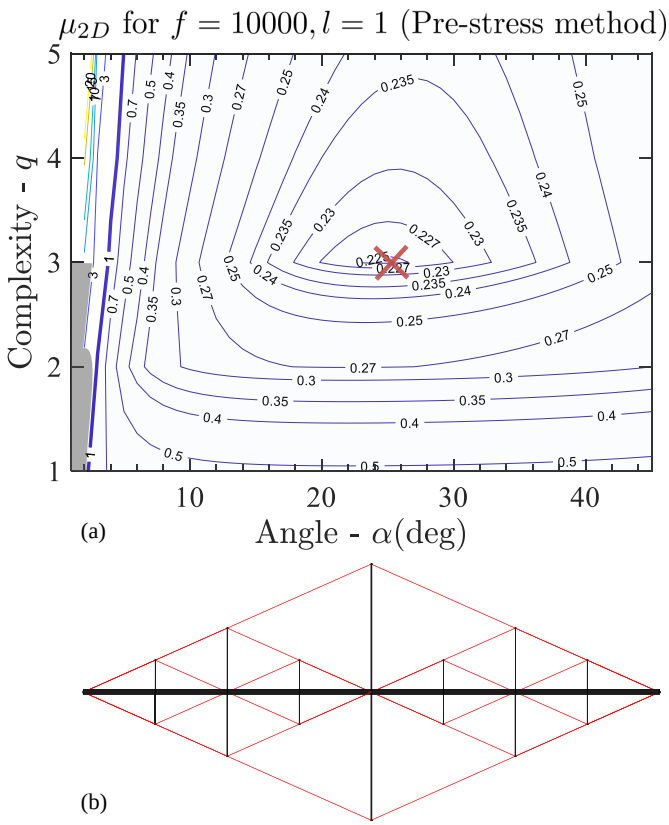

Figure 3.6: (a) Contour plot of mass ratio μ_{2D} for 2D T-bar structures with optimized pre-stress factor (γ_D). (b) Minimal mass configuration of the T-bar structure (marked with the '$\times$' in the contour) displaying calculated member cross-sections.

the mass ratio μ_{2D} is small (more mass savings by replacing the column with a T-bar). The value of the mass ratio increases with the increased value of the parameter f/l^2 and for $f/l^2 = 250000$ the mass ratio is greater than 1 ($\mu_{2D}(\gamma_D) = 1.0157 > 1$, $\mu_{2D}(\eta_D) = 1.0015 > 1$) for both methods indicating that the single column is the minimum mass structure.

Notice that for $f/l^2 = 1000000$ N/m^2, the single column is designed to avoid yielding failure and thus the mass of T-bar designed to avoid only local failures would be equal to the mass of the single column, $m_{T_{local}} = m_{col}$. Thus, the reason for the mass ratios $\mu_{2D} = 1.52$ (pre-stress method) and $\mu_{2D} = 1.51$ (area method) to be above 1 is entirely based on global stability to the structure, hence $\mu_{2D} = \phi_{2D} = 1.52$ (pre-stress method) and $\mu_{2D} = \phi_{2D} = 1.51$ (area method).

By comparing the results between the *pre-stress method* and the *area method* in Figs. 3.6

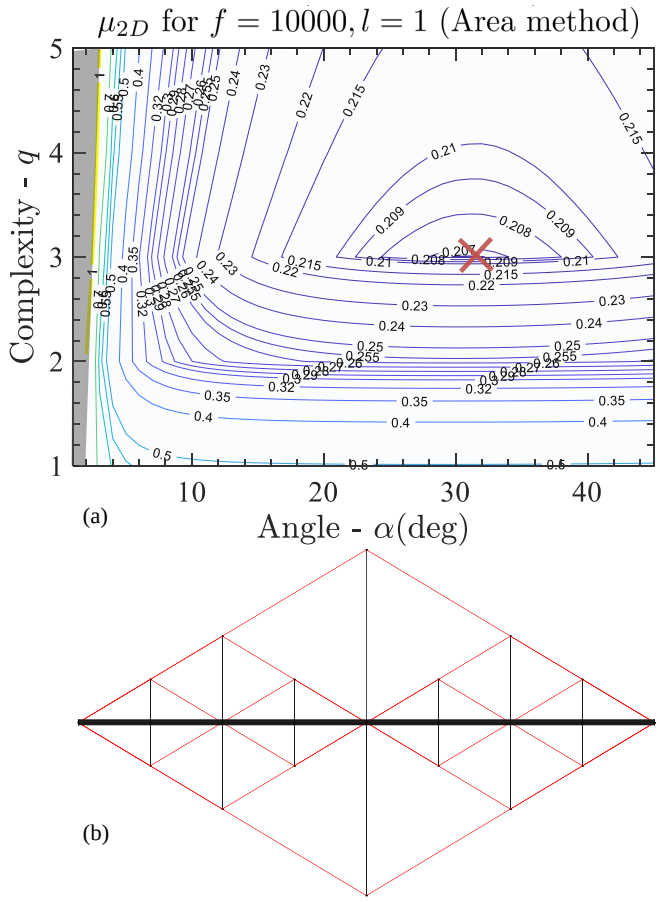

Figure 3.7: (a) Contour plots of mass ratio μ_{2D} for the 2D T-bar structure with optimized area factor (η_D). (b) Optimum configuration of the T-bar structure (marked with the '$\times$' in the contour) displaying calculated member cross-sections.

Table 3.1: Mass ratio μ_{2D} optimized with two different methods for different values of force f and length l. Units: f (N), l (m), and α (deg).

$\frac{f}{l^2}$	f	l	Pre-stress method				Area method			
			q	α	μ_{2D}	ϕ_{2D}	q	α	μ_{2D}	ϕ_{2D}
1000	1000	1	4	20	0.08	1.28	4	26	0.07	1.12
2500	2500	1	4	22	0.12	1.81	4	29	0.10	1.51
10000	10000	1	3	24	0.22	1.66	3	31	0.21	1.58
100000	1000	0.1	1	28	0.65	1.30	1	33	0.63	1.26
250000	2500	0.1	1	31	1.01	1.53	1	33	1.00	1.51
1000000	10000	0.1	1	35	1.52	1.52	1	33	1.51	1.51

and 3.7, and Table 3.1, one observes that the two methods provide different minimal mass designs under the same loading and length requirements. Cross-section area A_{s_j} and member force $t_{s_j} = \gamma_j \|s_j\|$ are linearly related for tensile string members under yielding failure constraints through the equation $\sigma_s A_{s_j} = t_{s_j}$. For compressive bars under buckling failure constraints, the cross-section area A_{b_k} and member force $f_{b_k} = \lambda_k \|b_k\|$ are non-linearly related through the Euler buckling formula $(\pi E_b A_{b_k}^2)/(4\|b_k\|^2) = f_{b_k}$. In a T-bar structure, increasing tension in the strings increases the compressive forces in the bars and thus the area/mass of the bar members is non-linearly increased. Because of this, increasing the pre-stress in the T-bar structure (which increases the areas of strings and bars accordingly) in the *pre-stress method*; and only increasing the cross-section areas of the strings (without adding pre-stress) in the *area method*, provide different minimal mass results to prevent global buckling.

3.5.2 3D T-bar Structures

For 3D T-bar structures, we have to simultaneously consider the two pre-stress factors γ_P and γ_D for the pre-stress method and the two area factors η_P and η_D for the area method. It was found that the pre-stress of the planar strings γ_P is not a critical parameter to prevent global buckling and to minimize the mass of the structure. As such, this pre-stress value is kept at $\gamma_P = 10$ for the reminder of these examples. A contour plot of mass ratio μ_{3D} for optimized pre-stress factor (γ_D) as shown in Fig. 3.9(a). The global optimum configuration (marked with an '$\times$') was found to be $q = 3$ and $\alpha = 25^\circ$ with a mass ratio of $\mu_{3D} = 0.2500$. The darker shaded area in the figure corresponds to the region where no solution for γ_D was found to prevent global buckling. Figure 3.9(b) shows the optimum configuration of the T-bar structure.

It can also be inferred from Fig. 3.8 that the mass ratio μ_{3D} for the structure obtains a minimum value for a small value of pre-stress factor in planar strings. The lighter shaded area in the figure represents the region where mass ratio value is less than one ($\mu_{3D} < 1$).

It was also observed for the area method that the cross-section areas of the planar strings do not play a critical role in preventing global buckling. This can be confirmed from Fig. 3.10 as for any particular value of angle α the mass monotonically increases by increasing the area

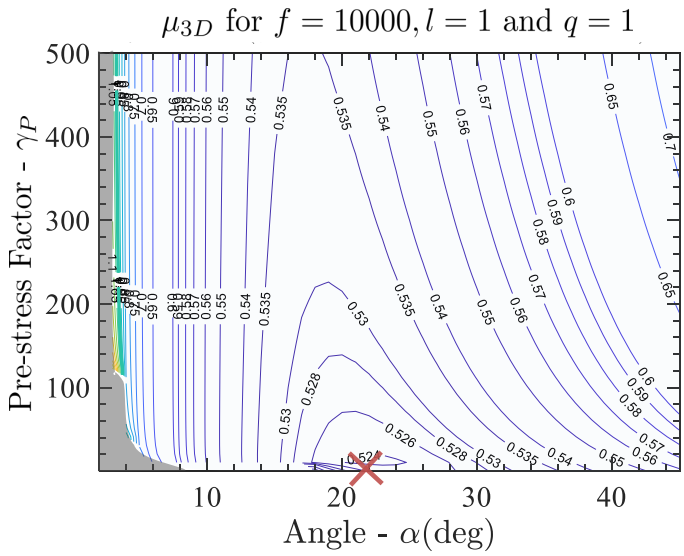

Figure 3.8: Contour plots of mass ratio μ_{3D} for the 3D T-bar structure for optimized pre-stress factor in diagonal strings (γ_D). The optimum solution is marked with '$\times$' in the contour plot.

factor η_P (y-axis). Therefore, a small value of $\eta_P = 10^{-4}$ is used in the presented examples. Figure 3.11(a)shows the contour levels of mass ratio μ_{3D} plotted for different values of angle α and complexity q. It shows a global minimum achieved at $q = 3$ and $\alpha = 31°$. This optimum solution of $\mu_{3D} = 0.2159$ obtained from Fig. 3.11(a) has lower mass than that obtained by optimizing the pre-stress factor γ_D. The optimum configuration of the T-bar structure drawn to the scale is shown in Fig. 3.11(b).

Table 3.2 provides the optimum α and q for different combinations of force f and length l. It is observed from the table that for all combinations of f and l, the method of optimizing area factor η_D provides lower mass solutions than those obtained by optimizing the pre-stress factor γ_D. Similar to the results observed in Table 3.1, the value of mass ratio μ_{3D} increases by increasing the value of f/l^2 and the mass ratio becomes greater than 1 ($\mu_{3D}(\gamma_D) = 1.0429 > 1, \mu_{3D}(\eta_D) = 1.0163 > 1$) for $f/l^2 = 250000$ where the single column is the optimal mass solution.

Similar to Table 3.1, for $f/l^2 = 1000000$ N/m^2, the single column is designed to avoid yielding failure and thus the mass of T-bar designed to avoid only local failures would be equal to mass of the single column, $m_{T_{local}} = m_{col}$. Thus, the reason for the mass ratios $\mu_{3D} = 1.56$ (pre-stress

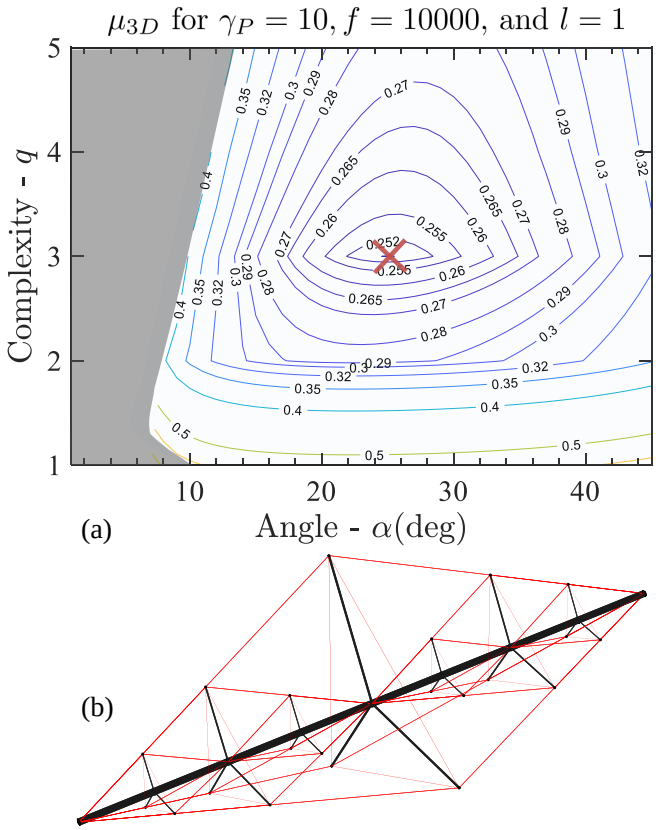

Figure 3.9: (a) Contour plots of mass ratio μ_{3D} for a fixed pre-stress factor in the planar strings ($\gamma_P = 10$) and optimized pre-stress factor in diagonal strings (γ_D). (b) Optimum configuration of the T-bar structure (marked with the '$\times$' in the contour) displaying calculated member cross-sections.

method) and $\mu_{2D} = 1.54$ (area method) to be above 1 is entirely based on providing global stability to the structure, hence $\mu_{3D} = \phi_{3D} = 1.56$ (pre-stress method) and $\mu_{3D} = \phi_{3D} = 1.54$ (area method).

3.6 Conclusions

This chapter presented a novel approach to design minimum mass tensegrity T-bar lattices, which can be integrated into lightweight load-bearing architectured materials. The topology and shape of the T-bar-based lattices are optimized to prevent global buckling of the T-bars while minimizing their mass. The methodology developed in this chapter allows for the determination of the complexity q, aperture angle α, and pre-stress distribution or member cross-sections areas

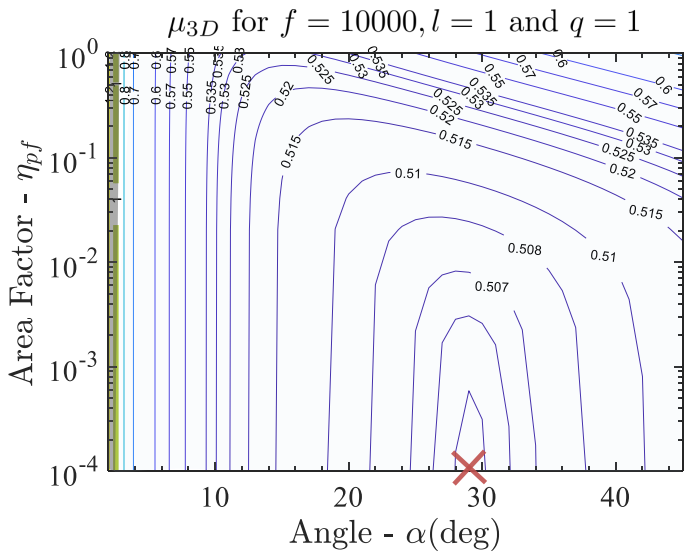

Figure 3.10: Contour plots of mass ratio μ_{3D} for the 3D T-bar structure for optimized diagonal area factor (η_D). The optimum solution is marked with '$\times$'.

Table 3.2: Mass ratio μ_{3D} optimized with two different approaches for different values of force f and length l. Units: f (N), l (m), and α (deg).

$\frac{f}{l^2}$	f	l	Pre-stress method				Area method			
			q	α	μ_{3D}	ϕ_{3D}	q	α	μ_{3D}	ϕ_{3D}
1000	1000	1	4	19	0.10	1.60	4	27	0.07	1.12
2500	2500	1	4	22	0.14	2.12	4	29	0.11	1.66
10000	10000	1	3	25	0.25	1.89	3	31	0.21	1.58
100000	1000	0.1	1	28	0.66	1.32	1	33	0.64	1.28
250000	2500	0.1	1	31	1.04	1.57	1	33	1.01	1.53
1000000	10000	0.1	1	36	1.56	1.56	1	33	1.54	1.54

of 2D or 3D T-bar structures with minimal mass for given compressive force f and T-bar length l. In earlier work of designing minimum mass T-bar structures, only 2D T-bar structures, or T-bars limited to complexity 1, were considered. This chapter extended the work on minimum mass design of tensegrity T-bar structures by Skelton [6] where only 2-dimensional T-bar structures were considered for both local and global failures.

The chapter first provided an analytical solution for the mass of a T-bar structure of arbitrary shape, topology, and pre-stress distribution considering local failure modes. The pre-stress

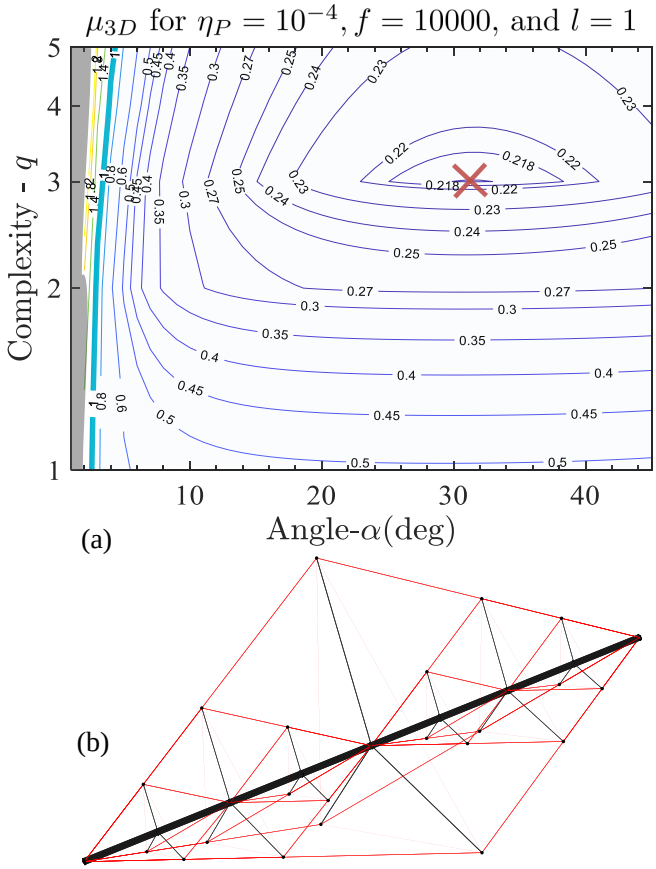

Figure 3.11: (a) Contour plots of mass ratio μ_{3D} for a fixed area factor in the planar strings ($\eta_P = 10^{-4}$) and optimized area factor in diagonal strings (η_D) with different complexities q. (b) Optimum configuration of the T-bar structure (marked with the '$\times$' in the contour) displaying calculated member cross-sections.

distribution or string cross-section areas are then designed such that global buckling is also prevented with minimum mass. The utilized approach to minimize the mass of complexity $q > 1$ T-bar structures was developed by sequentially designing the T-bar units introduced at each self-similar formative iteration. Finally, the chapter developed a general methodology to minimize the mass of both 2D and 3D T-bar structures for given force f and length l in terms of optimization variables: complexity q, angle α, pre-stress γ_p, and cross-section area of each member in the structure. The examples considered for both 2D and 3D structures provided a global minimal mass T-bar design for given force f and length l. For 3D structures, it was observed that planar strings are not critical in preventing global buckling of the structure and hence a small value of

pre-stress factor γ_P and area factor η_P was used in designing the structure. The obtained results showed that the method of optimizing the cross-section area of the strings provides lower mass designs than those obtained by optimizing the pre-stress distribution for both 2D and 3D structures. The developed model can be used to design tensegrities for components of lightweight composite structures and architectured materials with load-bearing capabilities and structural integrity.

4. DESIGN OF MINIMUM MASS TENSEGRITY D-BAR STRUCTURE

This chapter details the design of tensegrity D-bar structures, which have been shown to serve basic units in the design of lightweight compressive structures. This research work provides the analytical formulas to obtain the optimal complexity and minimum mass of the structure for given compressive force and given length of the structure. It is an important result that there exists a unique value of complexity which optimizes the mass of the structure. All the members in the structure are designed for local failures as D-bar structures are not subject to global buckling for a feasible engineering design structure. This work extends the previous work on D-bar structures where only buckling constraints were considered to design the compressive members by considering both yielding and buckling failures. The normalized mass of D-bar structures is then compared to the normalized mass of well-known T-bar structures for a set of given compressive force and length where normalization is done with the mass of continuum compressive columns.

4.1 Introduction

Minimum mass design of tensegrity structures have been studied in detail for different types of loading conditions [6, 19, 23]. Tensegrity T-bar and D-bar structures have been shown to provide optimum (minimum mass) designs to sustain given compressive load for a given length of the structure [6]. In the previous work by Skelton [6], only buckling failure was considered in calculating the minimum cross-section areas of bar (compressive) members and only yielding failure was considered in designing string (tensile) members with minimum cross-sectional areas. Recent work on T-bar structures provided the comprehensive methodology to design the structure with both local and global failure criteria [45].

This article would focus on the minimum mass design of D-bar structures for compressive loading with both yielding and buckling constraints in designing each member of the structure to obtain reliable results. Previous research on D-bar structure includes its use as actuators and sensors where actuators/sensors gain were analytically calculated for different complexities and

different angles of the D-bar structure[22]. D-bar systems were also studied as mass-efficient mechanical energy absorption systems for its use in high impact loading conditions such as lander and shock absorption structures [21]. In the mentioned work, it was shown that there always exists a set of complexity q and angle α such that the D-bar system stores more energy than a continuum compressive column until its failure [21]. A case study was also done on the design of tensegrity lander along with a detailed comparative study of classic six strut tensegrity lander [27, 2]. The design methodology to tune the ratio of the stress in the overall D-bar systems to that of their members were recently discussed [55]. The paper also discusses the inclusion of shape memory alloy-based strings to introduce energy dissipation capabilities [55].

A complexity 1 ($q = 1$) D-bar structure has 4 bars and 1 string as shown in Fig. 4.1(a). A complexity 2 ($q = 2$) D-bar structure is formed by replacing every bar member with another D-bar structure of complexity 1 (*D-bar fractal*) as shown in Fig. 4.1(b). Similarly, higher complexities structures can be formed by replacing every bar with a *D-bar fractal* using this concept of self-similar iterations. For a given length of D-bar structure, the variables needed to define a D-bar structure are: complexity q and angle parameters α_i for $i = 1, 2, \cdots, q$ for each self-similar iteration i, that goes up to complexity q. Let us define p as the number of strings in each D-bar unit, where $p = 2$ will result in a 2-dimensional D-bar system (shown in Fig. 4.1) and $p \geq 3$ will result in 3-dimensional structures (shown in Fig. 4.2). The 3-dimensional D-bar structure with $p = 3$ and complexities $q = 1$ and $q = 2$ are shown in Fig. 4.2.

The complexity of a D-bar system can be arbitrarily increased to a very large number. Figure 4.3 shows D-bar structure of complexity $q = 8$ and $p = 2$ for different values of angle α. The entire space gets filled up for such high complexity q and high value of angle α as shown in Fig. 4.3. Such high complexity D-bar systems guide the path for designing tensegrity based meta-materials where the topology and alignment of the material fiber can be optimized to increase mass-efficiency.

4.2 Tensegrity D-bar System Analysis

The analytical formulas to calculate the optimal complexity and minimum mass for a D-bar tensegrity system subject to both yielding and buckling constraints are derived in this section. First,

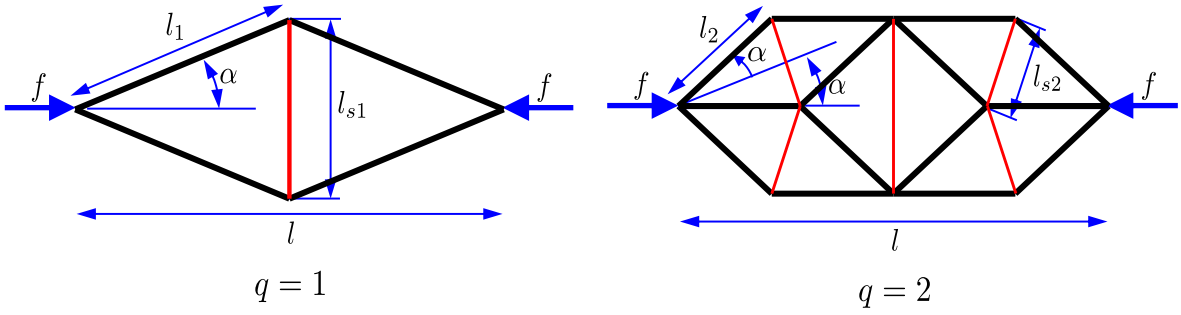

Figure 4.1: 2D Parameterization of tensegrity D-bar systems for complexities $q = 1, 2$ and $p = 2$.

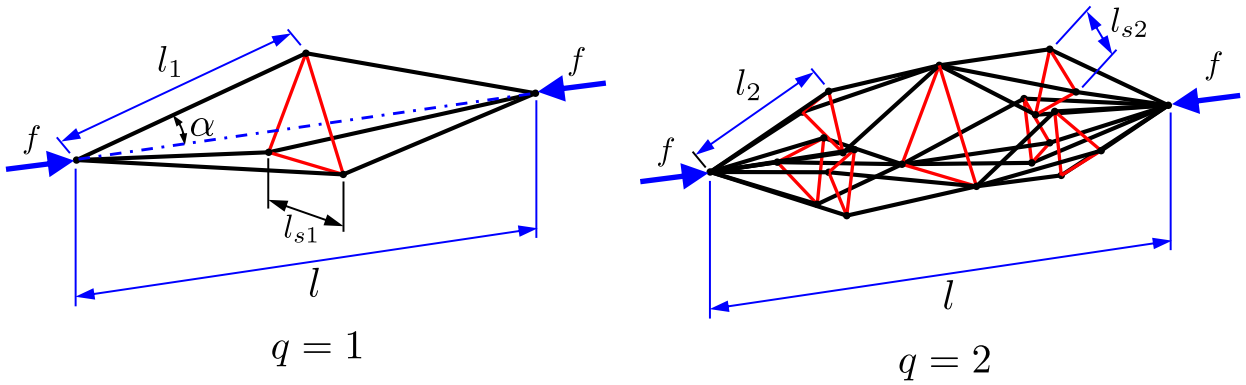

Figure 4.2: 3D Parameterization of tensegrity D-bar systems for complexities $q = 1, 2$ and $p = 3$.

we briefly go over the details of a D-bar system for the sake of completion and then derive the final result. The strings and the bars of the D-bar system are composed of homogeneous, isotropic, linear elastic materials. Fig. 4.2 shows D-bar system subject to an axial compressive force, f, applied at the endpoints of the D-bar for complexity $q = 1, 2$. The total length of the D-bar system is denoted by l, and α is the angle between the line connecting the endpoints of each D-bar unit and the line along any of its associated bars. In general, the set of D-bar units introduced at each iteration $i = 1, \ldots, q$, may have a different value for α [6]. The same value of α is assumed for all the D-bar units in the D-bar systems studied here for the sake of simplicity. For a more detailed discussion on this, please refer to [21].

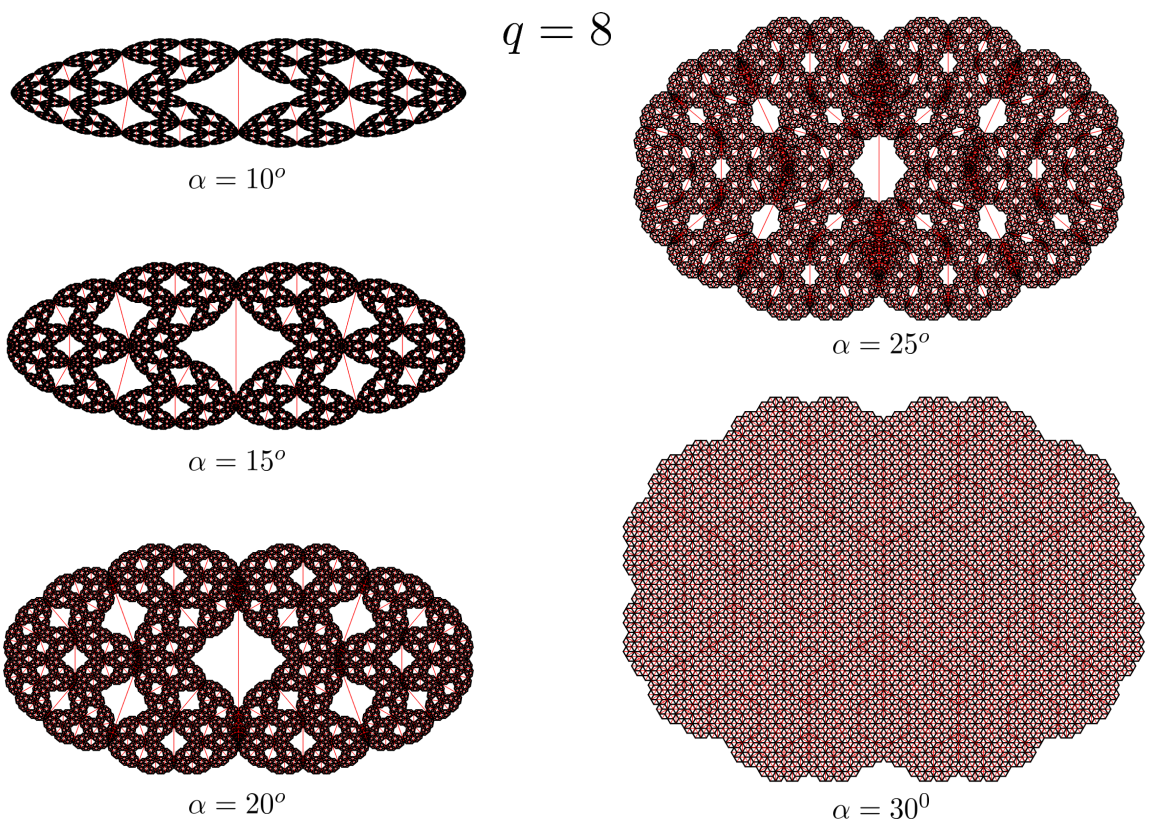

Figure 4.3: 2-Dimensional D-bar tensegrity structure of complexity $q = 8$ for different values of angle α.

Let us define the number of bars in a D-bar system as n_b and length of *all* the bars in a D-bar system of complexity q as l_q.

$$n_b = (2p)^q, \quad l_q = \frac{l}{(2\cos(\alpha))^q}. \tag{4.1}$$

Also, the number of strings and length of the strings introduced in each self-similar iteration is denoted as n_{si} and l_{si}, respectively.

$$n_{si} = 2^{i-1}p^i, \quad l_{si} = \frac{l\sin\left(\frac{\pi}{p}\right)\tan(\alpha)}{2^{i-1}\cos^{i-1}(\alpha)} \quad \text{for} \quad i = 1, \ldots, q. \tag{4.2}$$

The magnitude of the compressive force in the bars of the D-bar system, denoted by f_q, and

the magnitude of the tensile force in the strings introduced in each self-similar iteration, denoted by t_i, can easily be calculated as [6]:

$$f_q = \frac{f}{(p\cos(\alpha))^q}, \quad t_i = \frac{f\tan(\alpha)}{p^i \sin\left(\frac{\pi}{p}\right)\cos^{i-1}(\alpha)} \quad \text{for} \quad i = 1, \ldots, q. \tag{4.3}$$

After presenting the geometry and force distribution of D-bar systems with arbitrary complexity, we now present the minimal mass of a D-bar system under buckling constraints as the next Lemma.

Lemma 4.2.1. *Consider a D-bar system of length l, complexity q, angle parameter α, and p strings per D-bar unit subject to a compressive force of magnitude f. Suppose that the material comprising the bars has Young's modulus E_b, yield stress σ_b, and mass density ρ_b while the material comprising the strings has yield stress σ_s and mass density ρ_s. Then, the mass associated with the D-bar system considering buckling failure, m_{DB} is given as:*

$$m_{DB} = \frac{p^{\frac{q}{2}}\rho_b l^2}{2^{q-1}\cos^{\frac{5q}{2}}(\alpha)}\left(\frac{f}{\pi E_b}\right)^{\frac{1}{2}} + \frac{lf\rho_s(\sec^{2q}(\alpha)-1)}{\sigma_s}, \tag{4.4}$$

and, the mass associated with the D-bar system considering yielding failure, m_{DY} is given as:

$$m_{DY} = \frac{\rho_b}{\sigma_b}\frac{fl}{\cos^{2q}(\alpha)} + \frac{lf\rho_s(\sec^{2q}(\alpha)-1)}{\sigma_s}. \tag{4.5}$$

Proof: The derivation for Eq. (4.4) is given in [21]. To calculate the mass of the bars designed to fail under yielding constraint, we first calculate the minimum area required for each bar as:

$$A_q = \frac{f_q}{\sigma_b} = \frac{f}{\sigma_b(p\cos(\alpha))^q}. \tag{4.6}$$

The mass of each bar can now be calculated as:

$$m_q = \rho_b A_q l_q = \frac{\rho_b f l}{\sigma_b(2p\cos^2(\alpha))^q}, \tag{4.7}$$

which can be multiplied with the total number of bars in the system to get the total mass of the bars as:

$$m_b = n_b m_q = \frac{\rho_b}{\sigma_b} \frac{fl}{\cos^{2q}(\alpha)}. \tag{4.8}$$

Similar approach can be followed to calculate the mass of the strings m_s (also given in the appendix 3 of [21]). Finally, the total mass associated with the D-bar system under yielding can be calculated as $m_{DY} = m_b + m_s$. □

4.3 Optimal Complexity and Minimum Mass of the D-bar Structure

In this section, we provide the formulation to calculate the optimal complexity of the D-bar structure to minimize the mass. The analytical formulas to design minimum mass D-bar structures considering both yielding and buckling failures are derived, and it is shown that designing structure by only considering buckling failure of bars and yielding failure for strings may not yield the optimal solution.

4.3.1 Optimal Complexity Considering Local Failures

The mass of the D-bar system considering yielding failure, m_{DY}, is a monotonically increasing function and the mass considering buckling failure, m_{DB}, first goes down with increasing complexity and then goes up as the mass of the strings overcomes the savings in the bars, which is shown in Fig. 4.4(a). Moreover, the shaded region in Fig. 4.4(a) shows the feasible design region as the mass of the D-bar system has to be greater of mass calculated considering one of the failure criteria. Therefore, the minimum mass that can be achieved is $m_D = \min[\max(m_{DY}, m_{DB})]$ and the optimal complexity can be found at the intersection of the buckling and yielding failure.

Let us define q^* as a real-valued number at which, the two plots corresponding to the mass associated with the D-bar system considering buckling failure (m_{DB}) and yielding failure (m_{DY})

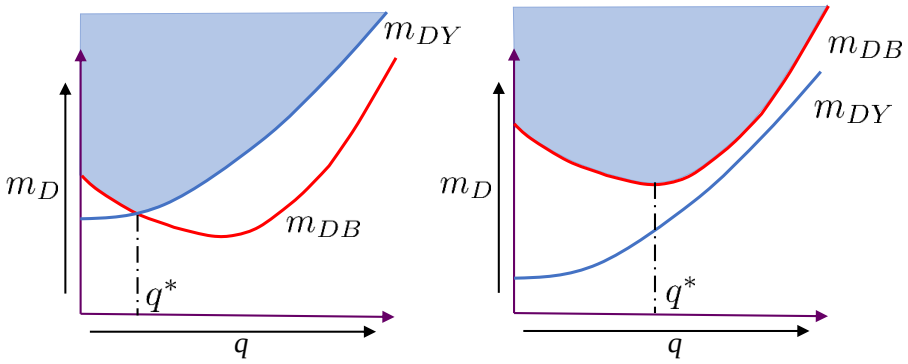

Figure 4.4: Shaded region in the plots represents the achievable minimum mass considering both buckling and yielding.

intersect as shown in Fig. 4.4(a). Then q^* can be calculated by equating m_{DB} and m_{DY} as:

$$m_{DY} = m_{DB}, \tag{4.9}$$

$$\frac{\rho_b}{\sigma_b}\frac{fl}{\cos^{2q}(\alpha)} = \frac{p^{\frac{q}{2}}\rho_b l^2}{2^{q-1}\cos^{\frac{5q}{2}}(\alpha)}\left(\frac{f}{\pi E_b}\right)^{\frac{1}{2}}, \tag{4.10}$$

which can be further simplified to obtain:

$$\left(\frac{4\cos(\alpha)}{p}\right)^{\frac{q^*}{2}} = \frac{2l\sigma_b}{\sqrt{\pi E_b f}}, \tag{4.11}$$

and taking natural log on both sides gives the solution for optimal complexity to minimize the mass of D-bar tensegrity system.

$$q^* = 2\ln\left(\frac{2l\sigma_b}{\sqrt{\pi E_b f}}\right)/\ln\left(\frac{4\cos(\alpha)}{p}\right). \tag{4.12}$$

Note that the solution of the Eq. (4.12) may not be an integer value. So to find the physically realizable complexity of the D-bar structure, we calculate $m_D = \min[\max(m_{DY}, m_{DB})]$ and corresponding complexity q_{opt} for complexities $q = \lfloor q^* \rfloor$ and $q = \lfloor q^* \rfloor + 1$, where $\lfloor \cdot \rfloor$ represents the greatest integer function.

Important Note: If $q^* \leq 0$, then the optimal complexity is $q_{opt} = 0$ which corresponds to

a single column bar. It means that the mass considering yielding failure is more than the mass considering buckling failure ($m_{DY} > m_{DB}$) for complexity $q = 0$.

Lemma 4.3.1. *The minimum mass for a compressive structure has a tightest lower bound of*

$$m_Y = \frac{\rho_b}{\sigma_b} fl. \tag{4.13}$$

Proof: As the mass corresponding to yielding failure is a monotonically increasing function with complexity q, and the optimum mass for a D-bar system would follow $m_D = \min[\max(m_{DY}, m_{DB})]$ over all complexities, the lowest possible mass that can be obtained for any compressive structure is m_{DY} for complexity ($q = 0$), i.e. $m_Y = \frac{\rho_b}{\sigma_b} fl$. □

4.3.2 Optimal Complexity Considering only Buckling Failure

The aim of this subsection is to show that the optimal complexity calculated in the previous section gives the optimal solution under some given conditions and there is no need to check for the optimal complexity considering buckling failure criteria only (infeasibility of Fig. 4.4(b)). To show that, let us write the mass of a single column considering buckling failure as:

$$m_B = 2l^2 \rho_b \left(\frac{f}{\pi E_b} \right)^{\frac{1}{2}}. \tag{4.14}$$

Let us define a non-dimensional quantity $\mu_{DB} = m_{DB}/m_B$ which can be written using Eqs. (4.4) and (4.14) as:

$$\mu_{DB} = \frac{p^{\frac{q}{2}}}{2^q \cos^{\frac{5q}{2}}(\alpha)} + \frac{\rho_s (\sec^{2q}(\alpha) - 1)(\pi E_b)^{\frac{1}{2}}}{2\sigma_s \rho_b} \left(\frac{f^{\frac{1}{2}}}{l} \right), \tag{4.15}$$

which can be simplified by the introduction of a variable ϵ as:

$$\mu_{DB} = \left(\frac{\sqrt{p}}{2} \sec^{\frac{5}{2}}(\alpha) \right)^q + \epsilon \sec^{2q}(\alpha) - \epsilon, \tag{4.16}$$

with

$$\epsilon = \frac{\rho_s(\pi E_b f)^{\frac{1}{2}}}{2\sigma_s \rho_b l}. \tag{4.17}$$

We define q_{b*} as the complexity which minimizes the D-bar mass under buckling constraint. The complexity q_{b*} can be calculated by taking partial derivative of m_{DB} or μ_{DB} w.r.t q as:

$$\frac{\partial m_{DB}}{\partial q} = \frac{\partial \mu_{DB}}{\partial q} = 0, \tag{4.18}$$

which after substitution from Eq. (4.15) gives:

$$\left(\frac{\sqrt{p}}{2}\sec^{\frac{5}{2}}(\alpha)\right)^{q_{b*}} \ln\left(\frac{\sqrt{p}}{2}\sec^{\frac{5}{2}}(\alpha)\right) + \epsilon \sec^{2q_{b*}}(\alpha)\ln\left(\sec^2(\alpha)\right) = 0, \tag{4.19}$$

and can be further simplified to obtain:

$$\left(\frac{4\cos(\alpha)}{p}\right)^{-q_{b*}/2} = \epsilon \frac{\ln\left(\cos^2(\alpha)\right)}{\ln\left(\frac{\sqrt{p}}{2}\sec^{\frac{5}{2}}(\alpha)\right)}. \tag{4.20}$$

Taking natural log on both sides of the above equation, we get:

$$-\frac{q_{b*}}{2}\ln\left(\frac{4\cos(\alpha)}{p}\right) = \ln\epsilon + \ln\left(\frac{\ln\left(\cos^2(\alpha)\right)}{\ln\left(\frac{\sqrt{p}}{2}\sec^{\frac{5}{2}}(\alpha)\right)}\right), \tag{4.21}$$

which after substitution for ϵ from Eq. (4.17) and some rearrangement gives:

$$q_{b*}\ln\left(\frac{4\cos(\alpha)}{p}\right) = 2\ln\left(\frac{2\sigma_s\rho_b l}{\rho_s(\pi E_b f)^{\frac{1}{2}}}\right) + 2\ln\left(\frac{\ln\left(\frac{\sqrt{p}}{2}\sec^{\frac{5}{2}}(\alpha)\right)}{\ln\left(\cos^2(\alpha)\right)}\right), \tag{4.22}$$

which again can be rearranged as:

$$q_{b*} \ln\left(\frac{4\cos(\alpha)}{p}\right) = 2\ln\left(\frac{2l\sigma_b}{(\pi E_b f)^{\frac{1}{2}}}\right) + 2\ln\left(\frac{\sigma_s \rho_b}{\sigma_b \rho_s}\right) + 2\ln\left(\frac{\ln\left(\frac{\sqrt{p}}{2}\sec^{\frac{5}{2}}(\alpha)\right)}{\ln\left(\cos^2(\alpha)\right)}\right). \tag{4.23}$$

Here we break the above equation as the sum of two parts as:

$$q_{b*} = 2\frac{\ln\left(\frac{2l\sigma_b}{(\pi E_b f)^{\frac{1}{2}}}\right)}{\ln\left(\frac{4\cos(\alpha)}{p}\right)} + 2\frac{\ln\left(\frac{\sigma_s \rho_b}{\sigma_b \rho_s}\right)}{\ln\left(\frac{4\cos(\alpha)}{p}\right)} + 2\ln\left(\frac{\ln\left(\frac{\sqrt{p}}{2}\sec^{\frac{5}{2}}(\alpha)\right)}{\ln\left(\cos^2(\alpha)\right)}\right) / \ln\left(\frac{4\cos(\alpha)}{p}\right). \tag{4.24}$$

Please notice that the above equation provides the optimal complexity of the D-bar structure to minimize the mass considering buckling failure for bars and yielding failure for strings. To show the infeasibility of Fig. 4.4(b), we show that optimal complexity obtained considering buckling failure (q_{b*}) is larger than the optimal complexity (q^*) obtained by the intersection of the yielding (m_{DY}) and buckling (m_{DB}) curves. This can be done by examining and substituting the first term in Eq. (4.24) as:

$$q_{b*} = q^* + 2\frac{\ln\left(\frac{\sigma_s \rho_b}{\sigma_b \rho_s}\right)}{\ln\left(\frac{4\cos(\alpha)}{p}\right)} + 2\ln\left(\frac{\ln\left(\frac{\sqrt{p}}{2}\sec^{\frac{5}{2}}(\alpha)\right)}{\ln\left(\cos^2(\alpha)\right)}\right) / \ln\left(\frac{4\cos(\alpha)}{p}\right), \tag{4.25}$$

where q^* (from Eq. (4.12)) represents the optimal complexity calculated considering the intersection of the curves corresponding to yielding and buckling failure.

Note that the value of the second term goes to zero if the material of the bars and strings is same and the value is greater than zero if the material used for strings has higher specific strength than the bars, which is usually the case with tensegrity structures. Also, notice that the third term in the equation only depends on p and angle α, and the value of the third term is always greater than zero for angle $\alpha < 23^o$ for $p = 2$ and angle $\alpha < 15^o$ for $p = 3$.

The above results show that the optimal complexity calculated considering only buckling is higher than the optimal complexity calculated at the intersection of two curves for given range

(angle $\alpha < 23^o$ for $p = 2$ and angle $\alpha < 15^o$ for $p = 3$) which is usually the range to provide minimum mass using D-bar systems.

4.4 Results and Discussion

This section provides the results detailing the minimum mass design of 2D and 3D D-bar structures using the approach developed in the previous section. The minimum mass is obtained by first calculating the optimal complexity of the structure for a given compressive force f and length l. The *mass ratio* μ is used to compare the mass of the D-bar structures m_D with that of a compressive column of solid circular cross-section, m_{col}, as:

$$\mu = \frac{m_D}{m_{col}}, \text{ where } m_{col} = \max\left(\frac{2\rho_b l^2\sqrt{f}}{\sqrt{\pi E_b}}, \frac{\rho_b l f}{\sigma_b}\right), \tag{4.26}$$

where both yielding and buckling failure criteria are considered in the calculation of the mass of the solid column. In the following subsections, μ_{2D} will be used for the mass ratio of 2D D-bars and μ_{3D} will be used for the mass ratio of 3D D-bars. A smaller value of mass ratio $\mu < 1$ represents more mass saving than a compressive column designed to take the same force for the same length. Material properties of aluminum are used for all bar members, string members and the compressive column ($E_s = E_b = 60$ GPa, $\sigma_s = \sigma_b = 110$ MPa, and $\rho_s = \rho_b = 2700$ kg/m^3).

4.4.1 2-Dimensional D-bar Structure

The 2-D D-bar structures are planar structures with $p = 2$ making them susceptible to out-of-plane global buckling. In these results, the global buckling for 2-D structures is not considered as the results are more for the theoretical understanding of minimal mass meta-materials.

Let us start by plotting the mass ratio μ_{2D} with angle α for different values of force f and length l, as shown in Fig. 4.5. It is observed that the mass ratio increases with the increased value of parameter $\frac{f}{l^2}$. Also notice that mass ratio monotonically increases with D-bar angle α, showing that a minimum mass D-bar structure is obtained for smallest value of angle which is possible

with current manufacturing capabilities. For $f = 2500N,\ l = 0.1m$, the mass ratio is less than 1 ($\mu_{2D} < 1$) for $0^o < \alpha \leq 4^o$ and becomes $\mu_{2D} = 1$ for $\alpha > 4^o$, however for $f = 10000N,\ l = 0.1m$, the mass ratio is 1 for the entire range of D-bar angle. This can be understood as for such large value of $\frac{f}{l^2} = 10^6$, the compressive column fails by yielding and thus one can not design a D-bar structure with less required mass.

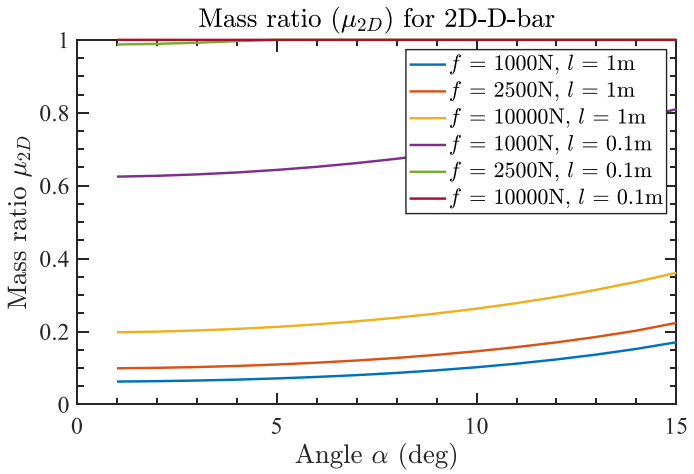

Figure 4.5: Plots of mass ratio μ_{2D} vs. D-bar Angle-α (deg) for the 2D D-bar structure with optimized complexity (q^*) for different set of values of force f and length l.

A similar trend is observed for the plots of optimal complexity q^* with angle α as shown in Fig. 4.6. The optimal complexity consistently decreases with increased value of the parameter $\frac{f}{l^2}$ and stays constant for change in angle α, except for the case of $f = 2500N,\ l = 0.1m$, where it is $q^* = 1$ for $0^o < \alpha \leq 4^o$ and $q^* = 0$ otherwise. For $f = 10000N,\ l = 0.1m$, the optimal complexity $q^* = 0$ for the entire range of angle stating the optimal mass solution to be a single compressive column.

Table 4.1 also provides optimum complexity q^* and angle α for different combinations of force f and length l. For a small value of the parameter $\frac{f}{l^2}$ (first column), the compressive column is more prone to buckling failure and thus more mass savings (mass ratio μ_{2D} is small) can be obtained by replacing the column with a D-bar system. The value of the mass ratio increases with

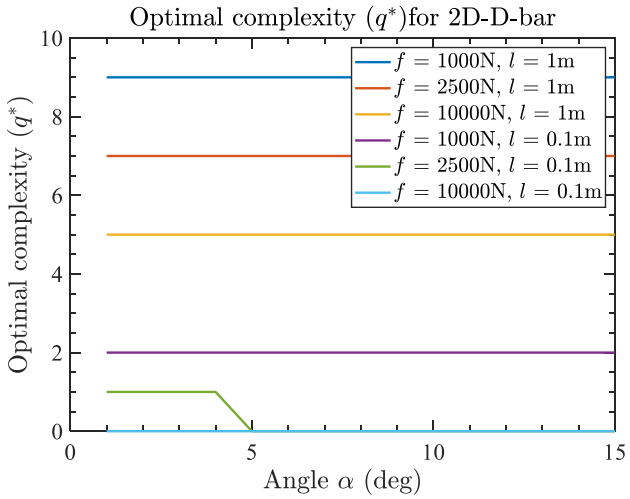

Figure 4.6: Plots of optimized complexity (q^*) vs. D-bar Angle-α (deg) for the 2D D-bar structure for different set of values of force f and length l.

the increased value of the parameter $\frac{f}{l^2}$ for both D-bar angles $\alpha = 5^o$ and $\alpha = 10^o$ and for last two values of $\frac{f}{l^2} = 250000$ and $\frac{f}{l^2} = 1000000$, the mass ratio becomes 1 ($\mu_{2D} = 1$) with an optimal complexity of $q^* = 0$) indicating that the single column is the minimum mass structure. The table also provides a comparison of mass ratio μ_{2D}^T optimized with two different methods for 2D T-bar structure and the mass ratio μ_{2D} for 2D D-bar structure [45]. It is observed that very similar values of the mass ratio are obtained with the area method design of T-bar structure with relatively low complexity and $5 * o$ D-bar structure with relatively high complexities.

Figure 4.7 shows a scaled design of 2D D-bar structures where calculated member cross-sections areas are used to provide better insight. The figure depicts the design of a single compressive column and the optimal configuration ($q^* = 1$) of 2D D-bar structures for two different values of angle $\alpha = 5^o$ and $\alpha = 10^o$ optimized for $f = 1500N$, $l = 0.1m$. The mass value for the column $m_{col} = 0.0048$Kg and for D-bar structures $m_D = 0.0037$ Kg ($\alpha = 5^o$) and $m_D = 0.0039$ Kg ($\alpha = 10^o$) are also shown in the figure.

Table 4.1: Comparison of mass ratio μ_{2D}^{T} optimized with two different methods for 2D T-bar structure (refer to Table 3.1) and mass ratio μ_{2D} for 2D D-bar structure for two values of angle α for different values of force f and length l. Units: f (N), l (m), and α (deg).

$\frac{f}{l^2}$	f	l	**T-bar**						**D-bar**			
			Pre-stress method			Area method			$\alpha = 5^o$		$\alpha = 10^o$	
			q	α	μ_{2D}^{T}	q	α	μ_{2D}^{T}	q^*	μ_{2D}	q^*	μ_{2D}
1000	1000	1	4	20	0.08	4	26	0.07	9	0.07	9	0.10
2500	2500	1	4	22	0.12	4	29	0.10	7	0.11	7	0.15
10000	10000	1	3	24	0.22	3	31	0.21	5	0.21	5	0.26
100000	1000	0.1	1	28	0.65	1	33	0.63	2	0.64	2	0.70
250000	2500	0.1	1	31	1.01	1	33	1.00	0	1.00	0	1.00
1000000	10000	0.1	1	35	1.52	1	33	1.51	0	1.00	0	1.00

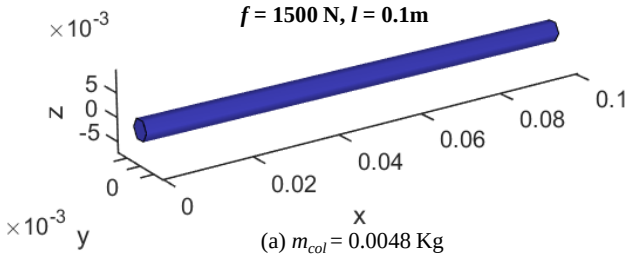

(a) m_{col} = 0.0048 Kg

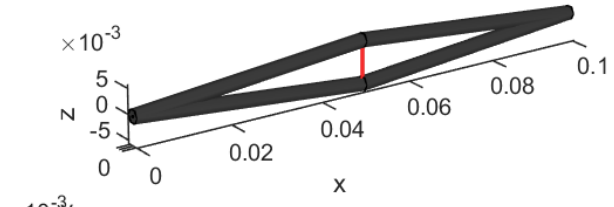

(b) m_D = 0.0037 Kg (μ_{2D} = 0.7760) for α = 5°

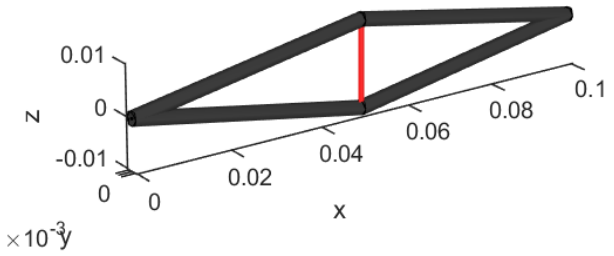

(c) m_D = 0.0039 Kg (μ_{2D} = 0. 8118) for α = 10°

Figure 4.7: Optimum configuration of the 2D D-bar structure for two different values of angle α for a chosen values of force f and length l displaying calculated member cross-sections.

4.4.2 3-Dimensional D-bar Structure

The 3-D D-bar structures are not prone to global buckling for a feasible D-bar angle ($\alpha \geq 2^o$). Thus only local failures are considered in the design of 3D D-bar structures, where bars are designed for both yielding, and buckling failure and strings are designed for only yielding failures. Similar to the last subsection, Fig. 4.8 provides the plots for mass ratio μ_{3D} and angle α with monotonically increasing value of mass ratio μ_{3D} for all sets of force f and length l. For higher values of $\frac{f}{l^2} = 1000000$, the mass ratio becomes one showing no mass saving with the D-bar structure design approach.

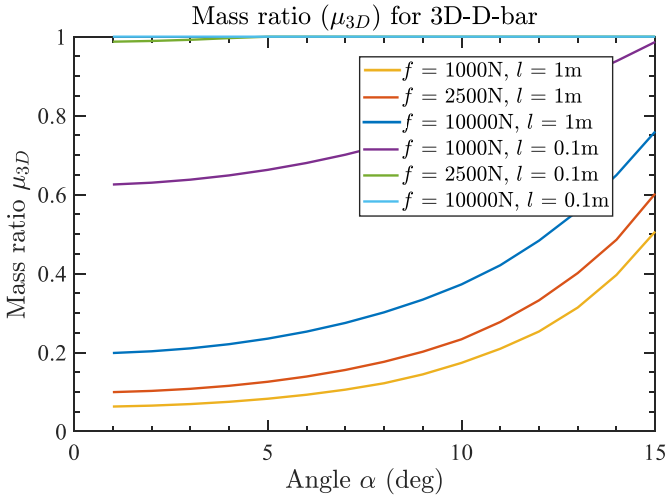

Figure 4.8: Plots of mass ratio μ_{3D} vs. D-bar Angle-α (deg) for the 3D D-bar structure with optimized complexity (q^*) for different set of values of force f and length l.

For first three values of $\frac{f}{l^2} = 1000, \frac{f}{l^2} = 2500$, and $\frac{f}{l^2} = 10000$, Fig. 4.9 shows constant values of optimal complexity (q^*) over the range of angle α. The optimal complexity decreases with increased value of parameter $\frac{f}{l^2}$ and finally becomes zero for $\frac{f}{l^2} = 1000000$. The interesting variation is observed for $\frac{f}{l^2} = 100000$ and $\frac{f}{l^2} = 250000$, where the line for optimal complexity stays constant for some value of angle α and then get decreased by 1. This can be explained as for such large values of the parameter $\frac{f}{l^2}$, higher values of angles can considerably increase the force

in the bars which restricts one more iteration of the D-bar structure.

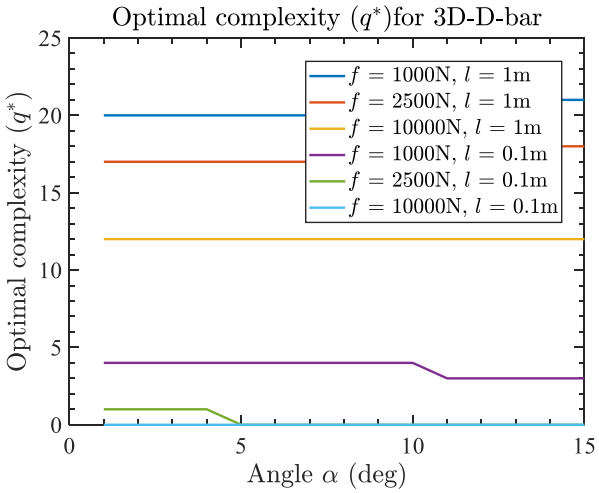

Figure 4.9: Plots of optimized complexity (q^*) vs. D-bar Angle-α (deg) for the 3D D-bar structure for different set of values of force f and length l.

Table 4.2 provides the optimum complexity q^* and angle α for the 3D D-bar structures. Similar to the previous table, for both D-bar angles, the value of the mass ratio increases with the increased value of the parameter $\frac{f}{l^2}$. Moreover, the mass ratio reaches 1 ($\mu_{3D} = 1$) for last two values of $\frac{f}{l^2} = 250000$ and $\frac{f}{l^2} = 1000000$. The table also provides comparison of the mass ratio μ_{3D} for 3D D-bar structure and the mass ratio μ_{3D}^T optimized with two different methods for 3D T-bar structure [45]. Similar observations and trends were observed for both the 3D and 2D D-bar structure as discussed for Table 4.1.

The cross-sections areas of all the members are calculated in plotting the scaled design of optimized 3D D-bar structure as shown in Fig. 4.10. The figure shows the optimal configuration of two 3D D-bar structures for angle values $\alpha = 5^o$ and $\alpha = 10^o$ and optimal complexity ($q^* = 2$). The minimum mass configuration of a single compressive column designed for $f = 1500N$, $l = 0.1m$ with $m_{col} = 0.0048$Kg is also given (same as Fig. 4.7). The mass ratio for 3D D-bar structures $\mu_{3D} = 0.7878$ for $\alpha = 5^o$ and $\mu_{3D} = 0.8608$ for $\alpha = 10^o$ are also given in the figure.

Table 4.2: Comparison of mass ratio μ_{3D}^{T} optimized with two different methods for 3D T-bar structure (refer to Table 3.2) and mass ratio μ_{3D} for 3D D-bar structure for two values of angle α for different values of force f and length l. Units: f (N), l (m), and α (deg).

$\frac{f}{l^2}$	f	l	**T-bar**						**D-bar**			
			Pre-stress method			Area method			$\alpha = 5^o$		$\alpha = 10^o$	
			q	α	μ_{3D}^{T}	q	α	μ_{3D}^{T}	q^*	μ_{3D}	q^*	μ_{3D}
1000	1000	1	4	19	0.10	4	27	0.07	20	0.08	20	0.17
2500	2500	1	4	22	0.14	4	29	0.11	17	0.12	17	0.23
10000	10000	1	3	25	0.25	3	31	0.21	12	0.23	12	0.37
100000	1000	0.1	1	28	0.66	1	33	0.64	4	0.66	4	0.79
250000	2500	0.1	1	31	1.04	1	33	1.01	0	1.00	0	1.00
1000000	10000	0.1	1	36	1.56	1	33	1.54	0	1.00	0	1.00

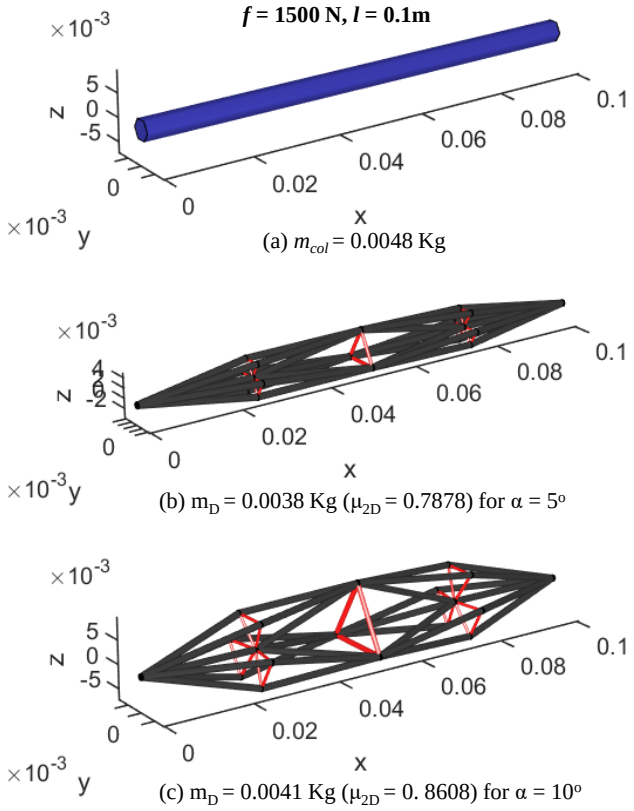

Figure 4.10: Optimum configuration of the 3D D-bar structure for two different values of angle α for a chosen values of force f and length l displaying calculated member cross-sections.

4.5 Conclusions

This chapter derived the analytical formulas to obtain the optimal complexity for the 2D and 3D D-bar structures. It is shown that the optimal complexity q^* depends on the D-bar angle α, compressive force f, length of the structure l, and the material properties of the bar members. It is interesting to note that the optimal complexity is independent of the string material. The minimum mass configuration of the D-bar systems, which considered both yielding and buckling failure for compressive members and yielding failures for tensile members, can be easily designed from the uniquely calculated optimal complexity of the structure. The chapter also derives an important relation between the optimal complexity calculated considering only buckling failures (q_{b*}) and optimal complexity calculated considering only both local failures (q^*). Finally, the results section provided a comparative study of the minimum mass design of T-bar and D-bar tensegrity structures for different sets of given compressive force and length.

5. DYNAMICS OF TENSEGRITY SYSTEMS*

[1] This chapter provides a single matrix-second-order nonlinear differential equation to simulate the dynamics of tensegrity systems with rigid bars and massive strings. The chapter allows to distribute the string mass into any specified number of point masses along the string while preserving the exact rigid bar dynamics. This formulation also allows modeling of skins and surfaces as a finite set of strings in the tensegrity dynamics. To reduce the complexity of the model, non-minimal coordinates (6 DOF for each bar instead of 5) were chosen. This is the key to give more accurate results in computer simulations since the mathematical structure of the model is simplified and exploited during numerical computations. A bar length correction algorithm is also provided for both class-1 and class-k tensegrity systems to correct the erroneous change in bar length because of computational errors during numerical integration. We characterize the control variable as the force density in each string. This allows control laws to be developed independently of the material chosen for the structural elements. A nonlinear transformation back to the physical control variables involves the material properties.

5.1 Introduction

The field of Multi-Body Dynamics includes rigid and elastic bodies connected in arbitrary ways. Most approaches use a minimal coordinate representation, eliminating redundant variables as the body connections are exploited one at a time until all the bodies are included into the system. One disadvantage of such methods is topology constraints, such as limiting the configuration of the rigid body connections to a topological tree. (See the TREETOPS software developed by company DYNACS [56]). Another computational disadvantage of these approaches is the reliance on transcendental functions to describe the positions of elements. *Tensegrity* systems [6] dynamics is a subset of the class of Multi-body dynamics which does not treat (thus far) rigid bodies of

[1]*Portions of this section are reprinted or adapted from [16] : Raman Goyal and Robert E. Skelton, "Tensegrity System Dynamics with Rigid Bars and Massive strings", Multibody System Dynamics, 46:203–228, 2019, DOI: 10.1007/s11044-019-09666-4.

arbitrary shape and inertia, but they allow any stabilizable topology of members.

The dynamics of the tensegrity structures has been explored in the past by various researchers. Murakami[57] developed the equations of motion for tensegrity structures using the Eulerian and Lagrangian approach which basically represent spatial and material formulations. These equations were then linearized about a reference configuration to perform the modal analysis. In part two of that paper, quasi-static analyses were performed which concluded that pre-stress and infinitesimal mechanism modes characterize the dynamics and statics of tensegrity structures. The linearized dynamics models for the different class of tensegrity structures were developed by Sultan et al.[58] and these models were further used by Masic and Skelton [59] to select the prestress for optimal dynamic/control performance. Ali and Smith [28] also wrote a linearized dynamic model around an equilibrium configuration to study the dynamic behavior of an active tensegrity structure. These linearized models are approximations and do not capture the correct dynamics of the structure. Tan and Pellegrino [60] studied the non-linear vibration of cable-stiffened pantographic deployable structures and showed that cable prestress is correlated with the natural frequencies of the system. Skelton and Nagase [61, 62] developed the non-linear tensegrity dynamics in vector form for a network of rods and strings neglecting the masses in the strings. Recently, Joono and Skelton [14] developed a second order matrix differential equation to describe the non-linear dynamics of any tensegrity structure. They used nonminimal coordinates and assumed the compressive elements to have no inertia about the longitudinal axis. The masses in the tension elements (strings) were also neglected in the formulation. In the present study, each compressive member can be a bar of certain radius i.e. can have some inertia about its longitudinal axis and masses in the strings is also incorporated.

At a fundamental level, the dynamics of these structures is straightforward since it relies simply on the dynamics of rigid bars and elastic models for strings. However, a rigorous and scalable approach to describing these structures is highly desirable. The nonlinear dynamic model developed here captures both the translational motion of the mass center of each bar and each cable, and the rotational dynamics of each bar, using Newton's second law. Therefore, the model allows

for the simulation of any tensegrity network with elastic massive string members and rigid bars. Certainly, there are many applications such as cable-stayed bridges in which the mass of the cables is as important as the mass of the bars. Furthermore, applications exist in which a membrane covering the surface of the structure is required. This dynamic model assumed the bars to be rigid and the length constraints are incorporated at the second derivative level in the formulation. This can lead to violations in length constraint during the numerical integration procedure. In the appendix, we provide an algorithm to correct the bar and time derivative of the bar vector to satisfy the length constraints (appendix A). The author believes that the other benefits of this formulation outweigh this shortcoming of the formulation. Finally, this chapter makes following contributions to the theory and mathematical modeling of tensegrity systems: *i*) It adds mass to tensile elements, *ii*) It adds string-to-string nodes, *iii*) It maintains a matrix-second-order nonlinear differential equation without any transcendental functions. *iv*) It provides a novel algorithm to correct the violations in bar length due to computational errors. Moreover, the absence of trigonometric functions leads to improved efficiency and accuracy of the dynamics simulation and control design. These equations are suitable for the design of control algorithms to control shape or other requirements of the system as the control variables (force density in each string) are linear in the dynamics formulation. These force densities can easily be converted into a physical quantity (tensions or rest-lengths of tensile elements) using a non-linear transformation.

5.2 Notation

5.2.1 Vector Notation

We distinguish a three-dimensional object that has magnitude and direction by bold letters. These are called Gibbs vectors in honor of the inventor of vector concepts in three-dimensional space [63]. In linear algebra, an $n \times 1$ matrix is called an *n*-dimensional vector, and obviously a 3×1 matrix would be called a 3-dimensional vector. But these are not Gibbs vectors and will not be bold here. For example, a vector $\mathbf{v}$ can be expressed in any specified frame of reference. Let the components of vector $\mathbf{v}$ in a *specified* set of coordinates be described by the 3×1 matrix v. The

components of the Gibbs vector $\mathbf{v}$ can be written simply as v, without bold. Scalars are also not bold, so the distinction between scalars and three by one matrices are made clear by the context.

Define a right-handed *dextral set* of unit vectors by these dot and cross product properties:

a) $\boldsymbol{e}_i \cdot \boldsymbol{e}_j = \delta_{ij}$

b) $\boldsymbol{e}_i \times \boldsymbol{e}_j = \boldsymbol{e}_k$ if (i,j,k) = (1,2,3) or (3,1,2) or (2,3,1)

Then define a *Vectrix* $\boldsymbol{\mathcal{E}}$ [64] by:

c) $\boldsymbol{\mathcal{E}} = \begin{bmatrix} \boldsymbol{e}_1 & \boldsymbol{e}_2 & \boldsymbol{e}_3 \end{bmatrix}, \quad \boldsymbol{\mathcal{E}}^{\mathsf{T}} = \begin{bmatrix} \boldsymbol{e}_1 \\ \boldsymbol{e}_2 \\ \boldsymbol{e}_3 \end{bmatrix}$

d) $\boldsymbol{\mathcal{E}}^{\mathsf{T}} \cdot \boldsymbol{\mathcal{E}} = I$ (due to (a) and (c))

Hence for two vectors expressed in the same frame ($\boldsymbol{b} = \boldsymbol{\mathcal{E}} b^{\mathcal{E}}$ and $\boldsymbol{a} = \boldsymbol{\mathcal{E}} a^{\mathcal{E}}$), it follows that:

e) $\boldsymbol{a} \cdot \boldsymbol{b} = (\boldsymbol{\mathcal{E}} a^{\mathcal{E}})^T \cdot (\boldsymbol{\mathcal{E}} b^{\mathcal{E}}) = a^{\mathcal{E}^{\mathsf{T}}} (\boldsymbol{\mathcal{E}}^{\mathsf{T}} \cdot \boldsymbol{\mathcal{E}}) b^{\mathcal{E}} = a^{\mathcal{E}^{\mathsf{T}}} b^{\mathcal{E}}$

f) $\boldsymbol{a} \times \boldsymbol{b} = (\boldsymbol{\mathcal{E}} a^{\mathcal{E}}) \times (\boldsymbol{\mathcal{E}} b^{\mathcal{E}}) = \boldsymbol{\mathcal{E}} \tilde{a}^{\mathcal{E}} b^{\mathcal{E}}, \quad \tilde{a}^{\mathcal{E}} = \begin{bmatrix} 0 & -a_3^{\mathcal{E}} & a_2^{\mathcal{E}} \\ a_3^{\mathcal{E}} & 0 & -a_1^{\mathcal{E}} \\ -a_2^{\mathcal{E}} & a_1^{\mathcal{E}} & 0 \end{bmatrix}$

where $\tilde{a}^{\mathcal{E}}$ is a skew-symmetric matrix composed of the 3 elements of $a^{\mathcal{E}}$, the vector $\boldsymbol{a} = (\boldsymbol{\mathcal{E}} a^{\mathcal{E}})$.

5.2.2 Kinematics

Consider a vector $\boldsymbol{v}$ described in two different reference frames. Let the Vectrix $\boldsymbol{\mathcal{E}} = \begin{bmatrix} \boldsymbol{e}_1 & \boldsymbol{e}_2 & \boldsymbol{e}_3 \end{bmatrix}$ denote the dextral set of unit vectors $\boldsymbol{e}_i$ that are inertially fixed. Let the Vectrix $\boldsymbol{\mathcal{B}} = \begin{bmatrix} \boldsymbol{b}_1 & \boldsymbol{b}_2 & \boldsymbol{b}_3 \end{bmatrix}$ be the body-fixed dextral set of $\boldsymbol{b}_i$ fixed in the coordinates of the rigid body.

Then, the unitary coordinate transformation $\boldsymbol{\mathcal{B}} = \boldsymbol{\mathcal{E}}\Theta$ and $\Theta^{\mathsf{T}}\Theta = I$ leads to:

$$\boldsymbol{\mathcal{B}} = \boldsymbol{\mathcal{E}}\Theta, \quad \Theta^{\mathsf{T}}\Theta = I \rightarrow \Theta^{\mathsf{T}}\dot{\Theta} = \tilde{\omega}^{\mathcal{B}} = \text{skew-symmetric}, \tag{5.1}$$

$$\boldsymbol{v} = \boldsymbol{\mathcal{E}}v^{\mathcal{E}}, \tag{5.2}$$

$$= \boldsymbol{\mathcal{B}}v^{\mathcal{B}}, \quad v^{\mathcal{E}} = \Theta v^{\mathcal{B}}, \tag{5.3}$$

where Θ represents the Direction Cosine Matrix (always unitary) and $v^{\mathcal{E}}$, $v^{\mathcal{B}}$ represent the components of the vector $\boldsymbol{v}$ as viewed, respectively, in coordinate frame $\boldsymbol{\mathcal{E}}$ and $\boldsymbol{\mathcal{B}}$. Then $\boldsymbol{v}$ and $\dot{\boldsymbol{v}}$ are simply:

$$\boldsymbol{v} = \boldsymbol{\mathcal{B}}v^{\mathcal{B}}, \tag{5.4}$$

$$\dot{\boldsymbol{v}} = \dot{\boldsymbol{\mathcal{B}}}v^{\mathcal{B}} + \boldsymbol{\mathcal{B}}\dot{v}^{\mathcal{B}} = \boldsymbol{\mathcal{B}}[\tilde{\omega}^{\mathcal{B}}v^{\mathcal{B}} + \dot{v}^{\mathcal{B}}], \tag{5.5}$$

where from Equation 5.1:

$$\dot{\boldsymbol{\mathcal{B}}} = \boldsymbol{\mathcal{E}}\dot{\Theta} = \boldsymbol{\mathcal{B}}\Theta^{\mathsf{T}}\dot{\Theta} = \boldsymbol{\mathcal{B}}\tilde{\omega}^{\mathcal{B}}, \tag{5.6}$$

and the angular velocity of frame $\boldsymbol{\mathcal{B}}$ relative to frame $\boldsymbol{\mathcal{E}}$ is:

$$\boldsymbol{\omega} = \boldsymbol{\mathcal{E}}\omega^{\mathcal{E}} = \boldsymbol{\mathcal{B}}\omega^{\mathcal{B}}, \quad \omega^{\mathcal{B}} = \begin{bmatrix} \omega_1^{\mathcal{B}} \\ \omega_2^{\mathcal{B}} \\ \omega_3^{\mathcal{B}} \end{bmatrix}. \tag{5.7}$$

5.3 Dynamics of a Single Rod

5.3.1 Rotational Dynamics

Consider a vector $\boldsymbol{r}$ locating the center of mass of the rod of length $l = \|\boldsymbol{b}\|$, where $\boldsymbol{b}$ is the vector along the rod. Let the *Vectrix* $\boldsymbol{\mathcal{E}}$ denote the dextral set of unit vectors $\boldsymbol{e}_i$ that are inertially fixed. Let the *Vectrix* $\boldsymbol{\mathcal{B}}$ be the body-fixed dextral set of unit vectors $\boldsymbol{b}_i$ fixed in the body of the rod,

with $\boldsymbol{b}_3$ pointing along the rod.

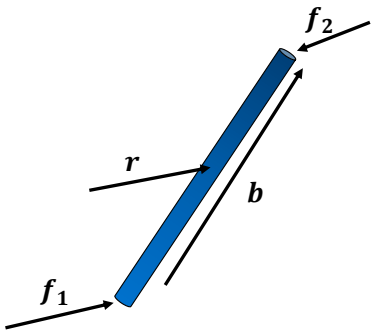

Figure 5.1: Tensegrity rod member vector nomenclature

The rod vector $\boldsymbol{b}$ of length l, described in body coordinates $\boldsymbol{\mathcal{B}}$ is:

$$\boldsymbol{b} = \boldsymbol{\mathcal{B}} b^{\mathcal{B}}, \quad b^{\mathcal{B}} = \begin{bmatrix} 0 & 0 & l \end{bmatrix}^{\mathsf{T}}, \tag{5.8}$$

and the time rate of change of the vector $\boldsymbol{b}$ is:

$$\dot{\boldsymbol{b}} = \dot{\boldsymbol{\mathcal{B}}} b^{\mathcal{B}} + \boldsymbol{\mathcal{B}} \dot{b}^{\mathcal{B}} = \dot{\boldsymbol{\mathcal{B}}} b^{\mathcal{B}} = \boldsymbol{\mathcal{B}} \tilde{\omega}^{\mathcal{B}} b^{\mathcal{B}}. \tag{5.9}$$

It is useful to compute $\boldsymbol{b} \times \dot{\boldsymbol{b}}$ as:

$$\boldsymbol{b} \times \dot{\boldsymbol{b}} = (\boldsymbol{\mathcal{B}} b^{\mathcal{B}}) \times (\dot{\boldsymbol{\mathcal{B}}} b^{\mathcal{B}}) = (\boldsymbol{\mathcal{B}} b^{\mathcal{B}}) \times (\boldsymbol{\mathcal{B}} \tilde{\omega}^{\mathcal{B}} b^{\mathcal{B}}), \tag{5.10}$$

$$= \boldsymbol{\mathcal{B}} \tilde{b}^{\mathcal{B}} \tilde{\omega}^{\mathcal{B}} b^{\mathcal{B}} = -\boldsymbol{\mathcal{B}} \tilde{b}^{\mathcal{B}} \tilde{b}^{\mathcal{B}} \omega^{\mathcal{B}} = -\boldsymbol{\mathcal{B}} (\tilde{b}^{\mathcal{B}})^2 \omega^{\mathcal{B}}. \tag{5.11}$$

Now, using the identity:

$$(\tilde{b}^{\mathcal{B}})^2 = -(b^{\mathcal{B}^{\mathsf{T}}} b^{\mathcal{B}} I - b^{\mathcal{B}} b^{\mathcal{B}^{\mathsf{T}}}), \tag{5.12}$$

Equation 5.11 becomes:

$$\boldsymbol{b} \times \dot{\boldsymbol{b}} = \boldsymbol{\mathcal{B}}(\|b^{\mathcal{B}}\|^2 I - b^{\mathcal{B}} b^{\mathcal{B}^\mathsf{T}})\omega^{\mathcal{B}}. \tag{5.13}$$

For our case, $b^{\mathcal{B}} = \begin{bmatrix} 0 & 0 & l \end{bmatrix}^\mathsf{T}$. Therefore:

$$\boldsymbol{b} \times \dot{\boldsymbol{b}} = \boldsymbol{\mathcal{B}} \left(l^2 I - \begin{bmatrix} 0 & 0 & 0 \\ 0 & 0 & 0 \\ 0 & 0 & l^2 \end{bmatrix} \right) \omega^{\mathcal{B}}, \tag{5.14}$$

$$= \boldsymbol{\mathcal{B}} \begin{bmatrix} I_2 & 0 \\ 0 & 0 \end{bmatrix} l^2 \omega^{\mathcal{B}} = \boldsymbol{\mathcal{B}} l^2 \begin{bmatrix} \omega_1^{\mathcal{B}} \\ \omega_2^{\mathcal{B}} \\ 0 \end{bmatrix} = l^2 \boldsymbol{\omega}_b. \tag{5.15}$$

Hence, the relationship between $\boldsymbol{\omega}_b$, the angular velocity of rod $\boldsymbol{b}$, and vectors $\boldsymbol{b}$ and $\dot{\boldsymbol{b}}$ is:

$$\boldsymbol{\omega}_b = \frac{\boldsymbol{b} \times \dot{\boldsymbol{b}}}{\|\boldsymbol{b}\|^2}. \tag{5.16}$$

Using Equation 5.16, the angular momentum of rod $\boldsymbol{b}$ about its mass center is:

$$\boldsymbol{h}_b = I_b \boldsymbol{\omega}_b, \tag{5.17}$$

$$= \left(\frac{m_b l^2}{12} + \frac{m_b r_b^2}{4} \right) \left(\frac{\boldsymbol{b} \times \dot{\boldsymbol{b}}}{l^2} \right), \tag{5.18}$$

$$\boldsymbol{h} = \boldsymbol{h}_b = \left(\frac{m_b}{12} + \frac{m_b r_b^2}{4l^2} \right) \boldsymbol{b} \times \dot{\boldsymbol{b}} = J \boldsymbol{b} \times \dot{\boldsymbol{b}}, \tag{5.19}$$

where $J = \frac{m_b}{12} + \frac{m_b r_b^2}{4l^2}$. The derivative with respect to time of the angular momentum of a rod member can then be formulated in terms of $\boldsymbol{b}$ and $\dot{\boldsymbol{b}}$ as follows:

$$\dot{\boldsymbol{h}} = J\dot{\boldsymbol{b}} \times \dot{\boldsymbol{b}} + J\boldsymbol{b} \times \ddot{\boldsymbol{b}}, \tag{5.20}$$

$$= J\boldsymbol{b} \times \ddot{\boldsymbol{b}}. \tag{5.21}$$

The time rate of change of the angular momentum vector $\boldsymbol{h}$ is equal to the sum of torques $\boldsymbol{\tau}$ acting on the rod member about its center of mass. The forces acting on the two opposite ends of the rod member are $\boldsymbol{f}_1$ and $\boldsymbol{f}_2$ as illustrated in Figure 5.1. The resulting torques are described here in terms of $\boldsymbol{b}$ as:

$$\dot{\boldsymbol{h}} = \boldsymbol{\tau}, \tag{5.22}$$

$$\dot{\boldsymbol{h}} = \frac{1}{2}\boldsymbol{b} \times (\boldsymbol{f}_2 - \boldsymbol{f}_1). \tag{5.23}$$

Equations 5.21 and 5.23 yield:

$$J\boldsymbol{b} \times \ddot{\boldsymbol{b}} = \frac{1}{2}\boldsymbol{b} \times (\boldsymbol{f}_2 - \boldsymbol{f}_1). \tag{5.24}$$

Equation 5.24 can be written in any coordinates, but we choose inertial coordinates for simpler forms of final equations. To simplify notation hereafter we define $b = b^{\mathcal{E}}$ where $\boldsymbol{b} = \boldsymbol{\mathcal{B}}b^{\mathcal{B}} = \boldsymbol{\mathcal{E}}b^{\mathcal{E}}$. Writing Equation 5.24 in inertial coordinates yields:

$$J\tilde{b}\ddot{b} = \frac{1}{2}\tilde{b}(f_2 - f_1). \tag{5.25}$$

An additional constraint must be added here to ensure that the rod vector b remains constant with length l. This constraint is described as follows:

$$b^{\mathsf{T}}b = l^2, \tag{5.26}$$

Differentiating the constant length constraint of Equation 5.26, a length constraint in terms of $\ddot{b}$ is

obtained:

$$\dot{b}^{\mathsf{T}}b + b^{\mathsf{T}}\dot{b} = 0 = 2b^{\mathsf{T}}\dot{b}, \tag{5.27}$$

$$\dot{b}^{\mathsf{T}}\dot{b} + b^{\mathsf{T}}\ddot{b} = 0, \tag{5.28}$$

$$b^{\mathsf{T}}\ddot{b} = -\dot{b}^{\mathsf{T}}\dot{b}. \tag{5.29}$$

The length constraint (Equation 5.29) and rotational dynamics (Equation 5.25), both in terms of $\ddot{b}$ can be re-expressed in matrix form as:

$$\begin{bmatrix} \tilde{b} \\ b^{\mathsf{T}} \end{bmatrix} \ddot{b} = \begin{bmatrix} \frac{1}{2J}\tilde{b}(f_2 - f_1) \\ -\dot{b}^{\mathsf{T}}\dot{b} \end{bmatrix}. \tag{5.30}$$

This is a simple linear algebra equality that can be solved for $\ddot{b}$. One can easily verify the existence condition for the solution and the full column rank of the matrix multiplying $\ddot{b}$. Therefore, denoting a matrix pseudo inverse by the superscript "+", the unique solution for $\ddot{b}$ is:

$$\ddot{b} = \begin{bmatrix} \tilde{b} \\ b^{\mathsf{T}} \end{bmatrix}^{+} \begin{bmatrix} \frac{1}{2J}\tilde{b}(f_2 - f_1) \\ -\dot{b}^{\mathsf{T}}\dot{b} \end{bmatrix}, \tag{5.31}$$

$$= \frac{1}{l^2}\begin{bmatrix} -\tilde{b} & b \end{bmatrix} \begin{bmatrix} \frac{1}{2J}\tilde{b}(f_2 - f_1) \\ -\dot{b}^{\mathsf{T}}\dot{b} \end{bmatrix}, \tag{5.32}$$

$$= \frac{1}{l^2}[-\frac{1}{2J}\tilde{b}\tilde{b}(f_2 - f_1) - b\dot{b}^{\mathsf{T}}\dot{b}], \tag{5.33}$$

$$= -\frac{1}{2Jl^2}(-l^2 I + bb^{\mathsf{T}})(f_2 - f_1) - \frac{1}{l^2}b\dot{b}^{\mathsf{T}}\dot{b}. \tag{5.34}$$

Since, $\tilde{b}\tilde{b} = -l^2 I + bb^{\mathsf{T}}$. Rearranging Equation 5.34 gives the final form of the vector equations for rotational dynamics:

$$J\ddot{b} = \frac{1}{2}(f_2 - f_1) - \frac{1}{2l^2}bb^{\mathsf{T}}(f_2 - f_1) - \frac{J}{l^2}b\dot{b}^{\mathsf{T}}\dot{b}. \tag{5.35}$$

The final equation represents the rod rotational dynamics including influences from the length constraint. Now we must address the translational dynamics.

5.3.2 Translational Dynamics

For a single rod in a tensegrity structure such as that illustrated in the free-body diagram of Figure 5.1, the inertial position of the rod center of mass is described by $\boldsymbol{r}$, the vector along the rod member is described by the vector $\boldsymbol{b}$, and the sum of the internal forces from the strings and the external forces, acting on the two ends of the rod, is described by $\boldsymbol{f_1}$ and $\boldsymbol{f_2}$, where $\boldsymbol{r} = \boldsymbol{\mathcal{E}} r^{\mathcal{E}}$, $\boldsymbol{f}_i = \boldsymbol{\mathcal{E}} f_i^{\mathcal{E}}$. For simplification, we write $r = r^{\mathcal{E}}$ and $f_i = f_i^{\mathcal{E}}$.

$$m_b \ddot{\boldsymbol{r}} = \boldsymbol{f}_1 + \boldsymbol{f}_2, \tag{5.36}$$

which can be written in inertial coordinates as:

$$m_b \ddot{r} = f_1 + f_2. \tag{5.37}$$

5.4 Matrix Formulation of Tensegrity Dynamics

Equations 5.35 and 5.37 can be used to describe the dynamics of any given rod member in a tensegrity structure. Describing a full tensegrity structure would consequently yield 2β vector equations for a system containing β rod members. However, we will assemble these equations in a matrix form to simplify the structure of the final equations.

Connectivity matrices are now introduced to relate the matrix of nodes, N, to the matrix of string vectors, S, and the matrix of rod vectors B. The i^{th} column of matrices N, S, and B are, respectively the inertial components of the vectors, $\mathbf{n}_i$, $\mathbf{s}_i$, and $\mathbf{b}_i$. We write these as n_i, s_i, and b_i. Define the string connectivity matrix by C_s^{T}, and the rod connectivity matrix by C_b^{T}. Then by inspection of the network, labeled with rod and string vectors, one can immediately write matrices (with entries of 0, 1, -1) to satisfy the definitions $S = NC_s^{\mathsf{T}}$ and $B = NC_b^{\mathsf{T}}$.

By convention, we choose to name the nodes at the base of rod vectors as $N_1 =$

$\begin{bmatrix} n_1 & n_2 & \cdots & n_\beta \end{bmatrix}$ and we choose to name the terminal ends of the rod vectors as $N_2 = \begin{bmatrix} n_{1+\beta} & n_{2+\beta} & \cdots & n_{2\beta} \end{bmatrix}$. Defining each rod end point as a node, a tensegrity consisting of $n = 2\beta$ nodes leads to a $3 \times n$ node matrix, $N = \begin{bmatrix} N_1 & N_2 \end{bmatrix}$, in which each column is the inertial position of a node. Also, for a network of β rods, define the $3 \times \beta$ matrix $B = \begin{bmatrix} b_1 & b_2 & \cdots & b_\beta \end{bmatrix}$.

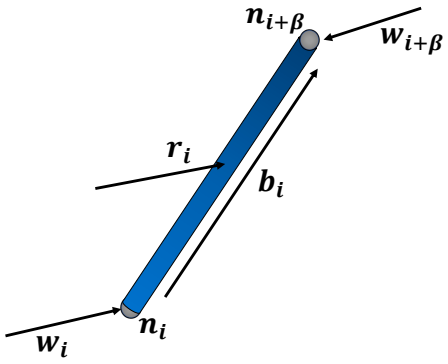

Figure 5.2: Tensegrity rod member numbering convention

The convention mentioned above yields $C_b = \begin{bmatrix} -I_\beta & I_\beta \end{bmatrix}$. In general, C_b is a $\beta \times n$ matrix in which each row describes the node connectivity of a rod member. That is, the row of C_b for a rod member connecting n_i to n_j will consist of a " $+1$" at the j^{th} column, a " -1" at the i^{th} column, and zeros elsewhere. Now, vectors locating the mass centers of the rods is defined as (r_i is the i^{th} column of matrix R):

$$R = N_1 + \frac{1}{2}B, \tag{5.38}$$

$$= N_1 + \frac{1}{2}(N_2 - N_1), \tag{5.39}$$

$$= N\frac{1}{2}\begin{bmatrix} I_\beta \\ I_\beta \end{bmatrix} = NC_r^{\mathsf{T}}. \tag{5.40}$$

For any n-dimensional column vector, we define the "hat" operator over a vector to form a

diagonal matrix from the elements of the vector. Then, the dynamic equations of the i^{th} rod b_i from Equation 5.35 are placed in the the i^{th} column of the matrix $\ddot{B}\hat{J}$:

$$\ddot{B}\hat{J} = \begin{bmatrix} \ddot{b}_1 & \ddot{b}_2 & \cdots & \ddot{b}_\beta \end{bmatrix} \begin{bmatrix} J_1 & 0 & \cdots & 0 \\ 0 & J_2 & \cdots & 0 \\ \vdots & \vdots & \ddots & \vdots \\ 0 & 0 & \cdots & J_\beta \end{bmatrix} = \begin{bmatrix} J_1\ddot{b}_1 & J_2\ddot{b}_2 & \cdots & J_\beta\ddot{b}_\beta \end{bmatrix}. \tag{5.41}$$

This process can be performed for the remaining three terms in Equation 5.35, as summarized below. Forces acting on the end points of each rod are described with the force matrix F, whose i^{th} column is the total force vector acting on the i^{th} node n_i from both internal (string and rod forces) and external sources. Hence, for the i^{th} rod, first and second terms give:

$$\frac{1}{2}(f_{2_i} - f_{1_i}) = \frac{1}{2}[FC_b^{\mathsf{T}}]_i, \tag{5.42}$$

$$-\frac{1}{2l^2} b_i b_i^{\mathsf{T}} (f_{2_i} - f_{1_i}) = -\frac{1}{2}[B\hat{l}^{-2}\lfloor B^{\mathsf{T}} F C_b^{\mathsf{T}} \rfloor]_i, \tag{5.43}$$

where we introduce the $\lfloor \circ \rfloor$ operator, which sets every off-diagonal element of the square matrix operand to zero. Now, the last term can be written as:

$$-\frac{J_i}{l_i^2} b_i \dot{b_i}^{\mathsf{T}} \dot{b_i} = -[B\hat{J}\hat{l}^{-2}\lfloor \dot{B}^{\mathsf{T}} \dot{B} \rfloor]_i. \tag{5.44}$$

Combining the four matrix expressions for the four original terms in Equation 5.35 gives a full matrix expression for $\ddot{B}$. This describes the rotational motion of every rod member in the system while including a constant length constraint.

$$\ddot{B}\hat{J} = \frac{1}{2} F C_b^{\mathsf{T}} - \frac{1}{2} B\hat{l}^{-2}\lfloor B^{\mathsf{T}} F C_b^{\mathsf{T}} \rfloor - B\hat{J}\hat{l}^{-2}\lfloor \dot{B}^{\mathsf{T}} \dot{B} \rfloor. \tag{5.45}$$

This expression can be simplified with the following definition of $\hat{\lambda}$:

$$\hat{\lambda} = -\hat{J}\hat{l}^{-2}\lfloor \dot{B}^{\mathsf{T}}\dot{B} \rfloor - \frac{1}{2}\hat{l}^{-2}\lfloor B^{\mathsf{T}}FC_b^{\mathsf{T}} \rfloor, \tag{5.46}$$

$$\ddot{B}\hat{J} = \frac{1}{2}FC_b^{\mathsf{T}} + B\hat{\lambda}. \tag{5.47}$$

Following the same process as that of the rotational dynamics, the translational dynamics must similarly be converted into a matrix expression. In this case, R is a $3 \times \beta$ matrix in which the i^{th} column describes the inertial position of center of mass of the i^{th} rod member. Using Equation 5.40:

$$m_{b_i}\ddot{r}_i = f_{1_i} + f_{2_i} = [\ddot{R}\hat{m}_b]_i = 2[FC_r^{\mathsf{T}}]_i, \tag{5.48}$$

$$\ddot{R}\hat{m}_b = 2FC_r^{\mathsf{T}}. \tag{5.49}$$

The matrix expressions for the rotational and translational dynamics of the full tensegrity system can be re-expressed as follows:

$$\begin{bmatrix} \ddot{B} & \ddot{R} \end{bmatrix} \begin{bmatrix} \hat{J} & 0 \\ 0 & \hat{m}_b \end{bmatrix} + \begin{bmatrix} B & R \end{bmatrix} \begin{bmatrix} -\hat{\lambda} & 0 \\ 0 & 0 \end{bmatrix} = F \begin{bmatrix} \frac{1}{2}C_b^{\mathsf{T}} & 2C_r^{\mathsf{T}} \end{bmatrix}. \tag{5.50}$$

Recognizing that $\begin{bmatrix} \frac{1}{2}C_b^{\mathsf{T}} & 2C_r^{\mathsf{T}} \end{bmatrix}^{-1} = \begin{bmatrix} C_b^{\mathsf{T}} & C_r^{\mathsf{T}} \end{bmatrix}^{\mathsf{T}}$ [14], Equation 5.50 is rewritten as follows:

$$\begin{bmatrix} \ddot{B} & \ddot{R} \end{bmatrix} \begin{bmatrix} \hat{J} & 0 \\ 0 & \hat{m}_b \end{bmatrix} \begin{bmatrix} C_b \\ C_r \end{bmatrix} + \begin{bmatrix} B & R \end{bmatrix} \begin{bmatrix} -\hat{\lambda} & 0 \\ 0 & 0 \end{bmatrix} \begin{bmatrix} C_b \\ C_r \end{bmatrix} = F, \tag{5.51}$$

$$\begin{bmatrix} \ddot{B} & \ddot{R} \end{bmatrix} \begin{bmatrix} \hat{J}C_b \\ \hat{m}_b C_r \end{bmatrix} + \begin{bmatrix} B & R \end{bmatrix} \begin{bmatrix} -\hat{\lambda}C_b \\ 0 \end{bmatrix} = F. \tag{5.52}$$

The definitions of the rod and center of mass connectivity matrices, $B = NC_b^{\mathsf{T}}$, and $R = NC_r^{\mathsf{T}}$,

can be re-expressed in matrix form and substituted into Equation 5.52:

$$\begin{bmatrix} B & R \end{bmatrix} = N \begin{bmatrix} C_b^{\mathsf{T}} & C_r^{\mathsf{T}} \end{bmatrix}, \tag{5.53}$$

$$\ddot{N} \begin{bmatrix} C_b^{\mathsf{T}} & C_r^{\mathsf{T}} \end{bmatrix} \begin{bmatrix} \hat{J} C_b \\ \hat{m}_b C_r \end{bmatrix} + N \begin{bmatrix} C_b^{\mathsf{T}} & C_r^{\mathsf{T}} \end{bmatrix} \begin{bmatrix} -\hat{\lambda} C_b \\ 0 \end{bmatrix} = F. \tag{5.54}$$

Expanding this gives:

$$\ddot{N}(C_b^{\mathsf{T}} \hat{J} C_b + C_r^{\mathsf{T}} \hat{m}_b C_r) - N(C_b^{\mathsf{T}} \hat{\lambda} C_b) = F. \tag{5.55}$$

The force matrix F has been described as containing the sum of forces acting on each node in the system. This can be subdivided into two elements: external forces and internal forces. Let w_i be the i^{th} column of the matrix W, where w_i is the external force acting on the node n_i. Internal forces, caused by tension in the string members, require knowledge of string member connectivity. The string connectivity matrix C_s is defined as $S = NC_s^{\mathsf{T}}$, where S is the string member matrix. For a tensegrity system consisting of α string members, S is of dimension $3 \times \alpha$, and C_s is of dimension $\alpha \times n$. The internal node forces caused by string tensions T can be described with TC_s.

In this work, string tension is described in terms of a "force density" γ. The tension vector in a string can be found as $\mathbf{t}_i = \mathbf{s}_i \gamma_i$ where $\mathbf{s}_i$ is the string vector or the i^{th} column of matrix S (Modeling of elastic string is given in appendix 5.9.1). Then, the matrix of string tensions T equals $S\hat{\gamma}$, which equals $NC_s^{\mathsf{T}}\hat{\gamma}$. Based on this, the internal forces acting on nodes caused by string tensions is $NC_s^{\mathsf{T}}\hat{\gamma}C_s$. The full force matrix expression can then be written and substituted into Equation 5.55:

$$F = W - NC_s^{\mathsf{T}}\hat{\gamma}C_s, \tag{5.56}$$

$$\ddot{N}(C_b^{\mathsf{T}} \hat{J} C_b + C_r^{\mathsf{T}} \hat{m}_b C_r) + N(C_s^{\mathsf{T}}\hat{\gamma}C_s - C_b^{\mathsf{T}} \hat{\lambda} C_b) = W. \tag{5.57}$$

By defining matrices M, K, and W, a compact matrix form for the full nonlinear translational

and rotational dynamics of a full tensegrity system is written as:

$$\ddot{N}M + NK = W, \tag{5.58}$$

$$M = C_b^{\mathsf{T}} \hat{J} C_b + C_r^{\mathsf{T}} \hat{m} C_r, \tag{5.59}$$

$$K = C_s^{\mathsf{T}} \hat{\gamma} C_s - C_b^{\mathsf{T}} \hat{\lambda} C_b. \tag{5.60}$$

5.5 String-to-string Point Mass Nodes

The model derived in Section 4 assumes massless strings. It is important to develop a method that includes string masses. This is achieved by dividing the string in several small strings and connecting them with point masses. The added point mass node will connect only to strings and no rods (string-to-string nodes). Using this approach, a string member is modeled by subdividing the original string into n connected string members with $n-1$ connection point masses. The positions of the point masses along the string can be chosen based on the respective length of the connected strings which in turn can be chosen to match the extensional stiffness of the original string.

We describe the process of modeling string masses by denoting two types of nodes: rod nodes, which are the end points of rods, and string nodes, which are the locations of string-to-string connections that have a point mass associated with them. The full node matrix can consequently be split as $N = \begin{bmatrix} N_b & N_s \end{bmatrix}$. Here, N_b is a $3 \times 2\beta$ matrix in which each column is the position of a rod node n_b, and N_s is a $3 \times \sigma$ matrix in which each column is the position of a string node n_s. Variables β and σ represent the number of rods and number of string nodes respectively. Note that the rod and string nodes can be extracted from the node matrix N with the definition of two new connectivity matrices, C_{nb} and C_{ns}:

$$N_b = N \begin{bmatrix} I_{2\beta} \\ 0 \end{bmatrix} = N C_{nb}^{\mathsf{T}}, \tag{5.61}$$

$$N_s = N \begin{bmatrix} 0 \\ I_\sigma \end{bmatrix} = NC_{ns}^{\mathsf{T}}, \tag{5.62}$$

where $I_{2\beta}$ and I_σ are identity matrices of size 2β and σ respectively. The matrix representing the positions of center of mass, R, can similarly be broken into two components: R_b, which describes the center of mass locations for each rod member, and R_s, which describes the location of each string point mass:

$$R_b = N_b C_r^{\mathsf{T}} = NC_{nb}^{\mathsf{T}} C_r^{\mathsf{T}}, \tag{5.63}$$

$$R_s = N_s = NC_{ns}^{\mathsf{T}}. \tag{5.64}$$

Similarly, the expression for the rod member matrix B can be rewritten as:

$$B = N_b C_b^{\mathsf{T}} = NC_{nb}^{\mathsf{T}} C_b^{\mathsf{T}}. \tag{5.65}$$

Note that the rod connectivity matrix remains unchanged from its original definition preceding Equation 5.42. The original string connectivity matrix C_s must be redefined as new string members are being added to the model. Here, C_s is divided into two parts: the first, C_{sb}, describing rod-to-string joints and the second, C_{ss}, describing string-to-string joints:

$$S = NC_s^{\mathsf{T}} = \begin{bmatrix} N_b & N_s \end{bmatrix} \begin{bmatrix} C_{sb}^{\mathsf{T}} \\ C_{ss}^{\mathsf{T}} \end{bmatrix}, \tag{5.66}$$

The force matrix F is augmented to include both the sum of forces acting on rod nodes, F_b, as well as string nodes, F_s:

$$F = \begin{bmatrix} F_b & F_s \end{bmatrix} = W - NC_s^{\mathsf{T}} \hat{\gamma} C_s, \tag{5.67}$$

Now, we need to write the translational dynamics of the newly defined string nodes which are modeled as point masses. We define m_{si} as the mass of the i^{th} string node, r_{si} as the position of

that node and f_{si} as the total force acting on that node. Their translational dynamics in both vector and matrix form can simply be written as:

$$m_{s_i}\ddot{r}_{s_i} = f_{s_i} = [\ddot{R}_s\hat{m}_s]_i = F_{s_i}, \tag{5.68}$$

$$\ddot{R}_s\hat{m}_s = F_s. \tag{5.69}$$

The dynamics of the rod members (Equations 5.46, 5.47 and 5.49) must be slightly modified to incorporate the subdivision of the force matrix F as $F = \begin{bmatrix} F_b & F_s \end{bmatrix}$.

$$\hat{\lambda} = -\hat{J}\hat{l}^{-2}\lfloor \dot{B}^{\mathsf{T}}\dot{B}\rfloor - \frac{1}{2}\hat{l}^{-2}\lfloor B^{\mathsf{T}}F_bC_b^{\mathsf{T}}\rfloor, \tag{5.70}$$

$$\ddot{B}\hat{J} = \frac{1}{2}F_bC_b^{\mathsf{T}} + B\hat{\lambda}, \tag{5.71}$$

$$\ddot{R}_b\hat{m}_b = 2F_bC_r^{\mathsf{T}}. \tag{5.72}$$

Equations 5.69, 5.71, and 5.72 can be written in a matrix form as follows:

$$\begin{bmatrix} \ddot{B} & \ddot{R}_b & \ddot{R}_s \end{bmatrix} \begin{bmatrix} \hat{J} & 0 & 0 \\ 0 & \hat{m}_b & 0 \\ 0 & 0 & \hat{m}_s \end{bmatrix} + \begin{bmatrix} B & R_b & R_s \end{bmatrix} \begin{bmatrix} -\hat{\lambda} & 0 & 0 \\ 0 & 0 & 0 \\ 0 & 0 & 0 \end{bmatrix} = \begin{bmatrix} \frac{1}{2}F_bC_b^{\mathsf{T}} & 2F_bC_r^{\mathsf{T}} & F_s \end{bmatrix}. \tag{5.73}$$

Because the force matrix F has been defined as $F = \begin{bmatrix} F_b & F_s \end{bmatrix}$, the force term is rewritten in terms of F as:

$$\begin{bmatrix} \ddot{B} & \ddot{R}_b & \ddot{R}_s \end{bmatrix} \begin{bmatrix} \hat{J} & 0 & 0 \\ 0 & \hat{m}_b & 0 \\ 0 & 0 & \hat{m}_s \end{bmatrix} + \begin{bmatrix} B & R_b & R_s \end{bmatrix} \begin{bmatrix} -\hat{\lambda} & 0 & 0 \\ 0 & 0 & 0 \\ 0 & 0 & 0 \end{bmatrix} = F \begin{bmatrix} \frac{1}{2}C_b^{\mathsf{T}} & 2C_r^{\mathsf{T}} & 0 \\ 0 & 0 & I \end{bmatrix}. \tag{5.74}$$

Using $\begin{bmatrix} \frac{1}{2}C_b^{\mathsf{T}} & 2C_r^{\mathsf{T}} \end{bmatrix}^{-1} = \begin{bmatrix} C_b^{\mathsf{T}} & C_r^{\mathsf{T}} \end{bmatrix}^{\mathsf{T}}$, it can also be shown that:

$$\begin{bmatrix} \frac{1}{2}C_b^\mathsf{T} & 2C_r^\mathsf{T} & 0 \\ 0 & 0 & I \end{bmatrix}^{-1} = \begin{bmatrix} C_b & 0 \\ C_r & 0 \\ 0 & I \end{bmatrix}. \tag{5.75}$$

The previous expression allows us to rewrite Equation 5.74 as follows:

$$\begin{bmatrix} \ddot{B} & \ddot{R}_b & \ddot{R}_s \end{bmatrix} \begin{bmatrix} \hat{J} & 0 & 0 \\ 0 & \hat{m}_b & 0 \\ 0 & 0 & \hat{m}_s \end{bmatrix} \begin{bmatrix} C_b & 0 \\ C_r & 0 \\ 0 & I \end{bmatrix} + \begin{bmatrix} B & R_b & R_s \end{bmatrix} \begin{bmatrix} -\hat{\lambda} & 0 & 0 \\ 0 & 0 & 0 \\ 0 & 0 & 0 \end{bmatrix} \begin{bmatrix} C_b & 0 \\ C_r & 0 \\ 0 & I \end{bmatrix} = F. \tag{5.76}$$

Having previously defined B, R_b, and R_s in terms of N and connectivity matrices, the following expression can be substituted into the matrix expression for the full system dynamics:

$$\begin{bmatrix} B & R_b & R_s \end{bmatrix} = N \begin{bmatrix} C_{nb}^\mathsf{T} C_b^\mathsf{T} & C_{nb}^\mathsf{T} C_r^\mathsf{T} & C_{ns}^\mathsf{T} \end{bmatrix}. \tag{5.77}$$

$$\begin{aligned} \ddot{N} \begin{bmatrix} C_{nb}^\mathsf{T} C_b^\mathsf{T} & C_{nb}^\mathsf{T} C_r^\mathsf{T} & C_{ns}^\mathsf{T} \end{bmatrix} \begin{bmatrix} \hat{J} & 0 & 0 \\ 0 & \hat{m}_b & 0 \\ 0 & 0 & \hat{m}_s \end{bmatrix} \begin{bmatrix} C_b & 0 \\ C_r & 0 \\ 0 & I \end{bmatrix} \\ + N \begin{bmatrix} C_{nb}^\mathsf{T} C_b^\mathsf{T} & C_{nb}^\mathsf{T} C_r^\mathsf{T} & C_{ns}^\mathsf{T} \end{bmatrix} \begin{bmatrix} -\hat{\lambda} & 0 & 0 \\ 0 & 0 & 0 \\ 0 & 0 & 0 \end{bmatrix} \begin{bmatrix} C_b & 0 \\ C_r & 0 \\ 0 & I \end{bmatrix} = F. \end{aligned} \tag{5.78}$$

Multiplying this out, substituting Equation 5.67 for F, and rearranging yields the following expression for the full system dynamics:

$$\ddot{N} \begin{bmatrix} C_{nb}^\mathsf{T} C_b^\mathsf{T} \hat{J} C_b + C_{nb}^\mathsf{T} C_r^\mathsf{T} \hat{m}_b C_r & C_{ns}^\mathsf{T} \hat{m}_s \end{bmatrix} + N \begin{bmatrix} C_s^\mathsf{T} \hat{\gamma} C_{sb} - C_{nb}^\mathsf{T} C_b^\mathsf{T} \hat{\lambda} C_b & C_s^\mathsf{T} \hat{\gamma} C_{ss} \end{bmatrix} = W. \tag{5.79}$$

Following the example set in Equation 5.58, a compact matrix form for the full system dynamics including string masses can be obtained with the following definitions of M_s and K_s.

$$\ddot{N}M_s + NK_s = W, \tag{5.80}$$

$$M_s = \begin{bmatrix} C_{nb}^{\mathsf{T}}(C_b^{\mathsf{T}}\hat{J}C_b + C_r^{\mathsf{T}}\hat{m}_b C_r) & C_{ns}^{\mathsf{T}}\hat{m}_s \end{bmatrix}, \tag{5.81}$$

$$K_s = \begin{bmatrix} C_s^{\mathsf{T}}\hat{\gamma}C_{sb} - C_{nb}^{\mathsf{T}}C_b^{\mathsf{T}}\hat{\lambda}C_b & C_s^{\mathsf{T}}\hat{\gamma}C_{ss} \end{bmatrix}, \tag{5.82}$$

where substituting the value of F_b in Equation 5.70 gives $\hat{\lambda}$ as:

$$\hat{\lambda} = -\hat{J}\hat{l}^{-2}\lfloor \dot{B}^{\mathsf{T}}\dot{B} \rfloor - \frac{1}{2}\hat{l}^{-2}\lfloor B^{\mathsf{T}}(W - S\hat{\gamma}C_s)C_{nb}^{\mathsf{T}}C_b^{\mathsf{T}} \rfloor. \tag{5.83}$$

5.6 Equilibrium Calculations

The dynamics equations developed above can be used to solve for values of force densities in strings(γ) and bars(λ) by putting the acceleration term equal to zero ($\ddot{N} = 0$).

$$NK_s = W, \tag{5.84}$$

$$N\begin{bmatrix} C_s^{\mathsf{T}}\hat{\gamma}C_{sb} - C_{nb}^{\mathsf{T}}C_b^{\mathsf{T}}\hat{\lambda}C_b & C_s^{\mathsf{T}}\hat{\gamma}C_{ss} \end{bmatrix} = W, \tag{5.85}$$

$$N(\begin{bmatrix} C_s^{\mathsf{T}}\hat{\gamma}C_{sb} & C_s^{\mathsf{T}}\hat{\gamma}C_{ss} \end{bmatrix} - \begin{bmatrix} C_{nb}^{\mathsf{T}}C_b^{\mathsf{T}}\hat{\lambda}C_b & 0 \end{bmatrix}) = W, \tag{5.86}$$

$$N(C_s^{\mathsf{T}}\hat{\gamma}[C_{sb} \;\; C_{ss}] - \begin{bmatrix} C_{nb}^{\mathsf{T}}C_b^{\mathsf{T}}\hat{\lambda}C_b & 0 \end{bmatrix}) = W, \tag{5.87}$$

$$N(C_s^{\mathsf{T}}\hat{\gamma}C_s - C_{nb}^{\mathsf{T}}C_b^{\mathsf{T}}\hat{\lambda}C_b \begin{bmatrix} I & 0 \end{bmatrix}) = W, \tag{5.88}$$

$$N(C_s^{\mathsf{T}}\hat{\gamma}C_s - C_{nb}^{\mathsf{T}}C_b^{\mathsf{T}}\hat{\lambda}C_b C_{nb}) = W, \tag{5.89}$$

$$S\hat{\gamma}C_s - B\hat{\lambda}C_b C_{nb} = W. \tag{5.90}$$

From equation 5.89, K_s can also be written as $K_s = C_s^{\mathsf{T}}\hat{\gamma}C_s - C_{nb}^{\mathsf{T}}C_b^{\mathsf{T}}\hat{\lambda}C_bC_{nb}$. Now, let's take the i^{th} column of the above equation as

$$S\hat{\gamma}C_se_i - B\hat{\lambda}C_bC_{nb}e_i = We_i, \tag{5.91}$$

Using the identity $\hat{x}y = \hat{y}x$ for x and y being column vectors.

$$\widehat{S(C_se_i)}\gamma - \widehat{B(C_bC_{nb}e_i)}\lambda = We_i, \tag{5.92}$$

$$\left[\widehat{S(C_se_i)} \quad -\widehat{B(C_bC_{nb}e_i)}\right]\begin{bmatrix}\gamma\\ \lambda\end{bmatrix} = We_i. \tag{5.93}$$

Stacking all the columns till n^{th} column, we get

$$\begin{bmatrix} \widehat{S(C_se_1)} & -\widehat{B(C_bC_{nb}e_1)} \\ \widehat{S(C_se_2)} & -\widehat{B(C_bC_{nb}e_2)} \\ \vdots & \vdots \\ \widehat{S(C_se_n)} & -\widehat{B(C_bC_{nb}e_n)} \end{bmatrix}\begin{bmatrix}\gamma\\ \lambda\end{bmatrix} = \begin{bmatrix} We_1 \\ We_2 \\ \vdots \\ We_n \end{bmatrix}, \tag{5.94}$$

which can be simply written as

$$A \begin{bmatrix} \gamma \\ \lambda \end{bmatrix} = W_{vec}, \;\; \gamma \geq 0. \tag{5.95}$$

5.7 Class k Tensegrity Systems

A simple modification of the derived dynamics allows for handling of Class k tensegrity structures (k rods connected to a node through a ball joint). Here, “Class" denotes the maximum number of rod members present at a given node in the definition of the structure topology. If there are no rod-to-rod joints, the structure is said to be of Class 1. If there is at least one node in which two rods are connected, it is said to be of Class 2, and so on.

In this model, Class k structures (where $k > 1$) are handled by converting each Class k joint into k Class 1 nodes constrained to coincide at all times with a constraint matrix and Lagrange multipliers.

The linear constraint equation is written as:

$$NP = D, \tag{5.96}$$

where P is a $n \times c$ and D is a $3 \times c$ matrix specified such that constrained nodes are set equal to one another where c is the number of constraints required. For example, if nodes 1 and 2 must coincide at all times, a column of P and D would be specified such that $NP = D$ gives $n_1 - n_2 = 0$. Adding this linear constraint will introduce some constraint forces written as ΩP^{T} and will lead to the new dynamics:

$$\ddot{N} M_s + N K_s = W + \Omega P^{\mathsf{T}}, \tag{5.97}$$

where

$$K_s = \begin{bmatrix} C_s^{\mathsf{T}} \hat{\gamma} C_{sb} - C_{nb}^{\mathsf{T}} C_b^{\mathsf{T}} \hat{\lambda} C_b & C_s^{\mathsf{T}} \hat{\gamma} C_{ss} \end{bmatrix}, \tag{5.98}$$

$$\hat{\lambda} = -\hat{J}\hat{l}^{-2}\lfloor \dot{B}^{\mathsf{T}}\dot{B} \rfloor - \frac{1}{2}\hat{l}^{-2}\lfloor B^{\mathsf{T}}(W + \Omega P^{\mathsf{T}} - S\hat{\gamma}C_s)C_{nb}^{\mathsf{T}}C_b^{\mathsf{T}} \rfloor, \tag{5.99}$$

and Ω is the $3 \times c$ matrix of Lagrange multipliers satisfying the dynamics and constraints at all time-steps. The Lagrange multipliers required to maintain these constraints can be thought of as contact forces at the Class k nodes [14].

5.7.1 Reduced-order dynamics

Adding the linear constraints into the dynamics will restrict the motion in certain dimensions, thus reducing the order of the dynamics to a span a smaller space. The dynamics Equation 5.97 can be reduced into a smaller dimensional equation by augmenting it with the constraint Equation 5.96. To this end, we use the singular value decomposition (SVD) of matrix P as:

$$P = U\Sigma V^{\mathsf{T}} = \begin{bmatrix} U_1 & U_2 \end{bmatrix} \begin{bmatrix} \Sigma_1 \\ 0 \end{bmatrix} \begin{bmatrix} V^{\mathsf{T}} \end{bmatrix}, \tag{5.100}$$

where $U \in \mathbb{R}^{n\times n}$ and $V \in \mathbb{R}^{c\times c}$ are both unitary matrices, $U_1 \in \mathbb{R}^{n\times c}$ and $U_2 \in \mathbb{R}^{n\times(n-c)}$ are submatrices of U, and $\Sigma_1 \in \mathbb{R}^{c\times c}$ is a diagonal matrix of positive singular values. By defining

$$\eta = [\eta_1 \;\; \eta_2] \triangleq NU = [NU_1 \;\; NU_2], \tag{5.101}$$

the constraint Equation 5.96 can be modified as:

$$NP = NU\Sigma V^{\mathsf{T}} = [\eta_1 \;\; \eta_2] \begin{bmatrix} \Sigma_1 \\ 0 \end{bmatrix} \begin{bmatrix} V^{\mathsf{T}} \end{bmatrix} = D, \tag{5.102}$$

which implies:

$$\eta_1 = DV\Sigma_1^{-1}, \;\; \dot{\eta}_1 = 0, \;\; \ddot{\eta}_1 = 0. \tag{5.103}$$

Here, η_1 represents the no-motion space in transformed coordinates. Moreover, η_2 will evolve according to the constrained dynamics in new coordinate system. Using Equations 5.100-5.103, the dynamics equation 5.97 can be rewritten as:

$$\ddot{N}UU^{\mathsf{T}}M_s + NUU^{\mathsf{T}}K_s = W + \Omega V\Sigma^{\mathsf{T}}U^{\mathsf{T}}, \tag{5.104}$$

$$\Rightarrow \ddot{\eta}_2 U_2^{\mathsf{T}}M_s + \eta_1 U_1^{\mathsf{T}}K_s + \eta_2 U_2^{\mathsf{T}}K_s = W + \Omega V\Sigma_1^{\mathsf{T}}U_1^{\mathsf{T}}. \tag{5.105}$$

Post-multiplying the above equation by a non-singular matrix $[U_2 \;\; M_s^{-1}U_1]$ will yield two parts, where first part gives the second order differential equation for the reduced dynamics:

$$\ddot{\eta}_2 U_2^{\mathsf{T}}M_sU_2 + \eta_2 U_2^{\mathsf{T}}K_sU_2 = WU_2 - \eta_1 U_1^{\mathsf{T}}K_sU_2, \tag{5.106}$$

$$\Rightarrow \ddot{\eta}_2 M_2 + \eta_2 K_2 = \widetilde{W}. \tag{5.107}$$

with $M_2 = U_2^{\mathsf{T}}M_sU_2$ and $K_2 = U_2^{\mathsf{T}}K_sU_2$, and the second part gives an algebraic equation that is used to solve for the Lagrange multiplier:

$$\ddot{\eta}_2 U_2^{\mathsf{T}}M_sM_s^{-1}U_1 + \eta_1 U_1^{\mathsf{T}}K_sM_s^{-1}U_1 + \eta_2 U_2^{\mathsf{T}}K_sM_s^{-1}U_1 = WM_s^{-1}U_1 + \Omega V\Sigma_1^{\mathsf{T}}U_1^{\mathsf{T}}M_s^{-1}U_1, \tag{5.108}$$

$$\Rightarrow NK_sM_s^{-1}U_1 - \Omega P^{\mathsf{T}}M_s^{-1}U_1 = WM_s^{-1}U_1. \tag{5.109}$$

Notice that K_s is also a function of Ω from Equations 5.98-5.99, making it a linear algebra problem. The analytical expression to solve the Lagrange Multiplier (Ω) is given in section B.1.

5.8 Energy Calculation

The kinetic energy stored in the structure is:

$$KE = 1/2 \sum_{i=1}^{\beta} (m_{bi} \dot{r}_{bi}^{\mathsf{T}} \dot{r}_{bi} + J_i \dot{b}_i^{\mathsf{T}} \dot{b}_i + m_{si} \dot{r}_{si}^{\mathsf{T}} \dot{r}_{si}), \tag{5.110}$$

$$= 1/2 \, Tr(\dot{R}_b \hat{m}_b \dot{R}_b^{\mathsf{T}} + \dot{B} \hat{J} \dot{B}^{\mathsf{T}} + \dot{R}_s \hat{m}_s \dot{R}_s^{\mathsf{T}}), \tag{5.111}$$

$$= 1/2 \, Tr \left(\dot{N} [C_{nb}^{\mathsf{T}} (C_b^{\mathsf{T}} \hat{J} C_b + C_r^{\mathsf{T}} \hat{m}_b C_r) \quad C_{ns}^{\mathsf{T}} \hat{m}_s] \dot{N}^{\mathsf{T}} \right), \tag{5.112}$$

$$= 1/2 \, Tr \left(\dot{N} M_s \dot{N}^{\mathsf{T}} \right). \tag{5.113}$$

For class-K, this can be written as:

$$KE = 1/2 \, Tr \left(\dot{\eta}_2 M_2 \dot{\eta}_2^{\mathsf{T}} \right). \tag{5.114}$$

Now, the potential energy can be written as:

$$PE = 1/2 \sum_{i=1}^{\alpha} (\frac{1}{k_i} t_i^{\mathsf{T}} t_i), \tag{5.115}$$

$$= 1/2 \, Tr(T \hat{k}^{-1} T^{\mathsf{T}}), \tag{5.116}$$

$$= 1/2 \, Tr(S \hat{\gamma} \hat{k}^{-1} \hat{\gamma} S^{\mathsf{T}}), \tag{5.117}$$

and the work done on the system can be written as:

$$WD = \int_{T_i}^{T_f} Tr \, (W \dot{N}^{\mathsf{T}}) dt, \tag{5.118}$$

Therefore, the total energy at any time can be written as:

$$TE(T_f) = KE(T_i) + PE(T_i) + WD, \tag{5.119}$$

$$= 1/2 \, Tr \left(\dot{N}_i M_s \dot{N}_i^{\mathsf{T}} \right) + 1/2 \, Tr(S_i \hat{\gamma}_i \hat{k}^{-1} \hat{\gamma}_i S_i^{\mathsf{T}}) + \int_{T_i}^{T_f} Tr(W \dot{N}^{\mathsf{T}}) dt. \tag{5.120}$$

From principal of conservation of energy:

$$KE(T_f) + PE(T_f) = KE(T_i) + PE(T_i) + WD, \tag{5.121}$$

$$Tr\left(\dot{N}_f M_s \dot{N}_f^{\mathsf{T}}\right) + Tr(S_f \hat{\gamma}_f \hat{k}^{-1} \hat{\gamma}_f S_f^{\mathsf{T}}) = Tr\left(\dot{N}_i M_s \dot{N}_i^{\mathsf{T}}\right) + Tr(S_i \hat{\gamma}_i \hat{k}^{-1} \hat{\gamma}_i S_i^{\mathsf{T}}) + 2\int_{T_i}^{T_f} Tr(W\dot{N}^{\mathsf{T}})dt. \tag{5.122}$$

5.9 Stiffness and Damping in String

5.9.1 Open-loop Simulations

Tension in the strings is produced by stretching them beyond their rest length. Let the rest length of the i^{th} string be denoted by ρ_i, extensional stiffness by k_i, damping constant by c_i, and string vector by s_i. Assuming that strings follow Hooke's law and viscous friction damping model, the tension in a string is written as:

$$\|t_i\| = k_i(\|s_i\| - \rho_i) + c_i \frac{s_i^{\mathsf{T}} \dot{s}_i}{\|s_i\|}, \tag{5.123}$$

$$\gamma_i = \frac{\|t_i\|}{\|s_i\|} = k_i\left(1 - \frac{\rho_i}{\|s_i\|}\right) + c_i \frac{s_i^{\mathsf{T}} \dot{s}_i}{\|s_i\|^2}. \tag{5.124}$$

Note that if $\rho_i > \|s_i\|$, although above equation gives a negative value, tension in the string should be substituted to zero as a string can never push along its length. Similarly, the final value of the tension t_i or force density γ_i can also never be negative for any string. Now, we write these equations in matrix form as:

$$\hat{\gamma} = \big(I - \lfloor S^{\mathsf{T}} S \rfloor^{-\frac{1}{2}} \hat{\rho}\big)\hat{k} + \lfloor S^{\mathsf{T}} \dot{S} \rfloor \lfloor S^{\mathsf{T}} S \rfloor^{-1} \hat{c}, \tag{5.125}$$

$$T = S\hat{\gamma} = S\big(I - \lfloor S^{\mathsf{T}} S \rfloor^{-\frac{1}{2}} \hat{\rho}\big)\hat{k} + S\lfloor S^{\mathsf{T}} \dot{S} \rfloor \lfloor S^{\mathsf{T}} S \rfloor^{-1} \hat{c}, \tag{5.126}$$

where i^{th} column in matrix T represents the vector of string tension in the i^{th} string. This equation can again be written as

$$T = S\hat{\gamma} = (S - S_0)\hat{k} + S\lfloor S^{\mathsf{T}}\dot{S}\rfloor\lfloor S^{\mathsf{T}}S\rfloor^{-1}\hat{c}, \tag{5.127}$$

where $S_0 = S\lfloor S^{\mathsf{T}}S\rfloor^{-\frac{1}{2}}\hat{\rho}$ represents the matrix containing the rest length vectors. Therefore, Equations 5.124-5.126 provide the required tension model for elastic strings used in the dynamic simulation of tensegrity systems.

5.9.2 Closed-loop Control

For the closed-loop control of the system, one can change the rest lengths of the strings according to the following formula:

$$\hat{\gamma}\hat{k}^{-1} - \lfloor S^{\mathsf{T}}\dot{S}\rfloor\lfloor S^{\mathsf{T}}S\rfloor^{-1}\hat{c}\hat{k}^{-1} = I - \lfloor S^{\mathsf{T}}S\rfloor^{-\frac{1}{2}}\hat{\rho}, \tag{5.128}$$

$$\hat{\rho} = \lfloor S^{\mathsf{T}}S\rfloor^{\frac{1}{2}}\left\{I + \lfloor S^{\mathsf{T}}\dot{S}\rfloor\lfloor S^{\mathsf{T}}S\rfloor^{-1}\hat{c}\hat{k}^{-1} - \hat{\gamma}\hat{k}^{-1}\right\}, \tag{5.129}$$

$$\Rightarrow\hat{\rho} = \lfloor S^{\mathsf{T}}S\rfloor^{\frac{1}{2}}(I - \hat{\gamma}\hat{k}^{-1}) + \lfloor S^{\mathsf{T}}\dot{S}\rfloor\lfloor S^{\mathsf{T}}S\rfloor^{-\frac{1}{2}}\hat{c}\hat{k}^{-1}. \tag{5.130}$$

While solving the control algorithm, we put a constraint that γ should always be greater than or equal to zero.

5.10 Examples of the Implemented Model

All the dynamic simulations are performed using a Matlab based software developed using this formulation. The numerical integration package used in this software is fourth-order Runge-Kutta. Bar length correction was used only for class-k structure simulation. There was no significant violation (around machine precision 10^{-16}) in bar length constraint during simulations of other examples. Therefore, the bar length correction algorithm was not used for those examples. It is also advisable to use the bar length correction algorithm only if necessary (appendix A).

5.10.1 Influence of String Subdivision on Tensegrity Prism Dynamics

First, the dynamic simulation of a Class-1 triangular tensegrity prism with massive strings is shown in Figure 5.3. To demonstrate the modeling of flexible string members with mass, each string member in the prism is subdivided into 5 members by inserting 4 string-to-string nodes (point masses) along the original string member. Initial conditions are specified to simulate the dynamics. In the absence of external forces, tensegrity prism has a known equilibrium solution of $\gamma_v = \sqrt{3}\gamma_t = \sqrt{3}\gamma_b$, where γ_v, γ_t and γ_b represent the force density in vertical, top and bottom string respectively [6].

For demonstration purposes, bar masses are specified as $m_b = 1$ kg, and point masses are specified as $m_s = 0.01$ kg. Bar lengths, based on specified initial node positions, are $l_b = 1.4142$ m long and all string members are given stiffness values of $k = 100$ N/m. Initial force density values are deliberately specified as $\gamma_t = \gamma_b = \gamma_v = 30$ N/m to induce motion.

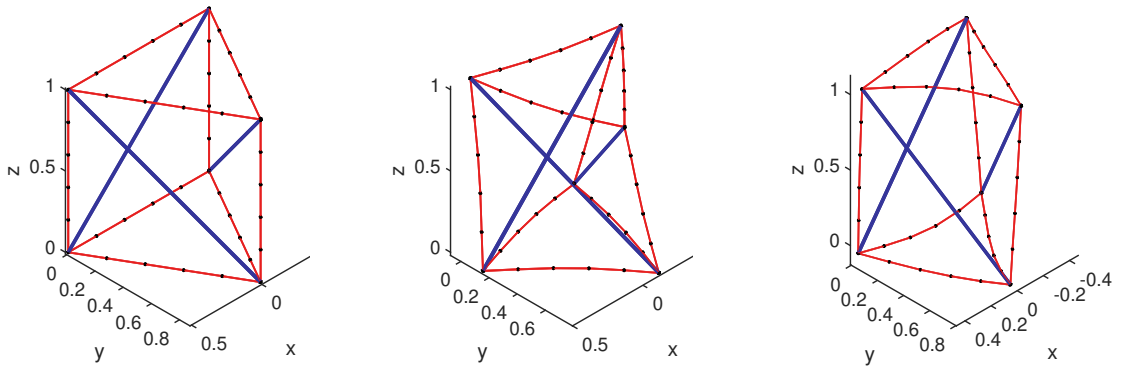

(a) t = 0 sec (b) t = 0.5 sec (c) t = 1 sec

Figure 5.3: Simulation time-lapse of prism structure using string-to-string connections to model string mass. (Bars are shown in blue and strings are shown in red)

Second, we demonstrate that when modeling string mass, the systems dynamics converge as the number of segments used in modeling the string members increases. In this case, the string members of the prism structure are modeled with 1 to 10 string segments. Figure 5.4 shows the

prism structure string segments modeled with 1, 5, and 10 “child” string segments.

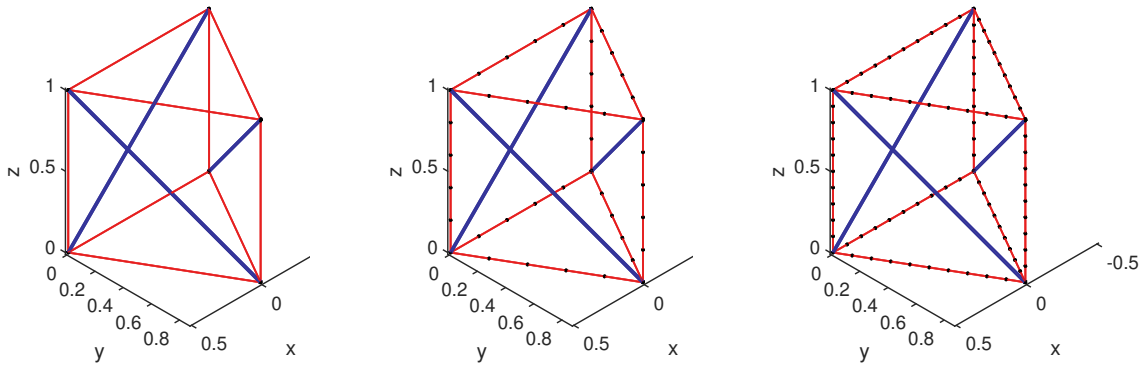

Figure 5.4: Prism structure string members modeled with varying number of string segments.

The case in which each string member is modeled with a single string segment represents the case in which string mass is neglected. For the remaining cases, the stiffness values of the original 9 “parent” string members are converted into equivalent stiffness values for their “children” string segments. Similarly, a specified parent string mass is specified and distributed across the generated child point mass nodes. The same initial condition is applied to each case to allow direct comparison of the resulting dynamical response. Figure 5.5 shows the node 1 y-coordinate time histories for a number of these simulation cases. It is evident here that as the number of string segments used increases, the dynamical response converges.

To get better insight, one can compare all cases with the final simulation case, which uses 10 string segments as per the original string member. Computing the spatial distance between node 1 in each case vs node 1 in the final case at each time step gives a time-history representing the discrepancy between the given and final cases. The square sum of this spatial discrepancy over the simulation time-span i.e. the $\mathcal{L}_2$ norm of the spatial distance between the node 1 position with respect to the node 1 position in the final case, can then be used to quantify the total error between the given and final cases. The difference in the dynamic response decreases rapidly as the number of string segments is increased. For this example, the error was found to be less than 0.5% for the

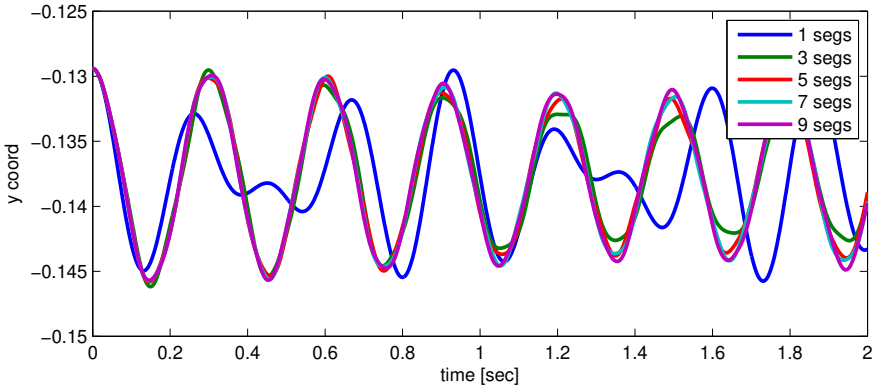

Figure 5.5: Node coordinate dynamical response convergence.

last 9^{th} to 10^{th} division.

5.10.2 Dynamics of a D-bar structure with one node inertially fixed

This example will demonstrate the dynamics of a Class-k structure. The structure we simulate here is a D-bar structure. A complexity-1 D-bar structure consists of 4 compressive members connected in a diamond shape with 2 tensile members along the diagonal [6]. As the maximum number of bars connected at any node is 2, it is a “Class 2" structure.

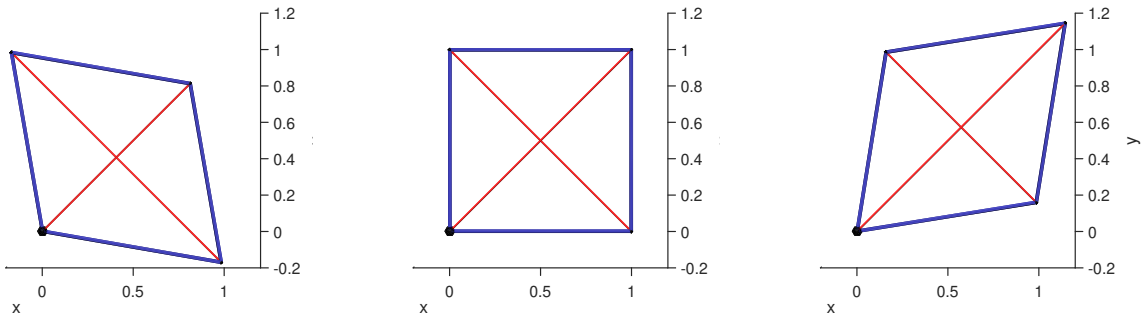

(a) t = 0 sec (b) t = 0.5 sec (c) t = 1 sec

Figure 5.6: Simulation time-lapse of a D-bar structure.

Here, we simulate the dynamics of the structure with one node (shown in black) fixed to the ground i.e. inertial position of the node remains constant. For demonstration purposes, each bar

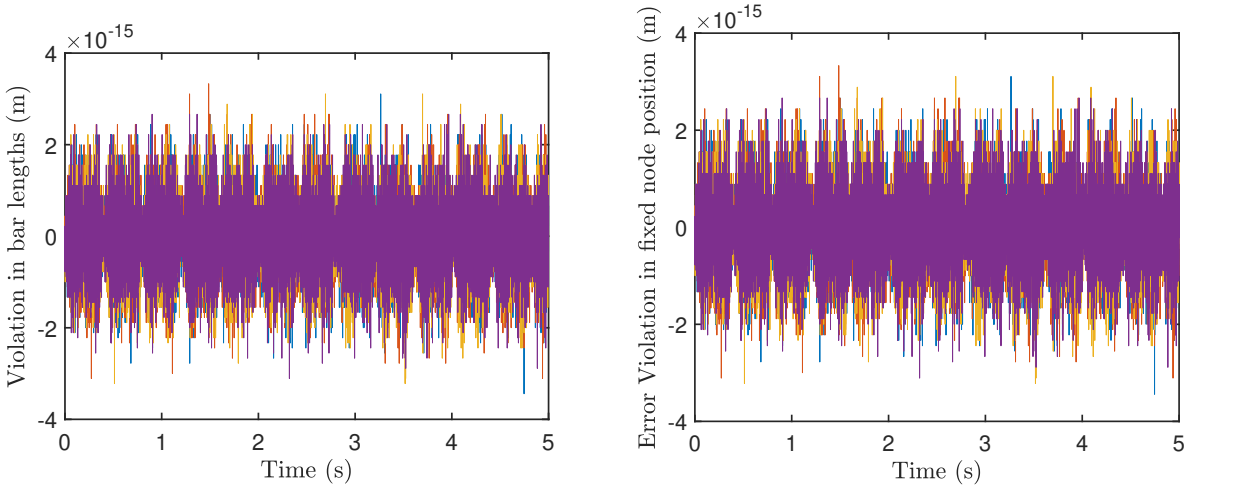

(a) Error violations in bar lengths

(b) Error violations in x,y, and z coordinates of the fixed node

Figure 5.7: Results for Constraint D-bar structure.

is $l_b = 1$m long and has a mass of $m_b = 1$kg. Both string members are given a stiffness value of $k = 100$ N/m and different prestress (force density) to induce motion. Figure 5.6 shows three time-lapse images of the simulation. Simulation results show that both, fixed position constraint and pin joint constraints (bar to bar connection) are satisfied all the time (up to machine precision) as shown in Figure 5.7b. Figure 5.7a shows that the length of all the bars also remains constant throughout the simulation verifying the efficacy of the results.

5.10.3 Dynamics of a flexible membrane having only tensile members

In this example, we demonstrate the dynamics of a “Class 0" structure consisting solely of string members – a cylindrical string mesh membrane. The configuration of the strings in this membrane has been chosen to be derived from a Double Helix Tensegrity (DHT) structure with all the bars removed. Figure 5.8a shows the typical structure of this configuration. We define the complexity of the structure by p and q where p is defined as the number of nodes on the circular ring and q is the number of circular rings in longitudinal direction[25]. It can be better approximated to a continuous membrane by increasing the complexity of the structure as shown in Figure 5.8b.

To demonstrate the dynamics of this membrane, we start from the equilibrium position of the

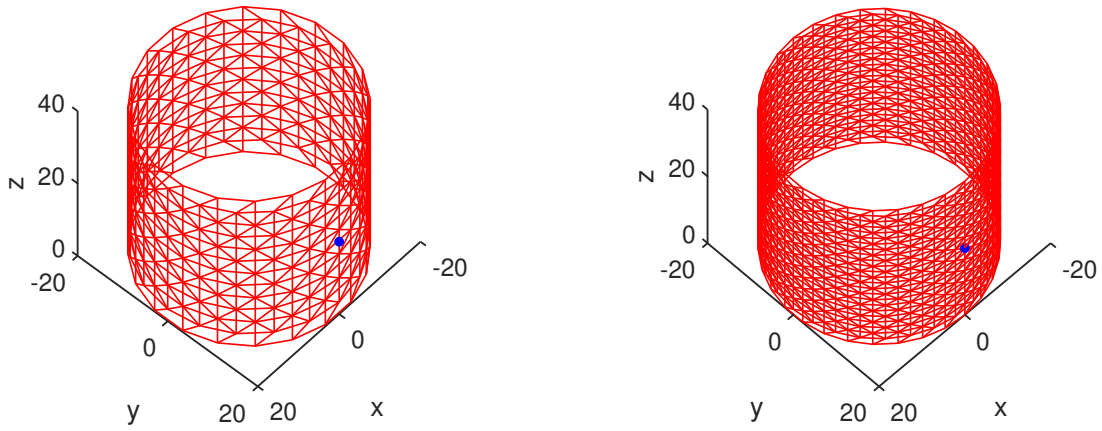

(a) Low complexity

(b) High complexity

Figure 5.8: DHT structure without bars (R = 20m and L = 40m).
(End caps are not shown but included in the maths)

structure with 1 atmospheric pressure difference from inside to the outside of the cylinder. The stiffness in the string was calculated such that the length ratio (unstretched string length to current string length) is 0.975 at the equilibrium position. The mass of individual string has been used from the minimum mass calculation, required to take 1 atmospheric pressure. The material properties used for this simulation are of UHMWPE (spectra). Damping is also added in the strings to get the η (Damping Coefficient) value of 0.1. The appendix shows the formulation to add damping in the strings 5.9.1. Figure 5.9a and 5.9b show the radial motion of the center nodes (shown as blue dots) of two membranes (Low and High complexity) in presence of 5% instantaneous change in pressure. Notice the attenuation in the vibration response along the radial direction, depicting the effect of damping included in the dynamics. No motion in the vertical direction was observed as the membrane will elongate equally in the upward and downward direction with respect to the center node.

5.10.4 Dynamic simulation of a six bars Tensegrity ball as Planetary Lander

The example demonstrates the capability of the formulation to perform the dynamic simulation with inputs from the external environment. A dynamic simulation result was shown when a

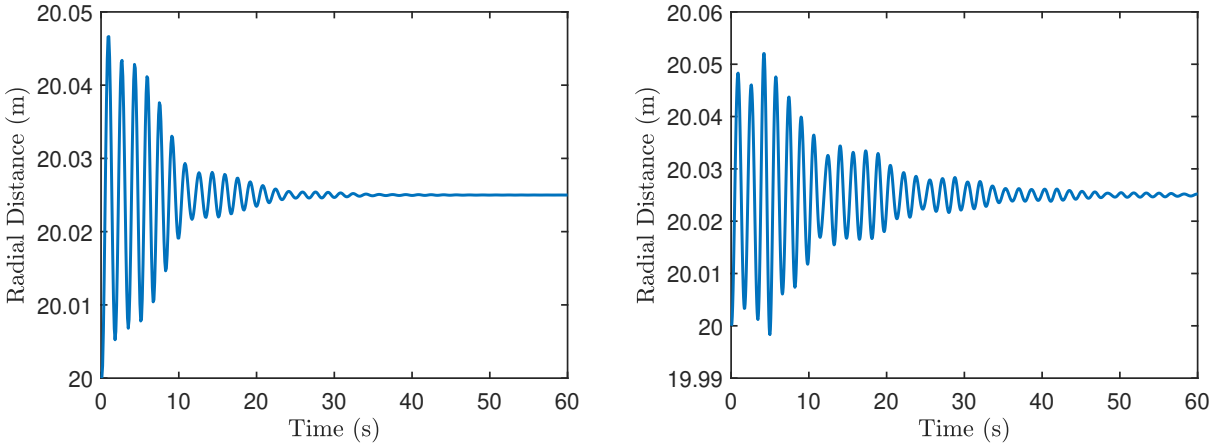

(a) Radial Motion for Low Complexity

(b) Radial Motion for High Complexity

Figure 5.9: Time history of motion of the center nodes (shown as blue dots) (R = 20 m and L = 40 m)

tensegrity lander [2] with 6 bars and 24 strings was dropped from a height of 3.5 meters. For this simulation, the ground was modelled as a spring-damper system of stiffness $k_g = 10^4$ N/m and damping $c_g = 10$ N-s/m. An initial prestress value of $\gamma = 1000$ N/m was used for all the strings which result in self-equilibrium for the structure. The mass of each bar was assumed to be $m_b = 1$ Kg and string mass was assumed to be $m_s = 0.1$ Kg. The stiffness value of each string was assumed to be $k = 5000$N/m with a damping coefficient value $c = 10$ N-s/m.

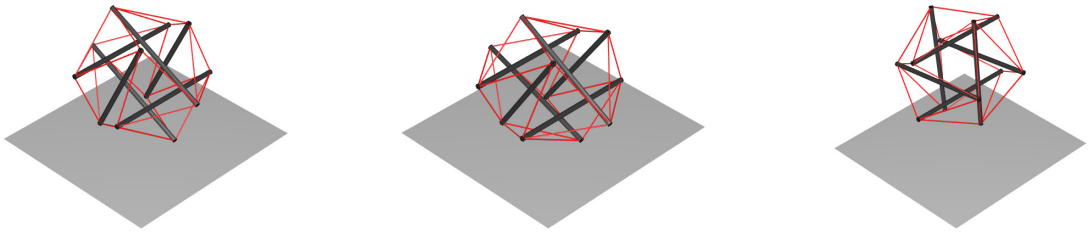

(a) t = 0.825 sec

(b) t = 0.850 sec

(c) t = 0.875 sec

Figure 5.10: Simulation time-lapse of a Tensegrity Lander.

Figure 5.10 shows the time-lapse images of the lander as it hits the ground. Figure 5.11a shows the vertical distance of the center of mass of the lander from the ground. Notice that as we model both ground and strings with some damping, the vertical distance keeps decreasing. Figure 5.11b shows the error in the bar length of one of the bars during the simulation.

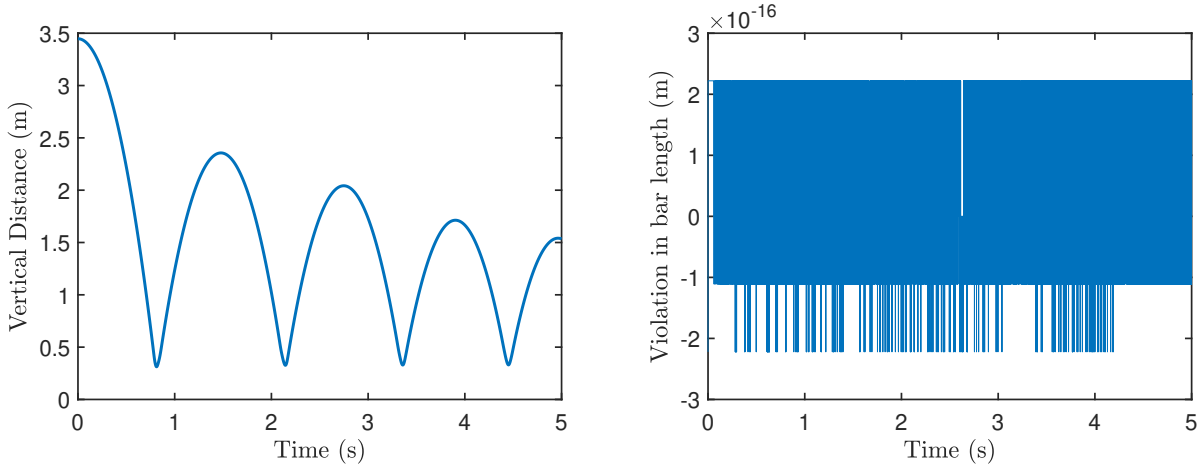

(a) Vertical distance of Center of Mass from the ground.

(b) Error violation in the one of the bar length.

Figure 5.11: Results for Tensegrity Lander.

5.10.5 Tensegrity prism with elastic skin

This example demonstrates how an elastic skin membrane can be modeled as a mesh of string-to-string joints, and how the addition of skin membranes to a given structure can increase its stiffness. The developed dynamical model, by including string-to-string connections, allows generation of interconnected elastic string meshes that can be attached to bar members. An elastic skin membrane can be modeled as a mesh of interconnected string members with any number of topologies. Figure 5.12 shows a prism structure with skin added using one example topology generation method that allows parameterizable complexity. In this case, a node is placed at the center of each external polygon of the structure, and string members are generated that connect the node to the vertices of its parent panel. This can be done recursively for n iterations.

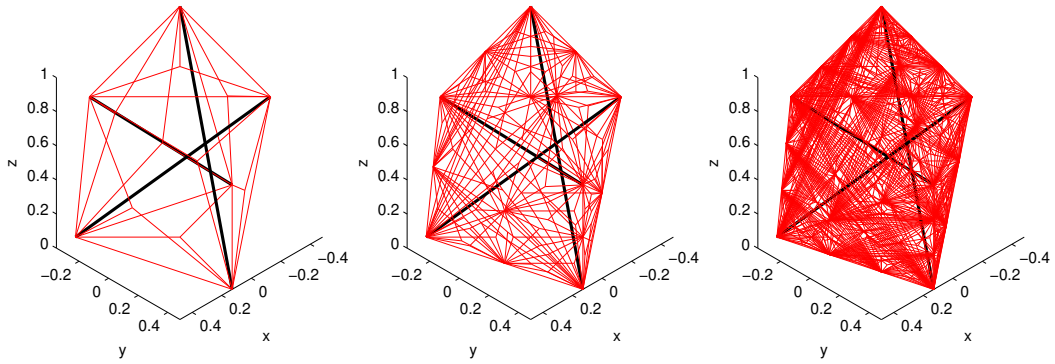

Figure 5.12: Prism structure with elastic skin modeled with varying complexity.

To illustrate how the inclusion of skin affects the dynamical response of a structure, skin panels are added to the top and bottom surfaces of a prism structure (illustrated in Figure 5.13). Simulations are performed for the structure with and without the skin panels with identical initial conditions for the original string members to allow comparison. Comparing the node 1 z-coordinate time histories for the structure with and without the skin membranes shows that displacement is reduced with the inclusion of the skin.

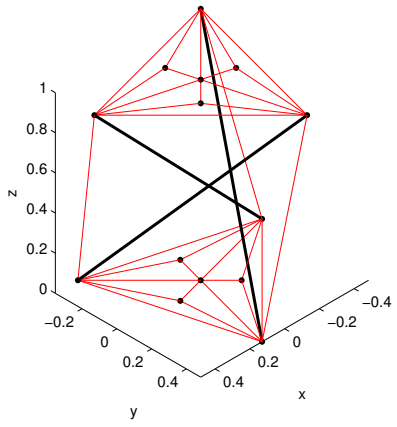

Figure 5.13: Prism structure with elastic skin added to top and bottom panels. Complexity $n = 2$

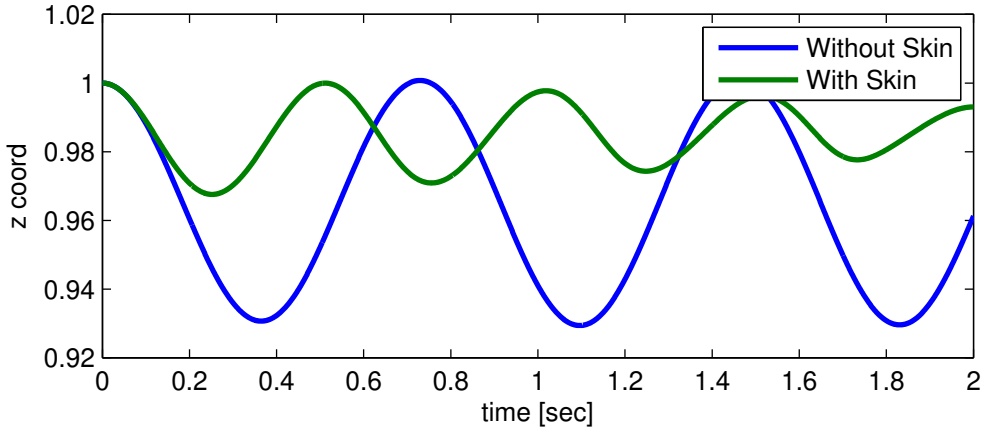

Figure 5.14: Stiffness comparison of prism structure with and without skin panels shown in Figure 5.13

.

5.11 Software Description

A software with the name: Modeling of Tensegrity Structures (MOTES) also came out as the result of this thesis which was published in The Journal of Open Source Software [65]. MOTES provided two categories for the analysis of any tensegrity structure. First, the static analysis provides the minimum mass of the tensegrity structure by optimizing for the tensile force in the strings and compressive force in the bars for no external force (self-equilibrium state) and in the presence of a given external force. The optimization problem is written as a *Linear Programming* to solve for the minimum mass required under yielding constraints. The software also allows to solve for the minimum mass under buckling and yielding failure criteria through a *non-linear optimization* solver. Second, the dynamic analysis uses a second-order matrix differential equation to simulate the dynamics of any complexity of tensegrity structure [16]. This dynamic model assumes the bars to be rigid and strings to show elastic behaviour (Hookean). The software runs a self-developed modified Runge-Kutta integration package to solve the nonlinear differential equations. A bar length correction scheme is used to correct the dynamics response that might incur random errors because of computational limitations. This analytical correction step also restricts the errors in connection constraints for class-k structures. The class-k, bar-to-bar connections (ball

joints) are formulated as linear constraints. These constraints in the motion space give rise to constraint forces in the structure. An analytical solution is provided to solve for the constraint forces, and a reduced order model is developed to simulate the dynamics in the restricted motion space. The mass in the strings is also included in the dynamics by discretizing the string into several point masses along the length of the string. This complete mathematical model for the tensegrity dynamics is developed in our recent dynamics paper [16].

The software is being used to develop various tensegrity structures like Tensegrity robotic arm, Tensegrity antenna, Tensegrity lander, and Space Habitat, where we integrate structure and control design to get the required performance. The software was also used as a part of the class curriculum for the course '*AERO-489/689 Design Elective: Advanced Statics and Dynamics of Flexible Structures: Tensegrity Systems*' which was offered in spring 2019.

5.12 Conclusions

This chapter develops the nonlinear dynamic models of any multibody system composed of a network of bars in compression and cables in tension. This is accomplished by having any connection between bars or strings that behave mathematically as frictionless ball joints. The capability to have string-to-string connections allow the approximations of membranes or nets. Such surfaces allow a mathematical treatment to integrate advantages of tensegrity and origami structures. The capability to have bar-to-bar connections removes previous criticism of tensegrity as "only soft structures". The approach to Class-k tensegrity (bar-to-bar connections) is to add Lagrange multipliers to accommodate the constraint forces due to bar-to-bar connections, and then reduce the dynamic model by using the constraint equation. The Lagrange multipliers appear linearly and are computed from a linear algebra problem. Writing the dynamics in non-minimal coordinates avoids the use of transcendental functions, providing a very simple second order matrix differential equation. The non-linear dynamics is linear in control variables (force densities in the strings), which allows control laws to be written independently of the material properties of the strings. A bar length correction algorithm is also provided to satisfy the bar length constraints at both zero and first-order derivative. The algorithm should be used only if necessary.

A number of conclusions can be made based on the presented work. First, the ability to include string-to-string joints in the developed dynamical model allows for modeling and simulation of massive string members, elastic skin membranes, and Class 0 string meshes. Modeling and simulation results for each of these cases have been presented. Second, it is evident that accounting for string mass in simulation changes the dynamical response of a given structure. Simulation results show that even structures with low total string mass relative to bar mass exhibit this discrepancy. Third, when modeling string mass, the dynamical response of the structure converges as the number of string segments used increases. Finally, it has been shown that the inclusion of elastic skin membranes on a structure can increase the stiffness of the structure.

6. GYROSCOPIC DYNAMICS OF TENSEGRITY SYSTEMS*

[1] Mechanics and control of innovative gyroscopic structural systems are detailed in this chapter. By adding controllable spinning wheels to a network of controllable, axially loaded strings and bars, it is shown that the mobility and manipulation of the structural system are enhanced. Using principles of mechanics, a nonlinear dynamic model is presented to modulate the torque produced by the network of spatially distributed gyroscopes. Equations of motion, formulated as a second-order matrix differential equation, provide a trajectory for the nodal displacement of the bars, along with the wheel's spin degree of freedom. While the gyroscopic robotics concept is scalable to an arbitrarily large network, this research aims to identify elemental modules to override fundamental design principles of the innovative structural systems. Dynamic simulation and experimental verification on a planar D-bar tensegrity structure are used to demonstrate the utility of one such fundamental building block of the gyroscopic robotic system.

6.1 Introduction

Tensegrity structures are defined as a stable configuration of pre-stressable structures composed of compressive (bars/struts) and tensile members (strings/cables). Researchers show that tensegrity structures provide a minimal mass solution to structures designed for compressive loading [6] and tensile loading under stiffness constraints [20]. These structures also provide the capability to change the stiffness without changing the shape of the structure. This can help in achieving a high range of compliance in soft robotics applications [18]. Harvard biologist Don Ingber called tensegrity architecture as 'architecture of life' [36], which is evident by examining the human body where the tensions in the tendons actuate bones of the skeleton. A large number of redundant control inputs (tension in the strings) makes the system robust, which is crucial for next-generation robots.

[1]*Portions of this section are reprinted or adapted from [66] : Raman Goyal, Muhao Chen, Manoranjan Majji and Robert E Skelton, "Gyroscopic Tensegrity System Dynamics", Robotics and Automation Letters, 5(2), 1239 – 1246, 2020, DOI: 10.1109/LRA.2020.2967288. Copyright © 2020, IEEE. Reproduced with permission.

An extra degree of control can be added to these systems by attaching gyroscopic wheels to some of the bar members. This chapter discusses this new class of mechanical systems formed by adding gyroscopes to tensegrity structures. Spacecraft attitude and orientation control are typically accomplished using momentum wheels or control moment gyroscopes [67, 64]. Gyroscopes have been used to minimize the sensitivity of the end-effector location in the presence of disturbance forces [68]. In large space structures such as the international space station, massive monolithic wheels are arranged on steerable gimbals, to generate gyroscopic torques in order to accomplish attitude control [69, 70]. Motivated by the expense of large masses in space, we ask the fundamental question as to what would be an optimal arrangement of mass distribution of the rotational kinetic energy, so as to maximize the efficacy of the gyroscopic torques generated by the system. While this is an open question, the tensegrity paradigm provides a framework to provide a systematic answer to this question. The ability to harness a gyroscopic torque by executing translational pivoting motion of the bars, equipped with rotating wheels, provides a new modality of structural system mobility and manipulation. While space structures such as the habitats are positively impacted, a variety of terrestrial applications are also affected by a systematic development of tools for mechanics and control of gyroscopic systems [34]. Building on these foundations, the optimal utilization of the control redundancy introduced by the spatial distribution of the gyroscopes will be possible. A typical actuator redundancy present in traditional tensegrity systems along with the added control of gyroscopic forces will allow for the accommodation of a wide variety of disturbance forces encountered in practical robotic applications making the system more robust. In order to affect moment transfer, it is necessary that the tensegrity structures be of class 2 or greater, so as to efficiently transfer the reaction moments to the subsystem of interest. This chapter formulates a matrix-second-order nonlinear differential equation without any transcendental functions to simulate the dynamics of a general tensegrity system with or without gyroscopes. The advantages of the formulation and the contributions of this work are summarized as follows:

- There are no topological constraints (rigid body connections to form a topological tree) as

non-minimal representation is used in the formulation.

- The absence of transcendental functions results in improved efficiency and accuracy of the dynamics simulation and control design.
- This work systematically derived the dynamics of a general *gyroscopic tensegrity system*, which provides an extra degree of freedom to control the shape and attitude of the structure.
- These equations are suitable for the design of control law to control the shape and attitude of the structure as the control variables (force density in each string) are linear in the dynamics formulation.

The chapter is structured as follows: Section 6.2 develops the equations for rotational and translational motion of a rigid bar with an attached wheel. Section 6.3 provides the complete dynamics formulation for any gyroscopic tensegrity structure in a compact second-order matrix differential equation along with a vector differential equation to capture the angular position of the wheel. In section 6.4, the reduced-order dynamic model for class-k tensegrity system is developed by projecting the constrained space to a smaller subspace. A physical model of planar D-bar structure [6] with gyros attached to each member is first described, and then an experiment is run to show the application of the proposed work in controlling the attitude of the structure by changing the shape (by controlling the length of the strings). Section 6.5 also provides the results developed from the dynamic simulation validating the experiment. Finally, the conclusions and brief discussion for the chapter are given in the end.

6.2 Dynamics of a Bar with Wheel

In this section, we develop the dynamics of a rigid bar with an attached wheel. The rigid bar is defined as an axisymmetric body with no inertia about the longitudinal axis. It is also assumed that the bar is subjected to external forces only at its two ends. We use the notations and kinematics developed in our recent paper [16] to formulate the dynamics. Let us define $\boldsymbol{b}$ as a vector along the bar and vector $\boldsymbol{r}$ representing the position vector of the center of mass of the bar, as shown in Fig. 6.1.

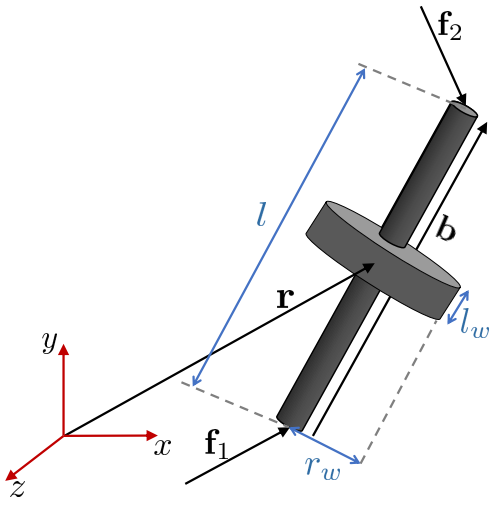

Figure 6.1: Tensegrity bar member vector nomenclature.

The bar vector $\boldsymbol{b}$ is described in body coordinates $\boldsymbol{\mathcal{B}}$ as:

$$\boldsymbol{b} = \boldsymbol{\mathcal{B}} b^{\mathcal{B}}, \quad b^{\mathcal{B}} = \begin{bmatrix} 0 & 0 & l \end{bmatrix}^{\mathsf{T}}, \tag{6.1}$$

where l is the length of the rigid bar and the inertial derivative of the vector $\boldsymbol{b}$ is calculated as:

$$\dot{\boldsymbol{b}} = \dot{\boldsymbol{\mathcal{B}}} b^{\mathcal{B}} + \boldsymbol{\mathcal{B}} \dot{b}^{\mathcal{B}} = \dot{\boldsymbol{\mathcal{B}}} b^{\mathcal{B}} = \boldsymbol{\mathcal{B}} \tilde{\omega}^{\mathcal{B}} b^{\mathcal{B}}. \tag{6.2}$$

Using the above two equations, the angular velocity of bar $\boldsymbol{\omega}_b$ can be written as (shown in [16]):

$$\boldsymbol{\omega}_b = \frac{\boldsymbol{b} \times \dot{\boldsymbol{b}}}{l^2}, \quad \boldsymbol{\omega}_b = \boldsymbol{\mathcal{B}} \begin{bmatrix} \omega_1^{\mathcal{B}} \\ \omega_2^{\mathcal{B}} \\ 0 \end{bmatrix} = \boldsymbol{\mathcal{B}} \omega_b^{\mathcal{B}}. \tag{6.3}$$

and the angular momentum of bar $\boldsymbol{b}$ about its mass center can be written as:

$$\boldsymbol{h}_b = J_b \boldsymbol{\omega}_b, \quad J_b = \frac{m_b l^2}{12}, \tag{6.4}$$

$$\boldsymbol{h}_b = \frac{m_b}{12} \boldsymbol{b} \times \dot{\boldsymbol{b}}. \tag{6.5}$$

The angular momentum of the wheel of radius r_w, thickness l_w, the wheel spin speed $\omega_3^{\mathcal{B}}$, and the wheel angular velocity vector $\boldsymbol{\omega_w}$ are related by:

$$\boldsymbol{h}_w = \boldsymbol{\mathcal{B}} J_w^{\mathcal{B}} \omega^{\mathcal{B}}, \tag{6.6}$$

where

$$\boldsymbol{\omega}_w = \boldsymbol{\mathcal{B}} \begin{bmatrix} \omega_1^{\mathcal{B}} \\ \omega_2^{\mathcal{B}} \\ \omega_3^{\mathcal{B}} \end{bmatrix}, \quad J_w^{\mathcal{B}} = \begin{bmatrix} J_1 & 0 & 0 \\ 0 & J_1 & 0 \\ 0 & 0 & J_3 \end{bmatrix}, \tag{6.7}$$

$$J_1 = J_2 = \frac{m_w}{12}(3r_w^2 + l_w^2), \quad J_3 = \frac{1}{2} m_w r_w^2. \tag{6.8}$$

Using Eqs. (6.5) and (6.6), the total angular momentum vector of the joint member can be written in terms of $\boldsymbol{b}$ and $\dot{\boldsymbol{b}}$ as:

$$\boldsymbol{h} = \boldsymbol{h}_b + \boldsymbol{h}_w, \tag{6.9}$$

$$\boldsymbol{h} = \frac{m_b}{12} \boldsymbol{b} \times \dot{\boldsymbol{b}} + \boldsymbol{\mathcal{B}} J_w^{\mathcal{B}} \omega^{\mathcal{B}}, \tag{6.10}$$

$$\boldsymbol{h} = \left(\frac{m_b l^2}{12} + J_1 \right) \frac{\boldsymbol{b} \times \dot{\boldsymbol{b}}}{l^2} + \omega_3^{\mathcal{B}} J_3 \frac{\boldsymbol{b}}{l}, \tag{6.11}$$

$$\boldsymbol{h} = J_t \boldsymbol{b} \times \dot{\boldsymbol{b}} + J_a l \omega_3^{\mathcal{B}} \boldsymbol{b}, \tag{6.12}$$

where $J_t = \frac{m_b}{12} + \frac{J_1}{l^2}$, $J_a = \frac{J_3}{l^2}$.

Now, the inertial derivative of the angular momentum vector $\boldsymbol{h}$ is equal to the total torque about the mass center of the body. The resulting torque can be written as the sum of pure torques $\boldsymbol{\tau}$ and

the torque due to the forces acting on the two ends of the bar:

$$\dot{\boldsymbol{h}} = \boldsymbol{\tau} + \frac{1}{2}\boldsymbol{b} \times (\boldsymbol{f}_2 - \boldsymbol{f}_1), \tag{6.13}$$

$$J_t \boldsymbol{b} \times \ddot{\boldsymbol{b}} + J_a l \dot{\omega}_3^{\mathcal{B}} \boldsymbol{b} + J_a l \omega_3^{\mathcal{B}} \dot{\boldsymbol{b}} = \boldsymbol{\tau} + \frac{1}{2}\boldsymbol{b} \times (\boldsymbol{f}_2 - \boldsymbol{f}_1). \tag{6.14}$$

Now, we write the above equation in inertial coordinates with $b = b^{\mathcal{E}}$ and $\omega_w = \omega_3^{\mathcal{B}}$ as:

$$J_t \tilde{b}\ddot{b} + J_a l \dot{\omega}_w b + J_a l \omega_w \dot{b} = \tau + \frac{1}{2}\tilde{b}(f_2 - f_1). \tag{6.15}$$

Similar to [16], a rigid bar length constraint of the following form is added:

$$b^{\mathsf{T}} b = l^2, \;\; b^{\mathsf{T}} \dot{b} = 0, \;\; b^{\mathsf{T}} \ddot{b} = -\dot{b}^{\mathsf{T}} \dot{b}. \tag{6.16}$$

The length constraint appended with rotational dynamics (Eq. (6.15)) can be expressed in matrix form as:

$$\begin{bmatrix} \tilde{b} \\ b^{\mathsf{T}} \end{bmatrix} \ddot{b} = \begin{bmatrix} \frac{1}{J_t}\left(\tau + \frac{1}{2}\tilde{b}(f_2 - f_1) - J_a l \dot{\omega}_w b - J_a l \omega_w \dot{b}\right) \\ -\dot{b}^{\mathsf{T}} \dot{b} \end{bmatrix}. \tag{6.17}$$

The above linear algebra problem (Eq. (6.17)) has solution for $\ddot{b}$ *if and only if* the vector on the right hand side lies in the range space of the coefficient matrix:

$$\left(I - \frac{1}{l^2} \begin{bmatrix} \tilde{b} \\ b^{\mathsf{T}} \end{bmatrix} \begin{bmatrix} -\tilde{b} & b^{\mathsf{T}} \end{bmatrix} \right) \times \begin{bmatrix} \frac{1}{J_t}(\tau + \frac{1}{2}\tilde{b}(f_2 - f_1) - J_a l \dot{\omega}_w b - J_a l \omega_w \dot{b}) \\ -\dot{b}^{\mathsf{T}} \dot{b} \end{bmatrix} = 0, \tag{6.18}$$

where I is the identity matrix of the appropriate dimension. The above equation after further simplification reduces to:

$$\frac{b b^{\mathsf{T}} \tau}{l^2} - J_a l \dot{\omega}_w b - \frac{J_a l \omega_w b b^{\mathsf{T}} \dot{b}}{l^2} = 0, \tag{6.19}$$

which after using bar length constraint ($b^{\mathsf{T}}\dot{b} = 0$) becomes:

$$b^{\mathsf{T}}\tau = J_a l^3 \dot{\omega}_w. \tag{6.20}$$

Writing $\tau = \tau_{\parallel} + \tau_{\perp}$, where $\tau_{\parallel}$ is the component along the bar and $\tau_{\perp}$ is perpendicular to the bar, we get:

$$b^{\mathsf{T}}\tau_{\parallel} = J_a l^3 \dot{\omega}_w. \tag{6.21}$$

Also, since the coefficient matrix of $\ddot{b}$ in Eq. (6.17) has full column rank, there is a unique solution for $\ddot{b}$, which is given as:

$$J_t\ddot{b} = \frac{(l^2 I - bb^{\mathsf{T}})}{2l^2}(f_2 - f_1) - \frac{\tilde{b}\tau}{l^2} + \frac{J_a\omega_w\tilde{b}\dot{b}}{l} - \frac{J_t b\dot{b}^{\mathsf{T}}\dot{b}}{l^2}. \tag{6.22}$$

Again using $\tau = \tau_{\parallel} + \tau_{\perp}$, we get the two final equations for rotational dynamics as:

$$J_t\ddot{b} = \frac{(l^2 I - bb^{\mathsf{T}})}{2l^2}(f_2 - f_1) - \frac{\tilde{b}\tau_{\perp}}{l^2} + \frac{J_a\omega_w\tilde{b}\dot{b}}{l} - \frac{J_t b\dot{b}^{\mathsf{T}}\dot{b}}{l^2}, \tag{6.23}$$

$$b^{\mathsf{T}}\tau_{\parallel} = J_a l^3 \dot{\omega}_w. \tag{6.24}$$

The above equations represent the bar-wheel system rotational dynamics along with the bar length constraint.

Finally, the translational dynamics of the bar-wheel system can be written in inertial coordinates from Fig. 6.1 as:

$$(m_b + m_w)\ddot{r} = f_1 + f_2, \tag{6.25}$$

where m_b and m_w are the mass of the bar and mass of the wheel, respectively. The translational dynamics (Eq. (6.25)) together with rotational dynamics (Eqs. (6.23-6.24)), fully describes the motion of the bar-gyro member.

The mass in the strings can be modelled by dividing the mass of the string into several point masses. This is achieved by adding *string-to-string nodes* that have the associated mass of the string. *String-to-string nodes* only have string-end connections and thus no bar-end is present at string-to-string node, e.g.: node n_7 in Fig. 6.2. The dynamics for such nodes can be written as:

$$m_s \ddot{r}_s = f_s, \tag{6.26}$$

where m_s is the mass of the point node and r_s is the position vector of the node.

6.3 Matrix Form of the System Dynamics

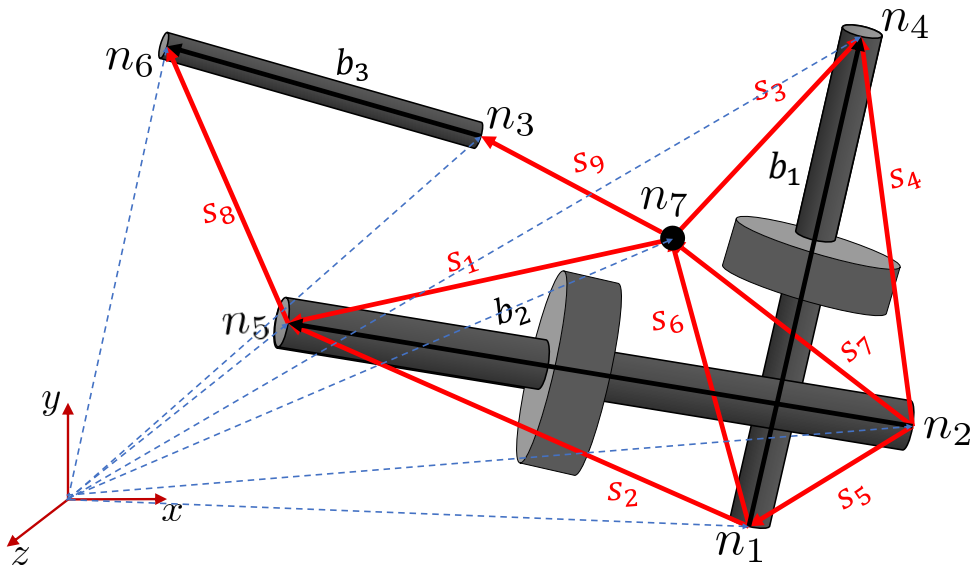

Figure 6.2: General tensegrity system representation with nodal matrices $N_1 = [n_1\ n_2\ n_3]$, $N_2 = [n_4\ n_5\ n_6]$, and $N_s = [n_7]$. Bar matrix $B = [b_1\ b_2\ b_3]$ and string matrix $S = [s_1\ s_2\ \cdots\ s_9]$ are also shown.

The aim of this section is to write the system dynamics in a compact matrix form for assumed β number of bar-wheel member. Let us denote the node position vector: $n_i = [n_{ix}\ n_{iy}\ n_{iz}]^\mathsf{T} \in \mathbb{R}^{3\times 1}$ and the matrix containing the position of the nodes at the base of a bar vector as $N_1 = \begin{bmatrix} n_1\ n_2\ \cdots\ n_\beta \end{bmatrix} \in \mathbb{R}^{3\times\beta}$, the position of the nodes at the terminal ends of the bar vectors as

$N_2 = \begin{bmatrix} n_{1+\beta}\, n_{2+\beta}\, \cdots\, n_{2\beta} \end{bmatrix} \in \mathbb{R}^{3\times\beta}$, and the string-to-string nodes to be stacked similarly in $N_s \in \mathbb{R}^{3\times\sigma}$, as shown in Fig. 6.2. So the full node matrix can consequently be split as $N = \begin{bmatrix} N_1\, N_2\, N_s \end{bmatrix} \in \mathbb{R}^{3\times(2\beta+\sigma)}$ where σ is the number of string-to-string nodes. Let us also define matrix $B = \begin{bmatrix} b_1\, b_2\, \cdots\, b_\beta \end{bmatrix} \in \mathbb{R}^{3\times\beta}$, where each column represents the bar vector b_i. This convention yields $B = NC_b^{\mathsf{T}}$ with $C_b = \begin{bmatrix} -I_\beta\, I_\beta\, \mathbf{0} \end{bmatrix} \in \mathbb{R}^{\beta\times(2\beta+\sigma)}$ as a bar connectivity matrix describing which two nodes form a particular bar and $I_\beta \in \mathbb{R}^{\beta\times\beta}$ is the identity matrix. Similarly, we define $R = NC_r^{\mathsf{T}} \in \mathbb{R}^{3\times\beta}$ with $C_r = 1/2 \begin{bmatrix} I_\beta\, I_\beta\, \mathbf{0} \end{bmatrix} \in \mathbb{R}^{\beta\times(2\beta+\sigma)}$ and each vector in R represents the center position vector r_i.

To write the dynamics in a compact matrix form, we take each term in Eq. (6.23) and arrange them as a vector in a matrix, e.g. $J_t = \begin{bmatrix} J_{t,1} & J_{t,2} & \cdots & J_{t,\beta} \end{bmatrix}^{\mathsf{T}} \in \mathbb{R}^{\beta\times1}$. Then, the left side of Eq. (6.23) is the i^{th} column of the matrix $\ddot{B}\hat{J}_t$:

$$\ddot{B}\hat{J}_t = \begin{bmatrix} J_{t,1}\ddot{b}_1 & J_{t,2}\ddot{b}_2 & \cdots & J_{t,\beta}\ddot{b}_\beta \end{bmatrix}, \tag{6.27}$$

where the “hat" operator over a vector forms a diagonal matrix from the elements of the vector.

This process can similarly be performed for the remaining terms in Eq. (6.23), as summarized below. Similar to N, we can define $F \in \mathbb{R}^{3\times(2\beta+\sigma)}$ containing its columns as the total force vector acting on the i^{th} node n_i. Converting the $\frac{1}{2}(f_2 - f_1)$ term into a matrix form, we get:

$$\frac{1}{2}(f_2 - f_1) \longrightarrow \frac{1}{2}FC_b^{\mathsf{T}}, \tag{6.28}$$

$$-\frac{1}{2l^2}bb^{\mathsf{T}}(f_2 - f_1) \longrightarrow -B\frac{1}{2}\hat{l}^{-2}\lfloor B^{\mathsf{T}}FC_b^{\mathsf{T}}\rfloor, \tag{6.29}$$

where we introduce the $\lfloor\circ\rfloor$ operator, which sets every off-diagonal element of the square matrix

operand to zero. Similarly, the other terms can be written as:

$$\frac{J_a}{l}\omega_w\tilde{b}\dot{b} \longrightarrow \tilde{B}\hat{\dot{B}}\hat{J}_a\hat{\omega}_w\hat{l}^{-1}, \tag{6.30}$$

with $\tilde{B} \triangleq \begin{bmatrix}\tilde{b}_1 & \tilde{b}_2 & \cdots & \tilde{b}_\beta\end{bmatrix} \in \mathbb{R}^{3\times 3\beta}$, where $\tilde{b}_i$ is a skew-symmetric matrix formed using the elements of the vector b_i, and

$$-\frac{\tilde{b}\tau_\perp}{l^2} \longrightarrow -\tilde{B}\hat{\mathcal{T}}\hat{l}^{-2}, \tag{6.31}$$

$$-\frac{J_t}{l^2}b\dot{b}^\mathsf{T}\dot{b} \longrightarrow -B\hat{J}_t\hat{l}^{-2}\lfloor\dot{B}^\mathsf{T}\dot{B}\rfloor. \tag{6.32}$$

Substituting for matrix expressions from Eqs. (6.27-6.32) in Eq. (6.23), the following full matrix expression for $\ddot{B}$ is obtained as:

$$\ddot{B}\hat{J}_t \;=\; \frac{1}{2}FC_b^\mathsf{T} \;-\; \frac{1}{2}B\hat{l}^{-2}\lfloor B^\mathsf{T}FC_b^\mathsf{T}\rfloor \;-\; \tilde{B}\hat{\mathcal{T}}\hat{l}^{-2} \;+\; \tilde{B}\hat{\dot{B}}\hat{J}_a\hat{\omega}_w\hat{l}^{-1} \;-\; B\hat{J}_t\hat{l}^{-2}\lfloor\dot{B}^\mathsf{T}\dot{B}\rfloor, \tag{6.33}$$

which can be further simplified with the following definition of $\hat{\lambda} \in \mathbb{R}^{\beta\times\beta}$ as:

$$\hat{\lambda} = -\hat{J}_t\hat{l}^{-2}\lfloor\dot{B}^\mathsf{T}\dot{B}\rfloor - \frac{1}{2}\hat{l}^{-2}\lfloor B^\mathsf{T}FC_b^\mathsf{T}\rfloor, \tag{6.34}$$

$$\ddot{B}\hat{J}_t = \frac{1}{2}FC_b^\mathsf{T} + B\hat{\lambda} - \tilde{B}\hat{\mathcal{T}}\hat{l}^{-2} + \tilde{B}\hat{\dot{B}}\hat{J}_a\hat{\omega}_w\hat{l}^{-1}. \tag{6.35}$$

Finally, writing Eq. (6.24) into a matrix form, with $\tau_\parallel = \frac{b}{l}\tau_b$, where τ_b is scalar representing the torque along the bar, we get:

$$\tau_b = J_a l^2\dot{\omega}_w \longrightarrow \tau_B = \hat{J}_a\hat{l}^2\dot{\omega}_W, \tag{6.36}$$

where $\tau_B = [\tau_{b1}\ \tau_{b2}\cdots\tau_{b\beta}]^\mathsf{T} \in \mathbb{R}^{\beta\times 1}$ and $\dot{\omega}_W = [\dot{\omega}_{w1}\ \dot{\omega}_{w2}\cdots\dot{\omega}_{w\beta}]^\mathsf{T} \in \mathbb{R}^{\beta\times 1}$.

The translational dynamics must similarly be converted into a matrix expression as:

$$(m_b + m_w)\ddot{r} = f_1 + f_2 \longrightarrow \ddot{R}\hat{m}_t = 2FC_r^{\mathsf{T}}. \tag{6.37}$$

Similarly, the dynamics of the string-to-string node can be put into a matrix form as:

$$m_s\ddot{r}_s = f_s \longrightarrow \ddot{R}_s\hat{m}_s = F_s. \tag{6.38}$$

Note that the bar and string nodes can be extracted from the node matrix N with two new definitions of matrix $N_b \in \mathbb{R}^{3\times 2\beta}$ and matrix $N_s \in \mathbb{R}^{3\times\sigma}$ as:

$$N_b = \begin{bmatrix} N_1 & N_2 \end{bmatrix} = N \begin{bmatrix} I_{2\beta} \\ 0 \end{bmatrix} = NC_{nb}^{\mathsf{T}}, \tag{6.39}$$

$$N_s = N \begin{bmatrix} 0 \\ I_\sigma \end{bmatrix} = NC_{ns}^{\mathsf{T}}. \tag{6.40}$$

Similar to bar connectivity matrix, we now define string connectivity matrix $C_s \in \mathbb{R}^{\alpha\times(2\beta+\sigma)}$, where α is the number of strings. The matrix C_s can be separated into two parts: $C_{sb} \in \mathbb{R}^{\alpha\times 2\beta}$, for bar-to-string joints, and $C_{ss} \in \mathbb{R}^{\alpha\times\sigma}$, for string-to-string joints:

$$S = NC_s^{\mathsf{T}} = \begin{bmatrix} N_b & N_s \end{bmatrix} \begin{bmatrix} C_{sb}^{\mathsf{T}} \\ C_{ss}^{\mathsf{T}} \end{bmatrix} \in \mathbb{R}^{3\times\alpha}. \tag{6.41}$$

The original expression for the force matrix F remains unchanged, though it is now describing the sum of forces acting on bar nodes, F_b, and forces on string nodes, F_s.

$$F = \begin{bmatrix} F_b & F_s \end{bmatrix} \tag{6.42}$$

After formulating matrix forms in Eqs. (6.35-6.38), we combine them together as:

$$\begin{bmatrix} \ddot{B} & \ddot{R}_b & \ddot{R}_s \end{bmatrix} \begin{bmatrix} \hat{J}_t & 0 & 0 \\ 0 & \hat{m}_t & 0 \\ 0 & 0 & \hat{m}_s \end{bmatrix} + \begin{bmatrix} B & R_b & R_s \end{bmatrix} \begin{bmatrix} -\hat{\lambda} & 0 & 0 \\ 0 & 0 & 0 \\ 0 & 0 & 0 \end{bmatrix} = F \begin{bmatrix} \frac{1}{2}C_b^{\mathsf{T}} & 2C_r^{\mathsf{T}} & 0 \\ 0 & 0 & I \end{bmatrix} + \begin{bmatrix} \tilde{B}\hat{\dot{B}}\hat{J}_a\hat{\omega}_w\hat{l}^{-1} - \tilde{B}\hat{\mathcal{T}}\hat{l}^{-2} & 0 & 0 \end{bmatrix}. \quad (6.43)$$

The following identity:

$$\begin{bmatrix} \frac{1}{2}C_b^{\mathsf{T}} & 2C_r^{\mathsf{T}} & 0 \\ 0 & 0 & I \end{bmatrix}^{-1} = \begin{bmatrix} C_b & 0 \\ C_r & 0 \\ 0 & I \end{bmatrix}, \quad (6.44)$$

can be used in Eq. (6.43) to get:

$$\begin{bmatrix} \ddot{B} & \ddot{R}_b & \ddot{R}_s \end{bmatrix} \begin{bmatrix} \hat{J}_t & 0 & 0 \\ 0 & \hat{m}_t & 0 \\ 0 & 0 & \hat{m}_s \end{bmatrix} \begin{bmatrix} C_b & 0 \\ C_r & 0 \\ 0 & I \end{bmatrix} + \begin{bmatrix} B & R_b & R_s \end{bmatrix} \begin{bmatrix} -\hat{\lambda} & 0 & 0 \\ 0 & 0 & 0 \\ 0 & 0 & 0 \end{bmatrix} \begin{bmatrix} C_b & 0 \\ C_r & 0 \\ 0 & I \end{bmatrix} = F + \begin{bmatrix} \tilde{B}\hat{\dot{B}}\hat{J}_a\hat{\omega}_w\hat{l}^{-1} - \tilde{B}\hat{\mathcal{T}}\hat{l}^{-2} & 0 & 0 \end{bmatrix} \begin{bmatrix} C_b & 0 \\ C_r & 0 \\ 0 & I \end{bmatrix}, \quad (6.45)$$

and after using the previously defined expressions:

$$\begin{bmatrix} B & R_b & R_s \end{bmatrix} = N \begin{bmatrix} C_{nb}^{\mathsf{T}}C_b^{\mathsf{T}} & C_{nb}^{\mathsf{T}}C_r^{\mathsf{T}} & C_{ns}^{\mathsf{T}} \end{bmatrix}, \quad (6.46)$$

we get:

$$\ddot{N}\begin{bmatrix} C_{nb}^{\mathsf{T}}C_b^{\mathsf{T}} & C_{nb}^{\mathsf{T}}C_r^{\mathsf{T}} & C_{ns}^{\mathsf{T}} \end{bmatrix}\begin{bmatrix} \hat{J}_t & 0 & 0 \\ 0 & \hat{m}_t & 0 \\ 0 & 0 & \hat{m}_s \end{bmatrix}\begin{bmatrix} C_b & 0 \\ C_r & 0 \\ 0 & I \end{bmatrix}$$
$$+ N\begin{bmatrix} C_{nb}^{\mathsf{T}}C_b^{\mathsf{T}} & C_{nb}^{\mathsf{T}}C_r^{\mathsf{T}} & C_{ns}^{\mathsf{T}} \end{bmatrix}\begin{bmatrix} -\hat{\lambda} & 0 & 0 \\ 0 & 0 & 0 \\ 0 & 0 & 0 \end{bmatrix}\begin{bmatrix} C_b & 0 \\ C_r & 0 \\ 0 & I \end{bmatrix}$$
$$= F + \begin{bmatrix} \tilde{B}\hat{\dot{B}}\hat{J}_a\hat{\omega}_w\hat{l}^{-1} - \tilde{B}\hat{\mathcal{T}}\hat{l}^{-2} & 0 & 0 \end{bmatrix}\begin{bmatrix} C_b & 0 \\ C_r & 0 \\ 0 & I \end{bmatrix}. \quad (6.47)$$

Now, let us define "force density" γ_i as the tension per unit length in the i^{th} string $\mathbf{s}_i$. The tension vector in the string can be now be written as $\mathbf{t}_i = \mathbf{s}_i\gamma_i$. Combining the tension vectors, the matrix of string tensions $T \in \mathbb{R}^{3\times\alpha}$ is written as:

$$T = [t_1\ t_2\ \cdots\ t_\alpha] = S\hat{\gamma} = NC_s^{\mathsf{T}}\hat{\gamma}, \quad (6.48)$$

and the internal forces acting on nodes caused by string tensions are calculated as $NC_s^{\mathsf{T}}\hat{\gamma}C_s$. Let us also define w_i as the i^{th} column of the matrix $W \in \mathbb{R}^{3\times(2\beta+\sigma)}$, where w_i is the external force acting on the node n_i. The full force matrix expression can then be written as:

$$F = \begin{bmatrix} F_b & F_s \end{bmatrix} = W - NC_s^{\mathsf{T}}\hat{\gamma}C_s. \quad (6.49)$$

Substituting Eq. (6.49) for F, and rearranging yields the following expression for the full

system dynamics:

$$\ddot{N}\begin{bmatrix} C_{nb}^{\mathsf{T}} C_b^{\mathsf{T}} \hat{J}_t C_b + C_{nb}^{\mathsf{T}} C_r^{\mathsf{T}} \hat{m}_t C_r & C_{ns}^{\mathsf{T}} \hat{m}_s \end{bmatrix} + N\begin{bmatrix} C_s^{\mathsf{T}} \hat{\gamma} C_{sb} - C_{nb}^{\mathsf{T}} C_b^{\mathsf{T}} \hat{\lambda} C_b & C_s^{\mathsf{T}} \hat{\gamma} C_{ss} \end{bmatrix}$$
$$= W + \begin{bmatrix} (\tilde{B}\dot{\hat{B}}\hat{J}_a \hat{\omega}_w \hat{l}^{-1} - \tilde{B}\hat{\mathcal{T}}\hat{l}^{-2}) C_b & 0 \end{bmatrix}, \quad (6.50)$$

which can be written in compact matrix form with the following definitions of M_s, K_s, and W_T as:

$$\ddot{N} M_s + N K_s = W_T, \quad (6.51)$$

$$\tau_B = \hat{J}_a \hat{l}^2 \dot{\omega}_W, \quad (6.52)$$

where

$$M_s = \begin{bmatrix} C_{nb}^{\mathsf{T}} (C_b^{\mathsf{T}} \hat{J}_t C_b + C_r^{\mathsf{T}} \hat{m}_t C_r) & C_{ns}^{\mathsf{T}} \hat{m}_s \end{bmatrix}, \quad (6.53)$$

$$K_s = \begin{bmatrix} C_s^{\mathsf{T}} \hat{\gamma} C_{sb} - C_{nb}^{\mathsf{T}} C_b^{\mathsf{T}} \hat{\lambda} C_b & C_s^{\mathsf{T}} \hat{\gamma} C_{ss} \end{bmatrix}, \quad (6.54)$$

$$\hat{\lambda} = -\hat{J}_t \hat{l}^{-2} \lfloor \dot{B}^{\mathsf{T}} \dot{B} \rfloor - \frac{1}{2} \hat{l}^{-2} \lfloor B^{\mathsf{T}} (W - N C_s^{\mathsf{T}} \hat{\gamma} C_s) C_b^{\mathsf{T}} \rfloor, \quad (6.55)$$

$$W_T = W + \begin{bmatrix} (\tilde{B}\dot{\hat{B}}\hat{J}_a \hat{\omega}_w \hat{l}^{-1} - \tilde{B}\hat{\mathcal{T}}\hat{l}^{-2}) C_b & 0 \end{bmatrix}, \quad (6.56)$$

$\tau_B = [\tau_{b1}\ \tau_{b2} \cdots \tau_{b\beta}]^{\mathsf{T}}$ and $\dot{\omega}_W = [\dot{\omega}_{w1}\ \dot{\omega}_{w2} \cdots \dot{\omega}_{w\beta}]^{\mathsf{T}}$.

6.4 Class-K Tensegrity Systems

In class-k tensegrity systems, multiple bars are connected (ball joint) at a node such that there is no torque/moment transfer from one bar member to any other bar member. The structure is said to be of class-1 if the maximum number of bars present at any nodes is one and class-k if the maximum number of bars present at any node is k [6]. The dynamics of class-k tensegrity structures (for $k > 1$) can be easily extended from the formulation developed in the previous section. Each class-k joint can be handled by creating $k-1$ virtual nodes which are constrained to

coincide at all times with the use of Lagrange constraint forces. These constraints are written as:

$$NP = D, \tag{6.57}$$

where $P \in \mathbb{R}^{(2\beta+\sigma)\times c}$ and $D \in \mathbb{R}^{3\times c}$ are specified such that constrained nodes coincide at all times and the number of added constraints is denoted as c. Adding the linear constraints introduce Lagrange constraint forces (ΩP^{T}) resulting in the new dynamics:

$$\ddot{N}M_s + NK_s = W_T + \Omega P^{\mathsf{T}}, \tag{6.58}$$

where $\Omega \in \mathbb{R}^{3\times c}$ is a matrix of Lagrange multipliers satisfying the dynamics constraints at all time-steps and the force density in the bars changes according to the following equation:

$$\hat{\lambda} = -\hat{J}\hat{l}^{-2}\lfloor \dot{B}^{\mathsf{T}}\dot{B}\rfloor - \frac{1}{2}\hat{l}^{-2}\lfloor B^{\mathsf{T}}(W + \Omega P^{\mathsf{T}} - S\hat{\gamma}C_s)C_{nb}^{\mathsf{T}}C_b^{\mathsf{T}}\rfloor. \tag{6.59}$$

The Lagrange multipliers required to maintain these constraints can be thought of as contact forces at the Class k nodes [14].

6.4.1 Reduced-order dynamics

The added constraints reduced the order of the system dynamics to a smaller dimension manifold. Here, we use the same procedure developed in [16] by starting with the constraint equation:

$$NP = NU\Sigma V^{\mathsf{T}} = [\eta_1 \;\; \eta_2] \begin{bmatrix} \Sigma_1 \\ 0 \end{bmatrix} \begin{bmatrix} V^{\mathsf{T}} \end{bmatrix} = D, \tag{6.60}$$

where the matrices U, Σ, and V are numerically generated by performing the Singular Value Decomposition (SVD) of the full *column rank matrix* P as $P = U\Sigma V^{\mathsf{T}} = [U_1 \;\; U_2] \begin{bmatrix} \Sigma_1 \\ 0 \end{bmatrix} \begin{bmatrix} V^{\mathsf{T}} \end{bmatrix}$,

and $[\eta_1 \;\; \eta_2] \triangleq NU$, to get:

$$\eta_1 = DV\Sigma_1^{-1}, \;\; \dot{\eta}_1 = 0, \;\; \ddot{\eta}_1 = 0. \tag{6.61}$$

The constant value of variable η_1 represents the constraint space (no-motion space) and η_2 represents the reduced space in the new coordinate system. The dynamics equation (Eq. (6.58)) can now be rewritten as:

$$\ddot{N}UU^{\mathsf{T}}M_s + NUU^{\mathsf{T}}K_s = W_T + \Omega V\Sigma^{\mathsf{T}}U^{\mathsf{T}}, \tag{6.62}$$

$$\ddot{\eta}_2 U_2^{\mathsf{T}}M_s + \eta_1 U_1^{\mathsf{T}}K_s + \eta_2 U_2^{\mathsf{T}}K_s = W_T + \Omega V\Sigma_1^{\mathsf{T}}U_1^{\mathsf{T}}. \tag{6.63}$$

Post-multiplying the above equation by a non-singular matrix $[M_s^{-1}U_1 \;\; U_2]$ will result in two parts, where the first part gives an algebraic equation that is used to solve for the Lagrange multiplier:

$$NK_sM_s^{-1}U_1 - \Omega P^{\mathsf{T}}M_s^{-1}U_1 = W_TM_s^{-1}U_1, \tag{6.64}$$

Notice that K_s is also a function of Ω, making it a linear algebra problem. The analytical expression to solve the Lagrange Multiplier (Ω) is given in appendix B.2.

The second part gives a second-order matrix differential equation for the reduced order dynamics:

$$\ddot{\eta}_2 U_2^{\mathsf{T}}M_sU_2 + \eta_2 U_2^{\mathsf{T}}K_sU_2 = W_TU_2 - \eta_1 U_1^{\mathsf{T}}K_sU_2. \tag{6.65}$$

6.5 Simulation and Experimental Setup

The experimental setup shown in Fig. 6.3 is a planar D-bar tensegrity structure [6] with gimbal motors (T-MOTOR GB54-1) attached to each of the four 12 inch wooden bars (shown in black). Each bar in the system is connected to two other bars through a hinge joint which is allowed to slide along the vertical and horizontal straight lines. The shape (D-bar angle) and orientation of

the D-bar structure is controlled by the strings, as shown in Fig. 6.3. The IMU sensor (BWT61CL Bluetooth MPU6050) is used to measure the angular rotation of the structure. The material used for the strings is spectra (UHMWPE). The strings are passed through 3D printed pulleys (green) to reduce the amount of friction. Both the horizontal strings are independently controlled by two MX-12W DYNAMIXEL servo motors attached to the pulleys. ARDUINO MEGA2560 was used to communicate and control the gyro motors by a C++ script, and dynamixel servos were controlled by its embedded driver through a python script.

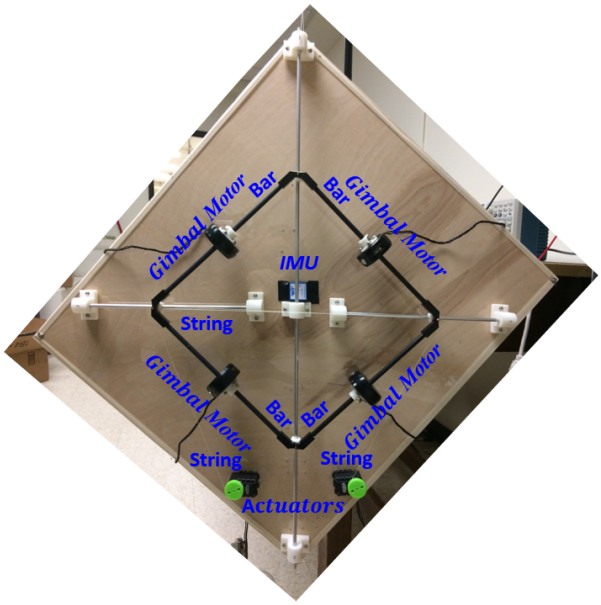

Figure 6.3: Experimental setup for gyroscopic tensegrity D-bar structure.

Figure 6.4 shows the same setup to perform a dynamic simulation with the initial configuration in XY-plane. The initial configuration is an equilibrium configuration with no prestress in the horizontal strings and gyro wheels rotating at a constant speed of 715 rpm. The angular momentum vector for each bar-wheel system is also shown in Fig. 6.4 to give the sense of direction of wheel rotation.

The dynamic simulation on gyroscopic D-bar tensegrity structure was performed by reducing

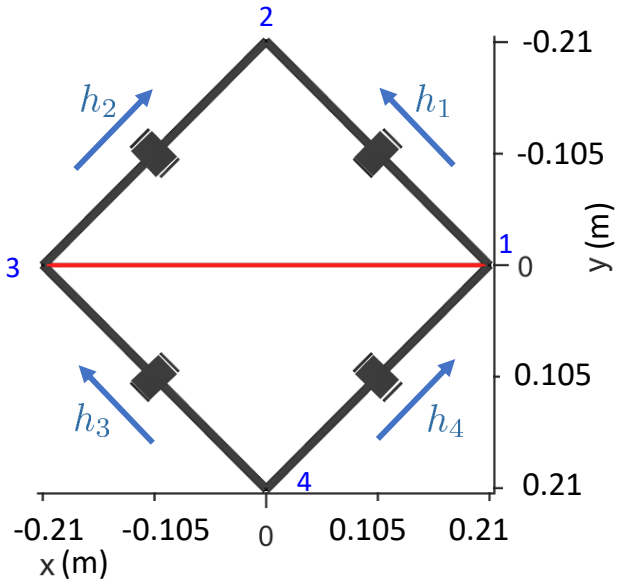

Figure 6.4: Simulation setup for gyroscopic tensegrity D-bar structure.

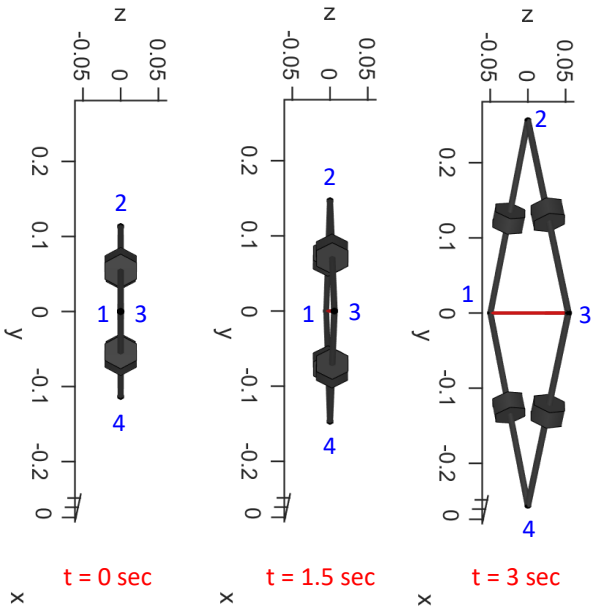

Figure 6.5: Dynamic simulation time-lapse of gyroscopic tensegrity D-bar structure with rotating wheel.

the distance between node-1 and node-3 to 1/3 of the initial distance. The three time-lapse images of the dynamic simulation for time $t = 0$ sec, $t = 1.5$ sec, and $t = 3$ sec are shown in Fig. 6.5.

These configurations are shown by looking at YZ-plane to distinctly show the change in orientation of the plane containing the D-bar structure. The rotation of the plane by changing the length of the strings (hence, the direction of the angular momentum vector) can also be understood by the conservation of the angular momentum of the system. A similar change in the orientation of the plane was observed in the experiment performed by reducing the length of the horizontal strings. Three time-lapse images of the experiment are shown in Fig. 6.6, which agrees with the proposed approach to control the attitude and derived dynamics of the gyroscopic tensegrity structures.

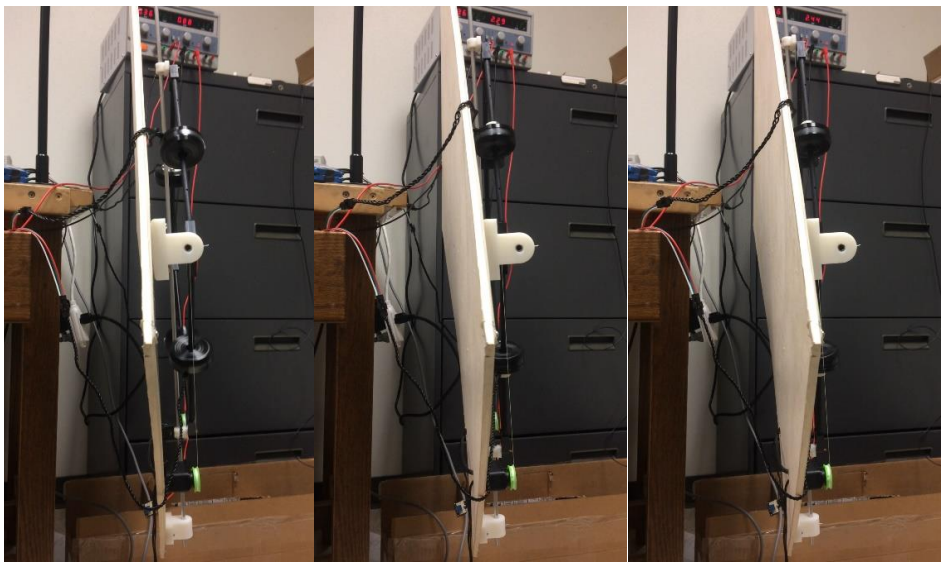

Figure 6.6: Experimental setup time-lapse of gyroscopic tensegrity D-bar structure with rotating wheel.

Figure 6.7 shows the time history of variation in x,y, and z coordinates of all the four nodes performed using dynamic simulation. As the length of the horizontal string is reduced, x-coordinate of nodes n_1 and n_3 varies (closer) while nodes n_2 and n_4 moves (away) in y-direction. Due to the presence of gyroscopic forces in Fig. 6.7(a), a significant motion was observed in the z-direction. Nodes n_1 and n_3 were observed to have a displacement of $\approx$2cm in z-direction, which qualitatively matches the experimental results from Fig. 6.6. No motion was observed in

z-direction for the case of zero gyroscopic wheels spin speed as shown in Fig. 6.7(b).

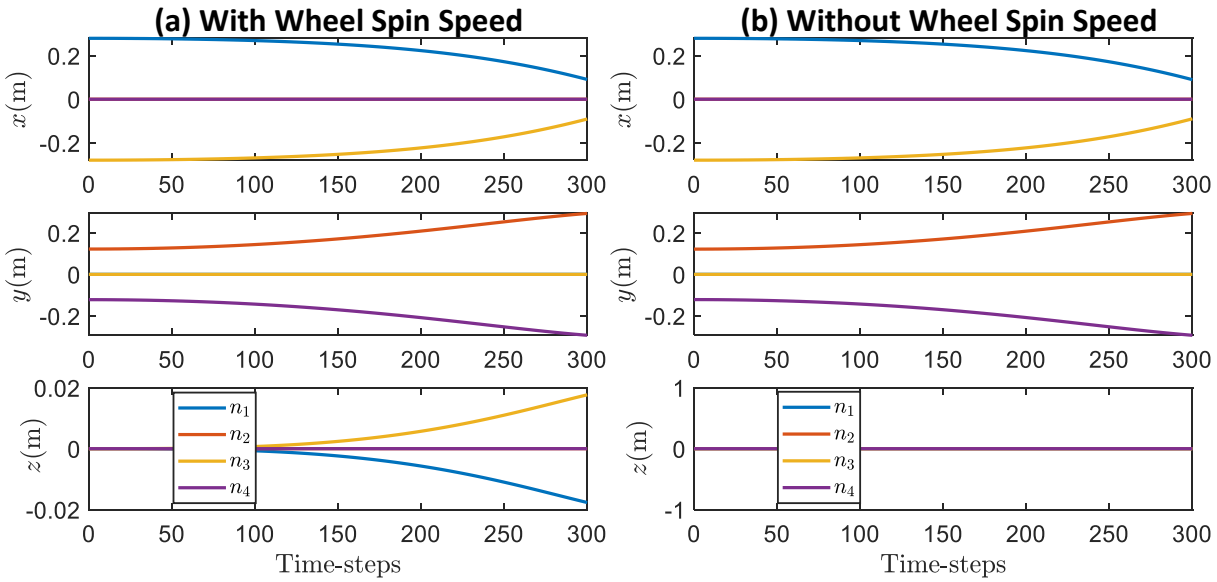

Figure 6.7: Simulation result with variation in x,y, and z coordinates of all the four nodes with time.

Figure 6.8(a) plots the variation in z-coordinate of all the four nodes obtained from the experimental results with the specified wheel spin speed. Figure 6.8(a) shows substantial motion in z-direction for nodes n_1 and n_3, which was calculated from the angular measurement data obtained from the onboard IMU. The motion of the nodes in the z-direction follows the same trend, but a smaller displacement is observed due to the added (unaccounted) inertia of the entire setup. Figure 6.8(b) plots the variation in z-coordinate with zero wheel spin speed. No significant motion (rotation) was observed in the absence of gyroscopic forces. This validates our approach to construct the experimental setup and shows a good match with the simulation and experimental results.

Figure 6.9 provides the plot for error in satisfying bar length constraints with the time-steps of the simulation. The error in constraint violation is of the order 10^{-15} representing the accuracy of the formulated dynamics that avoids transcendental functions.

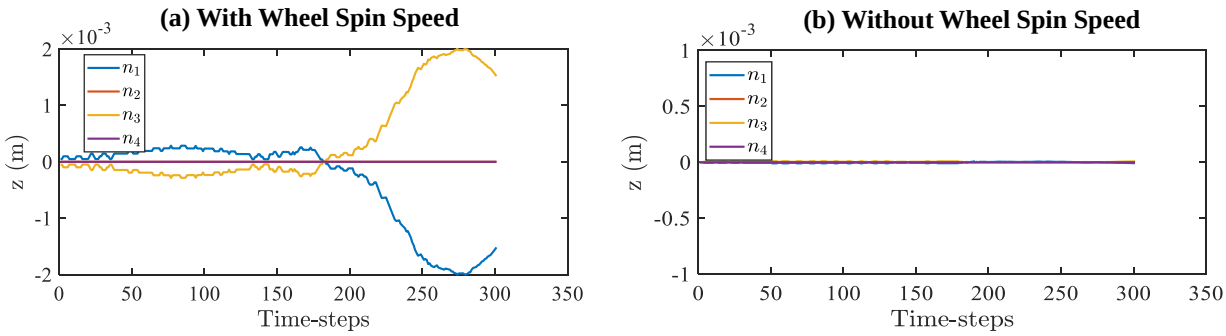

Figure 6.8: Experimental result with variation in x,y, and z coordinates of all the four nodes with time.

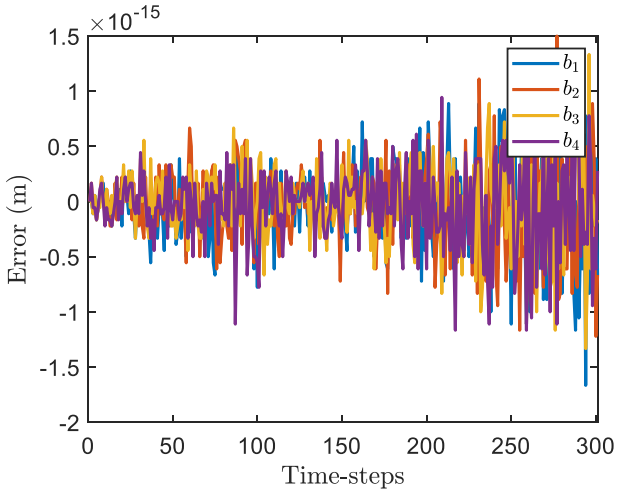

Figure 6.9: Plot for error in bar length constraint for all time-steps.

In this article, we have provided an overview of the modeling of tensegrity structures that can be used as the mechanism for enabling very high DOF robots, in particular, tensegrity robots. We have also studied model-based and data-based approaches

6.6 Conclusions

This chapter provided a systematic approach to derive the dynamics of any tensegrity system with gyroscopic wheels attached to its bars. The second-order matrix differential equation along with a second-order vector differential equation describes the equations of motion in the presence of external forces and torques on the bars. The matrix differential equation provides the

information on position and orientation of the bar, and the vector differential equation provides the information on the angular position of the wheels. A reduced-order model is also developed for the class-k tensegrity structures to increase the accuracy and computational efficiency of the formulation. Finally, it was shown that the orientation of the structure could be controlled by controlling the shape, i.e., by controlling the length of the stings. This chapter formulates the mechanics of gyroscopic tensegrity systems and paves the path to form control principles associated with the design, development, and control of such structures.

7. CONTROL OF TENSEGRITY SYSTEMS*

[1] This chapter proposes a model-based approach to control the shape of the structure or the position of the end effector for a soft-robotic application. In this approach, the nonlinear dynamics of the tensegrity system is used to regulate position, velocity, and acceleration to the specified reference trajectory. The formulation uses state feedback to obtain the solution for the control (tension in the strings) as a *linear programming* problem. The shape control for the gyroscopic tensegrity systems was also discussed and it was observed that these systems increase the reachable space for the structure by providing the orientation control (rotation about the arm axis) due to gyroscopic forces. The control approach for disturbance rejection of the tensegrity system is further studied in the chapter. In this approach, the vectorized formulation for nonlinear dynamics of the tensegrity system is developed and used in conjunction with a second-order output regulator to reject the disturbance. Moreover, the formulation to calculate the control gains to bound the errors for five different types of problems is also provided. The formulation uses the Linear Matrix Inequalities (LMIs) approach to get the desired performance bounds on error, e.g. $\mathcal{H}_\infty$, generalized $\mathcal{H}_2$, LQR and *covariance control* problem.

7.1 Introduction

The design of high DOF soft robotic systems has attracted increasing interest in recent years [72, 73]. In this regard, tensegrity structures offer a tantalizing prospect for the principled design of such soft robotic systems. The minimal mass architecture along with the variable stiffness characteristic makes it suitable for civil-engineering structures [74, 75], for soft robotic applications like planetary landers [29], flexible robots [76, 18], and deployable space structures [32]. Some of the researchers used a model-based approach [76, 18] and some used learning/evolutionary algorithm based approach [29, 31, 77] to control the tensegrity structures

[1]*Portions of this section are reprinted or adapted from [71] : R. Wang, R. Goyal, S. Chakravorty, and R. Skelton, "Model and Data Based Approaches to the Control of Tensegrity Robots," in IEEE Robotics and Automation Letters. DOI: 10.1109/LRA.2020.2979891. Copyright © 2020, IEEE. Reproduced with permission.

but no discussion has been given in the past to compare the two methods. The Central Pattern Generator(CPG) controller mimicking our biological neural circuits [78, 79] and Model Predictive Control (MPC) approaches have been used recently to control tensegrity structures but only for smaller systems [76]. Robotic path planning and manipulators were also recently developed using tensegrity structures [80, 81].

The control of tensegrity systems amounts to the design of a nonlinear stochastic controller for a very high DOF complex nonlinear system. Controlling an unknown dynamical system adaptively has a rich history in control literature [82, 83]. This classical literature provides a rigorous analysis of the asymptotic performance and stability of the closed-loop system, mostly for linear systems or finite-state and control space systems. The optimal control of a possibly unknown nonlinear dynamical system with continuous state and action space is a significantly more challenging problem. Even with a known model, computing an optimal control law requires solving a dynamic programming problem. The 'curse of dimensionality' associated with dynamic programming makes solving such problems computationally intractable, except under special structural assumptions on the underlying system. *Learning to control* problems where the model of the system is unknown or is too large or complex for a tractable control synthesis, also suffers from this computational complexity issues. For the model-based methods, the computational time is often negligible if the analytical model is known. We exploit this advantage of the tensegrity structures as very precise dynamic models are available due to the 1-dimensional deformation motion of each member [16, 84]. The optimal control problems can further be solved posing them as feasibility problems by providing different kinds of bounds on the performance [85].

The contributions of the chapter are as follows: we first provide the full-order models and reduced-order models for controlling the shape of high DOF class-k tensegrity design. A tensegrity T_2D_1 robotic arm example is used to show the extension from a stowed configuration, and then the end effector of the arm is shown to reach a desired given position in 3-dimensional space. Then, the shape control formulation for the gyroscopic tensegrity system was derived, and it was shown that this allows to rotate the arm about its axis, which was not possible with the standard tensegrity

model. In the last part, the vectorized formulation for nonlinear tensegrity dynamics in the presence of some given disturbance is provided. The vector form allows us to find the control gains to bound different kinds of errors for full and reduced-order controllers. The LMI formulation was used to solve for the control gains to bound the errors for different kinds of disturbances.

7.2 Shape Control for Class K Tensegrity Systems

One of the important steps in writing the control of this nonlinear dynamic system into a linear programming problem is to be able to write the force densities in the bar $\lambda = [\lambda_1\ \lambda_2\ \cdots\ \lambda_\beta]^\mathsf{T}$ in terms of the linear function of force densities in the strings $\gamma = [\gamma_1\ \gamma_2\ \cdots\ \gamma_\alpha]^\mathsf{T}$. This is required in order to write down control only as a function of force densities in the strings. Let us start by writing λ from equation 5.99 as:

$$\hat{\lambda} = -\hat{J}\hat{l}^{-2}\lfloor \dot{B}^\mathsf{T}\dot{B}\rfloor - \frac{1}{2}\hat{l}^{-2}\lfloor B^\mathsf{T}(W + \Omega P^\mathsf{T} - S\hat{\gamma}C_s)C_{nb}^\mathsf{T}C_b^\mathsf{T}\rfloor. \tag{7.1}$$

The i^{th} diagonal element of the above matrix can be extracted by multiplying the above equation from the left by e_i^T and from the right by e_i as:

$$\lambda_i = -J_i l_i^{-2} e_i^\mathsf{T}\lfloor \dot{B}^\mathsf{T}\dot{B}\rfloor e_i - \frac{1}{2}l_i^{-2}e_i^\mathsf{T}\lfloor B^\mathsf{T}(W + \Omega P^\mathsf{T} - S\hat{\gamma}C_s)C_{nb}^\mathsf{T}C_b^\mathsf{T}\rfloor e_i, \tag{7.2}$$

which again after using the definition of the operator $\lfloor \circ \rfloor$ can be written as:

$$\lambda_i = -J_i l_i^{-2}||\dot{b_i}||^2 - \frac{1}{2}l_i^{-2}b_i^\mathsf{T}(W + \Omega P^\mathsf{T})C_{nb}^\mathsf{T}C_b^\mathsf{T}e_i + \frac{1}{2}l_i^{-2}b_i^\mathsf{T}S\hat{\gamma}C_sC_{nb}^\mathsf{T}C_b^\mathsf{T}e_i. \tag{7.3}$$

Using the identity $\hat{x}y = \hat{y}x$ on the last term for x and y being the column vectors, we get:

$$\lambda_i = -J_i l_i^{-2}||\dot{b_i}||^2 - \frac{1}{2}l_i^{-2}b_i^\mathsf{T}(W + \Omega P^\mathsf{T})C_{nb}^\mathsf{T}C_b^\mathsf{T}e_i + \frac{1}{2}l_i^{-2}b_i^\mathsf{T}\overbrace{S(C_sC_{nb}^\mathsf{T}C_b^\mathsf{T}e_i)}\gamma. \tag{7.4}$$

Now, stacking all these scalars into a column gives:

$$\lambda = \Lambda\gamma + \tau, \tag{7.5}$$

where $\Lambda = \begin{bmatrix} \Lambda_1^\mathsf{T} & \Lambda_2^\mathsf{T} & \cdots & \Lambda_\beta^\mathsf{T} \end{bmatrix}^\mathsf{T}$, $\tau = \begin{bmatrix} \tau_1^\mathsf{T} & \tau_2^\mathsf{T} & \cdots & \tau_\beta^\mathsf{T} \end{bmatrix}^\mathsf{T}$, $\Lambda_i = \frac{1}{2} l_i^{-2} b_i^\mathsf{T} \widehat{S(C_s C_{nb}^\mathsf{T} C_b^\mathsf{T} e_i)}$, and

$\tau_i = -J_i l_i^{-2} ||\dot{b}_i||^2 - \frac{1}{2} l_i^{-2} b_i^\mathsf{T} (W + \Omega P^\mathsf{T}) C_{nb}^\mathsf{T} C_b^\mathsf{T} e_i$, for $i = 1, 2 \cdots \beta$.

7.2.1 Controller for Full-Order Dynamics Model

In this section, we write down the control algorithm to control the position of certain nodes in the structure. Let us define the position of those nodes by $Y = LNR$, where $L \in \mathbf{R}^{n_l \times 3}$ is a matrix that defines the x, y or z coordinates of the node and $R \in \mathbf{R}^{n \times n_r}$ matrix defines which nodes to be controlled. $\bar{Y}$ defines the final desired location of the nodes that we want to go from Y to $\bar{Y}$. Therefore, the error in the positions at any time can be written as:

$$E = Y - \bar{Y}, \tag{7.6}$$

$$E = LNR - \bar{Y}, \tag{7.7}$$

and its first and second derivatives with respect to time can be written as:

$$\dot{E} = L\dot{N}R, \tag{7.8}$$

$$\ddot{E} = L\ddot{N}R. \tag{7.9}$$

Now, let us write the non-linear dynamics of tensegrity systems in a general form as:

$$\dot{x} = f(x) + g(x)u \rightarrow \ddot{N} = f(N, \dot{N}) + g(N)(\hat{u})h(N, \dot{N}), \tag{7.10}$$

where $(\hat{u})$ is the diagonal matrix made from the control input and we want to derive the states to

some position $Y(t) \rightarrow \bar{Y}(t)$. Let us define the lyapunov function $V(N, \dot{N})$ as:

$$V = \frac{1}{2}\,\mathrm{tr}(E^{\mathsf{T}}\Theta E + \dot{E}^{\mathsf{T}}\dot{E}) > 0 \;\; \forall\, [E,\; \dot{E}] \neq 0, \tag{7.11}$$

where $\mathrm{tr}(\cdot)$ is the trace and the matrix $\Theta > 0$ is positive definite, which can be used to change the weights between error and error velocity. Let us write the first derivative w.r.t. time as:

$$\dot{V} = \mathrm{tr}(\dot{E}^{\mathsf{T}}\Theta E + \dot{E}^{\mathsf{T}}\ddot{E}), \tag{7.12}$$

where the goal is to get the time derivative to be:

$$\dot{V} = -\,\mathrm{tr}(\dot{E}^{\mathsf{T}}\Psi\dot{E}) < 0, \;\; \Phi > 0. \tag{7.13}$$

Substituting the above equation to previous equation, we get:

$$-\,\mathrm{tr}(\dot{E}^{\mathsf{T}}\Psi\dot{E}) = \mathrm{tr}(\dot{E}^{\mathsf{T}}\Theta E + \dot{E}^{\mathsf{T}}\ddot{E}), \tag{7.14}$$

$$\mathrm{tr}(\dot{E}^{\mathsf{T}}\ddot{E} + \dot{E}^{\mathsf{T}}\Psi\dot{E} + \dot{E}^{\mathsf{T}}\Theta E) = 0, \tag{7.15}$$

which after using the properties of trace operator, gives the final equation as:

$$\ddot{E} + \dot{E}\Psi + E\Theta = 0. \tag{7.16}$$

Notice that this gives a second-order differential equation in the error dynamics to derive the error to zero. The idea is to move the nodes from the current position to the desired position by aptly choosing the control gain parameters matrices Ψ and Θ. Now, we derive the final equations for the lyapunov controller mentioned earlier to generate the solution for the control as the linear programming problem. Let us start by substituting for $E, \dot{E}$ and $\ddot{E}$ in Eq. (7.16) to obtain:

$$L\ddot{N}R + L\dot{N}R\Psi + (LNR - \bar{Y})\Theta = 0. \tag{7.17}$$

Further substituting for $\ddot{N}$ from equation 5.97, we get:

$$L(W + \Omega P^{\mathsf{T}} - NK_s)M_s^{-1}R + L\dot{N}R\Psi + (LNR - \bar{Y})\Theta = 0, \tag{7.18}$$

$$LNK_sM_s^{-1}R = L(W + \Omega P^{\mathsf{T}})M_s^{-1}R + L\dot{N}R\Psi + (LNR - \bar{Y})\Theta. \tag{7.19}$$

Taking the i^{th} column of the matrices from the above equation gives:

$$LNK_sM_s^{-1}Re_i = \Big(L(W + \Omega P^{\mathsf{T}})M_s^{-1}R + L\dot{N}R\Psi + (LNR - \bar{Y})\Theta\Big)\, e_i. \tag{7.20}$$

Taking the left hand side and substitute K_s which can also be written as $K_s = C_s^{\mathsf{T}}\hat{\gamma}C_s - C_{nb}^{\mathsf{T}}C_b^{\mathsf{T}}\hat{\lambda}C_bC_{nb}$, we get:

$$LNK_sM_s^{-1}Re_i = LN(C_s^{\mathsf{T}}\hat{\gamma}C_s - C_{nb}^{\mathsf{T}}C_b^{\mathsf{T}}\hat{\lambda}C_bC_{nb})M_s^{-1}Re_i, \tag{7.21}$$

$$LNK_sM_s^{-1}Re_i = LNC_s^{\mathsf{T}}\hat{\gamma}C_sM_s^{-1}Re_i - LNC_{nb}^{\mathsf{T}}C_b^{\mathsf{T}}\hat{\lambda}C_bC_{nb}M_s^{-1}Re_i, \tag{7.22}$$

and using the identity $\hat{x}y = \hat{y}x$ for the right-hand side terms gives:

$$LNK_sM_s^{-1}Re_i = LNC_s^{\mathsf{T}}\widehat{(C_sM_s^{-1}Re_i)}\gamma - LNC_{nb}^{\mathsf{T}}C_b^{\mathsf{T}}\widehat{(C_bC_{nb}M_s^{-1}Re_i)}\lambda. \tag{7.23}$$

Substituting for λ in terms of γ from equation 7.5 gives:

$$LNK_sM_s^{-1}Re_i = LNC_s^{\mathsf{T}}\widehat{(C_sM_s^{-1}Re_i)}\gamma - LNC_{nb}^{\mathsf{T}}C_b^{\mathsf{T}}\widehat{(C_bC_{nb}M_s^{-1}Re_i)}(\Lambda\gamma + \tau), \tag{7.24}$$

which again can be written by combining the terms together as:

$$LNK_sM_s^{-1}Re_i = \Big(\widehat{LNC_s^{\mathsf{T}}(C_sM_s^{-1}Re_i)} - \widehat{LNC_{nb}^{\mathsf{T}}C_b^{\mathsf{T}}(C_bC_{nb}M_s^{-1}Re_i)\Lambda}\Big)\gamma$$

$$- \widehat{LNC_{nb}^{\mathsf{T}}C_b^{\mathsf{T}}(C_bC_{nb}M_s^{-1}Re_i)\tau}. \quad (7.25)$$

Substituting the above expression back for the left-hand side in equation 7.20, we get:

$$\Big(\widehat{LNC_s^{\mathsf{T}}(C_sM_s^{-1}Re_i)} - \widehat{LNC_{nb}^{\mathsf{T}}C_b^{\mathsf{T}}(C_bC_{nb}M_s^{-1}Re_i)\Lambda}\Big)\gamma =$$

$$\Big(L(W+\Omega P^{\mathsf{T}})M_s^{-1}R + L\dot{N}R\Psi + (LNR-\bar{Y})\Theta\Big)e_i + \widehat{LNC_{nb}^{\mathsf{T}}C_b^{\mathsf{T}}(C_bC_{nb}M_s^{-1}Re_i)\tau}. \quad (7.26)$$

Finally, stacking up all the matrices on the left and vectors on the right, we get:

$$\begin{bmatrix} \Gamma_1 \\ \Gamma_2 \\ \vdots \\ \Gamma_{n_r} \end{bmatrix} \gamma = \begin{bmatrix} \mu_1 \\ \mu_2 \\ \vdots \\ \mu_{n_r} \end{bmatrix}, \quad (7.27)$$

where

$$\Gamma_i = \overbrace{LNC_s^{\mathsf{T}}(C_s M_s^{-1} Re_i)} - \overbrace{LNC_{nb}^{\mathsf{T}} C_b^{\mathsf{T}}(C_b C_{nb} M_s^{-1} Re_i)}\Lambda \tag{7.28}$$

$$\mu_i = \Big(L(W + \Omega P^{\mathsf{T}})M_s^{-1}R + L\dot{N}R\Psi + (LNR - \bar{Y})\Theta\Big)e_i + \overbrace{LNC_{nb}^{\mathsf{T}} C_b^{\mathsf{T}}(C_b C_{nb} M_s^{-1} Re_i)}\tau \tag{7.29}$$

$$i = 1, 2 \ldots n_r \tag{7.30}$$

7.2.2 Controller for Reduced-Order Dynamics Model

In the previous subsection, the control algorithm was designed for the full-order dynamics model. In this section, we use the reduced-order dynamics model to control the structure. The error in the position at any time can be written as:

$$E = LNR - \bar{Y}, \tag{7.31}$$

$$E = L[\eta_1 \;\; \eta_2]U^{\mathsf{T}}R - \bar{Y}, \tag{7.32}$$

$$E = L(\eta_1 U_1^{\mathsf{T}} + \eta_2 U_2^{\mathsf{T}})R - \bar{Y}. \tag{7.33}$$

Notice that now the error is written in terms of reduced-order constant state matrix η_1 and time-varying state matrix η_2. Similar to the previous section, we use a second-order differential equation in error dynamics to derive the error to zero.

$$\ddot{E} + \dot{E}\Psi + E\Theta = 0, \tag{7.34}$$

$$L\ddot{\eta}_2 U_2^{\mathsf{T}} R + L\dot{\eta}_2 U_2^{\mathsf{T}} R\Psi + [L(\eta_1 U_1^{\mathsf{T}} + \eta_2 U_2^{\mathsf{T}})R - \bar{Y}]\Theta = 0, \tag{7.35}$$

where $\dot{\eta_1} = \ddot{\eta_1} = 0$ was used from the dynamics model formulation. Further substituting for $\ddot{\eta_2}$ from equation 5.107, we get:

$$L(\widetilde{W} - \eta_2 K_2)M_2^{-1}U_2^{\mathsf{T}}R + L\dot{\eta_2}U_2^{\mathsf{T}}R\Psi + [L(\eta_1 U_1^{\mathsf{T}} + \eta_2 U_2^{\mathsf{T}})R - \bar{Y}]\Theta = 0, \tag{7.36}$$

which again can be written after substituting for $\widetilde{W}$ from dynamics formulation as:

$$L(WU_2 - \eta_1 U_1^{\mathsf{T}}K_s U_2 - \eta_2 U_2^{\mathsf{T}}K_s U_2)M_2^{-1}U_2^{\mathsf{T}}R + L\dot{\eta_2}U_2^{\mathsf{T}}R\Psi + [L(\eta_1 U_1^{\mathsf{T}} + \eta_2 U_2^{\mathsf{T}})R - \bar{Y}]\Theta = 0. \tag{7.37}$$

Rearranging the above equation to collect all the known and unknown terms together, we get:

$$LWU_2M_2^{-1}U_2^{\mathsf{T}}R + L\dot{\eta_2}U_2^{\mathsf{T}}R\Psi + [L(\eta_1 U_1^{\mathsf{T}} + \eta_2 U_2^{\mathsf{T}})R - \bar{Y}]\Theta = L(\eta_1 U_1^{\mathsf{T}}K_s U_2 + \eta_2 U_2^{\mathsf{T}}K_s U_2)M_2^{-1}U_2^{\mathsf{T}}R. \tag{7.38}$$

Notice that everything on the left side of the equation is known. Let us define it as:

$$\mathcal{C} \triangleq LWU_2M_2^{-1}U_2^{\mathsf{T}}R + L\dot{\eta_2}U_2^{\mathsf{T}}R\Psi + [L(\eta_1 U_1^{\mathsf{T}} + \eta_2 U_2^{\mathsf{T}})R - \bar{Y}]\Theta, \tag{7.39}$$

and write the right hand side of the equation (7.38) as:

$$L(\eta_1 U_1^{\mathsf{T}}K_s U_2 + \eta_2 U_2^{\mathsf{T}}K_s U_2)M_2^{-1}U_2^{\mathsf{T}}R = LNK_s \underbrace{U_2M_2^{-1}U_2^{\mathsf{T}}}_{M_{sn}}R. \tag{7.40}$$

We now take the i^{th} column of the above matrix and follow the procedure used in the previous Full-order controller design:

$$LNK_sM_{sn}Re_i = LN(C_s^{\mathsf{T}}\hat{\gamma}C_s - C_{nb}^{\mathsf{T}}C_b^{\mathsf{T}}\hat{\lambda}C_bC_{nb})M_{sn}Re_i, \tag{7.41}$$

$$LNK_sM_{sn}Re_i = LNC_s^{\mathsf{T}}\hat{\gamma}C_sM_{sn}Re_i - LNC_{nb}^{\mathsf{T}}C_b^{\mathsf{T}}\hat{\lambda}C_bC_{nb}M_{sn}Re_i, \tag{7.42}$$

and using the identity $\hat{x}y = \hat{y}x$ for the right-hand side terms gives:

$$LNK_sM_{sn}Re_i = LNC_s^{\mathsf{T}}\widehat{(C_sM_{sn}Re_i)}\gamma - LNC_{nb}^{\mathsf{T}}C_b^{\mathsf{T}}\widehat{(C_bC_{nb}M_{sn}Re_i)}\lambda. \tag{7.43}$$

Substituting for λ in terms of γ from equation 7.5 gives:

$$LNK_sM_{sn}Re_i = LNC_s^{\mathsf{T}}\widehat{(C_sM_{sn}Re_i)}\gamma - LNC_{nb}^{\mathsf{T}}C_b^{\mathsf{T}}\widehat{(C_bC_{nb}M_{sn}Re_i)}(\Lambda\gamma + \tau), \tag{7.44}$$

which again can be written by combining the terms together as:

$$LNK_sM_{sn}Re_i = \Big(LNC_s^{\mathsf{T}}\widehat{(C_sM_{sn}Re_i)} - LNC_{nb}^{\mathsf{T}}C_b^{\mathsf{T}}\widehat{(C_bC_{nb}M_{sn}Re_i)}\Lambda\Big)\gamma$$

$$- LNC_{nb}^{\mathsf{T}}C_b^{\mathsf{T}}\widehat{(C_bC_{nb}M_{sn}Re_i)}\tau. \tag{7.45}$$

Let us write the vector form of equation (7.38) as:

$$LNK_sM_{sn}Re_i = \mathcal{C}e_i. \tag{7.46}$$

Now, substituting it back to the vector equation of equation (7.38), we get:

$$\Big(\overbrace{LNC_s^{\mathsf{T}}(C_sM_{sn}Re_i)} - \overbrace{LNC_{nb}^{\mathsf{T}}C_b^{\mathsf{T}}(C_bC_{nb}M_{sn}Re_i)}\Lambda\Big)\gamma - \overbrace{LNC_{nb}^{\mathsf{T}}C_b^{\mathsf{T}}(C_bC_{nb}M_{sn}Re_i)}\tau = \mathcal{C}e_i, \tag{7.47}$$

$$\Big(\overbrace{LNC_s^{\mathsf{T}}(C_sM_{sn}Re_i)} - \overbrace{LNC_{nb}^{\mathsf{T}}C_b^{\mathsf{T}}(C_bC_{nb}M_{sn}Re_i)}\Lambda\Big)\gamma = \mathcal{C}e_i + \overbrace{LNC_{nb}^{\mathsf{T}}C_b^{\mathsf{T}}(C_bC_{nb}M_{sn}Re_i)}\tau. \tag{7.48}$$

Finally, stacking up all these matrices on left and vectors on right, we get:

$$\begin{bmatrix} \Gamma_1 \\ \Gamma_2 \\ \vdots \\ \Gamma_{n_r} \end{bmatrix} \gamma = \begin{bmatrix} \mu_1 \\ \mu_2 \\ \vdots \\ \mu_{n_r} \end{bmatrix}, \tag{7.49}$$

where

$$\Gamma_i = \overbrace{LNC_s^{\mathsf{T}}(C_sM_{sn}Re_i)} - \overbrace{LNC_{nb}^{\mathsf{T}}C_b^{\mathsf{T}}(C_bC_{nb}M_{sn}Re_i)}\Lambda \tag{7.50}$$

$$\mu_i = \mathcal{C}e_i + \overbrace{LNC_{nb}^{\mathsf{T}}C_b^{\mathsf{T}}(C_bC_{nb}M_{sn}Re_i)}\tau \tag{7.51}$$

$$\mathcal{C} = LWM_{sn}R + L\dot{\eta}_2U_2^{\mathsf{T}}R\Psi + [L(\eta_1U_1^{\mathsf{T}} + \eta_2U_2^{\mathsf{T}})R - \bar{Y}]\Theta \tag{7.52}$$

$$M_{sn} = U_2M_2^{-1}U_2^{\mathsf{T}} \text{ for } i = 1, 2 \cdots n_r \tag{7.53}$$

7.2.3 Controlling the Velocity and Acceleration

For controlling the node positions, we write the error in position as $E_p = L_p N R_p - \bar{Y}_p$ where subscript p is used for the position. Next, we use a second-order differential equation to derive the error to zero, which results in a linear equation for the force densities in the string (refer equation 7.49). The same equation can again be written in a compact form as:

$$\Gamma_p \gamma = \mu_p, \quad \gamma \geq 0. \tag{7.54}$$

For controlling the velocity, we write the error in the velocity of certain nodes as:

$$E_v = L_v \dot{N} R_v - \dot{\bar{Y}}_v, \tag{7.55}$$

$$E_v = L_v \dot{\eta}_2 U_2^{\mathsf{T}} R_v - \dot{\bar{Y}}_v, \tag{7.56}$$

$$\dot{E}_v + E_v \Psi_v = 0, \tag{7.57}$$

and use a first-order differential equation to derive the error in velocity to zero. Only first derivative of error E_v is required as the control variable, force density γ in the strings come out at the same level of differential. Following the same derivation as used in the previous subsections, we can write the linear equation to control the nodal velocities as:

$$\begin{bmatrix} \Gamma_{v1} \\ \Gamma_{v2} \\ \vdots \\ \Gamma_{v_{nr}} \end{bmatrix} \gamma = \begin{bmatrix} \mu_{v1} \\ \mu_{v2} \\ \vdots \\ \mu_{v_{nr}} \end{bmatrix}, \quad \gamma \geq 0, \tag{7.58}$$

where

$$\Gamma_{vi} = L_v N \overbrace{C_s^{\mathsf{T}}(C_s M_{sn} R_v e_i)} - L_v N C_{nb}^{\mathsf{T}} \overbrace{C_b^{\mathsf{T}}(C_b C_{nb} M_{sn} R_v e_i)}\Lambda \tag{7.59}$$

$$\mu_{vi} = L_v W M_{sn} R_v e_i + (L_v \dot{\eta}_2 U_2^{\mathsf{T}} R_v - \bar{\dot{Y}}_v)\Psi_v e_i + L_v N C_{nb}^{\mathsf{T}} \overbrace{C_b^{\mathsf{T}}(C_b C_{nb} M_{sn} R_v e_i)}\tau \tag{7.60}$$

$$M_{sn} = U_2 M_2^{-1} U_2^{\mathsf{T}} \text{ for } i = 1, 2 \cdots v_{n_r} \tag{7.61}$$

which again can be written in the compact form as:

$$\Gamma_v \gamma = \mu_v, \quad \gamma \geq 0. \tag{7.62}$$

To control the acceleration of the nodes, the error can be written as:

$$E_a = L_a \ddot{N} R_a - \bar{\ddot{Y}}_a \tag{7.63}$$

$$E_a = L_a \ddot{\eta}_2 U_2^{\mathsf{T}} R_a - \bar{\ddot{Y}}_a, \tag{7.64}$$

which can be directly converted to a linear equation in control variable by equating it to zero as $E_a = 0$. Following the same procedure, we get the linear algebra equation to solve for control variable as:

$$\begin{bmatrix} \Gamma_{a1} \\ \Gamma_{a2} \\ \vdots \\ \Gamma_{a_{n_r}} \end{bmatrix} \gamma = \begin{bmatrix} \mu_{a1} \\ \mu_{a2} \\ \vdots \\ \mu_{a_{n_r}} \end{bmatrix}, \quad \gamma \geq 0, \tag{7.65}$$

where

$$\Gamma_{ai} = L_a N C_s^{\mathsf{T}} \widehat{(C_s M_{sn} R_a e_i)} - L_a N C_{nb}^{\mathsf{T}} C_b^{\mathsf{T}} \widehat{(C_b C_{nb} M_{sn} R_a e_i)} \Lambda \tag{7.66}$$

$$\mu_{ai} = (L_a W M_{sn} R_a - \ddot{\bar{Y}}_a) e_i + L_a N C_{nb}^{\mathsf{T}} C_b^{\mathsf{T}} \widehat{(C_b C_{nb} M_{sn} R_a e_i)} \tau \tag{7.67}$$

$$M_{sn} = U_2 M_2^{-1} U_2^{\mathsf{T}} \text{ for } i = 1, 2 \cdots a_{n_r} \tag{7.68}$$

which again can be written in the compact form as:

$$\Gamma_a \gamma = \mu_a, \quad \gamma \geq 0. \tag{7.69}$$

Finally, combining the equations 7.54, 7.62, and 7.69 allows to simultaneously control the position, velocity and acceleration of different nodes in the structure.

$$\begin{bmatrix} \Gamma_p \\ \Gamma_v \\ \Gamma_a \end{bmatrix} \gamma = \begin{bmatrix} \mu_p \\ \mu_v \\ \mu_a \end{bmatrix}, \quad \gamma \geq 0. \tag{7.70}$$

7.3 Control of Gyroscopic Class K Tensegrity Systems

The gyroscopic forces in this new system allow us to control the shape of the structure in a plane where even strings are not present. In other words, this new system increases the controllability of the structure and allows for a larger controllable space. We use the similar concept discussed above and use a second-order differential equation in the error dynamics to derive the error to zero

with control gain parameters matrices Ψ and Θ:

$$\ddot{E} + \dot{E}\Psi + E\Theta = 0, \tag{7.71}$$

$$L\ddot{N}R + L\dot{N}R\Psi + (LNR - \bar{Y})\Theta = 0. \tag{7.72}$$

Further substituting for $\ddot{N}$ from equation 6.51, we get:

$$L(W_T + \Omega P^{\mathsf{T}} - NK_s)M_s^{-1}R + L\dot{N}R\Psi + (LNR - \bar{Y})\Theta = 0, \tag{7.73}$$

$$LNK_sM_s^{-1}R = L(W_T + \Omega P^{\mathsf{T}})M_s^{-1}R + L\dot{N}R\Psi + (LNR - \bar{Y})\Theta. \tag{7.74}$$

Taking the i^{th} column of the matrices from the above equation gives:

$$LNK_sM_s^{-1}Re_i = \left(L\left(W + \begin{bmatrix}(\tilde{B}\hat{\dot{B}}\hat{J}_a\hat{l}^{-1}\hat{\omega}_w)C_b & 0\end{bmatrix} + \Omega P^{\mathsf{T}}\right)M_s^{-1}R + L\dot{N}R\Psi + (LNR - \bar{Y})\Theta\right)e_i. \tag{7.75}$$

Taking the left hand side and substitute K_s which can also be written as $K_s = C_s^{\mathsf{T}}\hat{\gamma}C_s - C_{nb}^{\mathsf{T}}C_b^{\mathsf{T}}\hat{\lambda}C_bC_{nb}$, we get:

$$LNK_sM_s^{-1}Re_i = LNC_s^{\mathsf{T}}\hat{\gamma}C_sM_s^{-1}Re_i - LNC_{nb}^{\mathsf{T}}C_b^{\mathsf{T}}\hat{\lambda}C_bC_{nb}M_s^{-1}Re_i, \tag{7.76}$$

which by following the procedure described earlier can be written as:

$$LNK_sM_s^{-1}Re_i = \Big(\widehat{LNC_s^{\mathsf{T}}(C_sM_s^{-1}Re_i)} - \widehat{LNC_{nb}^{\mathsf{T}}C_b^{\mathsf{T}}(C_bC_{nb}M_s^{-1}Re_i)\Lambda}\Big)\gamma$$

$$- \widehat{LNC_{nb}^{\mathsf{T}}C_b^{\mathsf{T}}(C_bC_{nb}M_s^{-1}Re_i)}\tau. \quad (7.77)$$

Taking the left-hand side and taking out the angular speed of the wheels ω_w:

$$\begin{aligned}
&\left(L\left(W + \begin{bmatrix}(\tilde{B}\hat{\dot{B}}\hat{J}_a\hat{l}^{-1}\hat{\omega}_w)C_b & 0\end{bmatrix} + \Omega P^{\mathsf{T}}\right)M_s^{-1}R + L\dot{N}R\Psi + (LNR - \bar{Y})\Theta\right)e_i \\
&= L\begin{bmatrix}(\tilde{B}\hat{\dot{B}}\hat{J}_a\hat{l}^{-1}\hat{\omega}_w)C_b & 0\end{bmatrix}M_s^{-1}Re_i + \Big(L(W + \Omega P^{\mathsf{T}})M_s^{-1}R + L\dot{N}R\Psi + (LNR - \bar{Y})\Theta\Big)e_i
\end{aligned} \quad (7.78)$$

$$\begin{aligned}
&L\begin{bmatrix}(\tilde{B}\hat{\dot{B}}\hat{J}_a\hat{l}^{-1}\hat{\omega}_w)C_b & 0\end{bmatrix}M_s^{-1}Re_i + \Big(L(W + \Omega P^{\mathsf{T}})M_s^{-1}R + L\dot{N}R\Psi + (LNR - \bar{Y})\Theta\Big)e_i \\
&= L\begin{bmatrix}\tilde{B}\hat{\dot{B}}\hat{J}_a\hat{l}^{-1}\hat{\omega}_wC_b & 0\end{bmatrix}\begin{bmatrix}M_{sb}^{-1} \\ M_{ss}^{-1}\end{bmatrix}Re_i + \Big(L(W + \Omega P^{\mathsf{T}})M_s^{-1}R + L\dot{N}R\Psi + (LNR - \bar{Y})\Theta\Big)e_i \\
&= L\tilde{B}\hat{\dot{B}}\hat{J}_a\hat{l}^{-1}\hat{\omega}_wC_bM_{sb}^{-1}Re_i + \Big(L(W + \Omega P^{\mathsf{T}})M_s^{-1}R + L\dot{N}R\Psi + (LNR - \bar{Y})\Theta\Big)e_i.
\end{aligned} \quad (7.79)$$

Now, using the identity $\hat{x}y = \hat{y}x$ for the first term gives:

$$L\begin{bmatrix}(\tilde{B}\hat{\dot{B}}\hat{J}_a\hat{l}^{-1}\hat{\omega}_w)C_b & 0\end{bmatrix}M_s^{-1}Re_i + \Big(L(W+\Omega P^{\mathsf{T}})M_s^{-1}R + L\dot{N}R\Psi + (LNR-\bar{Y})\Theta\Big)e_i$$

$$= L\tilde{B}\hat{\dot{B}}\hat{J}_a\hat{l}^{-1}\widehat{(C_bM_{sb}^{-1}Re_i)}\omega_w + \Big(L(W+\Omega P^{\mathsf{T}})M_s^{-1}R + L\dot{N}R\Psi + (LNR-\bar{Y})\Theta\Big)e_i. \quad (7.80)$$

Substituting the above expression back for the left-hand side in equation 7.75, we get:

$$\Big(LNC_s^{\mathsf{T}}\widehat{(C_sM_s^{-1}Re_i)} - LNC_{nb}^{\mathsf{T}}C_b^{\mathsf{T}}\widehat{(C_bC_{nb}M_s^{-1}Re_i)}\Lambda\Big)\gamma - L\tilde{B}\hat{\dot{B}}\hat{J}_a\hat{l}^{-1}\widehat{(C_bM_{sb}^{-1}Re_i)}\omega_w =$$

$$\Big(L(W+\Omega P^{\mathsf{T}})M_s^{-1}R + L\dot{N}R\Psi + (LNR-\bar{Y})\Theta\Big)e_i + LNC_{nb}^{\mathsf{T}}C_b^{\mathsf{T}}\widehat{(C_bC_{nb}M_s^{-1}Re_i)}\tau. \quad (7.81)$$

Finally, stacking up all the matrices on the left and vectors on the right, we get:

$$\begin{bmatrix}\Gamma_1\\ \Gamma_2\\ \vdots\\ \Gamma_{n_r}\end{bmatrix}\gamma = \begin{bmatrix}\mu_1\\ \mu_2\\ \vdots\\ \mu_{n_r}\end{bmatrix} + \begin{bmatrix}\Upsilon_1\\ \Upsilon_2\\ \vdots\\ \Upsilon_{n_r}\end{bmatrix}\omega_w, \quad (7.82)$$

where

$$\Gamma_i = LNC_s^{\mathsf{T}}\widehat{(C_s M_s^{-1} Re_i)} - LNC_{nb}^{\mathsf{T}} C_b^{\mathsf{T}}\widehat{(C_b C_{nb} M_s^{-1} Re_i)}\Lambda$$

$$\mu_i = \Big(L(W + \Omega P^{\mathsf{T}})M_s^{-1}R + L\dot{N}R\Psi + (LNR - \bar{Y})\Theta\Big)e_i + LNC_{nb}^{\mathsf{T}} C_b^{\mathsf{T}}\widehat{(C_b C_{nb} M_s^{-1} Re_i)}\tau,$$

$$\Upsilon_i = L\tilde{B}\hat{\dot{B}}\hat{J}_a\hat{l}^{-1}\widehat{(C_b M_{sb}^{-1} Re_i)}, \quad i = 1, 2 \ldots n_r.$$

7.4 Simulation Results for the Tensegrity Robotic Arm

To define our design of the tensegrity robotic arm, we use the concept of fractals or self-similar iterations. The structure is made from a T-bar of complexity $q_T = n$ where at the last stage horizontal compressive members are replaced with a D-bar structure of complexity $q_D = 1$ to yield a $T_n D_1$ Tensegrity structure. In this section, simulation results are given to show the extension of the robotic arm from a stowed configuration to an extended configuration and its movement (angular motion) to reach any particular point in a given 3-dimensional hemisphere. All the dynamic simulations are performed using a Matlab based software developed using this formulation. The numerical integration package used in this software is fourth-order Runge-Kutta.

7.4.1 Extension from a Stowed Configuration

In this subsection, we extend the $T_2 D_1$ tensegrity structure from a stowed configuration to an extended configuration. This can be understood as controlling the shape of the structure from some initial configuration, shown in Fig. 7.1, to a final configuration which is shown in Fig. 7.2.

We use the control algorithm developed in the previous section to control the shape of the structure, which drives the errors to zero by carefully designing a trajectory based on the control

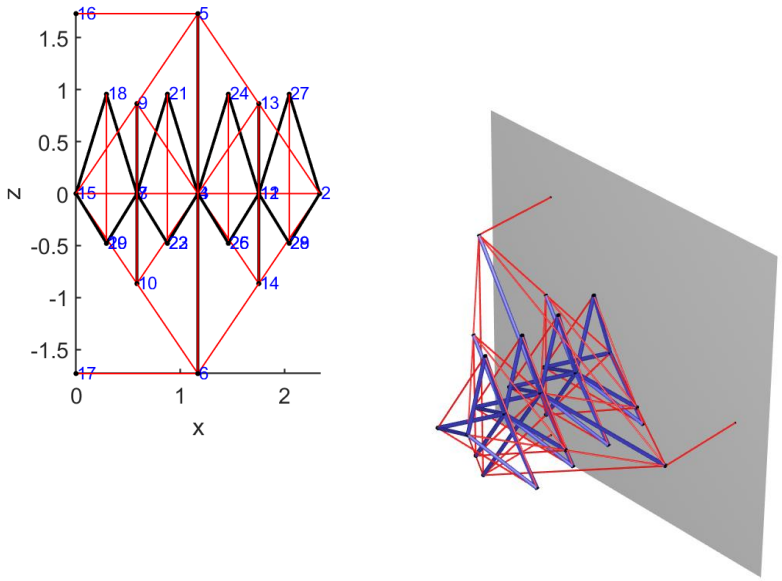

Figure 7.1: Initial configuration of tensegrity T_2D_1 structure.

gains. Figure 7.3a shows the trajectory for the errors in the node position for nodes n_1, n_2 and n_3. Notice that the error goes to zero and stays there after roughly 2 sec. Similar plots for nodes (n_{11}, n_{12} and n_{13}) and nodes (n_{21}, n_{22} and n_{23}) are shown in Fig. 7.3b and Fig. 7.3c, respectively. Notice the small error in y and z directions as the arm extends along its length which lies along the x axis as shown in Fig.7.2.

The following plots show the node position trajectories for different nodes during the extension of the tensegrity arm. Figure 7.4a shows the node position trajectories for nodes n_1, n_2 and n_3. Notice that as the arm extends, the x coordinates for the nodes increases and settle for the desired value, and as the length of the bars are constant, the z coordinates of the nodes decrease and finally reaches the steady-state position. This can also be understood as the arm extends in length; the thickness of the arm decreases. The similar node position plots for nodes (n_{11}, n_{12} and n_{13}) and nodes (n_{21}, n_{22} and n_{25}) are shown in Fig. 7.4b and Fig. 7.4c, respectively.

Finally, Fig. 7.5 shows the control inputs required to extend the tensegrity T_2D_1 arm structure. The control inputs in these systems are assumed to be the force density in the strings, which can be uniquely converted to the rest length of the strings. The figure shows trajectories only for nine

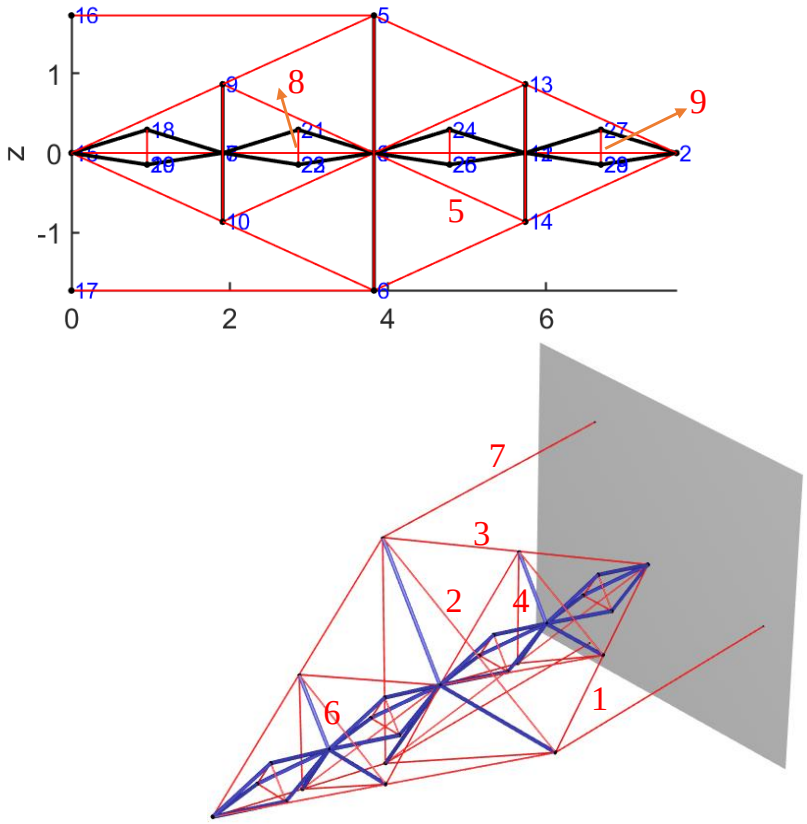

Figure 7.2: Final configuration of tensegrity T_2D_1 structure.

strings in the structure as due to the symmetry of the structure, other strings will follow the same trend and can easily be recognized. Notice that the control values reach a steady-state value after 2 seconds, but small changes in the strings can still be expected as tensegrity structures have multiple equilibrium solutions for a given configuration of the structure.

7.4.2 Tip movement in 3-dimensional hemisphere

The previous subsection extended the tensegrity arm to the desired location, and in this subsection, we control the shape of the structure (angular motion) for the tip of the arm to reach any particular point in given 3-dimensional hemisphere. The reduced-order dynamic model was used in controlling the shape of the structure. Figure 7.6 shows the initial configuration of the structure with the tip of the arm pointing along the length of the arm. In this example, we aim to move the tip to the arm to the desired location corresponding to the configuration shown in Fig. 7.7.

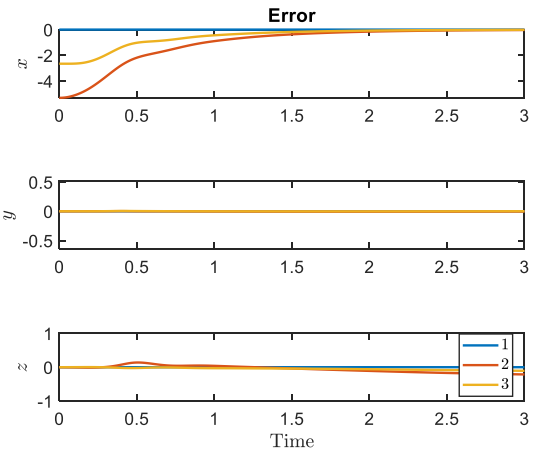

(a) Nodes - (n_1, n_2 and n_3)

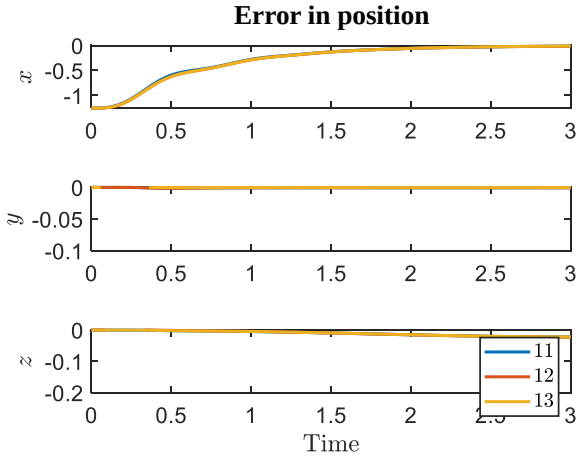

(b) Nodes - (n_{11}, n_{12} and n_{13})

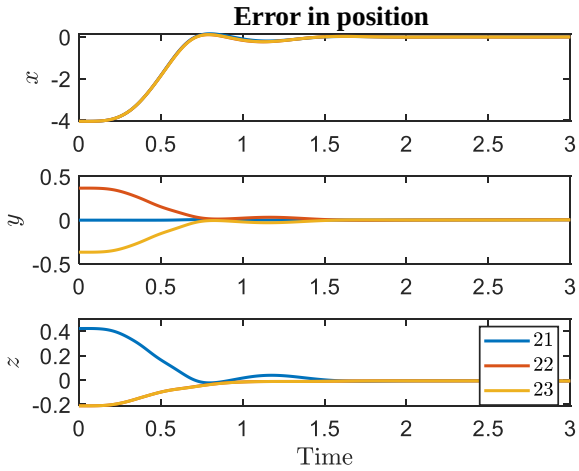

(c) Nodes - (n_{21}, n_{22} and n_{23})

Figure 7.3: Plot for error in node-positions for the extension of tensegrity T_2D_1 structure.

It is relatively difficult to reach the desired position for the tip of the arm without specifying the position of the other nodes in the structure. Therefore, to perform this simulation, the node positions of the final configuration was first calculated based on the kinematic analysis. Figure 7.8a shows the plots for the n_1, n_2 and n_3. Notice that for this simulation, both the x coordinate and y coordinate change (refer Fig. 7.7) and reach a steady state value in around 5 seconds. Small disturbances are observed in z direction also as the arm moves to the desired position. Fig. 7.8b and Fig. 7.8c show the similar plots depicting the errors in the node position for nodes errors in the

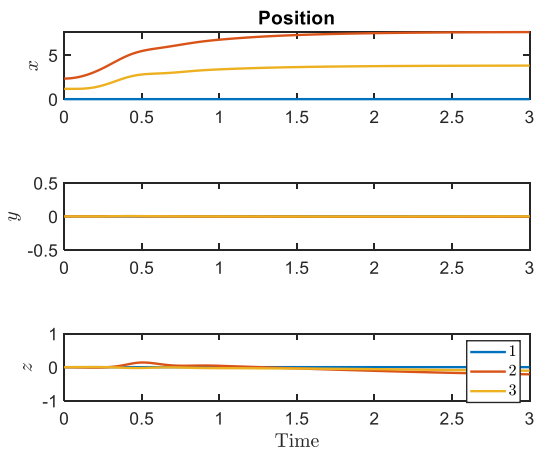

(a) Nodes - (n_1, n_2 and n_3)

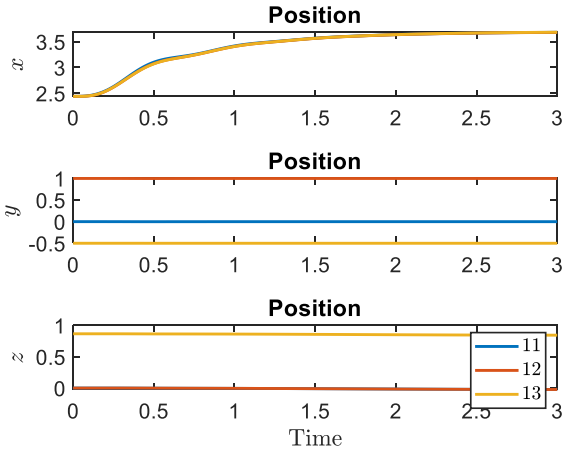

(b) Nodes - (n_{11}, n_{12} and n_{13})

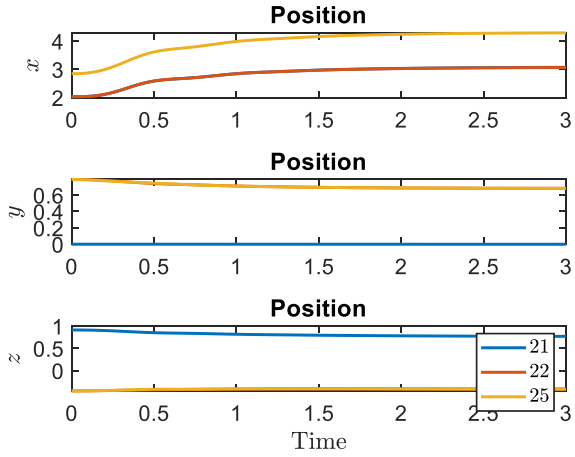

(c) Nodes - (n_{21}, n_{22} and n_{25})

Figure 7.4: Node-position trajectories for the extension of tensegrity T_2D_1 structure.

node position for nodes (n_{11}, n_{12} and n_{13}) and nodes (n_{21}, n_{22} and n_{23}), respectively.

The following plots show the node position trajectories for different nodes during the movement of the tip of the robotic arm to reach a given desired position in the 3-dimensional space. The node position trajectories for nodes n_1, n_2 and n_3 are shown in Fig. 7.9a. Notice the change in position of all the three coordinates to meet the requirement of reaching the desired configuration. The similar changes in the node position plots for nodes (n_{11}, n_{12} and n_{13}) and nodes (n_{21}, n_{22} and n_{25}) are shown in Fig. 7.9b and Fig. 7.9c, respectively.

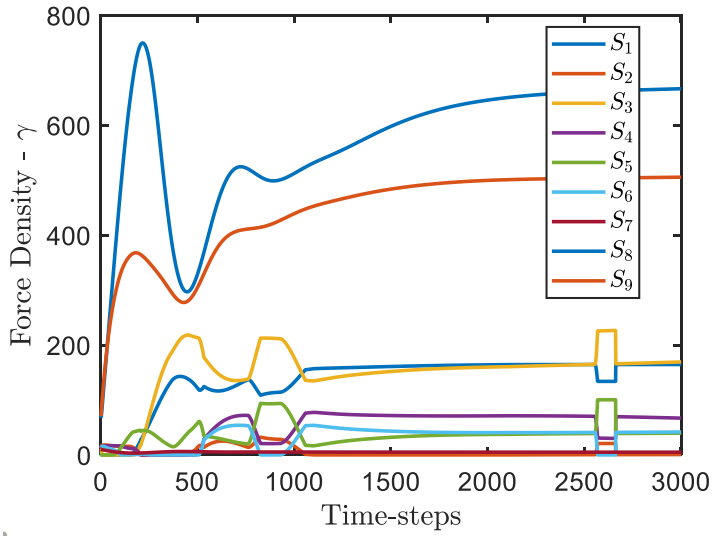

Figure 7.5: Trajectories for force-densities in the strings for the extension of tensegrity T_2D_1 structure.

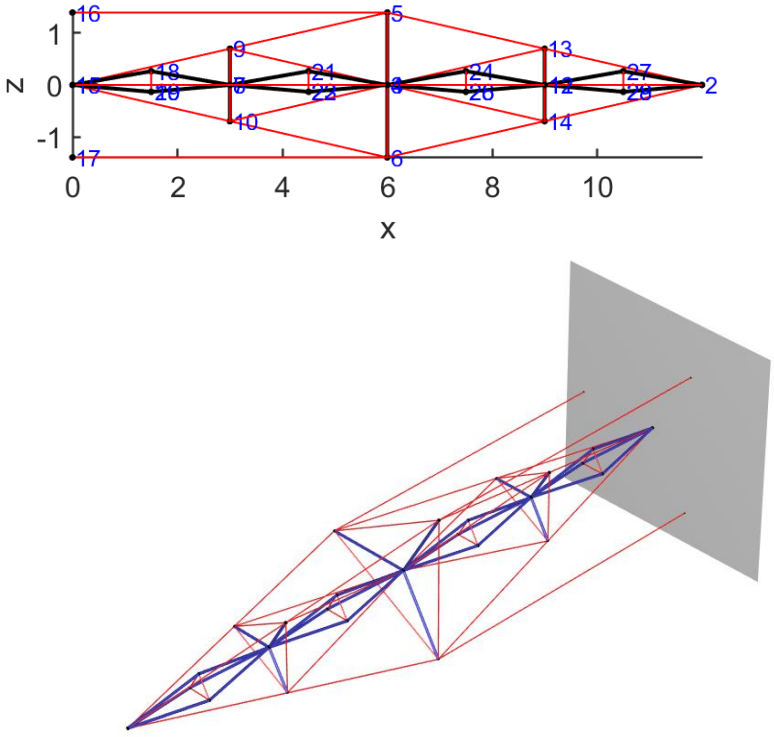

Figure 7.6: Initial configuration of tensegrity T_2D_1 structure for angular rotation.

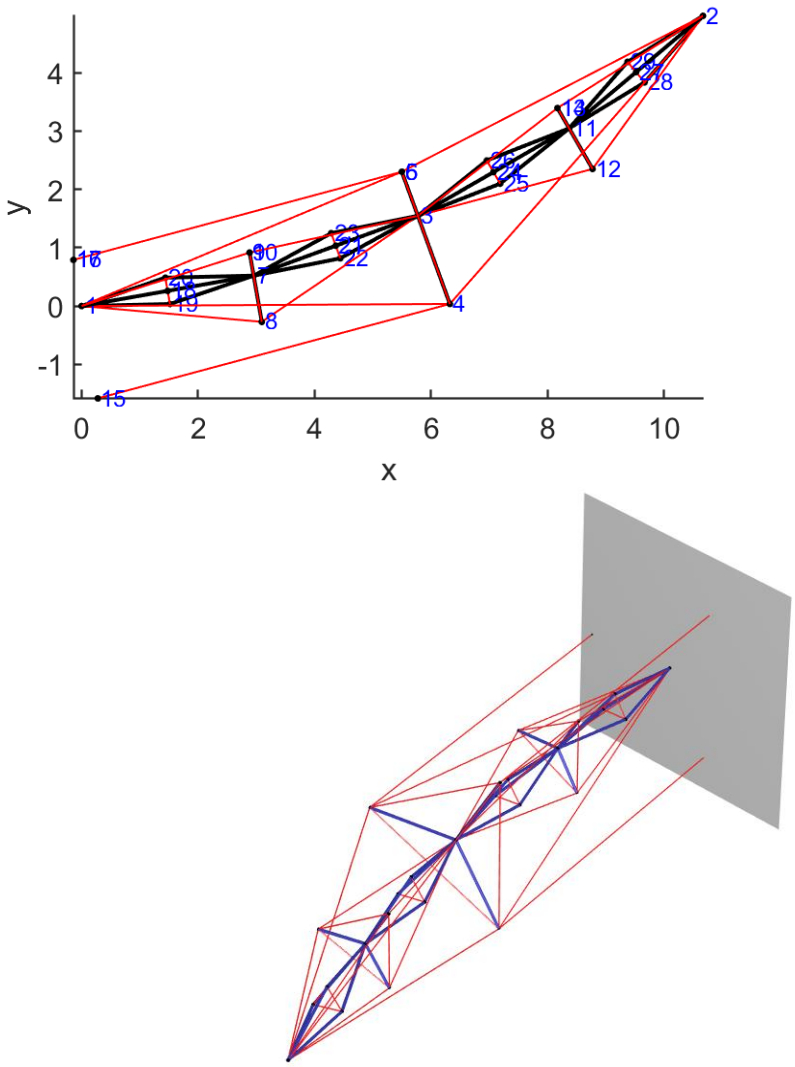

Figure 7.7: Final configuration of tensegrity T_2D_1 structure for angular rotation.

Finally, Fig. 7.10 shows the control inputs required to move the tip of the tensegrity robotic T_2D_1 arm structure. The real physical control for the tensegrity structure is the rest length of the strings. However, the control algorithm developed in this chapter calculates the force density in the strings. The figure shows the trajectories for some of the strings in the process. The rest of the strings follow the same trend due to the symmetry of the structure.

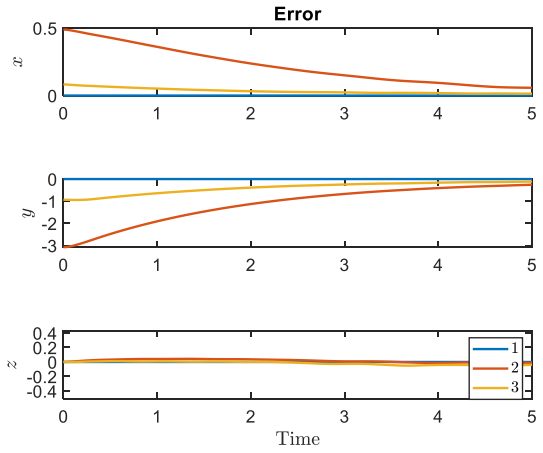

(a) Nodes - (n_1, n_2 and n_3)

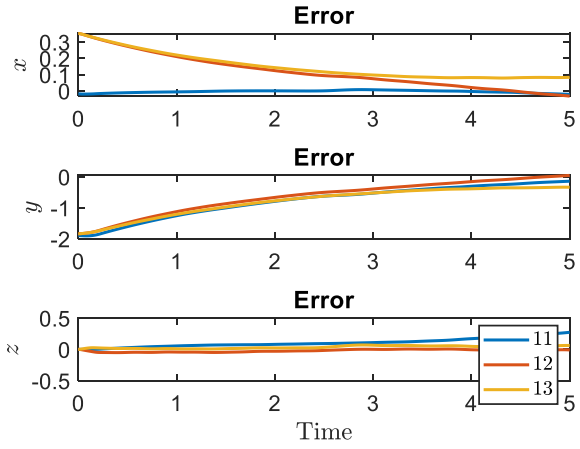

(b) Nodes - (n_{11}, n_{12} and n_{13})

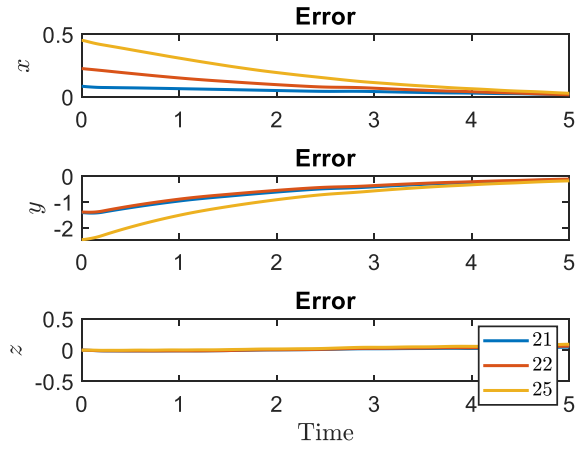

(c) Nodes - (n_{21}, n_{22} and n_{23})

Figure 7.8: Plot for error in node-position for the angular rotation of tensegrity T_2D_1 structure.

7.4.3 Rotation of the Arm using Gyroscopic System

With the normal tensegrity systems, we cannot rotate the robotic arm around its axis (along the length of the arm). In other words, the last section of the robotic arm which is a D-bar, cannot be rotated about its axis (the line connecting two ends) by simply controlling the rest lengths of the string. However, we can achieve this rotation using gyroscopic tensegrity systems, which is needed in order to hold something to the right orientation for an arm. The gyroscopic wheels in this robotic system are needed only for the last D-bar section of the arm. In this simulation result,

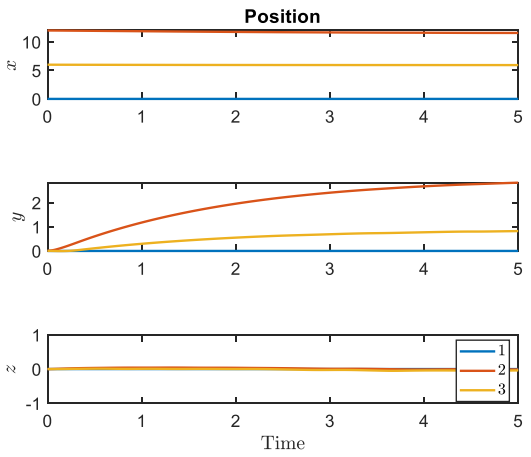

(a) Nodes - (n_1, n_2 and n_3)

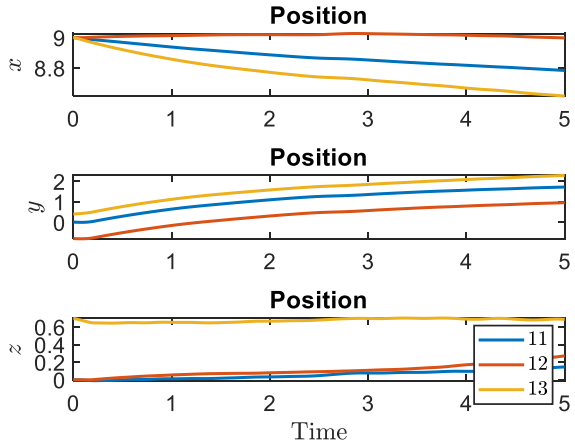

(b) Nodes - (n_{11}, n_{12} and n_{13})

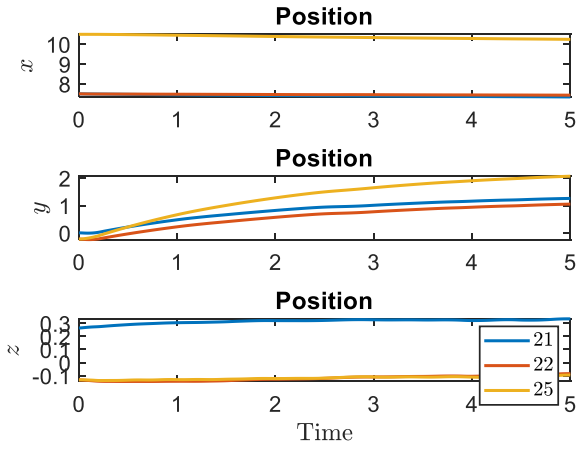

(c) Nodes - (n_{21}, n_{22} and n_{23})

Figure 7.9: Node-position trajectories for the angular rotation of tensegrity T_2D_1 structure.

the rotation for a D-bar structure is shown to achieve the desired orientation. The objective here is to rotate the D-bar structure from the initial configuration to the final configuration, as shown in Fig. 7.11. Notice the nodes n_3, n_4, and n_5 in both configurations to see the different orientation of the D-bar section of the robotic arm.

Figure 7.12 shows the plots for error in node-position in the orientation control of the gyroscopic tensegrity D-bar structure. The error in the figure reaches a steady-state value of zero in around 2.5 seconds for all the three axes. Notice that the x axis is shown to have no initial and

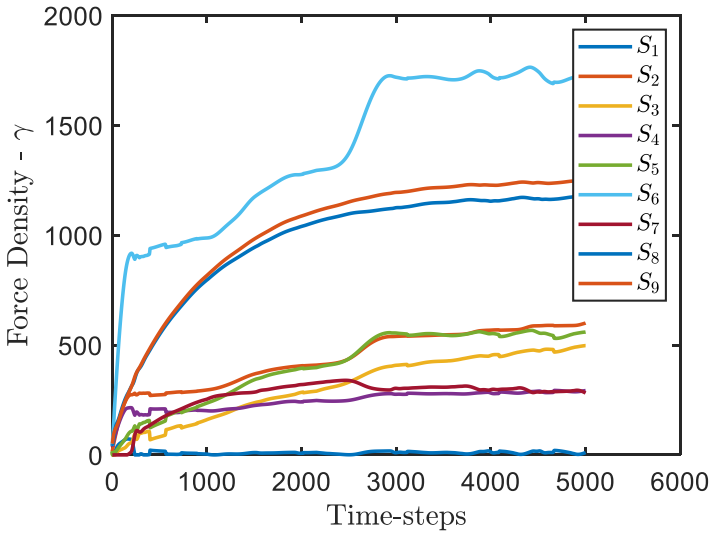

Figure 7.10: Trajectories for force-densities in the strings for the angular rotation of tensegrity T_2D_1 structure.

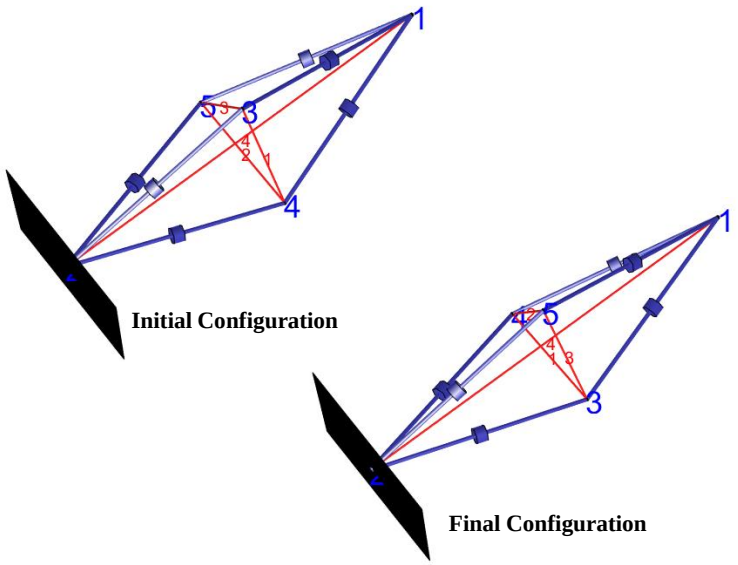

Figure 7.11: Initial and final configuration of the gyroscopic tensegrity D-bar structure.

final error, it is because the matrix L in the formulation was chosen to control only y and z axis:

$$L = \begin{bmatrix} 0 & 1 & 0 \\ 0 & 0 & 1 \end{bmatrix}. \tag{7.83}$$

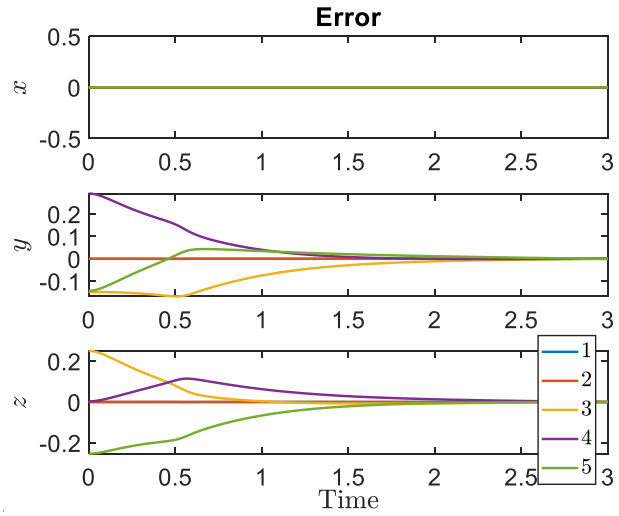

Figure 7.12: Plot for error in node-position in the orientation control of gyroscopic tensegrity D-bar structure.

Figure. 7.13a shows the node position trajectories in controlling the orientation of the gyroscopic tensegrity D-bar structure. The plots corresponding to y and z axis show the movement for the rotation as the values change from the initial configuration to the final configuration. The node velocity trajectories in the orientation control of gyroscopic D-bar are shown in Fig. 7.13b. The velocity for all the nodes reaches the steady-state value of zero depicting that the structure has reached the desired final configuration and will stay there.

The control inputs (force densities in the string) required to rotate the gyroscopic D-bar are shown in Fig. 7.14. The force densities for the first three strings (S_1, S_2, and S_3) which are part of the D-bar triangle, follow the same trend due to the symmetry of the structure and reach a steady-state value along with the last string S_4. Notice that only these four strings are needed in rotating the entire tensegrity T_2D_1 robotic arm about its axis as the last D-bar is connected by a ball joint structure.

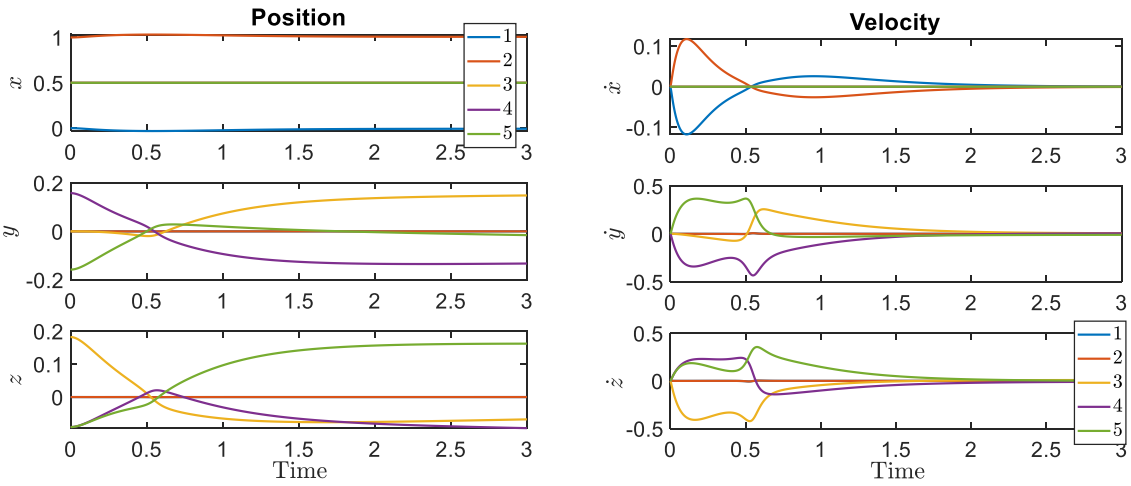

(a) Position trajectories (b) Velocity trajectories

Figure 7.13: Trajectories in controlling the orientation of gyroscopic tensegrity D-bar structure.

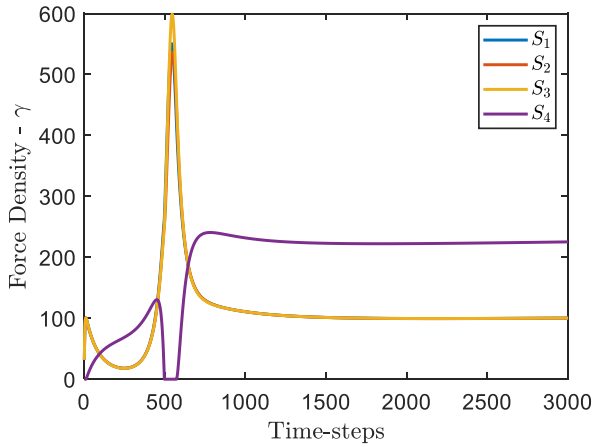

Figure 7.14: Trajectories for force-densities in the strings in the orientation control of gyroscopic tensegrity D-bar structure.

7.5 Vectorized Equations for Tensegrity Dynamics

Let us write the second-order matrix differential equation describing dynamics of any tensegrity structure in the presence of some disturbance w as:

$$\ddot{N}M_s + NK_s = W_T + w, \tag{7.84}$$

where matrices M and K are defined as:

$$M_s = \begin{bmatrix} C_{nb}^{\mathsf{T}}(C_b^{\mathsf{T}}\hat{J}C_b + C_r^{\mathsf{T}}\hat{m}_b C_r) & C_{ns}^{\mathsf{T}}\hat{m}_s \end{bmatrix}, \tag{7.85}$$

$$K_s = \begin{bmatrix} C_s^{\mathsf{T}}\hat{\gamma}C_{sb} - C_{nb}^{\mathsf{T}}C_b^{\mathsf{T}}\hat{\lambda}C_b & C_s^{\mathsf{T}}\hat{\gamma}C_{ss} \end{bmatrix}. \tag{7.86}$$

Taking the i^{th} row of Eq. (7.84):

$$e_i^{\mathsf{T}}\ddot{N}M_s + e_i^{\mathsf{T}}NK_s = e_i^{\mathsf{T}}W_T + e_i^{\mathsf{T}}w \;\text{ for }\; i = 1, 2, 3 \;\;, \tag{7.87}$$

and writing the equation for $i = 1$, we get:

$$\ddot{x}^{\mathsf{T}}M_s + x^{\mathsf{T}}K_s = e_1^{\mathsf{T}}W_T + e_1^{\mathsf{T}}w, \tag{7.88}$$

which after taking the transpose becomes:

$$M_s\ddot{x} + K_s x = W_T^{\mathsf{T}}e_1 + w^{\mathsf{T}}e_1, \tag{7.89}$$

and after stacking all the three equations gives:

$$\begin{bmatrix} M_s & 0 & 0 \\ 0 & M_s & 0 \\ 0 & 0 & M_s \end{bmatrix}\ddot{n} + \begin{bmatrix} K_s & 0 & 0 \\ 0 & K_s & 0 \\ 0 & 0 & K_s \end{bmatrix} n = \begin{bmatrix} W_T^{\mathsf{T}}e_1 \\ W_T^{\mathsf{T}}e_2 \\ W_T^{\mathsf{T}}e_3 \end{bmatrix} + \begin{bmatrix} w^{\mathsf{T}}e_1 \\ w^{\mathsf{T}}e_2 \\ w^{\mathsf{T}}e_3 \end{bmatrix}, \tag{7.90}$$

where $n = [n_{1x}\ n_{2x} \cdots n_{Nx}\ n_{1y}\ n_{2y} \cdots n_{Ny}\ n_{1z}\ n_{2z} \cdots n_{Nz}]^{\mathsf{T}}$. This can also be written using the kronecker product ($\otimes$) as:

$$(I_3 \otimes M_s)\ddot{n} + (I_3 \otimes K_s)n = \mathcal{W} + w_{vec}, \tag{7.91}$$

and can finally be written in the second-order vector differential equation as:

$$\mathcal{M}\ddot{n} + \mathcal{K}n = \mathcal{W} + w_{vec}, \tag{7.92}$$

where $\mathcal{W} = [e_1^\mathsf{T} W \; e_2^\mathsf{T} W \; e_3^\mathsf{T} W]^\mathsf{T}$, $\mathcal{M} = (I_3 \otimes M)$ and $\mathcal{K} = (I_3 \otimes K)$.

The above equation is in vector form and we add linear constraints of the form:

$$An = d \tag{7.93}$$

where $A \in \mathbb{R}^{N_c \times 3n}$ and N_c represents the number of constraints. The linear constraints will restrict the motion in certain directions and will add some constraint forces in the dynamics. Let us define the constraints forces as f_c which satisfies $f_c^\mathsf{T} \delta n = 0$ for any arbitrary displacement (δn) because of no virtual work condition.

$$f_c^\mathsf{T} \delta n = 0 \tag{7.94}$$

$$A\delta n = 0 \tag{7.95}$$

$$\begin{bmatrix} f_c^\mathsf{T} \\ A \end{bmatrix} \delta n = 0 \tag{7.96}$$

The above equation should be satisfied for arbitrary displacement (δn). This will be true if the coefficient matrix will have rank deficiency. Hence, we can write

$$f_c = A^\mathsf{T} \omega \tag{7.97}$$

where $\omega \in \mathbb{R}^{N_c \times 1}$ represents the vector containing Lagrange multipliers. Adding this constraint force to our dynamics, we get

$$\mathcal{M}\ddot{n} + \mathcal{K}n = \mathcal{W} + w_{vec} + A^\mathsf{T} \omega. \tag{7.98}$$

We divide $A = [A_1\ A_2\ A_3]$, where $A_1, A_2, A_3 \in \mathbb{R}^{N_c \times n}$ then

$$\hat{\lambda} = -\hat{J}\hat{l}^{-2}\lfloor \dot{B}^{\mathsf{T}}\dot{B}\rfloor - \frac{1}{2}\hat{l}^{-2}\lfloor B^{\mathsf{T}}(W_T + [A_1^{\mathsf{T}}\omega\ A_2^{\mathsf{T}}\omega\ A_3^{\mathsf{T}}\omega]^{\mathsf{T}} - S\hat{\gamma}C_s)C_{nb}^{\mathsf{T}}C_b^{\mathsf{T}}\rfloor, \tag{7.99}$$

7.5.1 Reduced-order dynamics

Adding the linear constraints into the dynamics will restrict the motion in certain dimensions, thus reducing the order of the dynamics to a span a smaller space. To this end, we use the singular value decomposition (SVD) of matrix A as:

$$A = U\Sigma V^{\mathsf{T}} = U \begin{bmatrix} \Sigma_1 & 0 \end{bmatrix} \begin{bmatrix} V_1^{\mathsf{T}} \\ V_2^{\mathsf{T}} \end{bmatrix} \tag{7.100}$$

where $U \in \mathbb{R}^{N_c \times N_c}$ and $V \in \mathbb{R}^{3n \times 3n}$ are both unitary matrices, $V_1 \in \mathbb{R}^{3n \times N_c}$ and $V_2 \in \mathbb{R}^{3n \times (3n - N_c)}$ are submatrices of U, and $\Sigma_1 \in \mathbb{R}^{N_c \times N_c}$ is a diagonal matrix of positive singular values. By defining

$$\eta = \begin{bmatrix} \eta_1 \\ \eta_2 \end{bmatrix} \triangleq V^{\mathsf{T}}n = \begin{bmatrix} V_1^{\mathsf{T}}n \\ V_2^{\mathsf{T}}n \end{bmatrix} \tag{7.101}$$

the constraint Equation (7.93) can be modified as:

$$An = U\Sigma V^{\mathsf{T}}n = U \begin{bmatrix} \Sigma_1 & 0 \end{bmatrix} \begin{bmatrix} \eta_1 \\ \eta_2 \end{bmatrix} = d, \tag{7.102}$$

which implies:

$$\eta_1 = \Sigma_1^{-1}U^{\mathsf{T}}d, \quad \dot{\eta}_1 = 0, \quad \ddot{\eta}_1 = 0. \tag{7.103}$$

Here, η_1 represents the no-motion space in transformed coordinates. Moreover, η_2 will evolve according to the constrained dynamics in new coordinate system. Using Equations (7.100-7.103),

the dynamics equation (7.98) can be rewritten as:

$$\mathcal{M}VV^{\mathsf{T}}\ddot{n} + \mathcal{K}VV^{\mathsf{T}}n = \mathcal{W} + w_{vec} + A^{\mathsf{T}}\omega \tag{7.104}$$

$$\mathcal{M}V_2\ddot{\eta}_2 + \mathcal{K}V_1\eta_1 + \mathcal{K}V_2\eta_2 = \mathcal{W} + w_{vec} + V_1\Sigma_1U^{\mathsf{T}}\omega \tag{7.105}$$

Pre-multiplying the above equation by a non-singular matrix $[V_2 \;\; \mathcal{M}^{-1}V_1]^{\mathsf{T}}$ will yield two parts, where first part gives the second order differential equation for the reduced dynamics:

$$V_2^{\mathsf{T}}\mathcal{M}V_2\ddot{\eta}_2 + V_2^{\mathsf{T}}\mathcal{K}V_2\eta_2 = V_2^{\mathsf{T}}\mathcal{W} + V_2^{\mathsf{T}}w_{vec} - V_2^{\mathsf{T}}\mathcal{K}V_1\eta_1 \tag{7.106}$$

$$\Rightarrow \mathcal{M}_2\ddot{\eta}_2 + \mathcal{K}_2\eta_2 = \widetilde{\mathcal{W}} + \widetilde{w}_{vec}. \tag{7.107}$$

with $\mathcal{M}_2 = V_2^{\mathsf{T}}\mathcal{M}V_2$ and $\mathcal{K}_2 = V_2^{\mathsf{T}}\mathcal{K}V_2$, and the second part gives an algebraic equation that is used to solve for the Lagrange multiplier:

$$V_1^{\mathsf{T}}\mathcal{M}^{-1}\mathcal{M}V_2\ddot{\eta}_2 + V_1^{\mathsf{T}}\mathcal{M}^{-1}\mathcal{K}V_1\eta_1 + V_1^{\mathsf{T}}\mathcal{M}^{-1}\mathcal{K}V_2\eta_2 \\ = V_1^{\mathsf{T}}\mathcal{M}^{-1}(\mathcal{W} + w_{vec}) + V_1^{\mathsf{T}}\mathcal{M}^{-1}V_1\Sigma_1U^{\mathsf{T}}\omega \tag{7.108}$$

$$V_1^{\mathsf{T}}\mathcal{M}^{-1}\mathcal{K}V_1\eta_1 + V_1^{\mathsf{T}}\mathcal{M}^{-1}\mathcal{K}V_2\eta_2 - V_1^{\mathsf{T}}\mathcal{M}^{-1}V_1\Sigma_1U^{\mathsf{T}}\omega = V_1^{\mathsf{T}}\mathcal{M}^{-1}(\mathcal{W} + w_{vec}) \tag{7.109}$$

$$\Rightarrow V_1^{\mathsf{T}}\mathcal{M}^{-1}\mathcal{K}n - V_1^{\mathsf{T}}\mathcal{M}^{-1}A^{\mathsf{T}}\omega = V_1^{\mathsf{T}}\mathcal{M}^{-1}(\mathcal{W} + w_{vec}). \tag{7.110}$$

Notice that $\mathcal{K}$ is also a function of ω, making it a linear algebra problem, the solution for which is given in Appendix B.3.

7.5.2 Controller for Full-Order Dynamics Model

The error in the position of the nodes which is desired to be zero is defined as:

$$e = \mathcal{L}n - \bar{n}. \tag{7.111}$$

The second-order output equation can be written as:

$$\ddot{e} + \Psi\dot{e} + \Theta e = B_1 w, \tag{7.112}$$

which can be written in state-space form as:

$$\begin{bmatrix} \dot{e} \\ \ddot{e} \end{bmatrix} = \underbrace{\begin{bmatrix} 0 & I \\ -\Theta & -\Psi \end{bmatrix}}_{A_{cl}} \begin{bmatrix} e \\ \dot{e} \end{bmatrix} + \underbrace{\begin{bmatrix} 0 \\ B_1 \end{bmatrix}}_{B_{cl}} w. \tag{7.113}$$

We need to find the controller gain parameters Ψ and Θ, which we write in controller gain matrix G as:

$$G = \begin{bmatrix} -\Theta & -\Psi \end{bmatrix}, \tag{7.114}$$

and decompose the matrix A_{cl} as:

$$\begin{bmatrix} 0 & I \\ -\Theta & -\Psi \end{bmatrix} = \underbrace{\begin{bmatrix} 0 & I \\ 0 & 0 \end{bmatrix}}_{A_p} + \underbrace{\begin{bmatrix} 0 \\ I \end{bmatrix}}_{B_p} \begin{bmatrix} -\Theta & -\Psi \end{bmatrix}, \tag{7.115}$$

which allows us to write the closed-loop dynamics as:

$$\dot{x} = (A_p + B_p G)x + B_{cl} w, \;\; y = Cx. \tag{7.116}$$

Now, Eq. (7.112) is written after substitution from Eq. (7.111) as:

$$\mathcal{L}\ddot{n} + \Psi\mathcal{L}\dot{n} + \Theta(\mathcal{L}n - \bar{n}) = B_1 w, \tag{7.117}$$

which after multiplying Eq. (7.98) from left hand side by $\mathcal{M}^{-1}$ ($\mathcal{M}^{-1}\times$ Eq. (7.98)) and substitution

gives:

$$\mathcal{L}\mathcal{M}^{-1}(\mathcal{W} + A^{\mathsf{T}}\omega + w_{vec} - \mathcal{K}n) + \Psi\mathcal{L}\dot{n} + \Theta(\mathcal{L}n - \bar{n}) = B_1 w_{vec}, \tag{7.118}$$

Let us choose $B_1 = \mathcal{L}\mathcal{M}^{-1}$ (without loss of generality) to write:

$$\mathcal{L}\mathcal{M}^{-1}(\mathcal{W} + A^{\mathsf{T}}\omega - \mathcal{K}n) + \Psi\mathcal{L}\dot{n} + \Theta(\mathcal{L}n - \bar{n}) = 0, \tag{7.119}$$

Let us substitute for $\mathcal{K}$ from Eq. 7.92 to obtain:

$$\mathcal{L}\mathcal{M}^{-1}\left[\left(I_3 \otimes (C_s^{\mathsf{T}}\hat{\gamma}C_s)\right) - \left(I_3 \otimes (C_{nb}^{\mathsf{T}}C_b^{\mathsf{T}}\hat{\lambda}C_bC_{nb})\right)\right] n = \underbrace{\mathcal{L}\mathcal{M}^{-1}(\mathcal{W} + A^{\mathsf{T}}\omega) + \Psi\mathcal{L}\dot{n} + \Theta(\mathcal{L}n - \bar{n})}_{\mathcal{C}}, \tag{7.120}$$

and using the properties of kronecker product, we can further write it as:

$$\mathcal{L}\mathcal{M}^{-1}(I_3 \otimes C_s^{\mathsf{T}})(I_3 \otimes \hat{\gamma})(I_3 \otimes C_s)n \;=\; \mathcal{L}\mathcal{M}^{-1}(I_3 \otimes C_{nb}^{\mathsf{T}}C_b^{\mathsf{T}})(I_3 \otimes \hat{\lambda})(I_3 \otimes C_bC_{nb})n + \mathcal{C}. \tag{7.121}$$

Now, recognizing that the term $(I_3 \otimes C_s)n$ is a vector and $(I_3 \otimes \hat{\gamma})$ is a diagonal matrix, we use the property $\hat{x}y = x\hat{y}$ to get:

$$\mathcal{L}\mathcal{M}^{-1}(I_3 \otimes C_s^{\mathsf{T}})\widehat{((I_3 \otimes C_s)n)}(\mathbb{1} \otimes \hat{\gamma}) = \mathcal{L}\mathcal{M}^{-1}(I_3 \otimes C_{nb}^{\mathsf{T}}C_b^{\mathsf{T}})\widehat{((I_3 \otimes C_bC_{nb})n)}(\mathbb{1} \otimes \hat{\lambda}) + \mathcal{C}, \tag{7.122}$$

where $\mathbb{1} \triangleq [1\ 1\ 1]^{\mathsf{T}}$ and can again be written as:

$$\underbrace{\left[\mathcal{L}\mathcal{M}^{-1}(I_3 \otimes C_s^{\mathsf{T}})((I_3 \otimes C_s)n)(\mathbb{1} \otimes I_\alpha)\right]}_{\mathbb{A}} \gamma$$

$$= \underbrace{\left[\mathcal{L}\mathcal{M}^{-1}(I_3 \otimes C_{nb}^{\mathsf{T}} C_b^{\mathsf{T}})((I_3 \otimes C_b C_{nb})n)(\mathbb{1} \otimes I_\beta)\right]}_{\mathbb{B}} \lambda + \mathcal{C}. \quad (7.123)$$

Let us use Eq. (7.5) to write the above mentioned equation as:

$$\mathbb{A}\gamma = \mathbb{B}(\Lambda\gamma + \tau) + \mathcal{C}, \quad (7.124)$$

which can be re-written after combining terms for force density γ to generate a linear equation as:

$$(\mathbb{A} - \mathbb{B}\Lambda)\gamma = \mathbb{B}\tau + \mathcal{C}. \quad (7.125)$$

7.5.3 Controller for Reduced-Order Dynamics Model

The error in the position of the nodes which is desired to be zero is defined as:

$$e = \mathcal{L}n - \bar{n} = \mathcal{L}(V_1\eta_1 + V_2\eta_2) - \bar{n}. \quad (7.126)$$

The second-order output equation can be written as:

$$\ddot{e} + \Psi\dot{e} + \Theta e = B_1 w, \quad (7.127)$$

which is written after substitution from Eq. (7.126) as:

$$\mathcal{L}V_2\ddot{\eta_2} + \Psi\mathcal{L}V_2\dot{\eta_2} + \Theta(\mathcal{L}V_1\eta_1 + \mathcal{L}V_2\eta_2 - \bar{n}) = B_1 w, \tag{7.128}$$

where $\dot{\eta_1} = \ddot{\eta_1} = 0$ was used from the dynamics model formulation and which after multiplying Eq. (7.107) from left hand side by $\mathcal{M}_2^{-1}$ ($\mathcal{M}_2^{-1}\times$ Eq. (7.107)) and substitution gives:

$$\mathcal{L}V_2\mathcal{M}_2^{-1}(\widetilde{\mathcal{W}} + \widetilde{w}_{vec} - \mathcal{K}_2\eta_2) + \Psi\mathcal{L}V_2\dot{\eta_2} + \Theta(\mathcal{L}V_1\eta_1 + \mathcal{L}V_2\eta_2 - \bar{n}) = B_1 w_{vec}, \tag{7.129}$$

Let us choose $B_1 = \mathcal{L}V_2\mathcal{M}_2^{-1}V_2^{\mathsf{T}}$ (without loss of generality) to write:

$$\mathcal{L}V_2\mathcal{M}_2^{-1}(\widetilde{\mathcal{W}} - \mathcal{K}_2\eta_2) + \Psi\mathcal{L}V_2\dot{\eta_2} + \Theta(\mathcal{L}V_1\eta_1 + \mathcal{L}V_2\eta_2 - \bar{n}) = 0, \tag{7.130}$$

$$\mathcal{L}V_2\mathcal{M}_2^{-1}(V_2^{\mathsf{T}}\mathcal{W} - V_2^{\mathsf{T}}\mathcal{K}V_1\eta_1 - \mathcal{K}_2\eta_2) + \Psi\mathcal{L}V_2\dot{\eta_2} + \Theta(\mathcal{L}V_1\eta_1 + \mathcal{L}V_2\eta_2 - \bar{n}) = 0, \tag{7.131}$$

Let us substitute for $\mathcal{K}_2$ from Eq. 7.107 to obtain:

$$\mathcal{L}\underbrace{V_2\mathcal{M}_2^{-1}V_2^{\mathsf{T}}}_{\mathcal{M}_{sn}}\Big[\big(I_3 \otimes (C_s^{\mathsf{T}}\hat{\gamma}C_s)\big) - \Big(I_3 \otimes (C_{nb}^{\mathsf{T}}C_b^{\mathsf{T}}\hat{\lambda}C_bC_{nb})\Big)\Big](V_2\eta_2 + V_1\eta_1) =$$

$$\underbrace{\mathcal{L}V_2\mathcal{M}_2^{-1}V_2^{\mathsf{T}}\mathcal{W} + \Psi\mathcal{L}V_2\dot{\eta_2} + \Theta(\mathcal{L}V_1\eta_1 + \mathcal{L}V_2\eta_2 - \bar{n})}_{\mathcal{C}}, \tag{7.132}$$

and using the properties of kronecker product, we can further write it as:

$$\mathcal{L}\mathcal{M}_{sn}(I_3 \otimes C_s^{\mathsf{T}})(I_3 \otimes \hat{\gamma})(I_3 \otimes C_s)n \;=\; \mathcal{L}\mathcal{M}_{sn}(I_3 \otimes C_{nb}^{\mathsf{T}}C_b^{\mathsf{T}})(I_3 \otimes \hat{\lambda})(I_3 \otimes C_bC_{nb})n + \mathcal{C}. \tag{7.133}$$

Now, recognizing that the term $(I_3 \otimes C_s)n$ is a vector and $(I_3 \otimes \hat{\gamma})$ is a diagonal matrix, we use

the property $\hat{x}y = x\hat{y}$ to get:

$$\widehat{\mathcal{LM}_{sn}(I_3 \otimes C_s^{\mathsf{T}})((I_3 \otimes C_s)n)(\mathbb{1} \otimes \hat{\gamma})} = \widehat{\mathcal{LM}_{sn}(I_3 \otimes C_{nb}^{\mathsf{T}} C_b^{\mathsf{T}})((I_3 \otimes C_b C_{nb})n)(\mathbb{1} \otimes \hat{\lambda})} + \mathcal{C}, \tag{7.134}$$

and similar procedure can be followed as:

$$\underbrace{\left[\widehat{\mathcal{LM}_{sn}(I_3 \otimes C_s^{\mathsf{T}})((I_3 \otimes C_s)n)(\mathbb{1} \otimes I_\alpha)}\right]}_{\mathbb{A}} \gamma$$

$$= \underbrace{\left[\widehat{\mathcal{LM}_{sn}(I_3 \otimes C_{nb}^{\mathsf{T}} C_b^{\mathsf{T}})((I_3 \otimes C_b C_{nb})n)(\mathbb{1} \otimes I_\beta)}\right]}_{\mathbb{B}} \lambda + \mathcal{C}. \tag{7.135}$$

Let us use Eq. (7.5) to write the above mentioned equation as:

$$\mathbb{A}\gamma = \mathbb{B}(\Lambda\gamma + \tau) + \mathcal{C}, \tag{7.136}$$

which can be re-written after combining terms for force density γ to generate a linear equation as:

$$(\mathbb{A} - \mathbb{B}\Lambda)\gamma = \mathbb{B}\tau + \mathcal{C}. \tag{7.137}$$

7.6 Different bounds on errors

In the previous sections, the gains for the second-order differential equations were chosen to stabilize the output differential equation i.e. to derive the errors to zero. However, no performance

criteria was discussed in calculating the gains Θ and Ψ. This section solves this issue by formulating five different problems for bounding errors using the LMI framework. The gains for these five different problems are calculated using the semi-definite convex programming problem. A MatLab based CVX toolbox is used for numerical implementation.

The example for all the different bounds will have the simulation results discussed on the same tensegrity T_1D_1 robotic arm with the initial configuration shown in Fig. 7.15.

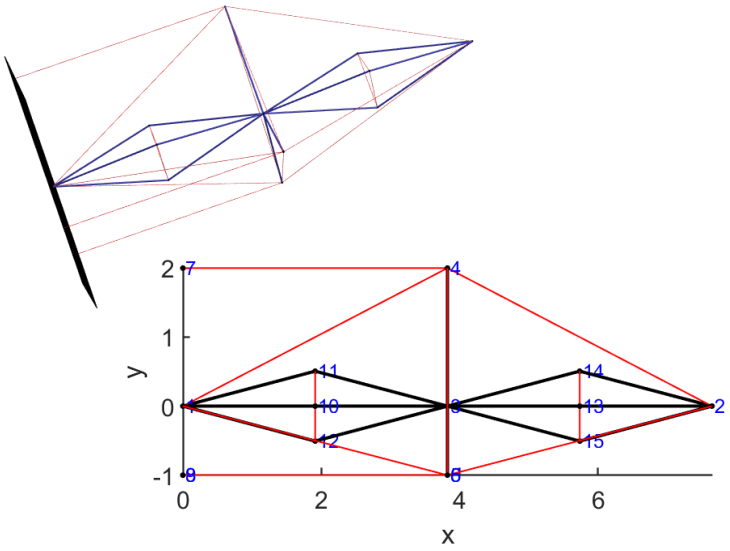

Figure 7.15: Initial configuration of the tensegrity T_1D_1 robotic arm.

7.6.1 Bound on $\mathcal{L}_\infty$ norm of error or Generalized $\mathcal{H}_2$ Problem

The peak value of a variable in the time domain is defined as $\mathcal{L}_\infty$ norm of the variable, i.e. $\|y\|^2_{\mathcal{L}_\infty} = \sup[y(t)^\mathsf{T} y(t)]$. The following result provides a bound on peak value such that $\|y\|_{\mathcal{L}_\infty} < \epsilon$, meaning that the peak value of $[y(t)^\mathsf{T} y(t)]$ is less than ϵ^2 in the presence of finite energy disturbance [86]. This problem can be solved as a Energy to peak gain - Γ_{ep} [85] or generalized

$\mathcal{H}_2$ problem [87].

$$\Gamma_{ep} \triangleq \sup_{\|w\|_{\mathcal{L}_2} \leq 1} \|y\|_{\mathcal{L}_\infty}, \tag{7.138}$$

$$\Gamma_{ep} = \inf_{Q} \|CQC^{\mathsf{T}}\|^{1/2} : A_{cl}Q + QA_{cl}^{\mathsf{T}} + B_{cl}B_{cl}^{\mathsf{T}} < 0,\ Q > 0. \tag{7.139}$$

Lemma 7.6.1. *The controller gain matrix G (c.f. Eq. (7.114)) for system given in Eq. (7.116), which provides a $\mathcal{L}_\infty$ bound on the error in the desired position can be solved as:*

$$\min \epsilon, \begin{bmatrix} \epsilon I & CQ \\ QC^{\mathsf{T}} & Q \end{bmatrix} > 0, \tag{7.140}$$

$$\begin{bmatrix} sym(A_pQ + B_pR) & B_{cl} \\ B_{cl}^{\mathsf{T}} & -I \end{bmatrix} < 0, \tag{7.141}$$

where $G = RQ^{-1}$.

Proof: The gain matrix G can calculated using Eq. (7.139) which can substituted with Eq. (7.116) to give:

$$\min \epsilon,\ \ \epsilon I - CQC^{\mathsf{T}} > 0,\ \ (A_p + B_pG)Q + Q(A_p + B_pG)^{\mathsf{T}} + B_{cl}B_{cl}^{\mathsf{T}} < 0, \tag{7.142}$$

which can be written as the following after using the Schur's complement with $Q > 0$ as:

$$\min \epsilon,\ \ \begin{bmatrix} \epsilon I & CQ \\ QC^{\mathsf{T}} & Q \end{bmatrix} > 0,\ \ \begin{bmatrix} sym(A_pQ + B_pGQ) & B_{cl} \\ B_{cl}^{\mathsf{T}} & -I \end{bmatrix} < 0, \tag{7.143}$$

which can be substituted as $R = GQ$ to obtain:

$$\begin{bmatrix} sym(A_pQ + B_pR) & B_{cl} \\ B_{cl}^{\mathsf{T}} & -I \end{bmatrix} < 0. \tag{7.144}$$

□

The first plot from Fig. 7.16 shows the norm of position error for the open-loop simulation for a finite energy force disturbance given at all node locations. The plot shows a periodic motion for the position error from the initial nominal configuration. The second plot in Fig. 7.16 shows the norm in position error for the closed-loop system with gains value $\Theta = 30I$ and $\Psi = 20I$. The chosen stable gains derive the system to zero but with a large value of peak value of error. The last plot in Fig. 7.16 shows the closed-loop performance with the gains calculated using the bounded $\mathcal{L}_\infty$ norm or generalized $\mathcal{H}_2$ problem for the depicted robotic arm. Notice that the peak value of the error has been brought down considerably using the LMI formulation described earlier. The theoretical value of the gain by solving the LMIs in Lemma 7.6.1 was calculated to be $\Gamma_{ep} = 1.00 \times 10^{-4}$ and the gain calculated using the simulation results was observed to be $\Gamma_{ep} = 6.82 \times 10^{-7}$, which satisfies the requirement. Moreover, the value from the simulation results was considerably smaller as the disturbance values of the output will only match the theoretical results for the worst-case disturbance. Figure 7.17 shows the trajectories for error in node positions for nodes (n_1, n_2, n_3 and n_4) for all the three cases mentioned earlier.

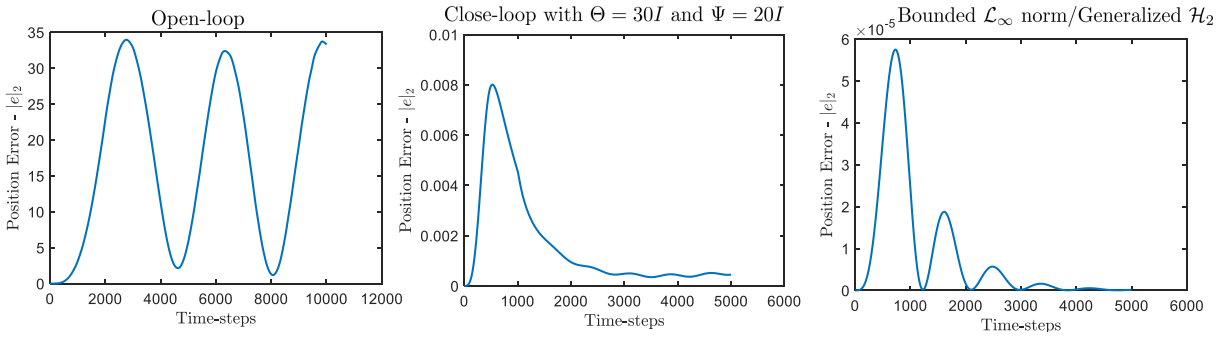

Figure 7.16: Plots of norm in position error for open-loop, closed loop with $\Theta = 30I$ and $\Psi = 20I$, and gains calculated using the bounded $\mathcal{L}_\infty$ norm or Generalized $\mathcal{H}_2$ Problem for the T_1D_1 robotic arm.

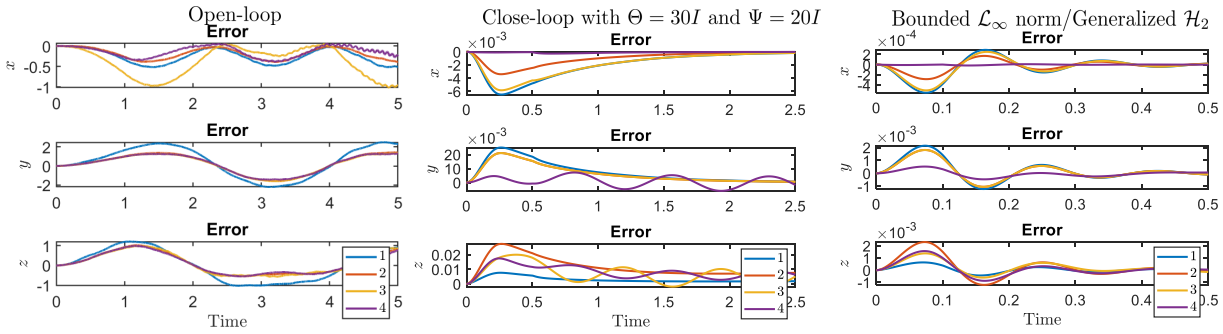

Figure 7.17: Trajectories of node positions (n_1, n_2, n_3 and n_4) for open-loop, closed loop with $\Theta = 30I$ and $\Psi = 20I$, and gains calculated using the bounded $\mathcal{L}_\infty$ norm or Generalized $\mathcal{H}_2$ Problem for the T_1D_1 robotic arm.

7.6.2 Bounded Γ_{ee} or $\mathcal{H}_\infty$ Problem

This subsection provides the result to bound the peak value of the frequency response of the transfer function $T(s) \triangleq C(sI - A_{cl})^{-1}B_{cl}$. The $\mathcal{H}_\infty$ Problem is defined as [88, 89]:

$$\|T\|_{H_\infty} \triangleq \sup_w \|T(jw)\| < \epsilon \tag{7.145}$$

which can also be understood in time domain analysis as the energy-to-energy gain problem [85]:

$$\Gamma_{ee} \triangleq \sup_{\|w\|_{\mathcal{L}_2} \leq 1} \|y\|_{\mathcal{L}_2} < \epsilon. \tag{7.146}$$

Lemma 7.6.2. *The controller gain matrix G (c.f. Eq. (7.114)) for system given in Eq. (7.116), which provides a $\mathcal{H}_\infty$ bound on the error in the desired position can be solved as:*

$$\begin{bmatrix} sym(A_pY + B_pL) & B_{cl} & YC^{\mathsf{T}} \\ B_{cl}^{\mathsf{T}} & -R & 0 \\ CY & 0 & -I \end{bmatrix} < 0,\ Y > 0,\ \ R = \epsilon^2 I, G = LY^{-1}. \tag{7.147}$$

Proof: The $\mathcal{H}_\infty$ problem with given ϵ and for a positive definite matrix $P > 0$ can be solved with

the following matrix inequality [87, 90]:

$$PA_{cl} + A_{cl}^{\mathsf{T}}P + PB_{cl}R^{-1}(PB_{cl})^{\mathsf{T}} + C^{\mathsf{T}}C < 0,\ P > 0,\ R = \epsilon^2 I > 0, \tag{7.148}$$

which can be written as:

$$A_{cl}Y + YA_{cl}^{\mathsf{T}} + B_{cl}R^{-1}B_{cl}^{\mathsf{T}} + YC^{\mathsf{T}}CY < 0,\ Y = P^{-1} > 0,\ R = \epsilon^2 I > 0, \tag{7.149}$$

which can substituted with Eq. (7.116) to give:

$$(A_pY + B_pGY) + (\cdot)^{\mathsf{T}} + \begin{bmatrix} B_{cl} & YC^{\mathsf{T}} \end{bmatrix} \begin{bmatrix} R^{-1} & \\ & I \end{bmatrix} \begin{bmatrix} B_{cl}^{\mathsf{T}} \\ CY \end{bmatrix} < 0, Y > 0, \tag{7.150}$$

and after using the Schur's complement with $R > 0$ and $L = GY$ can be written as:

$$\begin{bmatrix} sym(A_pY + B_pL) & B_{cl} & YC^{\mathsf{T}} \\ B_{cl}^{\mathsf{T}} & -R & 0 \\ CY & 0 & -I \end{bmatrix} < 0,\ Y > 0. \tag{7.151}$$

□

The following simulation results are generated using the same energy bounded disturbance used in the analysis of bounded $\mathcal{L}_\infty$ norm. The first two plots of Fig. 7.18 (same as Fig. 7.16) shows the norm of position error for the open-loop simulation for the closed loop system with gains value $\Theta = 30I$ and $\Psi = 20I$. The last plot in Fig. 7.18 shows the closed-loop performance with the gains calculated using the bounded Γ_{ee} or $\mathcal{H}_\infty$ problem. The theoretical value of the energy-to-energy gain was obtained to be $\Gamma_{ee} = 1.27 \times 10^{-5}$ by solving the LMIs in Lemma 7.6.2 and the gain in energy from disturbance to error for the simulation was observed to be $\Gamma_{ee} = 5.14 \times 10^{-9}$, which satisfies the requirement. Just as in the previous case, there would be some worst-case disturbance for this nonlinear system that would cause the error due to disturbance to meet the theoretical value.

The similar trend can be observed from Fig. 7.19, which shows the trajectories for error in node positions (n_1, n_2, n_3 and n_4) for all the three cases mentioned earlier.

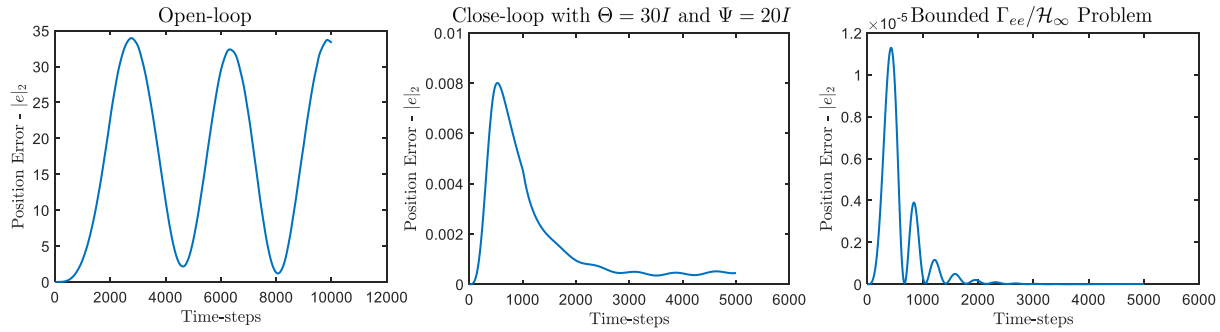

Figure 7.18: Plots of norm in position error for open-loop, closed loop with $\Theta = 30I$ and $\Psi = 20I$, and gains calculated using the bounded Γ_{ee} or $\mathcal{H}_\infty$ problem for the T_1D_1 robotic arm.

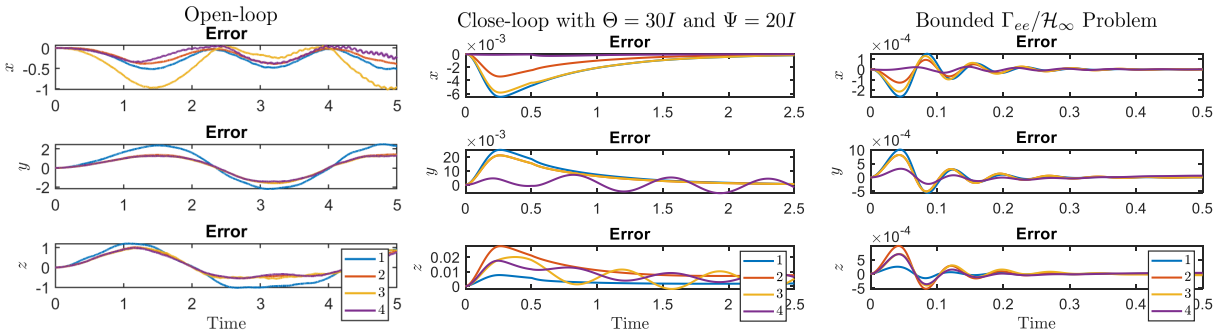

Figure 7.19: Trajectories of node positions (n_1, n_2, n_3 and n_4) for open-loop, closed loop with $\Theta = 30I$ and $\Psi = 20I$, and gains calculated using the bounded Γ_{ee} or $\mathcal{H}_\infty$ problem for the T_1D_1 robotic arm.

7.6.3 Bounded Γ_{ie} or LQR Problem

We define the linear quadratic regulator (LQR) problem to provide a performance bound $\epsilon > 0$ on the integral squared output such that $\|y\|_{\mathcal{L}_2} < \epsilon$ for any vector w_0 such that $w_0^{\mathsf{T}} w_0 \leq 1$, and $x_0 = 0$. The disturbance w is the impulsive disturbance $w(t) = w_0\delta(t)$. This can also be defined

as the peak disturbance to energy gain ($\|y\|_{\mathcal{L}_2}$) for the system [85].

$$\Gamma_{ie} \triangleq \sup_{w_0\delta(t)\leq 1} \|y\|_{\mathcal{L}_2}, \tag{7.152}$$

$$\Gamma_{ie} = \inf_{P} \|B_{cl}^{\mathsf{T}} P B_{cl}\|^{1/2} : PA_{cl} + A_{cl}^{\mathsf{T}} P + C^{\mathsf{T}} C < 0,\ P > 0. \tag{7.153}$$

Lemma 7.6.3. *The controller gain matrix G (c.f. Eq. (7.114)) for system given in Eq. (7.116), which provides a bound on the error $\Gamma_{ie} < \epsilon$ from the desired position can be solved as:*

$$\min \epsilon,\ \begin{bmatrix} \epsilon I & B_{cl}^{\mathsf{T}} \\ B_{cl} & Y \end{bmatrix} > 0,\ \begin{bmatrix} sym(A_p Y + B_p R) & Y C^{\mathsf{T}} \\ CY & -I \end{bmatrix} < 0, \tag{7.154}$$

where $G = RY^{-1}$.

Proof: The gain matrix G can calculated using Eq. (7.153) which can substituted with Eq. (7.116) to give:

$$\min \epsilon,\ \ \epsilon I - B_{cl}^{\mathsf{T}} P B_{cl} > 0,\ \ P(A_p + B_p G) + (A_p + B_p G)^{\mathsf{T}} P + C^{\mathsf{T}} C < 0, \tag{7.155}$$

and the last equation on both sides can be multiplied by $P^{-1} > 0$ to obtain:

$$\min \epsilon,\ \ \epsilon I - B_{cl}^{\mathsf{T}} P B_{cl} > 0,\ \ (A_p + B_p G)P^{-1} + P^{-1}(A_p + B_p G)^{\mathsf{T}} + P^{-1} C^{\mathsf{T}} C P^{-1} < 0, \tag{7.156}$$

which can be written as the following after using the Schur's complement with $Y = P^{-1}$ and $R = GY$ as:

$$\min \epsilon,\ \begin{bmatrix} \epsilon I & B_{cl}^{\mathsf{T}} \\ B_{cl} & Y \end{bmatrix} > 0,\ \begin{bmatrix} sym(A_p Y + B_p R) & Y C^{\mathsf{T}} \\ CY & -I \end{bmatrix} < 0. \tag{7.157}$$

□

The first plot from Fig. 7.20 shows the norm of position error for the open-loop simulation for an impulsive disturbance given at all node locations in terms of force. A periodic motion for the position error from the initial nominal configuration was observed for the open-loop system. The second plot in Fig. 7.20 shows the result for the closed-loop system with gains value $\Theta = 30I$ and $\Psi = 20I$. The chosen stable gains derive the system to zero but with large energy of the error ($\|y\|_{\mathcal{L}_2}$) as compared to the simulation obtained with the calculated gains using the Bounded Γ_{ie} solution. Notice the initial spike in error, but the total energy for the entire simulation is substantially less than the other two simulations. The theoretical value of the impulse-to-energy gain was obtained to be $\Gamma_{ie} = 1.98 \times 10^{-5}$ by solving the LMIs in Lemma 7.6.3 and the gain from impulsive disturbance to error energy for the simulation was observed to be $\Gamma_{ie} = 1.04 \times 10^{-10}$, which satisfies the requirement. Figure 7.21 shows the trajectories for error in node positions (n_1, n_2, n_3 and n_4) for all the three cases mentioned earlier. Notice that the values of the error in the last plot are much smaller than the values corresponding to the first two plots.

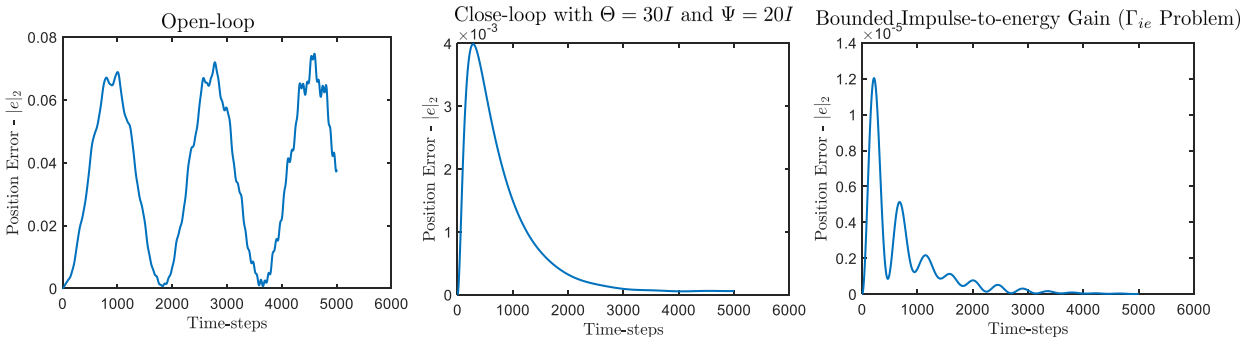

Figure 7.20: Plots of norm in position error for open-loop, closed loop with $\Theta = 30I$ and $\Psi = 20I$, and gains calculated using the bounded impulse to energy problem (Γ_{ie}) for the T_1D_1 robotic arm.

7.6.4 Bound on Covariance in position error

It is impossible to derive the error to precise zero in the presence of process noise; however, one can control the statistics of the error given the statistics of the noise [85, 87]. This subsection provides the required controller gain matrix to bound the covariance of the error in the position or

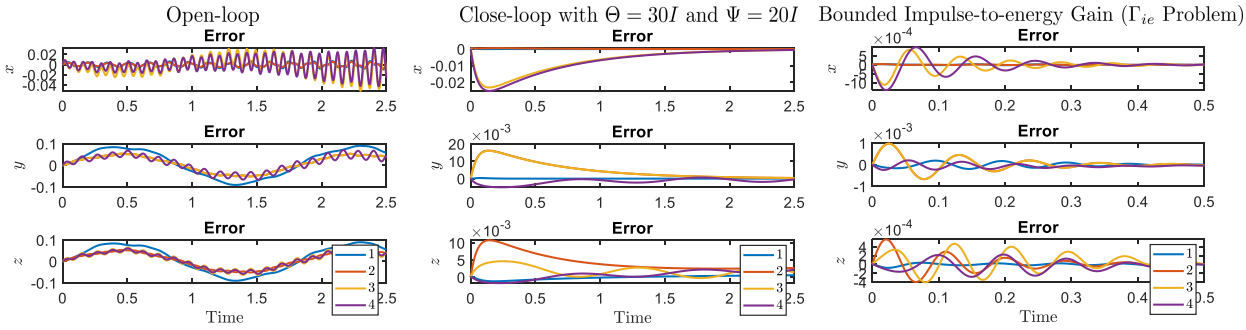

Figure 7.21: Trajectories of node positions (n_1, n_2, n_3 and n_4) for open-loop, closed loop with $\Theta = 30I$ and $\Psi = 20I$, and gains calculated using the bounded impulse to energy problem (Γ_{ie}) for the T_1D_1 robotic arm.

velocity of the nodes.

$$\dot{x} = (A_p + B_pG)x + B_{cl}w, \;\; y = Cx, \tag{7.158}$$

$$\mathcal{E}[yy^{\mathsf{T}}] = Y = CXC^{\mathsf{T}} < \bar{Y}. \tag{7.159}$$

Lemma 7.6.4. *The covariance bound on output ($Y = CXC^{\mathsf{T}} < \bar{Y}$) can be achieved with the following choices of controller gain matrix G (c.f. Eq. (7.114)) for system given in Eq. (7.116) for the zero-mean white noise of intensity $\mathcal{E}[ww^{\mathsf{T}}] = W$ for $X > 0$:*

$$\begin{bmatrix} \bar{Y} & CX \\ XC^{\mathsf{T}} & X \end{bmatrix} > 0, \quad \begin{bmatrix} sym(A_pX + B_pR) & B_{cl} \\ B_{cl}^{\mathsf{T}} & -W^{-1} \end{bmatrix} < 0, \tag{7.160}$$

where $G = RX^{-1}$.

Proof: The covariance matrix X for the linear system for a given system can be written as:

$$A_{cl}X + XA_{cl}^{\mathsf{T}} + B_{cl}WB_{cl}^{\mathsf{T}} < 0, \tag{7.161}$$

which can be used to bound the output covariance and after substitution from Eq. (7.116) can be

written as [85]:

$$CXC^{\mathsf{T}} < \bar{Y}, \;\; (A_p + B_pG)X + X(A_p + B_pG)^{\mathsf{T}} + B_{cl}WB_{cl}^{\mathsf{T}} < 0, \tag{7.162}$$

which again can be written as:

$$\begin{bmatrix} \bar{Y} & CX \\ XC^{\mathsf{T}} & X \end{bmatrix} > 0, \quad \begin{bmatrix} sym(A_pX + B_pR) & B_{cl} \\ B_{cl}^{\mathsf{T}} & -W^{-1} \end{bmatrix} < 0, \;\; R = GX. \tag{7.163}$$

□

Figure 7.22 shows the node position trajectories for nodes n_1, n_2, n_3 and n_4 for three different simulations performed with a zero-mean white noise disturbance given to all the nodes. The noise is characterized to be independent and identical (i.i.d) noise which appears as force disturbance. The first simulation is performed with the open-loop system, and the others are performed as the closed-loop system with full-state feedback. The second plots in Fig. 7.22 shows the results with randomly chosen stable gains $\Theta = 30I$ and $\Psi = 20I$ and the third plot shows the same simulation with the gains calculated using the bounded covariance $Y < \bar{Y}$.

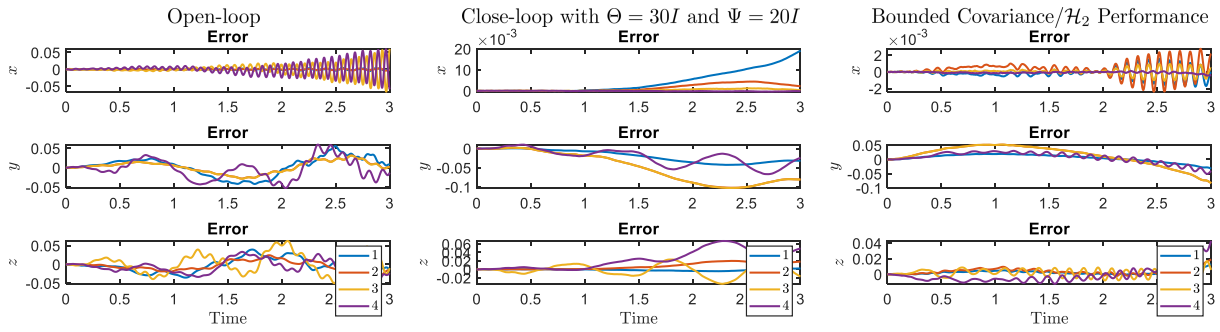

Figure 7.22: Trajectories of node positions (n_1, n_2, n_3 and n_4) for open-loop, closed loop with $\Theta = 30I$ and $\Psi = 20I$, and gains calculated using the bounded covariance or $\mathcal{H}_2$ performance for the T_1D_1 robotic arm.

7.6.5 Stabilizing Control

A simple requirement to effectively control the shape of the tensegrity structure is to stabilize the second-order output feedback differential equation (Eq. (7.112)). This can be achieved by making the matrix $(A_p + B_pG) < 0$ negative definite or $A_{cl}X + XA_{cl}^{\mathsf{T}} < 0,\ X > 0$, for the following equation:

$$\dot{x} = (A_p + B_pG)x + B_{cl}w,\ \ y = Cx. \tag{7.164}$$

Lemma 7.6.5. *The controller gain matrix G (c.f. Eq. (7.114)) for system given in Eq. (7.116), that will yield a stable controller can be solved as:*

$$(A_pX + B_pR) + (A_pX + B_pR)^{\mathsf{T}} < 0, \tag{7.165}$$

where $G = RX^{-1}$.

7.7 Bound on Bar length Error

The idea here is to use extra information provided by these bar length constraints in calculating the control gains to control the shape of the structure. The formulation provided here allows to add some convex constraints to choose the control gains to bound the $\mathcal{L}_\infty$ norm of the error in the length of the bars. The LMI constraints can be added with other convex constraints discussed in the previous section to reject different kinds of disturbances in the control of the tensegrity structure. Let us start by writing a bar vector for the i^{th} bar as:

$$b_i = (C_{b_i} \otimes I)n = (C_{b_i} \otimes I)(e + \bar{n}) = \mathcal{C}_{b_i}(e + \bar{n}). \tag{7.166}$$

Now, the desired performance to bound the error in bar length l_i for a particular compressive

bar member ($\bar{b}_i = \mathcal{C}_{b_i}\bar{n}$) can be written as:

$$z_i = \|\mathcal{C}_{b_i}(e + \bar{n})\| - l_i, \tag{7.167}$$

$$z_i = \|\mathcal{C}_{b_i}e + \bar{b}_i\| - l_i, \tag{7.168}$$

$$z_i = e^{\mathsf{T}}\mathcal{C}_{b_i}^{\mathsf{T}}\mathcal{C}_{b_i}e + 2\bar{b}_i^{\mathsf{T}}\mathcal{C}_{b_i}e. \tag{7.169}$$

Let us define $y_i \triangleq \mathcal{C}_{b_i}e$ and let us write the peak value of the error in the bar-length can be bound as:

$$\|z_i\|_{\mathcal{L}_\infty} < \epsilon_{b_i}, \tag{7.170}$$

$$\|y_i^{\mathsf{T}}y_i + 2\bar{b}_i^{\mathsf{T}}y_i\|_{\mathcal{L}_\infty} < \epsilon_{b_i}, \tag{7.171}$$

where ϵ_{b_i} is the maximum allowed value of the bar length error for the bar b_i.

It is important to notice that the actual problem at hand is to bound the $(y_i^{\mathsf{T}}y_i + 2\bar{b}_i^{\mathsf{T}}y_i)$ which can be done by bounding the peak value of $(y_i^{\mathsf{T}}y_i)$ using the formulation discussed further. Now, the aim here is to bound the maximum value of the y_i for all time as this is an easier problem to tackle, known as generalized $\mathcal{H}_2$ problem or energy to peak gain Γ_{ep} problem.

Lemma 7.7.1. *The S-Procedure or S-Lemma [91, 92]: Let A_1 and A_2 be symmetric matrices, b_1 and b_2 be vectors and c_1 and c_2 be real numbers. Assume that there is some x_0 such that the strict inequality $x_0^TA_1x_0 + 2b_1^Tx_0 + c_1 < 0$ holds. Then the implication*

$$x^TA_1x + 2b_1^Tx + c_1 \leq 0 \Longrightarrow x^TA_2x + 2b_2^Tx + c_2 \leq 0 \tag{7.172}$$

holds if and only if there exists some nonnegative number λ such that

$$\lambda\begin{bmatrix} A_1 & b_1 \\ b_1^T & c_1 \end{bmatrix} - \begin{bmatrix} A_2 & b_2 \\ b_2^T & c_2 \end{bmatrix} > 0. \tag{7.173}$$

Using the standard S-Procedure or S-Lemma [91, 92] given above, we can write the following for our problem:

$$y_i^{\mathsf{T}} y_i < \bar{\epsilon}_{b_i} \Rightarrow y_i^{\mathsf{T}} y_i + 2\bar{b}_i^{\mathsf{T}} y_i < \epsilon_{b_i} \tag{7.174}$$

$$\Updownarrow \tag{7.175}$$

$$\lambda \geq 0, \lambda \begin{bmatrix} I & 0 \\ 0 & -\bar{\epsilon}_{b_i} \end{bmatrix} - \begin{bmatrix} I & \bar{b}_i \\ \bar{b}_i^{\mathsf{T}} & -\epsilon_{b_i} \end{bmatrix} \geq 0, \tag{7.176}$$

which can again be written as the following to minimize the maximum value of error in the bar length:

$$\min\ \epsilon_{b_i},\ \lambda \geq 0,\ \begin{bmatrix} (\lambda - 1)I & -\bar{b}_i \\ -\bar{b}_i^{\mathsf{T}} & \epsilon_{b_i} - \lambda \bar{\epsilon}_{b_i} \end{bmatrix} \geq 0. \tag{7.177}$$

The above mentioned LMI for variables ϵ_{b_i} and λ and given value of $\bar{\epsilon}_{b_i}$ and $\bar{b}_i$ can be solved along with the LMIs mentioned earlier for bounding different kinds of errors. Another way to write this equation is by defining $\kappa = 1/\lambda$ and then writing the LMI as:

$$\max\ \bar{\epsilon}_{b_i},\ \kappa \geq 0,\ \begin{bmatrix} (1 - \kappa)I & -\kappa\bar{b}_i \\ -\kappa\bar{b}_i^{\mathsf{T}} & \kappa\epsilon_{b_i} - \bar{\epsilon}_{b_i} \end{bmatrix} \geq 0. \tag{7.178}$$

Notice that this LMI allows us to calculate the *maximum value* of bound to be put on ($y_i^{\mathsf{T}} y_i < \bar{\epsilon}_{b_i}$) by defining the desired bound on the bar length error ($y_i^{\mathsf{T}} y_i + 2\bar{b}_i^{\mathsf{T}} y_i < \epsilon_{b_i}$).

7.8 Conclusions

In this chapter, we studied a model-based approach to control tensegrity structures that can be used as the mechanism for enabling very high DOF robots. The chapter discussed both full-order models and reduced-order models for controlling the shape, velocity, and acceleration of certain nodes, for a high DOF class-k tensegrity designs. The shape control formulation for the gyroscopic

tensegrity system was also derived, which allows for added orientation control of the structure. A tensegrity T_2D_1 robotic arm example was used to show the efficacy of the formulation by allowing the end effector to reach anywhere in a 3-dimensional hemisphere. In the last half, a generalized vectorized tensegrity dynamics in the presence of some given disturbance is formulated for both full and reduced order. A second-order output regulator was used whose gains were calculated using the LMI framework to generate different kinds of performance bounds. The gains were solved as convex semi-definite programming problems.

8. INTEGRATING STRUCTURE, INFORMATION ARCHITECTURE AND CONTROL DESIGN*

[1] In the first half of the chapter, the nonlinear dynamics is linearized about an equilibrium point for both class-1 and class-k tensegrity systems, and then, the minimal-order system is calculated by removing the modes which corresponds to the change in bar length. The linear control theory is then used to reject the noises and disturbances. The formulation for different error bounds are used to get the desired performance, e.g. $\mathcal{H}_\infty$, generalized $\mathcal{H}_2$ and *covariance control* problem. The information architecture theory is also applied to find the precision of the actuators and sensors along with the controller for the covariance control problem. The main contribution of the chapter is to develop a Linear Matrix Inequality (LMI) framework to jointly optimize structure parameters, information architecture (actuator/sensor precision), and control law to get the required system performance. The tensegrity paradigm is used to integrate these different yet interdependent fields. A linearized tensegrity model as an affine function of initial prestress and force density as the control input is used to find the free structure parameter (optimal initial prestress in the strings), to satisfy performance and control energy upper bound. The precision of the sensors to measure the position and velocity of the nodes and the precision of actuators required to control the tension in the strings is also provided by the formulation. The complete problem is set as a covariance control problem where feasibility is achieved by bounding the covariance of the output as well as that of the control signals. The feedback loop is assumed to have a full-order dynamic compensator with its characteristic matrices chosen as optimization variables. The state feedback formulation is also provided with control gain as the optimization variable. The sub-optimal solution of this non-convex system design problem is found by iterating over an approximated convex problem through the use of a convexifying potential function which enables convergence

[1]*Portions of this section are reprinted or adapted from [93] : Raman Goyal and Robert E. Skelton, "Joint Optimization of Plant, Controller, and Sensor/Actuator Design", American Control Conference (ACC), 1507-1512, Philadelphia, PA, USA, July 10-12, 2019. DOI: 10.23919/ACC.2019.8814671. Copyright © 2020, IEEE. Reproduced with permission.

to a local minimum. This system-level optimization approach to design and control the tensegrity structures also provides the control law for the system.

8.1 Introduction

Traditionally structure design and control design have been treated as two separate problems where a structure is designed first, and then a control law is written to control the structure. It is only recently that researchers have realized the need for integrating the two disciplines. The idea is to design the structure and control algorithm to complement each other in achieving the required performance. Similarly, controller design (control algorithm) and signal processing (actuator and sensor precision) problems should be integrated to determine the required precision of sensors and actuators to guarantee desired output covariance bound. Basically, a system-level design approach is needed to make the best of all three disciplines where all components of the system are cooperatively designed to yield a specified system performance. The work of Li *et al.* [94] integrated control design and selection of information architecture (actuator and sensor precision) to meet specified performance requirement (output covariance upper bound) formulating the constraints in Linear Matrix Inequalities (LMIs) [85]. It is proven that integration of information architecture and control design is a convex problem for a linear plant with full-state feedback or full-order output feedback. Li *et al.* [94] also provides an ad hoc algorithm to reduce the set of required sensors or actuators. This is accomplished by repeatedly deleting the sensors or actuators with the least precision required until the design requirements cannot be met. Radhika *et al.* [95] made advancements in the information architecture theory by adding model uncertainty. More recently, various researchers have looked at the problem of finding a smaller set of sensors from a larger admissible set if precision is given a priori [96, 97].

Some researchers provided a framework to solve the instrument and control design problem [98] while others discussed the problem of integrated structure and control design assuming sensor and actuator precisions are known [99, 100, 101]. Grigoriadis *et al.* [101] provided a two-step solution to the simultaneous design problem of structure and control by iterating over two convex sub-problems. First, the structure parameters were fixed and a controller was designed to satisfy

the specified output covariance upper bound. In the second step, both the structure parameters and the controller are optimized such that the state covariance from the previous step was preserved. The algorithm iterates between these two steps to converge to a local minimum. Lu *et al.* [99] considered the more general structure parameterization and used mixed H_2/H_∞ performance criteria. However, this approach also constrained the closed-loop state covariance matrix to be preserved in the second step. These approaches find a solution in reduced domain space, which may not necessarily be an optimal solution to the combined problem. Another approach to solving the integrated problem is by convexifying LMIs methods [102, 103]. In this approach, the authors first formulate a nonlinear matrix inequality to satisfy the performance requirement and then add another nonlinear matrix inequality to finally generate an LMI. There are some conditions on the added nonlinear matrix inequality (convexifying potential function) which guarantees that the solution will reach a stationary point. The contribution of this chapter is to add prestress in the tensegrity structures as another dimension to this system design approach by integrating structure parameters as an optimization variable along with information architecture and controller design.

The author believes that tensegrity structures are best suited to integrate structure and control design due to its very accurate models of axially loaded members [16]. An accurate model of the system dynamics will yield precise control. Moreover, as tensegrity provides good efficiency for both structural and control avenue, it would be an ideal choice for various adaptive structures where structure and control parameters should be optimized simultaneously [6]. In tensegrity, one can change the stiffness of a tensegrity structure without changing the shape. Similarly, the shape can also be changed without changing the stiffness. This property of tensegrity structures makes it robust to various kinds of loading conditions.

The author also believes that this is the first time one integrated domain formulation is developed to solve for all three decision variables i.e. control design, information architecture, and structure design simultaneously. In this research work, we use the tensegrity paradigm to achieve this by framing it as a covariance control problem. The formulation of this chapter is as follows: First, an analytical formulation to linearize the nonlinear system about an equilibrium point is

provided for both full-order and reduced-order models. Then, the robust control theory to reject the disturbances with different error bounds for linear systems is applied on a tensegrity robotic arm, which is discussed in the previous chapter. Second, we describe a linear system in descriptor state-space form with plant matrices affine in structure parameters. We assume noisy actuators and measurement sensors and define the inverse of noise to be the precision of the actuators and sensors, respectively. The precision of the noisy actuators and sensors is considered as an optimization variable, and the cost of actuators and sensors is assumed to be directly proportional to their precision to add a budget constraint in the problem. Then, we write matrix inequalities to stabilize the system and to satisfy output and control covariance constraints [85]. The simultaneous design of a structure, information architecture, and controller results in nonlinear matrix inequalities even for linear systems. As the domain set is nonlinear inequalities (not proven to be non-convex), a convexifying LMI method is used to solve this system design problem by approximating it to a convex problem [103]. The convexification is achieved by adding a nonlinear matrix inequality with certain conditions. The iteration on the approximated convex sub-problem guarantees the solution to reach a stationary point. For the tensegrity paradigm, the linearized tensegrity dynamics model with initial prestress as linearly appearing free structure parameter is used with force density in the strings to be the control input for the system. The performance is defined to bound the displacement of some nodes while measuring the length of the strings or the position of the nodes. The final output of the optimization problem would be the initial prestress (free structure parameter), the precision of sensors/actuators, and the characteristics matrices for the dynamic controller. A simple design example of a three-story building with disturbance as an earthquake model is presented along with two tensegrity designs examples corresponding to a tensegrity lander and a robotic arm to show the effectiveness of the framework.

8.2 Linearized Tensegrity Dynamics

The nonlinear dynamics of a tensegrity structure of any complexity is derived in Chapter 5 [16]. To apply the optimization formulation developed in Section 2, the nonlinear equations are linearized and represented in the descriptor form such that prestress appears as a linear free

variable.

8.2.1 Class-1 Linearized Dynamics

Lemma 8.2.1. *The linearized dynamics of any class-1 tensegrity system in terms of linear variation in nodal coordinates $\tilde{n}$ can be written as:*

$$\mathcal{M}_1\ddot{\tilde{n}} + \mathcal{D}_1\dot{\tilde{n}} + \mathcal{K}_1\tilde{n} = \mathcal{P}_1\tilde{w} + \mathcal{B}_1\tilde{\gamma}, \tag{8.1}$$

where $\tilde{\gamma}$ is the linear variation in the force density, $\tilde{w}$ is the linear variation in external force, and

$$\mathcal{M}_1 \triangleq \mathcal{T}^{\mathsf{T}} M_{br}\mathcal{T},\ \mathcal{D}_1 \triangleq \mathcal{T}^{\mathsf{T}} D_{br}\mathcal{T}, \tag{8.2}$$

$$\mathcal{K}_1 \triangleq \mathcal{T}^{\mathsf{T}} K_{br}\mathcal{T} + \mathcal{P}_1\,(C_s^{\mathsf{T}} \otimes I)\,\widehat{(\bar{\gamma} \otimes \mathbb{1})}(C_s \otimes I), \tag{8.3}$$

$$\mathcal{P}_1 \triangleq \mathcal{T}^{\mathsf{T}} P_{br}\mathcal{T}^{-\mathsf{T}},\ \mathcal{B} \triangleq -\mathcal{P}_1(C_s^{\mathsf{T}} \otimes I)\hat{\bar{s}}, \tag{8.4}$$

$$\mathcal{T} \triangleq \left(\begin{bmatrix} C_bC_{nb} \\ C_rC_{nb} \\ C_{ns} \end{bmatrix} \otimes I\right), \quad \mathcal{T}^{-\mathsf{T}} = \left(\begin{bmatrix} \frac{1}{2}C_bC_{nb} \\ 2C_rC_{nb} \\ C_{ns} \end{bmatrix} \otimes I\right), \tag{8.5}$$

where $\mathbb{1} \triangleq [1\ \ 1\ \ 1]^{\mathsf{T}}$ with C_b, C_s, C_r and C_{ns} being the connectivity matrices for bars, strings, center of the bars and point masses, respectively. The matrices $C_{nb} = [I\quad 0], M_{br} \triangleq blkdiag(M_b, M_r, M_{rs})$, $D_{br} \triangleq blkdiag(D_b, \mathbf{0}, \mathbf{0})$, $K_{br} \triangleq blkdiag(K_b, \mathbf{0}, \mathbf{0})$, and $P_{br} \triangleq blkdiag(P_b, \mathbf{I}, \mathbf{I})$ are block diagonal matrices with $M_b \triangleq diag(J_1I, J_2I, ...)$, $M_r \triangleq diag(m_1I, m_2I, ...)$, $M_{rs} \triangleq diag(m_{s1}I, m_{s2}I, ...)$, $D_b \triangleq diag(D_{b1}, D_{b2}, ...)$, and $K_b \triangleq diag(K_{b1}, K_{b2}, ...)$.

$$D_{b1} \triangleq \frac{2J_1}{l_1^2}\bar{b}_1\dot{\bar{b}}_1^{\mathsf{T}}, \tag{8.6}$$

$$K_{b1} \triangleq \left[\frac{J_1}{l_1^2}\dot{\bar{b}}_1^{\mathsf{T}}\dot{\bar{b}}_1 + \frac{1}{2l_1^2}\bar{b}_1^{\mathsf{T}}(\bar{f}_2 - \bar{f}_1)\right] I + \frac{1}{2l_1^2}\bar{b}_1(\bar{f}_2 - \bar{f}_1)^{\mathsf{T}}, \tag{8.7}$$

$$P_{b1} \triangleq \frac{1}{2}\left(I - \frac{\bar{b}_1\bar{b}_1^{\mathsf{T}}}{l_1^2}\right), \tag{8.8}$$

where $P_b \triangleq diag(P_{b1}, P_{b2}, ...)$ with bar vector $\bar{b}_1$, string vector $\bar{s}_1$, bar velocity vector $\dot{\bar{b}}_1$, center of mass vector $\bar{r}_1$, center of mass velocity vector $\dot{\bar{r}}_1$, point mass vector $\bar{r}_{s1}$ and force $\bar{f}$, represents the vectors about which the dynamics is linearized.

Proof: The vector equations for rotational and translational dynamics of a bar are given as:

$$J_1\ddot{b}_1 + \frac{J_1}{l_1^2}b_1\dot{b_1}^{\mathsf{T}}\dot{b_1} = \frac{1}{2}(f_2 - f_1) - \frac{1}{2l_1^2}b_1b_1^{\mathsf{T}}(f_2 - f_1), \tag{8.9}$$

$$m_1\ddot{r}_1 = f_1 + f_2, \tag{8.10}$$

and the equation for a point mass (connecting string to string node) is given as:

$$m_{s1}\ddot{r}_{s1} = f_{s1}. \tag{8.11}$$

Let us linearize these equations about some equilibrium bar vector $\bar{b}_1$, bar velocity vector $\dot{\bar{b}}_1$, center of mass vector $\bar{r}_1$, center of mass velocity vector $\dot{\bar{r}}_1$, point mass vector $\bar{r}_{s1}$ and force $\bar{f}$ such that:

$$\tilde{b}_1 = b_1 - \bar{b}_1, \tilde{r}_1 = r_1 - \bar{r}_1, \tilde{r}_{s1} = r_{s1} - \bar{r}_{s1}, \dot{\tilde{b}}_1 = \dot{b}_1 - \dot{\bar{b}}_1, \dot{\tilde{r}}_1 = \dot{r}_1 - \dot{\bar{r}}_1, \tilde{f} = f - \bar{f}. \tag{8.12}$$

The linearized equations of motion for a bar and a point mass with $\tilde{b}_1,\ \tilde{r}_1,\ \tilde{r}_{s1}\ \dot{\tilde{b}}_1,\ \dot{\tilde{r}}_1,\ \dot{\tilde{r}}_{s1}$ being the linear variation can be written as:

$$\begin{aligned} J_1\ddot{\tilde{b}}_1 + \frac{J_1}{l_1^2}\dot{\bar{b}}_1^{\mathsf{T}}\dot{\tilde{b}}_1\tilde{b}_1 + \frac{2J_1}{l_1^2}\bar{b}_1\dot{\bar{b}}_1^{\mathsf{T}}\dot{\tilde{b}}_1 = \frac{1}{2}(\tilde{f}_2 - \tilde{f}_1) - \frac{1}{2l_1^2}\bar{b}_1^{\mathsf{T}}(\bar{f}_2 - \bar{f}_1)\tilde{b}_1 \\ - \frac{1}{2l_1^2}\bar{b}_1(\bar{f}_2 - \bar{f}_1)^{\mathsf{T}}\tilde{b}_1 - \frac{1}{2l_1^2}\bar{b}_1\bar{b}_1^{\mathsf{T}}(\tilde{f}_2 - \tilde{f}_1), \end{aligned} \tag{8.13}$$

$$m_1 \ddot{\tilde{r}}_1 = \tilde{f}_1 + \tilde{f}_2, \tag{8.14}$$

$$m_{s1} \ddot{\tilde{r}}_{s1} = \tilde{f}_{s1}. \tag{8.15}$$

Collecting the terms with $\ddot{\tilde{b}}_1,\ \dot{\tilde{b}}_1,\ \tilde{b}_1,\ \tilde{f},\ \ddot{\tilde{r}}_1$ and $\ddot{\tilde{r}}_{s1}$, we get:

$$\underbrace{[J_1 I]}_{M_{b1}} \ddot{\tilde{b}}_1 + \underbrace{\left[\frac{2J_1}{l_1^2}\bar{b}_1\dot{\bar{b}}_1^{\mathsf{T}}\right]}_{D_{b1}} \dot{\tilde{b}}_1 + \underbrace{\left[\left[\frac{J_1}{l_1^2}\dot{\bar{b}}_1^{\mathsf{T}}\dot{\bar{b}}_1 + \frac{1}{2l_1^2}\bar{b}_1^{\mathsf{T}}(\bar{f}_2 - \bar{f}_1)\right] I + \frac{1}{2l_1^2}\bar{b}_1(\bar{f}_2 - \bar{f}_1)^{\mathsf{T}}\right]}_{K_{b1}} \tilde{b}_1$$

$$= \begin{bmatrix} -\frac{1}{2}\left(I - \frac{\bar{b}_1\bar{b}_1^{\mathsf{T}}}{l_1^2}\right) & \frac{1}{2}\underbrace{\left(I - \frac{\bar{b}_1\bar{b}_1^{\mathsf{T}}}{l_1^2}\right)}_{P_{b1}} \end{bmatrix} \begin{bmatrix} \tilde{f}_1 \\ \tilde{f}_2 \end{bmatrix}, \tag{8.16}$$

$$M_{b1}\ddot{\tilde{b}}_1 + D_{b1}\dot{\tilde{b}}_1 + K_{b1}\tilde{b}_1 = \frac{1}{2}P_{b1}\begin{bmatrix} -I & I \end{bmatrix} \begin{bmatrix} \tilde{f}_1 \\ \tilde{f}_2 \end{bmatrix}, \tag{8.17}$$

$$\underbrace{[m_1 I]}_{M_{r1}} \ddot{\tilde{r}}_1 = \begin{bmatrix} I & I \end{bmatrix} \begin{bmatrix} \tilde{f}_1 \\ \tilde{f}_2 \end{bmatrix}, \tag{8.18}$$

$$\underbrace{[m_{s1} I]}_{M_{rs1}} \ddot{\tilde{r}}_{s1} = \tilde{f}_{s1}. \tag{8.19}$$

Now, stacking the bar vectors in one column and center of mass vectors in another column, we

get:

$$\begin{bmatrix} M_{b1} & & \\ & M_{b2} & \\ & & \ddots \end{bmatrix} \begin{bmatrix} \ddot{\tilde{b}}_1 \\ \ddot{\tilde{b}}_2 \\ \vdots \end{bmatrix} + \begin{bmatrix} D_{b1} & & \\ & D_{b2} & \\ & & \ddots \end{bmatrix} \begin{bmatrix} \dot{\tilde{b}}_1 \\ \dot{\tilde{b}}_2 \\ \vdots \end{bmatrix} + \begin{bmatrix} K_{b1} & & \\ & K_{b2} & \\ & & \ddots \end{bmatrix} \begin{bmatrix} \tilde{b}_1 \\ \tilde{b}_2 \\ \vdots \end{bmatrix}$$
$$= \begin{bmatrix} P_{b1} & & \\ & P_{b2} & \\ & & \ddots \end{bmatrix} \left(\frac{C_b}{2} \otimes I \right) \tilde{f}_b, \quad (8.20)$$

$$\begin{bmatrix} M_{r1} & & \\ & M_{r2} & \\ & & \ddots \end{bmatrix} \begin{bmatrix} \ddot{\tilde{r}}_1 \\ \ddot{\tilde{r}}_2 \\ \vdots \end{bmatrix} = (2C_r \otimes I) \tilde{f}_b, \quad (8.21)$$

$$\begin{bmatrix} M_{rs1} & & \\ & M_{rs2} & \\ & & \ddots \end{bmatrix} \begin{bmatrix} \ddot{\tilde{r}}_{s1} \\ \ddot{\tilde{r}}_{s2} \\ \vdots \end{bmatrix} = \tilde{f}_s, \quad (8.22)$$

which again can be simply written as:

$$M_b \ddot{\tilde{b}} + D_b \dot{\tilde{b}} + K_b \tilde{b} = P_b \left(\frac{1}{2} C_b C_{nb} \otimes I \right) \tilde{f}, \quad (8.23)$$

$$M_r \ddot{\tilde{r}} = (2C_r C_{nb} \otimes I) \tilde{f}, \quad (8.24)$$

$$M_{rs} \ddot{\tilde{r}}_s = (C_{ns} \otimes I) \tilde{f}. \quad (8.25)$$

Let us stack column of bar vectors on top of the column of the center of mass vectors as:

$$\begin{bmatrix} M_b & & \\ & M_r & \\ & & M_{rs} \end{bmatrix} \begin{bmatrix} \ddot{\tilde{b}} \\ \ddot{\tilde{r}} \\ \ddot{\tilde{r}}_s \end{bmatrix} + \begin{bmatrix} D_b & & \\ & \mathbf{0} & \\ & & \mathbf{0} \end{bmatrix} \begin{bmatrix} \dot{\tilde{b}} \\ \dot{\tilde{r}} \\ \dot{\tilde{r}}_s \end{bmatrix} + \begin{bmatrix} K_b & & \\ & \mathbf{0} & \\ & & \mathbf{0} \end{bmatrix} \begin{bmatrix} \tilde{b} \\ \tilde{r} \\ \tilde{r}_s \end{bmatrix}$$
$$= \begin{bmatrix} P_b & & \\ & I & \\ & & I \end{bmatrix} \left(\begin{bmatrix} \frac{1}{2} C_b C_{nb} \\ 2 C_r C_{nb} \\ C_{ns} \end{bmatrix} \otimes I \right) \tilde{f}, \quad (8.26)$$

Using $\begin{bmatrix} \tilde{b} \\ \tilde{r} \\ \tilde{r}_s \end{bmatrix} = \left(\begin{bmatrix} C_b C_{nb} \\ C_r C_{nb} \\ C_{ns} \end{bmatrix} \otimes I \right) \tilde{n}$ and defining

$$\mathcal{T} \triangleq \left(\begin{bmatrix} C_b C_{nb} \\ C_r C_{nb} \\ C_{ns} \end{bmatrix} \otimes I \right), \quad (8.27)$$

we see that

$$\mathcal{T}^{-\mathsf{T}} = \left(\begin{bmatrix} \frac{1}{2} C_b C_{nb} \\ 2 C_r C_{nb} \\ C_{ns} \end{bmatrix} \otimes I \right). \quad (8.28)$$

Substituting the above two equations in equation (8.26), we get:

$$M_{br} \mathcal{T} \ddot{\tilde{n}} + D_{br} \mathcal{T} \dot{\tilde{n}} + K_{br} \mathcal{T} \tilde{n} = P_{br} \mathcal{T}^{-\mathsf{T}} \tilde{f}. \quad (8.29)$$

Multiplying from the left-hand side by $\mathcal{T}^{\mathsf{T}}$, we get:

$$\mathcal{T}^{\mathsf{T}} M_{br} \mathcal{T} \ddot{\tilde{n}} + \mathcal{T}^{\mathsf{T}} D_{br} \mathcal{T} \dot{\tilde{n}} + \mathcal{T}^{\mathsf{T}} K_{br} \mathcal{T} \tilde{n} = \mathcal{T}^{\mathsf{T}} P_{br} \mathcal{T}^{-\mathsf{T}} \tilde{f}, \tag{8.30}$$

which after defining new variables can be written as:

$$\mathcal{M} \ddot{\tilde{n}} + \mathcal{D} \dot{\tilde{n}} + \mathcal{K} \tilde{n} = \mathcal{P} \tilde{f}. \tag{8.31}$$

8.2.1.1 Force density γ as control variable

The above formulated linearized dynamics is only for bars in the presence of some external force f. In order to include the forces due to tension in the strings, we can divide the force f into two parts: one as external force w and other as internal forces due to strings tension as t (actually formulated as γ). From the previous derivation, we know:

$$F = W - S\hat{\gamma} C_s, \tag{8.32}$$

which can be written in vector form as:

$$f = w - (C_s^{\mathsf{T}} \otimes I)\widehat{(\gamma \otimes \mathbb{1})} s, \tag{8.33}$$

where $\mathbb{1} = [1\ 1\ 1]^{\mathsf{T}}$. Linearizing the above equation about $\tilde{\gamma} = \gamma - \bar{\gamma}$, $\tilde{s} = s - \bar{s}$, and $\dot{\tilde{s}} = \dot{s} - \dot{\bar{s}}$, we get:

$$\tilde{f} = \tilde{w} - \underbrace{(C_s^{\mathsf{T}} \otimes I)\widehat{(\bar{\gamma} \otimes \mathbb{1})}}_{K_s} \tilde{s} - \underbrace{(C_s^{\mathsf{T}} \otimes I)\hat{\bar{s}}}_{K_\gamma} \tilde{\gamma}, \tag{8.34}$$

$$\tilde{f} = \tilde{w} - K_s \tilde{s} - K_\gamma \tilde{\gamma}, \tag{8.35}$$

Substituting the above equation in equation (8.31), we get:

$$\mathcal{M}\ddot{\tilde{n}} + \mathcal{D}\dot{\tilde{n}} + \mathcal{K}\tilde{n} = \mathcal{P}\tilde{w} - \mathcal{P}K_s\tilde{s} - \mathcal{P}K_\gamma\tilde{\gamma}. \tag{8.36}$$

Using $\tilde{s} = (C_s \otimes I)\tilde{n}$, the above equation can easily be converted to $\tilde{n}$ coordinates as:

$$\mathcal{M}\ddot{\tilde{n}} + \mathcal{D}\dot{\tilde{n}} + (\mathcal{K} + \mathcal{P}K_s(C_s \otimes I))\tilde{n} = \mathcal{P}\tilde{w} - \mathcal{P}K_\gamma\tilde{\gamma}, \tag{8.37}$$

$$\mathcal{M}_1\ddot{\tilde{n}} + \mathcal{D}_1\dot{\tilde{n}} + \mathcal{K}_1\tilde{n} = \mathcal{P}_1\tilde{w} + \mathcal{B}_1\tilde{\gamma}. \tag{8.38}$$

Notice that we assumed $\tilde{\gamma}$ to be the control input. In reality, the control input would be the rest length of the strings. This formulation is only applicable for closed loop control where we control the force density γ. □

8.2.1.2 String rest length ρ as the control variable - Linearizing force density γ

The above two subsections are formulated for closed-loop dynamics where γ is defined as input control variable. In this subsection, we convert γ to rest length to run open-loop dynamics simulations. Assuming that strings follow Hooke's law and viscous friction damping model, the tension in a string is written as:

$$\|t_i\| = k_i(\|s_i\| - \rho_i) + c_i\frac{s_i^\mathsf{T}\dot{s}_i}{\|s_i\|}, \tag{8.39}$$

$$\gamma_i = \frac{\|t_i\|}{\|s_i\|} = k_i\left(1 - \frac{\rho_i}{\|s_i\|}\right) + c_i\frac{s_i^\mathsf{T}\dot{s}_i}{\|s_i\|^2}, \tag{8.40}$$

where ρ_i is rest length of the string and force density γ_i can also be written as:

$$\gamma_i = k_i\left(1 - \frac{\rho_i}{(s_i^\mathsf{T}s_i)^{1/2}}\right) + c_i\frac{s_i^\mathsf{T}\dot{s}_i}{s_i^\mathsf{T}s_i}. \tag{8.41}$$

Linearizing the force density γ about equilibrium values ($\tilde{\gamma} = \gamma - \bar{\gamma}$, $\tilde{\rho} = \rho - \bar{\rho}$, $\tilde{s} = s - \bar{s}$, and $\dot{\tilde{s}} = \dot{s} - \dot{\bar{s}}$), we get:

$$\tilde{\gamma}_i = \underbrace{\left[\frac{k_i \bar{\rho}_i \bar{s}_i^{\mathsf{T}}}{(\bar{s}_i^{\mathsf{T}} \bar{s}_i)^{3/2}} + \frac{c_i \dot{\bar{s}}_i^{\mathsf{T}}}{\bar{s}_i^{\mathsf{T}} \bar{s}_i} - \frac{2 c_i \dot{\bar{s}}_i^{\mathsf{T}} \bar{s}_i \bar{s}_i^{\mathsf{T}}}{(\bar{s}_i^{\mathsf{T}} \bar{s}_i)^2}\right]}_{\zeta} \tilde{s}_i + \underbrace{\left[\frac{c_i \bar{s}_i^{\mathsf{T}}}{\bar{s}_i^{\mathsf{T}} \bar{s}_i}\right]}_{\kappa} \dot{\tilde{s}}_i - \underbrace{\frac{k_i}{(\bar{s}_i^{\mathsf{T}} \bar{s}_i)^{1/2}}}_{\iota} \tilde{\rho}_i. \tag{8.42}$$

Stacking the force densities for all the strings from the above equation will give:

$$\tilde{\gamma} = \begin{bmatrix} \zeta_1 & & \\ & \zeta_2 & \\ & & \ddots \end{bmatrix} \tilde{s} + \begin{bmatrix} \kappa_1 & & \\ & \kappa_2 & \\ & & \ddots \end{bmatrix} \dot{\tilde{s}} - \begin{bmatrix} \iota_1 & & \\ & \iota_2 & \\ & & \ddots \end{bmatrix} \tilde{\rho}, \tag{8.43}$$

$$\tilde{\gamma} = K_{ks} \tilde{s} + K_{cs} \dot{\tilde{s}} - K_{ps} \tilde{\rho}. \tag{8.44}$$

The above equation can be substituted to final linearized equation (8.37) as:

$$\mathcal{M} \ddot{\tilde{n}} + \mathcal{D} \dot{\tilde{n}} + (\mathcal{K} + \mathcal{P} K_s (C_s \otimes I)) \tilde{n} = \mathcal{P} \tilde{w} - \mathcal{P} K_\gamma (K_{ks} \tilde{s} + K_{cs} \dot{\tilde{s}} - K_{ps} \tilde{\rho}). \tag{8.45}$$

Again using $\tilde{s} = (C_s \otimes I) \tilde{n}$, the above equation can easily be converted to $\tilde{n}$ coordinates as:

$$\mathcal{M} \ddot{\tilde{n}} + (\mathcal{D} + \mathcal{P} K_\gamma K_{cs} (C_s \otimes I)) \dot{\tilde{n}} + (\mathcal{K} + \mathcal{P} K_s (C_s \otimes I) + \mathcal{P} K_\gamma K_{ks} (C_s \otimes I)) \tilde{n} = \mathcal{P} \tilde{w} + \mathcal{P} K_\gamma K_{ps} \tilde{\rho}. \tag{8.46}$$

The following equation can be obtained for the open-loop linearized dynamics by substituting for the $\tilde{\rho} = 0$:

$$\mathcal{M} \ddot{\tilde{n}} + (\mathcal{D} + \mathcal{P} K_\gamma K_{cs} (C_s \otimes I)) \dot{\tilde{n}} + (\mathcal{K} + \mathcal{P} K_s (C_s \otimes I) + \mathcal{P} K_\gamma K_{ks} (C_s \otimes I)) \tilde{n} = \mathcal{P} \tilde{w}. \tag{8.47}$$

8.2.2 Class-K Linearized Dynamics

The linearization of class-K dynamics is not that different from the class-1 dynamics. The only addition to the previous formulation are linear constraints.

8.2.2.1 Full-order Linearized Dynamics

The linear constraints can be written as:

$$NP = D, \tag{8.48}$$

which can be written in vector form as:

$$A\bar{n} = d, \quad A\tilde{n} = 0, \quad A = P^{\mathsf{T}} \otimes I, \quad d = vec(D). \tag{8.49}$$

As the constraints are already linear, they can be easily incorporated in the linearized dynamics as:

$$\mathcal{M}\ddot{\tilde{n}} + \mathcal{D}\dot{\tilde{n}} + \mathcal{K}\tilde{n} = \mathcal{P}\tilde{f} + A^{\mathsf{T}}\Omega, \tag{8.50}$$

where Ω is the lagrange multiplier. The second time derivative of the constraints can be written as:

$$A\ddot{\tilde{n}} = 0. \tag{8.51}$$

substituting the above equation in equation (8.50), we get:

$$A\mathcal{M}^{-1}\mathcal{D}\dot{\tilde{n}} + A\mathcal{M}^{-1}\mathcal{K}\tilde{n} = A\mathcal{M}^{-1}\mathcal{P}\tilde{f} + A\mathcal{M}^{-1}A^{\mathsf{T}}\Omega, \tag{8.52}$$

The above equation can be used to solve for Lagrange multiplier Ω as:

$$\Omega = (A\mathcal{M}^{-1}A^{\mathsf{T}})^{-1}\left[A\mathcal{M}^{-1}\mathcal{D}\dot{\tilde{n}} + A\mathcal{M}^{-1}\mathcal{K}\tilde{n} - A\mathcal{M}^{-1}\mathcal{P}\tilde{f}\right]. \tag{8.53}$$

Further substituting back the value of Ω in equation (8.50), we get:

$$\mathcal{M}\ddot{\tilde{n}} + \mathcal{D}\dot{\tilde{n}} + \mathcal{K}\tilde{n} = \mathcal{P}\tilde{f} + A^{\mathsf{T}}(A\mathcal{M}^{-1}A^{\mathsf{T}})^{-1}\left[A\mathcal{M}^{-1}\mathcal{D}\dot{\tilde{n}} + A\mathcal{M}^{-1}\mathcal{K}\tilde{n} - A\mathcal{M}^{-1}\mathcal{P}\tilde{f}\right]. \tag{8.54}$$

Collecting the terms, we get:

$$\mathcal{M}\ddot{\tilde{n}} + \left(I - A^{\mathsf{T}}(A\mathcal{M}^{-1}A^{\mathsf{T}})^{-1}A\mathcal{M}^{-1}\right)\mathcal{D}\dot{\tilde{n}} + \left(I - A^{\mathsf{T}}(A\mathcal{M}^{-1}A^{\mathsf{T}})^{-1}A\mathcal{M}^{-1}\right)\mathcal{K}\tilde{n} = \left(I - A^{\mathsf{T}}(A\mathcal{M}^{-1}A^{\mathsf{T}})^{-1}A\mathcal{M}^{-1}\right)\mathcal{P}\tilde{f}, \tag{8.55}$$

Let us define $\mathcal{L} \triangleq \left(I - A^{\mathsf{T}}(A\mathcal{M}^{-1}A^{\mathsf{T}})^{-1}A\mathcal{M}^{-1}\right)$:

$$\mathcal{M}\ddot{\tilde{n}} + \mathcal{L}\mathcal{D}\dot{\tilde{n}} + \mathcal{L}\mathcal{K}\tilde{n} = \mathcal{L}\mathcal{P}\tilde{f}. \tag{8.56}$$

Let us substitute $\tilde{f}$ in terms of $\tilde{w}$ and $\tilde{\gamma}$ from equation (8.35) as:

$$\mathcal{M}\ddot{\tilde{n}} + \mathcal{L}\mathcal{D}\dot{\tilde{n}} + \mathcal{L}\mathcal{K}\tilde{n} = \mathcal{L}\mathcal{P}\tilde{w} - \mathcal{L}\mathcal{P}K_s\tilde{s} - \mathcal{L}\mathcal{P}K_\gamma\tilde{\gamma}. \tag{8.57}$$

Using $\tilde{s} = (C_s \otimes I)\tilde{n}$, the above equation can easily be converted to $\tilde{n}$ coordinates as:

$$\mathcal{M}\ddot{\tilde{n}} + \mathcal{L}\mathcal{D}\dot{\tilde{n}} + \mathcal{L}(\mathcal{K} + \mathcal{P}K_s(C_s \otimes I))\tilde{n} = \mathcal{L}\mathcal{P}\tilde{w} - \mathcal{L}\mathcal{P}K_\gamma\tilde{\gamma}. \tag{8.58}$$

Now using $\tilde{\gamma} = K_{ks}\tilde{s} + K_{cs}\dot{\tilde{s}} - K_{ps}\tilde{\rho}$, and again using $\tilde{s} = (C_s \otimes I)\tilde{n}$, the above equation can easily be converted to $\tilde{n}$ coordinates as:

$$\mathcal{M}\ddot{\tilde{n}} + \mathcal{L}(\mathcal{D} + \mathcal{P}K_\gamma K_{cs}(C_s \otimes I))\dot{\tilde{n}} + \mathcal{L}(\mathcal{K} + \mathcal{P}K_s(C_s \otimes I) + \mathcal{P}K_\gamma K_{ks}(C_s \otimes I))\tilde{n}$$
$$= \mathcal{L}\mathcal{P}\tilde{w} + \mathcal{L}\mathcal{P}K_\gamma K_{ps}\tilde{\rho}. \quad (8.59)$$

The following equation can be obtained for the open-loop linearized dynamics by substituting for the $\tilde{\rho} = 0$:

$$\mathcal{M}\ddot{\tilde{n}} + \mathcal{L}(\mathcal{D} + \mathcal{P}K_\gamma K_{cs}(C_s \otimes I))\dot{\tilde{n}} + \mathcal{L}(\mathcal{K} + \mathcal{P}K_s(C_s \otimes I) + \mathcal{P}K_\gamma K_{ks}(C_s \otimes I))\tilde{n} = \mathcal{L}\mathcal{P}\tilde{w}. \quad (8.60)$$

8.2.2.2 Reduced-order Linearized Dynamics

Lemma 8.2.2. *The reduced-order linearized dynamics of any class-k tensegrity system can be written as:*

$$\mathcal{M}_k\ddot{\tilde{\eta}}_2 + \mathcal{D}_k\dot{\tilde{\eta}}_2 + \mathcal{K}_k\tilde{\eta}_2 = \mathcal{P}_k\tilde{w} + \mathcal{B}_k\tilde{\gamma}, \quad (8.61)$$

where $\mathcal{M}_k \triangleq V_2^\mathsf{T}\mathcal{M}_1V_2, \mathcal{D}_k \triangleq V_2^\mathsf{T}\mathcal{D}_1V_2, \mathcal{K}_k \triangleq V_2^\mathsf{T}\mathcal{K}_1V_2, \mathcal{P}_k \triangleq V_2^\mathsf{T}\mathcal{P}_1, \mathcal{B}_k \triangleq V_2^\mathsf{T}\mathcal{B}_1$*, with some linear constraints of the form for class-k structure as:*

$$A\tilde{n} = 0,\ U\begin{bmatrix}\Sigma_1 & 0\end{bmatrix}\begin{bmatrix}V_1^\mathsf{T}\\ V_2^\mathsf{T}\end{bmatrix}\tilde{n} = U\begin{bmatrix}\Sigma_1 & 0\end{bmatrix}\begin{bmatrix}\tilde{\eta}_1\\ \tilde{\eta}_2\end{bmatrix} = 0,$$

implying $\tilde{\eta}_1 = \dot{\tilde{\eta}}_1 = \ddot{\tilde{\eta}}_1 = 0$.

Proof:

Writing the equation (8.31) here again:

$$\mathcal{M}\ddot{\tilde{n}} + \mathcal{D}\dot{\tilde{n}} + \mathcal{K}\tilde{n} = \mathcal{P}\tilde{f}. \tag{8.62}$$

For Class-K structure we have some constraints of the form:

$$A\bar{n} = d, \quad A\tilde{n} = 0. \tag{8.63}$$

In the presence of these constraints, the new dynamics can be written as:

$$\mathcal{M}\ddot{\tilde{n}} + \mathcal{D}\dot{\tilde{n}} + \mathcal{K}\tilde{n} = \mathcal{P}\tilde{f} + A^{\mathsf{T}}\Omega. \tag{8.64}$$

Adding the linear constraints into the dynamics will restrict the motion in certain dimensions, thus reducing the order of the dynamics to a span a smaller space. To this end, we use the singular value decomposition (SVD) of matrix A as:

$$A = U\Sigma V^{\mathsf{T}} = U \begin{bmatrix} \Sigma_1 & 0 \end{bmatrix} \begin{bmatrix} V_1^{\mathsf{T}} \\ V_2^{\mathsf{T}} \end{bmatrix}, \tag{8.65}$$

where $U \in \mathbb{R}^{N_c \times N_c}$ and $V \in \mathbb{R}^{3n \times 3n}$ are both unitary matrices, $V_1 \in \mathbb{R}^{3n \times N_c}$ and $V_2 \in \mathbb{R}^{3n \times (3n - N_c)}$ are submatrices of V, and $\Sigma_1 \in \mathbb{R}^{N_c \times N_c}$ is a diagonal matrix of positive singular values. By defining

$$\eta = \begin{bmatrix} \eta_1 \\ \eta_2 \end{bmatrix} \triangleq V^{\mathsf{T}}\tilde{n} = \begin{bmatrix} V_1^{\mathsf{T}}\tilde{n} \\ V_2^{\mathsf{T}}\tilde{n} \end{bmatrix}, \tag{8.66}$$

the constraint Equation (8.63) can be modified as:

$$A\tilde{n} = U\Sigma V^{\mathsf{T}}\tilde{n} = U \begin{bmatrix} \Sigma_1 & 0 \end{bmatrix} \begin{bmatrix} \eta_1 \\ \eta_2 \end{bmatrix} = 0, \tag{8.67}$$

which implies:

$$\eta_1 = 0, \;\; \dot{\eta}_1 = 0, \;\; \ddot{\eta}_1 = 0. \tag{8.68}$$

Here, η_1 represents the no-motion space in transformed coordinates. Moreover, η_2 will evolve according to the constrained dynamics in new coordinate system. Using Equations (8.65-8.68), the dynamics equation (8.64) can be rewritten as:

$$\mathcal{M}V_2\ddot{\eta}_2 + \mathcal{D}V_2\dot{\eta}_2 + \mathcal{K}V_2\eta_2 = \mathcal{P}\tilde{f} + V_1\Sigma_1 U^{\mathsf{T}}\Omega, \tag{8.69}$$

Pre-multiplying the above equation by a non-singular matrix $[V_1 \;\; V_2]^{\mathsf{T}}$ will yield two parts, where second part gives the second order differential equation for the reduced dynamics:

$$V_2^{\mathsf{T}}\mathcal{M}V_2\ddot{\eta}_2 + V_2^{\mathsf{T}}\mathcal{D}V_2\dot{\eta}_2 + V_2^{\mathsf{T}}\mathcal{K}V_2\eta_2 = V_2^{\mathsf{T}}\mathcal{P}\tilde{f} + V_2^{\mathsf{T}}V_1\Sigma_1 U^{\mathsf{T}}\Omega,$$

$$\Rightarrow \mathcal{M}_2\ddot{\eta}_2 + \mathcal{D}_2\dot{\eta}_2 + \mathcal{K}_2\eta_2 = \mathcal{P}_2\tilde{f}. \tag{8.70}$$

with $\mathcal{M}_2 = V_2^{\mathsf{T}}\mathcal{M}V_2, \mathcal{D}_2 = V_2^{\mathsf{T}}\mathcal{D}V_2$, $\mathcal{K}_2 = V_2^{\mathsf{T}}\mathcal{K}V_2$, and $\mathcal{P}_2 = V_2^{\mathsf{T}}\mathcal{P}$.

Let us substitute $\tilde{f}$ in terms of $\tilde{w}$ and $\tilde{\gamma}$ from equation (8.35) as:

$$\mathcal{M}_2\ddot{\eta}_2 + \mathcal{D}_2\dot{\eta}_2 + \mathcal{K}_2\eta_2 = \mathcal{P}_2\tilde{w} - \mathcal{P}_2K_s\tilde{s} - \mathcal{P}_2K_\gamma\tilde{\gamma}, \tag{8.71}$$

Using $\tilde{s} = (C_s \otimes I)\tilde{n} = (C_s \otimes I)V_2\eta_2$, the above equation can easily be converted to $\tilde{n}$

coordinates as:

$$\mathcal{M}_2\ddot{\eta}_2 + \mathcal{D}_2\dot{\eta}_2 + (\mathcal{K}_2 + \mathcal{P}_2 K_s (C_s \otimes I) V_2)\eta_2 = \mathcal{P}_2\tilde{w} - \mathcal{P}_2 K_\gamma \tilde{\gamma}, \tag{8.72}$$

$$\mathcal{M}_k\ddot{\eta}_2 + \mathcal{D}_k\dot{\eta}_2 + \mathcal{K}_k\eta_2 = \mathcal{P}_k\tilde{w} + \mathcal{B}_k\tilde{\gamma}. \tag{8.73}$$

Now using $\tilde{\gamma} = K_{ks}\tilde{s} + K_{cs}\dot{\tilde{s}} - K_{ps}\tilde{\rho}$, and again using $\tilde{s} = (C_s \otimes I)V_2\eta_2$, the above equation can easily be converted to $\tilde{n}$ coordinates as:

$$\mathcal{M}_2\ddot{\eta}_2 + (\mathcal{D}_2 + \mathcal{P}_2 K_\gamma K_{cs}(C_s \otimes I)V_2)\dot{\eta}_2 + (\mathcal{K}_2 + \mathcal{P}_2 K_s (C_s \otimes I)V_2 + \mathcal{P}_2 K_\gamma K_{ks}(C_s \otimes I)V_2)\eta_2 = \mathcal{P}_2\tilde{w} + \mathcal{P}_2 K_\gamma K_{ps}\tilde{\rho}. \tag{8.74}$$

The following equation can be obtained for the open-loop linearized dynamics by substituting for the $\tilde{\rho} = 0$:

$$\mathcal{M}_2\ddot{\eta}_2 + (\mathcal{D}_2 + \mathcal{P}_2 K_\gamma K_{cs}(C_s \otimes I)V_2)\dot{\eta}_2 + (\mathcal{K}_2 + \mathcal{P}_2 K_s (C_s \otimes I)V_2 + \mathcal{P}_2 K_\gamma K_{ks}(C_s \otimes I)V_2)\eta_2 = \mathcal{P}_2\tilde{w}. \tag{8.75}$$

This completes the proof. □

8.3 Minimal-order linearized system

8.3.1 Class-1 Tensegrity System Dynamics

To generate the minimal order linearized dynamics model for both class-1 and class-k tensegrity system, we start with the linearized model for the class-1 system given in Eqn. (8.31):

$$\mathcal{M}\ddot{\tilde{n}} + \mathcal{D}\dot{\tilde{n}} + \mathcal{K}\tilde{n} = \mathcal{P}\tilde{f}, \tag{8.76}$$

and look for the modes in which the length of the bar is not changing. Let us start by writing the coordinate transformation from bar coordinates to nodes coordinates as:

$$\tilde{n} = \left(\begin{bmatrix} \frac{1}{2}C_{nb}^{\mathsf{T}}C_{b}^{\mathsf{T}} & 2C_{nb}^{\mathsf{T}}C_{r}^{\mathsf{T}} & C_{ns}^{\mathsf{T}} \end{bmatrix} \otimes I \right) \begin{bmatrix} \tilde{b} \\ \tilde{r} \\ \tilde{r}_s \end{bmatrix}, \tag{8.77}$$

Now, the mode corresponding to the length change for all the bars can be calculated using $\tilde{r} = \tilde{r}_s = 0$ and $\tilde{b} = \delta\bar{b}$. This can be understood as :

$$\delta\bar{n} = \left(\begin{bmatrix} \frac{1}{2}C_{nb}^{\mathsf{T}}C_{b}^{\mathsf{T}} & 2C_{nb}^{\mathsf{T}}C_{r}^{\mathsf{T}} & C_{ns}^{\mathsf{T}} \end{bmatrix} \otimes I \right) \begin{bmatrix} \delta\bar{b} \\ 0 \\ 0 \end{bmatrix}. \tag{8.78}$$

Note that the mode $\delta\bar{n}$ represents the motion in the linearized mode where the length of all the bars are changing by length δ. The modes corresponding to the length change of the i^{th} bar can be found by extracting the nodes related to that bar to create a $\delta\bar{n}_{1_i} \in \mathcal{R}^{6\times 1}$ vector. Now, we find 5 modes which are perpendicular to this mode corresponding to the i^{th} bar by finding the right null space for the $\delta\bar{n}_{1_i}^{\mathsf{T}}$ dimensional vector as $\delta\bar{n}_{2_i} = {}^{\perp}\delta\bar{n}_{1_i}^{\mathsf{T}} \in \mathcal{R}^{6\times 5}$. Now, the nodes can be arranged in their respective order to generate $\Phi_{1_i} \in \mathcal{R}^{6\beta\times 1}$ from $\bar{n}_{1_i}$ and $\Phi_{2_i} \in \mathcal{R}^{6\beta\times 5}$ from $\bar{n}_{2_i}$. The similar procedure can be done for all the bars to create $\Phi_1 = \begin{bmatrix} \dots \Phi_{1_i} \dots \end{bmatrix} \in \mathcal{R}^{6\beta\times\beta}$ and $\Phi_2 = \begin{bmatrix} \dots \Phi_{2_i} \dots \end{bmatrix} \in \mathcal{R}^{6\beta\times 5\beta}$. Finally, the coordinate transformation matrix $\Phi = [\Phi_1\ \Phi_2] \in \mathcal{R}^{6\beta\times 6\beta}$ can be formulated which spans the entire 6β dimensional space. Also, notice that each column of the matrix Φ can be scaled to have unit length which will result in the matrix Φ to be orthonormal, i.e., $\Phi^{-1} = \Phi^{\mathsf{T}}$.

Now, let us transform the coordinates from $\tilde{n}$ space to a new space ϕ space with $\tilde{n} = \Phi\phi$ and

substituting it into Eq. (8.1) to obtain:

$$\mathcal{M}\Phi\ddot{\phi} + \mathcal{D}\Phi\dot{\phi} + \mathcal{K}\Phi\phi = \mathcal{P}\tilde{f}, \tag{8.79}$$

which after multiplying from the left hand side by Φ^{T} can be written as:

$$\Phi^{\mathsf{T}}\mathcal{M}\Phi\ddot{\phi} + \Phi^{\mathsf{T}}\mathcal{D}\Phi\dot{\phi} + \Phi^{\mathsf{T}}\mathcal{K}\Phi\phi = \Phi^{\mathsf{T}}\mathcal{P}\tilde{f}. \tag{8.80}$$

Note that the feasible modes for the dynamics system with rigid bars are corresponding to Φ_2 and thus, the physically feasible reduced-order system can be written as:

$$\Phi_2^{\mathsf{T}}\mathcal{M}\Phi_2\ddot{\phi} + \Phi_2^{\mathsf{T}}\mathcal{D}\Phi_2\dot{\phi} + \Phi_2^{\mathsf{T}}\mathcal{K}\Phi_2\phi = \Phi_2^{\mathsf{T}}\mathcal{P}\tilde{f}. \tag{8.81}$$

It was numerically observed that the matrix $\Phi_2^{\mathsf{T}}\mathcal{K}_1\Phi_2$ was positive definite with feasible modes, which corresponds to 3 translational and 2 rotational motion for each bar.

8.3.2 Class-K Tensegrity System Dynamics

The linear constraint for the class-k system should be added corresponding to the transformed coordinates ϕ to only keep the feasible modes. It was mentioned earlier that the linear constraints $NP = D$ in the linearized vector form could be written as:

$$A\tilde{n} = 0, \quad A = P^{\mathsf{T}} \otimes I, \tag{8.82}$$

which can now be written in transformed coordinates as:

$$A_2\phi = 0, \quad A_2 \triangleq A\Phi_2, \;\; A = P^{\mathsf{T}} \otimes I. \tag{8.83}$$

Now, following the same procedure as described earlier, we can write the dynamics in even

more reduced-order as:

$$\Phi_2^{\mathsf{T}}\mathcal{M}\Phi_2\ddot{\phi} + \Phi_2^{\mathsf{T}}\mathcal{D}\Phi_2\dot{\phi} + \Phi_2^{\mathsf{T}}\mathcal{K}\Phi_2\phi = \Phi_2^{\mathsf{T}}\mathcal{P}\tilde{f} + A_2^{\mathsf{T}}\Omega. \tag{8.84}$$

where A_2 can be decomposed as:

$$A_2 = U_\phi \Sigma_\phi V_\phi^{\mathsf{T}} = U_\phi \begin{bmatrix} \Sigma_{1_\phi} & 0 \end{bmatrix} \begin{bmatrix} V_{1_\phi}^{\mathsf{T}} \\ V_{2_\phi}^{\mathsf{T}} \end{bmatrix}, \tag{8.85}$$

and by defining:

$$\eta_\phi = \begin{bmatrix} \eta_{1_\phi} \\ \eta_{2_\phi} \end{bmatrix} \triangleq V_\phi^{\mathsf{T}}\phi = \begin{bmatrix} V_{1_\phi}^{\mathsf{T}}\phi \\ V_{2_\phi}^{\mathsf{T}}\phi \end{bmatrix}, \tag{8.86}$$

the constraints can be modified as:

$$A_2\phi = U_\phi \begin{bmatrix} \Sigma_{1_\phi} & 0 \end{bmatrix} \begin{bmatrix} \eta_{1_\phi} \\ \eta_{2_\phi} \end{bmatrix} = 0, \tag{8.87}$$

implying:

$$\eta_{1_\phi} = 0, \;\; \dot{\eta}_{1_\phi} = 0, \;\; \ddot{\eta}_{1_\phi} = 0. \tag{8.88}$$

Now, the dynamics with the constrained system and no bar length change will evolve as:

$$\Phi_2^{\mathsf{T}}\mathcal{M}\Phi_2 V_{2_\phi}\ddot{\eta}_{2_\phi} + \Phi_2^{\mathsf{T}}\mathcal{D}\Phi_2 V_{2_\phi}\dot{\eta}_{2_\phi} + \Phi_2^{\mathsf{T}}\mathcal{K}\Phi_2 V_{2_\phi}\eta_{2_\phi} = \Phi_2^{\mathsf{T}}\mathcal{P}\tilde{f} + V_{1_\phi}\Sigma_{1_\phi}U_\phi^{\mathsf{T}}\Omega, \tag{8.89}$$

and pre-multiplying the above equation by a non-singular matrix $[V_{1_\phi} \;\; V_{2_\phi}]^{\mathsf{T}}$ will yield two parts,

where second part gives the second order differential equation for the reduced dynamics:

$$V_{2_\phi}^{\mathsf{T}}\Phi_2^{\mathsf{T}}\mathcal{M}\Phi_2 V_{2_\phi}\ddot{\eta}_{2_\phi} + V_{2_\phi}^{\mathsf{T}}\Phi_2^{\mathsf{T}}\mathcal{D}\Phi_2 V_{2_\phi}\dot{\eta}_{2_\phi} + V_{2_\phi}^{\mathsf{T}}\Phi_2^{\mathsf{T}}\mathcal{K}\Phi_2 V_{2_\phi}\eta_{2_\phi} = V_{2_\phi}^{\mathsf{T}}\Phi_2^{\mathsf{T}}\mathcal{P}\tilde{f} + V_{2_\phi}^{\mathsf{T}}V_{1_\phi}\Sigma_{1_\phi}U_\phi^{\mathsf{T}}\Omega, \tag{8.90}$$

which can finally be written as:

$$V_{2_\phi}^{\mathsf{T}}\Phi_2^{\mathsf{T}}\mathcal{M}\Phi_2 V_{2_\phi}\ddot{\eta}_{2_\phi} + V_{2_\phi}^{\mathsf{T}}\Phi_2^{\mathsf{T}}\mathcal{D}\Phi_2 V_{2_\phi}\dot{\eta}_{2_\phi} + V_{2_\phi}^{\mathsf{T}}\Phi_2^{\mathsf{T}}\mathcal{K}\Phi_2 V_{2_\phi}\eta_{2_\phi} = V_{2_\phi}^{\mathsf{T}}\Phi_2^{\mathsf{T}}\mathcal{P}\tilde{f}. \tag{8.91}$$

This is the final linearized minimal-order dynamics equation for the class-k tensegrity system.

8.4 Information Architecture and Control design using the linearized model

The example for all the different bounds will have the simulation results discussed on the same tensegrity T_1D_1 robotic arm with the initial configuration shown in Fig. 8.1.

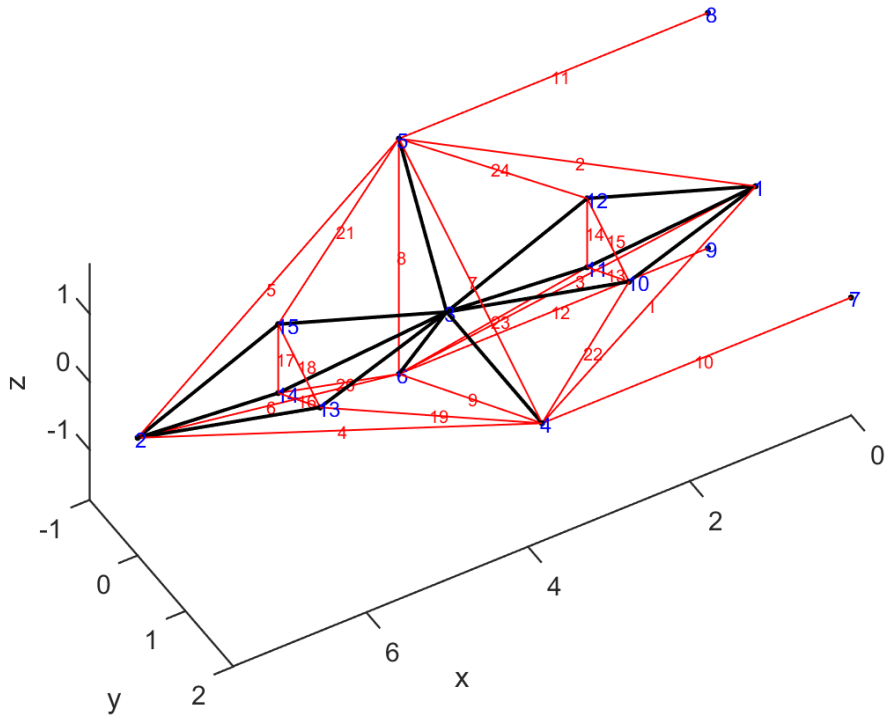

Figure 8.1: Initial configuration of the tensegrity T_1D_1 robotic arm.

8.4.1 Open-Loop response with different performance objectives

8.4.1.1 Bound on $\mathcal{L}_\infty$ norm of error or Generalized $\mathcal{H}_2$ Problem

This problem can be solved as a energy to peak gain - Γ_{ep} [85] or generalized $\mathcal{H}_2$ problem [87].

$$\Gamma_{ep} \triangleq \sup_{\|w\|_{\mathcal{L}_2} \leq 1} \|y\|_{\mathcal{L}_\infty}, \tag{8.92}$$

$$\Gamma_{ep} = \inf_{Q} \|CQC^\mathsf{T}\|^{1/2} : A_{cl}Q + QA_{cl}^\mathsf{T} + B_{cl}B_{cl}^\mathsf{T} < 0,\ Q > 0. \tag{8.93}$$

8.4.1.2 Bound on Covariance in position error

[87, 85] The covariance of the error in the position or velocity of the nodes can be bounded by bounding the covariance matrix X for the linear system as:

$$\mathcal{E}[yy^\mathsf{T}] = Y = CXC^\mathsf{T} < \bar{Y},\ \ A_{cl}X + XA_{cl}^\mathsf{T} + B_{cl}WB_{cl}^\mathsf{T} < 0,\ X > 0. \tag{8.94}$$

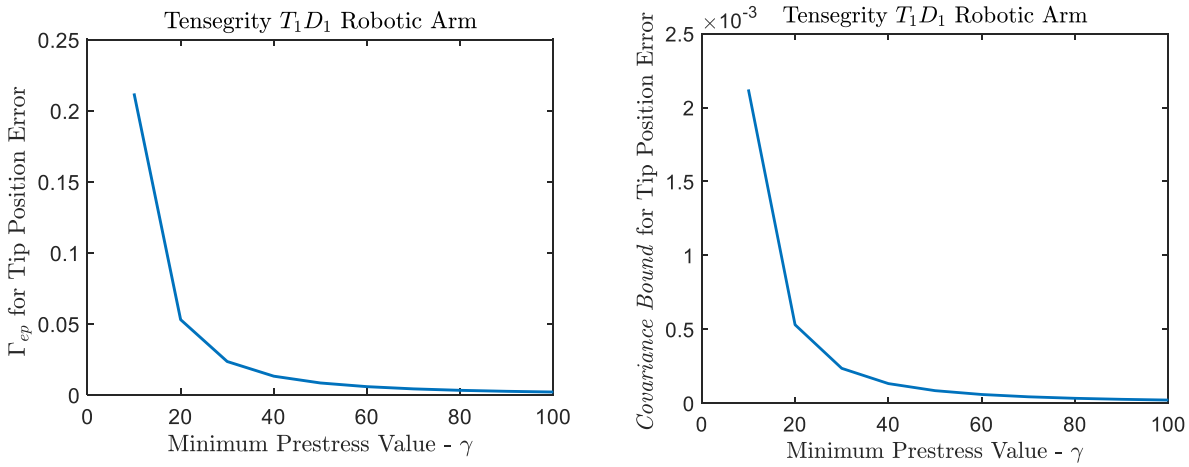

Figure 8.2: Left: Bound on $\mathcal{L}_\infty$ norm of error for different values of the scaled prestress. Right: Bound the covariance error for different values of the scaled prestress.

In Fig. 8.2, the plot on the left shows the bound on $\mathcal{L}_\infty$ norm of error for the tip for the

unit energy disturbance applied to all the nodes of T_1D_1 robotic arm for different values of the scaled prestress in the strings. As the prestress value increases, the structure becomes stiffer which reduces the motion of the tip of the arm. The same trend can be observed for the plot on the right that the covariance bound on error for the tip of T_1D_1 robotic arm for different values of the scaled prestress in the strings.

8.4.1.3 Bounded Γ_{ie} or LQR Problem

This can also be defined as the peak disturbance to energy gain ($\|y\|_{\mathcal{L}_2}$) for the system [85] can be solved with disturbance w as the impulsive disturbance $w(t) = w_0\delta(t)$:

$$\Gamma_{ie} \triangleq \sup_{w_0\delta(t)\leq 1} \|y\|_{\mathcal{L}_2}, \tag{8.95}$$

$$\Gamma_{ie} = \inf_{P} \|B_{cl}^{\mathsf{T}} P B_{cl}\|^{1/2} : PA_{cl} + A_{cl}^{\mathsf{T}} P + C^{\mathsf{T}} C < 0,\ P > 0. \tag{8.96}$$

8.4.1.4 Bounded Γ_{ee} or $\mathcal{H}_\infty$ Problem

The $\mathcal{H}_\infty$ Problem is defined as [88, 89, 87]: $\|T\|_{H_\infty} \triangleq \sup_w \|T(jw)\| < \epsilon$ which can also be understood in time domain analysis as the energy-to-energy gain problem [85]:

$$\Gamma_{ee} \triangleq \sup_{\|w\|_{\mathcal{L}_2}\leq 1} \|y\|_{\mathcal{L}_2} < \epsilon, \tag{8.97}$$

$$PA_{cl} + A_{cl}^{\mathsf{T}} P + PB_{cl} R^{-1} (PB_{cl})^{\mathsf{T}} + C^{\mathsf{T}} C < 0,\ P > 0,\ R = \epsilon^2 I > 0. \tag{8.98}$$

The plots on the left in Fig. 8.3 shows the impulse to energy bound for the error in the tip of T_1D_1 robotic arm for different values of the scaled prestress in the strings. The increased stiffness due to increased prestress reduces the values of Γ_{ie}. The same trend can be observed for the plot on the right for the $\mathcal{H}_\infty$ norm of the system which is also the gain from unit energy disturbance to energy in the error of the node position for the tip of T_1D_1 robotic arm. The value for the $\mathcal{H}_\infty$ norm decreases with the increased prestress.

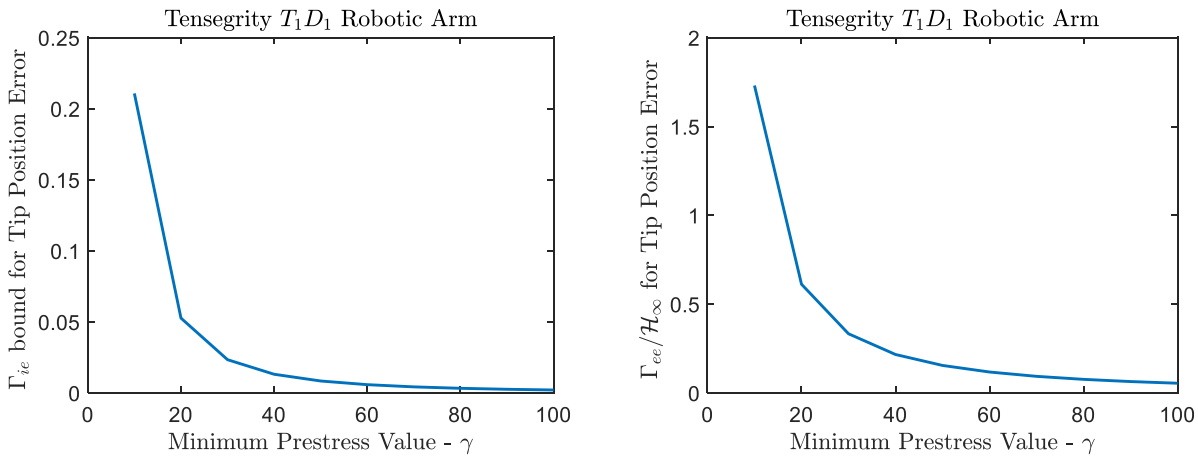

Figure 8.3: Left: Γ_{ie} bound for different values of the scaled prestress. Right: $\mathcal{H}_\infty$ bound for different values of the scaled prestress.

8.5 Closed-Loop response with different performance objectives

8.5.1 Information Architecture Design

This subsection is taken from the following paper by Li and Skelton [94]. A major direction of research is to extend control theory to include Information Precision and Architecture in control design, and to show the tractability of integrating the design of information precision and control. This enlarges the set of solved linear control problems, from solutions of linear controllers with sensors/actuators prespecified, to solutions which specify the sensor/actuator requirements jointly with the control solution [94]. Let us consider the linear control system:

$$\begin{bmatrix} \dot{x} \\ y \\ z \end{bmatrix} = \begin{bmatrix} A & D_p & B \\ C_y & D_y & B_y \\ C_z & D_z & 0 \end{bmatrix} \begin{bmatrix} x \\ w \\ u \end{bmatrix}, \quad \begin{bmatrix} u \\ \dot{x}_c \end{bmatrix} = \begin{bmatrix} D_c & C_c \\ B_c & A_c \end{bmatrix} \begin{bmatrix} z \\ x_c \end{bmatrix} = G \begin{bmatrix} z \\ x_c \end{bmatrix}. \tag{8.99}$$

Suppose that $D_y = 0$, $B_y = 0$, $D_p = [D_{pn} \quad D_a \quad 0]$, and $D_z = [0 \quad 0 \quad D_s]$. The vector $w^T = \begin{bmatrix} w_p^T & w_a^T & w_s^T \end{bmatrix}$ contains process noise w_p, actuator noise w_a, and sensor noise w_s. These disturbances are modeled as independent zero mean white noises with intensities W_p, W_a, and W_s, respectively. The process noise intensity W_p was assumed to be known and fixed. The actuator and

sensor precisions are defined as the inverse of the noise intensity (or variance in the discrete-time case) in each channel as:

$$\text{diag}(\gamma_a) \triangleq \Gamma_a \triangleq {W_a}^{-1}, \;\; \text{diag}(\gamma_s) \triangleq \Gamma_s \triangleq {W_s}^{-1}. \tag{8.100}$$

It was also assumed that the price of each actuator/sensor is proportional to the precision associated with that instrument. Therefore, the total cost of all actuators and sensors is:

$$\$ = p_a^T \gamma_a + p_s^T \gamma_s, \tag{8.101}$$

where p_a and p_s are vectors containing the price per unit of actuator precision and sensor precision, respectively.

Theorem 8.5.1. *[94] Let $\bar{\$}$ represent the budget; the allowed upper bound on sensor/actuator costs, and $\bar{\gamma}_a$ and $\bar{\gamma}_s$ represent the limit on available precisions of actuators and sensors. Then, there exists a dynamic controller G and choices of sensor/actuator precisions Γ_s, Γ_a that satisfy the constraints:*

$$\$ < \bar{\$}, \;\; \gamma_a < \bar{\gamma}_a, \;\; \gamma_s < \bar{\gamma}_s, \;\; \mathbb{E}[uu^T] < \bar{U}, \quad \mathbb{E}[yy^T] < \bar{Y}, \tag{8.102}$$

if and only if there exist matrices L, F, Q, X, Z, and vectors γ_a, and γ_s such that the following LMIs are satisfied:

$$p_a^T \gamma_a + p_s^T \gamma_s < \bar{\$}, \;\; \gamma_a < \bar{\gamma}_a, \;\; \gamma_s < \bar{\gamma}_s, \tag{8.103}$$

$$\begin{bmatrix} \bar{Y} & C_y X & C_y \\ (C_y X)^T & X & I \\ {C_y}^T & I & Z \end{bmatrix} > 0, \quad \begin{bmatrix} \bar{U} & L & 0 \\ L^T & X & I \\ 0 & I & Z \end{bmatrix} > 0, \quad \begin{bmatrix} \boldsymbol{\Phi}_{11} & \boldsymbol{\Phi}_{12} \\ \boldsymbol{\Phi}_{12}^T & \boldsymbol{\Phi}_{22} \end{bmatrix} < 0, \tag{8.104}$$

$$\boldsymbol{\Phi}_{11} = \boldsymbol{\phi} + \boldsymbol{\phi}^T, \;\; \boldsymbol{\phi} = \begin{bmatrix} AX + BL & A \\ Q & ZA + FC_z \end{bmatrix}, \tag{8.105}$$

$$\boldsymbol{\Phi}_{12} = \begin{bmatrix} D_{pn} & D_a & 0 \\ ZD_{pn} & ZD_a & FD_s \end{bmatrix}, \;\; \boldsymbol{\Phi}_{22} = \begin{bmatrix} -{W_P}^{-1} & 0 & 0 \\ 0 & -\Gamma_a & 0 \\ 0 & 0 & -\Gamma_s \end{bmatrix}. \tag{8.106}$$

Note that the matrix inequalities (8.103)–(8.106) are LMIs in the collection of variables $(L, F, Q, X, Z, \gamma_a, \gamma_s)$, hence, the joint control/sensor/actuator design is a convex problem. After a solution $(L, F, Q, X, Z, \gamma_a, \gamma_s)$ is found using the LMIs (8.103)–(8.106), then, the problem (8.102) is solved for the controller as:

$$G = \begin{bmatrix} 0 & I \\ V_l^{-1} & -V_l^{-1}ZB \end{bmatrix} \begin{bmatrix} Q - ZAX & F \\ L & 0 \end{bmatrix} \begin{bmatrix} 0 & V_r^{-1} \\ I & -C_z X V_r^{-1} \end{bmatrix}, \tag{8.107}$$

where V_l and V_r are left and right factors of the matrix $I - ZX$ (which can be found from the singular value decomposition $I - ZX = U\Sigma V^T = (U\Sigma^{1/2})(\boldsymbol{\Sigma}^{1/2}V^T) = (V_l)(V_r)$).

8.5.1.1 Result for T_1D_1 Robotic Arm with full state feedback

This subsection provides the results with disturbance as zero mean white noise applied to all the nodes and output as the tip of the T_1D_1 robotic arm. The plots are generated for process noise covariance of $W_p = 0.01$N and actuator and sensor precision bound $\bar{\gamma}_a = \bar{\gamma}_s = 1000$ with 1\$ price for unit precision value.

Figure 8.4 shows the plots for output covariance $\bar{Y}$ for the different values of input covariance bounds. Ten different curves are shown for different values of price bounds $\bar{\$}$. It can be observed from the figure that increasing the bound on available control reduces the covariance bound on output. The same is observed for relaxing the budget constraint as more precise sensors and actuators can be used to control the covariance.

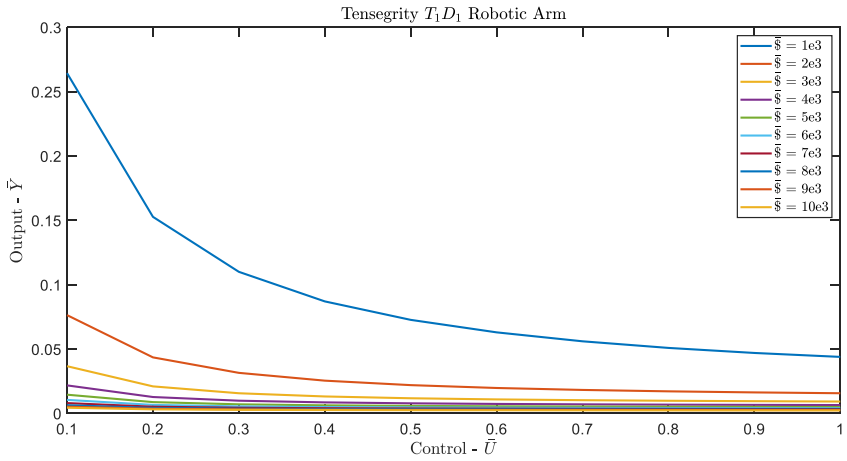

Figure 8.4: The plots between $\bar{Y}$ and $\bar{U}$ for different values of $\bar{\$}$ with both position and velocity of all the nodes available for feedback.

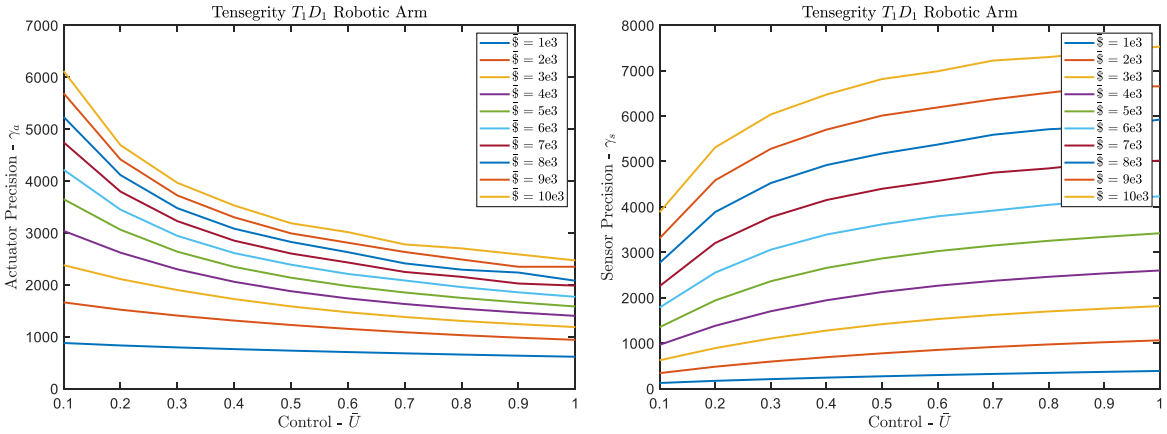

Figure 8.5: The plots between actuator/sensor precision γ_a/γ_s and $\bar{U}$ for different values of $\bar{\$}$ with both position and velocity of all the nodes available for feedback.

Figure 8.5 shows the plots for the total price of actuators and the total price of sensors for different bounds on the control input. It is obvious that both the prices for actuators and sensors will increase with the increase in budget constraints. However, one interesting observation was that the price for actuators decreases with an increase in $\bar{U}$, and the price for sensors increases with an increase in $\bar{U}$. It can be explained as with higher control capability, more precision is required on measurement as compared to precise actuation.

8.5.1.2 *Result for T_1D_1 Robotic Arm with only position as feedback*

Figure 8.6 shows the plots for $\bar{Y}$ and $\bar{U}$ for different values of $\bar{\$}$ with only position of all the nodes available for feedback. Note that the bound on the output covariance has increased due to less measurement information available for feedback. The same trend of decrease in output bound with relaxed input and budget constraint is observed here also.

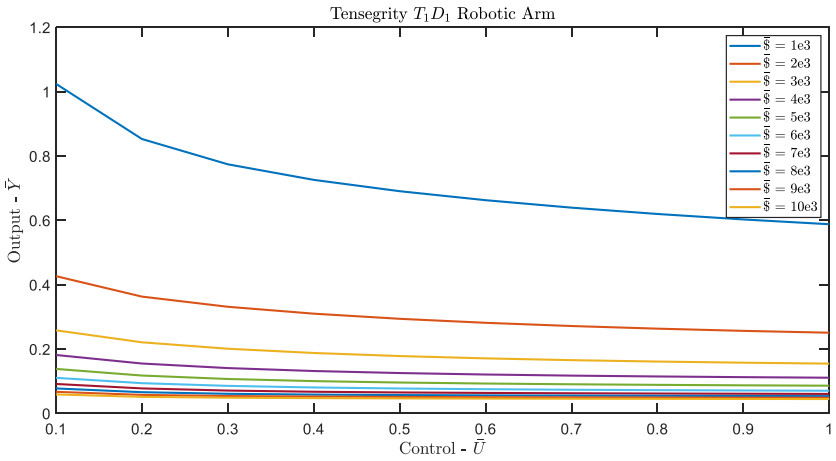

Figure 8.6: The plots between $\bar{Y}$ and $\bar{U}$ for different values of $\bar{\$}$ with only position of all the nodes available for feedback.

Figure 8.7 shows the plots for the total price of actuators and plots for the total price of sensors for different bounds on control input with only position available as feedback. A similar observation that the price for actuators decreases with an increase in $\bar{U}$ and price for sensors increases with an increase in $\bar{U}$ was also observed here.

Table 8.1 provides the result for sensor precision with least price required to bound the output and input covariance as $\bar{Y} = 0.1$ and $\bar{U} = 0.1$, respectively. The table provides the precision value with only positions available for the feedback. The precision value is given for all the nodes and along all the three axes. The most precise sensor is required for the position of the tip of the robotic arm which is the output to be controlled. Table 8.2 gives the precision values for the actuation of the strings. The highest precision is required for the strings - 4,5, and 6, which are

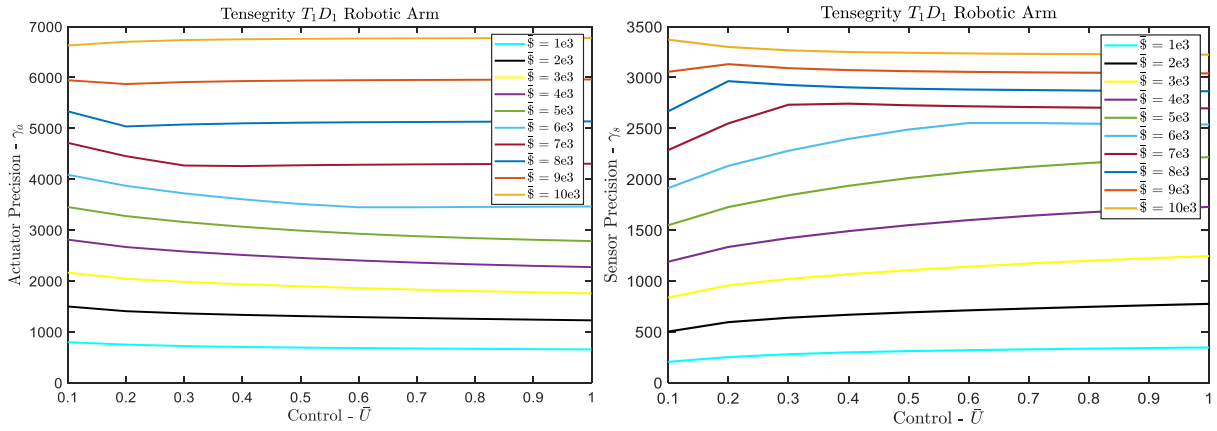

Figure 8.7: The plots between actuator/sensor precision γ_a/γ_s and $\bar{U}$ for different values of $\bar{\$}$ with only position of all the nodes available for feedback.

Table 8.1: Sensor Precision for the measurement of position of x, y and z coordinates of all the nodes except nodes n_1, n_7, n_8, n_9 (refer to Fig.8.1).

	n2	n3	n4	n5	n6	n10	n11	n12	n13	n14	n15
x	0.00	0.00	0.00	0.00	0.00	0.00	0.00	0.00	0.00	0.00	0.00
y	135.74	20.51	20.51	8.16	8.16	0.00	8.73	8.73	0.00	25.98	25.98
z	137.26	33.12	7.10	9.43	9.43	12.56	0.00	0.00	41.54	0.00	0.00

directly connected to node 2. The least precision is required for the strings - 7,8, and 9, which are required only to globally stabilize the T-bar part of the T_1D_1 robotic arm.

8.6 Integrating Structure, Information Architecture and Control Design

A continuous linear time-invariant system is described by the following *descriptor* state-space representation:

$$E(\alpha)\dot{x} = A(\alpha)x + Bu + D_p(\alpha)w_p + D_a(\alpha)w_a, \tag{8.108}$$

$$y = C_y(\alpha)x, \quad \text{(output)} \tag{8.109}$$

$$z = C_z x + D_s w_s, \quad \text{(measurement)} \tag{8.110}$$

Table 8.2: Actuator Precision for all the strings (refer to Fig.8.1).

Str No.	γ_a	Str No.	γ_a	Str No.	γ_a	Str No.	γ_a
1	38.09	7	9.16	13	10.44	19	31.23
2	37.54	8	9.18	14	13.85	20	30.46
3	37.54	9	9.16	15	10.44	21	30.46
4	68.49	10	43.93	16	63.22	22	34.49
5	67.34	11	43.26	17	70.42	23	34.08
6	67.34	12	43.26	18	63.22	24	34.08

where $x \in \mathbb{R}^n$ is the state of the system, $u \in \mathbb{R}^m$ is the control vector, $y \in \mathbb{R}^p$ is the output of the system, $z \in \mathbb{R}^\ell$ denotes the measurement vector, and w_i for $i = a, s, p$ are noisy inputs to the system. The vector α consists of generalized variable structure parameters that can be treated as decision variables in the system design problem. It is assumed that the following matrices are affine in the parameters α: $A(\alpha), E(\alpha), D_p(\alpha), D_a(\alpha)$ and $C_y(\alpha)$. Note that in a typical second-order system, it is paramount to adopt the descriptor representation in order to preserve the affine property of the system mass matrix. The matrix $E(\alpha)$ is also assumed to be full rank.

In the above model (8.108-8.110), the actuator noise is defined by w_a, sensor noise by w_s, and ambient process noise by w_p. These vectors are modeled as independent zero mean white noises with intensities W_a, W_s and W_p, respectively, i.e.:

$$\mathbb{E}_\infty(w_i) = 0, \tag{8.111}$$

$$\mathbb{E}_\infty(w_i w_i^\mathsf{T}) = W_i \delta(t - \tau), \tag{8.112}$$

where $i = a, s, p$, and $\mathbb{E}_\infty(x) = \lim_{t\to\infty} \mathbb{E}(x)$ which denotes the asymptotic expected value of the random variable x. We assume the process noise intensity W_p to be known and fixed. The actuator and sensor precisions are defined to be inversely proportional to the respective noise intensities.

$$\Gamma_a \triangleq W_a^{-1}, \;\; \Gamma_s \triangleq W_s^{-1}. \tag{8.113}$$

We also define the vectors γ_a and γ_s such that:

$$\Gamma_a \triangleq \text{diag}(\gamma_a), \;\; \Gamma_s \triangleq \text{diag}(\gamma_s). \tag{8.114}$$

As defined in [94], we associate a price to each actuator/sensor that is inversely proportional to the noise intensity associated with that instrument. In this work, prices associated with the structure parameters are also considered. Therefore, the total design price can be expressed as:

$$\$ = p_a^{\mathsf{T}}\gamma_a + p_s^{\mathsf{T}}\gamma_s + p_\alpha^{\mathsf{T}}\alpha, \tag{8.115}$$

where p_a, p_s and p_α are vectors containing the price per unit of actuator precision, sensor precision and price per unit of structure parameter, respectively. Now, the problem to be solved is defined as:

Design a dynamic compensator of the form:

$$\begin{aligned} \dot{x}_c &= A_c x_c + B_c z, \\ u &= C_c x_c + D_c z, \end{aligned} \tag{8.116}$$

and simultaneously select the structure parameter values, appropriate actuator and sensor precisions such that the following constraints are satisfied:

$$\begin{aligned} \$ < \bar{\$}, \;\; \gamma_a < \bar{\gamma}_a, \;\; \gamma_s < \bar{\gamma}_s, \;\; \bar{\alpha}_L < \alpha < \bar{\alpha}_U, \\ \mathbb{E}_\infty(uu^{\mathsf{T}}) < \bar{U}, \;\; \mathbb{E}_\infty(yy^{\mathsf{T}}) < \bar{Y} \end{aligned} \tag{8.117}$$

for given $\bar{\$}$, $\bar{U}$, $\bar{Y}$, $\bar{\gamma}_a$, $\bar{\gamma}_s$, $\bar{\alpha}_L$, and $\bar{\alpha}_U$.

8.6.1 Solution to the Dynamic Compensation Problem

Theorem 8.6.1. *Let a continuous time-invariant linear system be described by the descriptor state space equation (8.108), the output equation (8.109) and the measurement equation (8.110). There exist controller matrices A_c, B_c, C_c and structure parameters α such that the cost and performance*

constraints (8.117) are satisfied, if and only if for some constant matrix G, there exists a symmetric matrix Q, vectors γ_a, γ_s and α such that the following LMIs are satisfied:

$$p_a^{\mathsf{T}}\gamma_a + p_s^{\mathsf{T}}\gamma_s + p_\alpha^{\mathsf{T}}\alpha < \bar{\$}, \tag{8.118}$$

$$\gamma_a < \bar{\gamma}_a, \;\; \gamma_s < \bar{\gamma}_s, \tag{8.119}$$

$$\bar{\alpha}_L < \alpha < \bar{\alpha}_U, \tag{8.120}$$

$$\begin{bmatrix} \bar{U} & M_{cl} \\ M_{cl}^{\mathsf{T}} & Q \end{bmatrix} > 0, \quad \begin{bmatrix} \bar{Y} & C_{cl} \\ C_{cl}^{\mathsf{T}} & Q \end{bmatrix} > 0, \tag{8.121}$$

$$\begin{bmatrix} (\star) & B_{cl} & A_{cl} & E_{cl} \\ B_{cl}^{\mathsf{T}} & -W^{-1} & 0 & 0 \\ A_{cl}^{\mathsf{T}} & 0 & -Q & 0 \\ E_{cl}^{\mathsf{T}} & 0 & 0 & -Q \end{bmatrix} < 0, \tag{8.122}$$

where

$$(\star) = -(A_{cl} - E_{cl})G^{\mathsf{T}} - G(A_{cl} - E_{cl})^{\mathsf{T}} + GQG^{\mathsf{T}},$$

$$W = \begin{bmatrix} W_p & 0 & 0 \\ 0 & W_a & 0 \\ 0 & 0 & W_s \end{bmatrix}, \quad A_{cl} = \begin{bmatrix} A(\alpha) & BC_c \\ B_cC_z & A_c \end{bmatrix},$$

$$E_{cl} = \begin{bmatrix} E(\alpha) & 0 \\ 0 & I_n \end{bmatrix}, B_{cl} = \begin{bmatrix} D_p(\alpha) & D_a(\alpha) & 0 \\ 0 & 0 & B_cD_s \end{bmatrix},$$

$$C_{cl} = \begin{bmatrix} C_y(\alpha) & 0 \end{bmatrix}, \quad M_{cl} = \begin{bmatrix} 0 & C_c \end{bmatrix},$$

and I_n is a $n \times n$ identity matrix.

Proof. Let us define the augmented vector $\tilde{x}$ and w as:

$$\tilde{x}^{\mathsf{T}} = \begin{bmatrix} x^{\mathsf{T}} & x_c^{\mathsf{T}} \end{bmatrix}, \quad w^{\mathsf{T}} = \begin{bmatrix} w_p^{\mathsf{T}} & w_a^{\mathsf{T}} & w_s^{\mathsf{T}} \end{bmatrix}. \tag{8.123}$$

The closed loop dynamics for the state $\tilde{x}$ can be written in the descriptor representation form along with the output and control equations as:

$$E_{cl}\dot{\tilde{x}} = A_{cl}\tilde{x} + B_{cl}w, \tag{8.124}$$

$$y = C_{cl}\tilde{x}, \tag{8.125}$$

$$u = M_{cl}\tilde{x} + F_{cl}w, \tag{8.126}$$

where all the close loop matrices can easily be obtained from the system equations (8.108-8.110) and controller equations (8.116).

Defining $\bar{A}_{cl} = E_{cl}^{-1}A_{cl}$ and $\bar{B}_{cl} = E_{cl}^{-1}B_{cl}$ and rearranging equation (8.124) gives:

$$\dot{\tilde{x}} = \bar{A}_{cl}x + \bar{B}_{cl}w. \tag{8.127}$$

It is a standard result that the above closed loop system is stable if and only if there exists a positive definite symmetric matrix X such that:

$$\bar{A}_{cl}X + X\bar{A}_{cl}^{\mathsf{T}} + \bar{B}_{cl}W\bar{B}_{cl}^{\mathsf{T}} < 0. \tag{8.128}$$

Multiplying the inequality (8.128) from left by E_{cl} and from right by E_{cl}^{T} yields:

$$A_{cl}XE_{cl}^{\mathsf{T}} + E_{cl}XA_{cl}^{\mathsf{T}} + B_{cl}WB_{cl}^{\mathsf{T}} < 0. \tag{8.129}$$

Applying Schur's complement on (8.129) gives:

$$\begin{bmatrix} A_{cl}XE_{cl}^{\mathsf{T}} + E_{cl}XA_{cl}^{\mathsf{T}} & B_{cl} \\ B_{cl}^{\mathsf{T}} & -W^{-1} \end{bmatrix} < 0. \tag{8.130}$$

It can be shown that after substitution of E_{cl}, A_{cl} and B_{cl}, inequality (8.130) does not form an LMI since it is not affine in the decision variables A_c, B_c, α, etc. On completing the squares, the

inequality (8.130) can be rewritten as:

$$\begin{bmatrix} A_{cl}XA_{cl}^{\mathsf{T}} + E_{cl}XE_{cl}^{\mathsf{T}} & & B_{cl} \\ -(A_{cl}-E_{cl})X(A_{cl}-E_{cl})^{\mathsf{T}} & & \\ B_{cl}^{\mathsf{T}} & & -W^{-1} \end{bmatrix} < 0. \tag{8.131}$$

Defining $\delta \triangleq (A_c, B_c, C_c, \gamma_a, \gamma_s, \alpha, Q)$, $Q \triangleq X^{-1}$, and applying Schur's complement, we can write the inequality (8.131) as:

$$\mathbb{F}(\delta) \triangleq \begin{bmatrix} (\bullet) & B_{cl} & A_{cl} & E_{cl} \\ B_{cl}^{\mathsf{T}} & -W^{-1} & 0 & 0 \\ A_{cl}^{\mathsf{T}} & 0 & -Q & 0 \\ E_{cl}^{\mathsf{T}} & 0 & 0 & -Q \end{bmatrix} < 0, \tag{8.132}$$

where $(\bullet) = -(A_{cl} - E_{cl})X(A_{cl} - E_{cl})^{\mathsf{T}}$. Note that $\mathbb{F}(\delta)$ is not an LMI. Let us introduce the convexifying algorithm Lemma to write a new LMI.

Lemma 8.6.1. ***Convexifying Algorithm Lemma.*** *Let δ, η belong to a convex set ϕ, and $\mathbb{F}(\delta)$ be a first order differentiable non-convex matrix function. A convexifying potential function is a first order differentiable function $\mathbb{G}(\delta, \eta)$ such that the function $\mathbb{F}(\delta) + \mathbb{G}(\delta, \eta)$ is convex in δ for all $\delta, \eta \in \phi$. Thus, if $\mathbb{F}(\delta)$ satisfies certain conditions, a stationary point of the non-convex optimization problem*

$$\bar{\delta} = \arg\min_{\delta \in \Omega} f(\delta), \;\; \Omega = \{\delta \in \phi | \mathbb{F}(\delta) < 0\}, \tag{8.133}$$

can be obtained by iterating over a sequence of convex subproblems given by

$$\bar{\delta}_{k+1} = \arg\min_{\delta \in \Omega_k} f(\delta), \Omega_k = \{\delta \in \phi | \mathbb{F}(\delta) + \mathbb{G}(\delta, \delta_k) < 0\}. \tag{8.134}$$

To ensure that the optimality conditions of both optimization problems (8.133) and (8.134) are identical, the potential function $\mathbb{G}$ should be non-negative definite with $\mathbb{G}(\delta, \eta) = 0$ if and only if

$\delta = \eta$.

Remark 8.6.1. *The previous Lemma is proven and discussed in further detail in [103]. Although the Convexifying Algorithm will converge to a stationary point, a global solution is not guaranteed.*

To use the previous Lemma, let us define the matrix G as:

$$G(\eta) \triangleq (A_{cl} - E_{cl})X, \tag{8.135}$$

and the convexifying potential function as:

$$\mathbb{G}(\delta, \eta) \triangleq \begin{bmatrix} (*) & \mathbf{0} \\ \mathbf{0} & \mathbf{0} \end{bmatrix}, \tag{8.136}$$

$$(*) = (A_{cl} - E_{cl} - G(\eta)Q)X(A_{cl} - E_{cl} - G(\eta)Q)^{\mathsf{T}},$$

$$\mathbb{G}(\delta, \eta) \geq 0, \tag{8.137}$$

The matrix function $\mathbb{F}(\delta) + \mathbb{G}(\delta, \eta)$:

$$\begin{bmatrix} (\star) & B_{cl} & A_{cl} & E_{cl} \\ B_{cl}^{\mathsf{T}} & -W^{-1} & 0 & 0 \\ A_{cl}^{\mathsf{T}} & 0 & -Q & 0 \\ E_{cl}^{\mathsf{T}} & 0 & 0 & -Q \end{bmatrix} < 0, \tag{8.138}$$

where $(\star) = -(A_{cl} - E_{cl})G^{\mathsf{T}} - G(A_{cl} - E_{cl})^{\mathsf{T}} + GQG^{\mathsf{T}}$, is convex, where the dependency of the matrix G on η is omitted for brevity. The function $\mathbb{G}(\delta, \eta)$ satisfies the convexifying assumptions since it is positive semidefinite and $\mathbb{G}(\delta, \eta) = 0$ if and only if $\delta = \eta$. Furthermore, using Lemma (8.6.1), it can be shown that any solution to (8.138) will also satisfy (8.132) [103].

The second constraint of the constraint set (8.117) can be evaluated by substituting in the

expression for the control law (8.126) given by:

$$\mathbb{E}_\infty(uu^\mathsf{T}) = \mathbb{E}_\infty((M_{cl}\tilde{x})(M_{cl}\tilde{x})^\mathsf{T}) + \mathbb{E}_\infty((F_{cl}\tilde{w})(F_{cl}\tilde{w})^\mathsf{T}), \tag{8.139}$$

$$\mathbb{E}_\infty(uu^\mathsf{T}) < \bar{U}, \tag{8.140}$$

$$M_{cl}XM_{cl}^\mathsf{T} + F_{cl}WF_{cl}^\mathsf{T} < \bar{U}. \tag{8.141}$$

The second term can grow unbounded if $F_{cl} \neq 0$. Hence, substituting for $F_{cl} = 0$ in the above equation gives:

$$M_{cl}XM_{cl}^\mathsf{T} < \bar{U} \text{ and } D_c = 0 \ (D_s \text{ is full rank}). \tag{8.142}$$

and applying Schur's complement to first term results in left inequality of equation (8.121). It is then straightforward to show that the last constraint of (8.117) is satisfied if and only if

$$C_{cl}XC_{cl}^\mathsf{T} < \bar{Y}. \tag{8.143}$$

Applying Schur's complement to this inequality results in (8.121). Finally, first four constraints in (8.117) are first four inequalities of Theorem 8.6.1. □

Remark 8.6.2. *Assume that $\bar{\gamma}_a$ and $\bar{\gamma}_s$ are dictated by the marketplace. Let four parameters out of the set ($\bar{\alpha}_L$, $\bar{\alpha}_U$,$\bar{\$}$, $\bar{U}$, $\bar{Y}$) be hard constraints and let the fifth parameter, denoted $\bar{z}$, be any value for which the LMIs of Theorem 8.6.1 are feasible. The following iterative algorithm takes advantage of Lemma 8.6.1 to find an extrema for $\bar{z}$ (a minimum if $\bar{z} = \bar{\alpha}_U, \bar{\$}, \bar{U}, \bar{Y}$ or a maximum if $\bar{z} = \bar{\alpha}_L$).*

Extrema-Finding Algorithm using the Convexifying Potential Function

- Set fixed nominal values for $\bar{z}_0$ and α_0. Compute controller matrices $A_{c,0}$, $B_{c,0}$, $C_{c,0}$, precision vectors $\gamma_{a,0}$, $\gamma_{s,0}$ and inverse covariance matrix Q_0 according to [94] or some alternative method. Set ϵ to some prescribed tolerance and $k = 0$

- **Repeat:** Set $G_k \leftarrow (A_{cl}(\alpha_k) - E_{cl}(\alpha_k))Q_k^{-1}$

-For fixed $G = G_k$, find the extrema of $\bar{z}$ for which the LMIs of Theorem 8.6.1 are feasible

-Denote the solution ($\bar{z}_{k+1}$, α_{k+1}, $A_{c,k+1}$, $B_{c,k+1}$, $C_{c,k+1}$,$\gamma_{a,k+1}$, $\gamma_{s,k+1}$,Q_{k+1})

-Set k = k+1

- **Until:** $\|\bar{z}_k - \bar{z}_{k-1}\| < \epsilon$

8.7 State Feedback Problem

8.7.1 Problem Statement

Consider the situation where full-state feedback is available for measurement. The system can now be described as:

$$E(\alpha)\dot{x} = A(\alpha)x + Bu + D_p(\alpha)w_p + D_a(\alpha)w_a, \tag{8.144}$$

$$y = C_y(\alpha)x, \text{ (output)} \tag{8.145}$$

As there is no measurement noise, the total design price is expressed as:

$$\$ = p_a^{\mathsf{T}}\gamma_a + p_\alpha^{\mathsf{T}}\alpha. \tag{8.146}$$

The state feedback problem can now be defined as:

Design a state feedback controller $u = -Kx$ and simultaneously select the structure parameters and the actuator precisions such that the following constraints are satisfied:

$$\$ < \bar{\$}, \gamma_a < \bar{\gamma}_a, \bar{\alpha}_L < \alpha < \bar{\alpha}_U, \ \mathbb{E}_\infty(uu^{\mathsf{T}}) < \bar{U}, \mathbb{E}_\infty(yy^{\mathsf{T}}) < \bar{Y}, \tag{8.147}$$

for given $\bar{\$}$, $\bar{U}$, $\bar{Y}$, $\bar{\gamma}_a$, $\bar{\alpha}_L$, and $\bar{\alpha}_U$.

8.7.2 Solution to the State Feedback Problem

Lemma 8.7.1. *Let a continuous time-invariant linear system be described by the descriptor state space equation (8.144) and the output equation (8.145). There exists a controller gain K and structure parameters α such that the cost and performance constraints (8.147) are satisfied if and*

only if for some constant matrix G there exists a symmetric matrix Q and vectors γ_a and α such that the following LMIs are satisfied:

$$p_a^{\mathsf{T}}\gamma_a + p_\alpha^{\mathsf{T}}\alpha < \bar{\$}, \tag{8.148}$$

$$\gamma_a < \bar{\gamma}_a, \quad \bar{\alpha}_L < \alpha < \bar{\alpha}_U, \tag{8.149}$$

$$\begin{bmatrix} \bar{U} & K \\ K^{\mathsf{T}} & Q \end{bmatrix} > 0, \quad \begin{bmatrix} \bar{Y} & C_y(\alpha) \\ C_y(\alpha)^{\mathsf{T}} & Q \end{bmatrix} > 0, \tag{8.150}$$

$$\begin{bmatrix} (\star) & B_{cl} & A_{cl} & E(\alpha) \\ B_{cl}^{\mathsf{T}} & -W^{-1} & 0 & 0 \\ A_{cl}^{\mathsf{T}} & 0 & -Q & 0 \\ E^{\mathsf{T}}(\alpha) & 0 & 0 & -Q \end{bmatrix} < 0, \tag{8.151}$$

where

$$(\star) = -(A_{cl} - E(\alpha))G^{\mathsf{T}} - G(A_{cl} - E(\alpha))^{\mathsf{T}} + GQG^{\mathsf{T}},$$

$$W = \begin{bmatrix} W_p & 0 \\ 0 & W_a \end{bmatrix}, \quad A_{cl} = A(\alpha) - BK,$$

$$B_{cl} = \begin{bmatrix} D_p(\alpha) & D_a(\alpha) \end{bmatrix}.$$

Remark 8.7.1. *The proof is excluded as it follows very closely with Theorem 8.6.1.*

8.8 Tensegrity Formulation in Descriptor Form

Equation (8.61) for a class-k tensegrity structure can be represented in the following descriptor form:

$$\begin{bmatrix} I & 0 \\ 0 & \mathcal{M}_k \end{bmatrix} \begin{bmatrix} \dot{\eta}_2 \\ \ddot{\eta}_2 \end{bmatrix} = \begin{bmatrix} 0 & I \\ -\mathcal{K}_k & -\mathcal{D}_k \end{bmatrix} \begin{bmatrix} \eta_2 \\ \dot{\eta}_2 \end{bmatrix} + \begin{bmatrix} 0 \\ \mathcal{F}_k \end{bmatrix} w + \begin{bmatrix} 0 \\ \mathcal{B}_k \end{bmatrix} \gamma + \begin{bmatrix} 0 \\ \mathcal{B}_k \end{bmatrix} w_a. \tag{8.152}$$

Equation (8.152) can also represent class-1 dynamics when the subscript 'k' is omitted from

$\mathcal{M}_k, \mathcal{D}_k, \mathcal{K}_k, \mathcal{B}_k, \mathcal{F}_k$, and $\tilde{\eta}_2$ is replaced by $\tilde{n}$. In this problem formulation, we define the control input to be force density in the strings ($u = \gamma$), process noise to be ($w_p = w$), actuator noise to be w_a (same coefficient matrix), and structure parameter to be initial prestress or force density at equilibrium condition ($\alpha = \bar{\gamma}$). It is to be noted that $\mathcal{K}_k(\bar{\gamma})$ is affine in initial prestress value $\bar{\gamma}$ as:

$$\mathcal{K}_k(\bar{\gamma}) = V_2^{\mathsf{T}}\mathcal{T}^{\mathsf{T}}P_{br}\mathcal{T}\left(C_s^{\mathsf{T}} \otimes I\right)\widehat{(\bar{\gamma} \otimes \mathbb{1})}(C_s \otimes I)V_2 + V_2^{\mathsf{T}}\mathcal{T}^{\mathsf{T}}K_{br}(\bar{f}, \bar{b}, \dot{\bar{b}})\mathcal{T}V_2,$$

where $K_{br}(\bar{f}, \bar{b}, \dot{\bar{b}})$ can also be written as some affine function of $\bar{\gamma}$ as $K_{br}(\bar{f}, \bar{b}, \dot{\bar{b}}) = \mathcal{G}\bar{\gamma}$. Comparing it to system equation (8.108) in chapter 3, we see only system matrix $A(\alpha)$ to be dependent on structure parameter.

8.9 IASD Examples

8.9.1 A 3-story building example

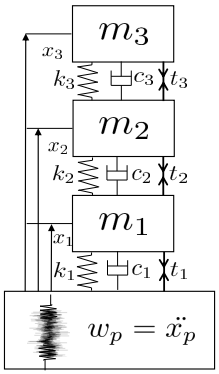

Figure 8.8: 3-Story Building Model

To illustrate the proposed concept of simultaneous optimization of the structure, information architecture, and control, we provide an example of a civil engineering structure. The idea is to design a three-story building to sustain an earthquake of given intensity with active or passive control. The building is modeled as a spring-mass-damper system with all springs, masses, and dampers as variable structure parameters, as shown in Fig. 8.8. The prestressed cables provide the

actuation force on three masses. The dynamics of the system can be written as:

$$\begin{bmatrix} I & 0 \\ 0 & \mathbb{M} \end{bmatrix} \begin{bmatrix} \dot{x} \\ \ddot{x} \end{bmatrix} = \begin{bmatrix} 0 & I \\ -\mathbb{K} & -\mathbb{C} \end{bmatrix} \begin{bmatrix} x \\ \dot{x} \end{bmatrix} + \begin{bmatrix} 0 \\ B_u \end{bmatrix} u + \begin{bmatrix} 0 \\ M \end{bmatrix} w_p + \begin{bmatrix} 0 \\ B_u \end{bmatrix} w_a.$$

where

$$\mathbb{K} = \begin{bmatrix} k_1 + k_2 & -k_2 & 0 \\ -k_2 & k_2 + k_3 & -k_3 \\ 0 & -k_3 & k_3 \end{bmatrix}, B_u = \begin{bmatrix} -1 & 1 & 0 \\ 0 & -1 & 1 \\ 0 & 0 & -1 \end{bmatrix}.$$

$\mathbb{M} = diag(m_1, m_2, m_3)$ and $\mathbb{C}$ can be written identical to $\mathbb{K}$. The control input is a vector of tensions in the cables $u = [t_1\ t_2\ t_3]^T$ and the disturbance due to earthquake (at acceleration level) is modeled as a zero-mean white noise with intensity $W_p = 1$ m^2/s^4, which multiplied by $M = [m_1\ 0\ 0]^T$ gives disturbance force transferred to the first floor due to earthquake. The output and measurement equations can be written as:

$$y = \begin{bmatrix} x_1 & x_2 - x_1 & x_3 - x_2 & \dot{x_1}\ \dot{x_2} - \dot{x_1}\ \dot{x_3} - \dot{x_2} \end{bmatrix}^T$$

$$y = c_y \begin{bmatrix} x \\ \dot{x} \end{bmatrix},\ z = \begin{bmatrix} x \\ \dot{x} \end{bmatrix} + I w_s. \tag{8.153}$$

where output to be minimized is the relative displacement and relative velocity between consecutive floors. We assume all the states are available for measurement with noisy sensors. Constraints used for this example are $\bar{\alpha}_L = 0.2\alpha_0, \bar{\alpha}_U = 3\alpha_0, \bar{\gamma}_a = 1e4, \bar{\gamma}_s = 1e4, p_a = p_s = p_\alpha = 20$.

8.9.1.1 Active to Passive Control

First, we show that minimum control required to bound the output covariance with a given budget constraint constantly decreases while optimizing structure parameters. The output covariance constraint is assumed to be $\mathbb{E}_\infty(y_i^2) = 0.01$ m^2 for $i = 1, 2, 3$ and $\mathbb{E}_\infty(y_i^2) = 0.1$ m^2/s^2

for $i = 4, 5, 6$. Fig. 8.9 shows the variation in structural parameters, when started from nominal values, and decrease in active control during optimization iterations. The required active control decreases from $\bar{U} = 4.5e4$ N^2 to $\bar{U} = 3.5e4$ N^2 when only springs and dampers are considered as optimization variable.

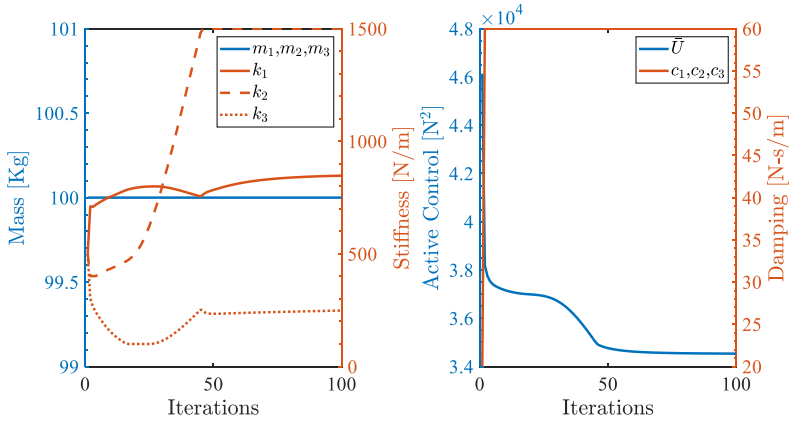

Figure 8.9: Variation in structure parameters with constant mass and required active control. ($\bar{Y} = diag(.01, .01, .01, .1, .1, .1), \bar{\$} = 1e5$).

Second, we assume all the structure parameters to be variables. Fig. 8.10 shows that the control required goes to zero with the optimized structure parameters. The structure can now sustain the earthquake with new passive design i.e., without any control.

8.9.1.2 Trade-off Analysis

The minimum cost required to achieve given output and control covariance is calculated along with the optimized structural parameters. Fig. 8.11 shows the variation in cost and structure parameters value during optimization iterations. As there are prices associated with all the structure parameters, their values go to their respective minimum bound to reduce dollar value. Basically, the algorithm fills up the upper bound on performance and control constraints by reducing the parameters and precisions values, which in turn reduces the total cost.

Finally, Fig. 8.12 shows the decrease in required cost as we relax the output covariance bound

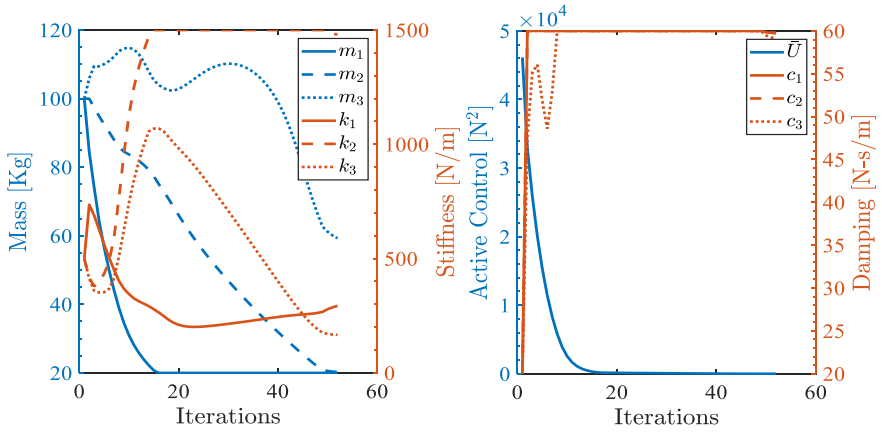

Figure 8.10: Variation in all structure parameters and transition from active to passive control. ($\bar{Y} = diag(.01, .01, .01, .1, .1, .1), \bar{\$} = 1e5$).

for a fixed control requirement. The sensor and actuator precision also monotonically decreases by relaxing the performance constraints. Also, note that more precise measurements are needed for displacement and velocity of the first floor as compared to other floors. A similar decreasing trend in dollar value was observed while relaxing the control covariance bound and fixing the output constraint.

8.9.2 Tensegrity Example - 2D lander

For a given 2D tensegrity structure shown in Figure 8.13, this section optimizes the optimal prestresses in each string, precisions of sensors and actuators, and matrices corresponding to the dynamic controller for covariance control. The bars are shown in black, and the strings are shown in red. The example is inspired by a tensegrity lander where the point mass (node 5) is the payload to capture the images, and the two bars are fixed to ground depicting the lander in the landed position.

The mass for both the bars are assumed to be $m_b = 1$Kg and the mass for point mass is assumed to be $m_s = 0.5$Kg. The tensegrity dynamics is linearized about the equilibrium configuration (corresponding to Figure 8.13) with prestress values of $\alpha_0 = \bar{\gamma} = [1, 2.76, 1, 1, 1, 1, 1]^\mathsf{T}$ and no external force. The disturbances come from the external force which is modeled as a zero-mean white noise with intensity $W_p = 1\text{N}^2$. The disturbances are present only on nodes 2, 3, and 5. All

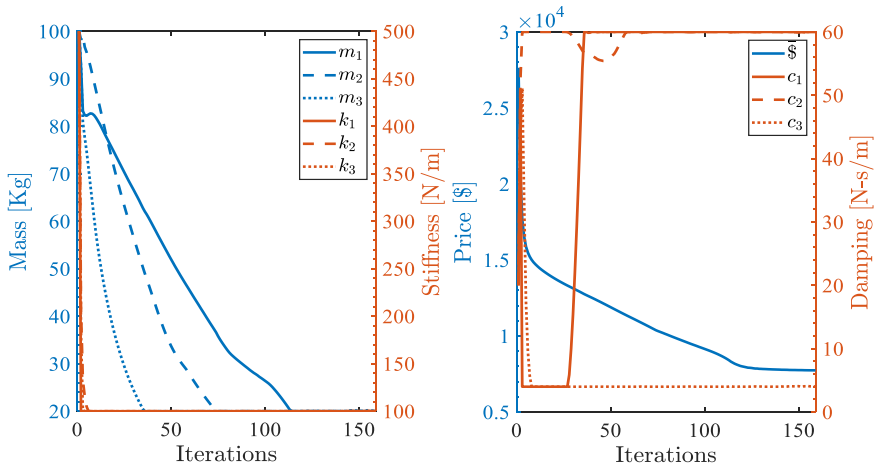

Figure 8.11: Variation in all structure parameters and price value.
($\bar{U} = 1e5, \bar{Y} = diag(.01, .01, .01, .1, .1, .1)$).

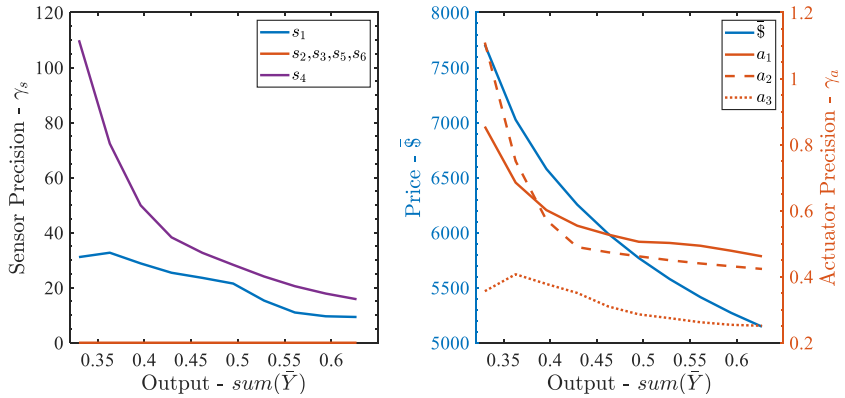

Figure 8.12: Variation in sensor and actuator precision and price value. ($\bar{U} = 1e5, \bar{\$} = 1e5$).

seven strings are actuated to control the structure. The output to be bound is the displacement of payload (node 5) in x and y-direction.

$$y = \begin{bmatrix} n_{5x} \\ n_{5y} \end{bmatrix} = C_y \begin{bmatrix} \eta_{2_\phi} \\ \dot{\eta}_{2_\phi} \end{bmatrix}, \; C_y = \begin{bmatrix} 0 & I \end{bmatrix} \Phi_2 V_{2_\phi} \begin{bmatrix} I & 0 \end{bmatrix}, \tag{8.154}$$

and the measurements are the positions and velocity of nodes 2, 3, and 5 (nodes 1 and 4 are fixed

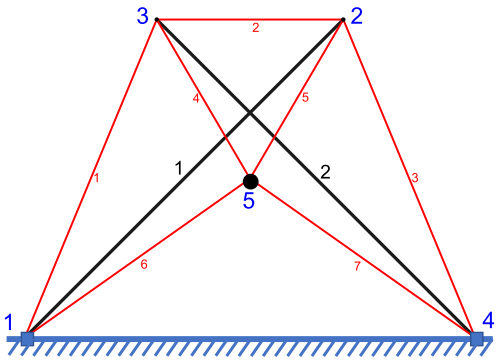

Figure 8.13: 2D Tensegrity Lander

to ground).

$$z = C_z \begin{bmatrix} \eta_{2_\phi} \\ \dot{\eta}_{2_\phi} \end{bmatrix} + I w_s, \; C_z = \begin{bmatrix} \Phi_2 V_{2_\phi} & 0 \\ 0 & \Phi_2 V_{2_\phi} \end{bmatrix}. \tag{8.155}$$

Some values assumed for this example are $\bar{\alpha}_L = 0.1\alpha_0$, $\bar{\alpha}_U = 10\alpha_0, \bar{\gamma}_a = \bar{\gamma}_s = 1e3, p_a = p_s = 2$, and $p_\alpha = 10$.

The surface plot in Figure 8.14 shows the variation in budget requirement $\bar{\$}$ as we change the input covariance bound $\bar{U}$ and output covariance bound $\bar{Y}$. The required budget monotonically decreases with a more relaxed performance constraint for all values of control input bounds. The same decreasing trend in budget follows as we increase the control input bound. This variation is small showing the relatively less strict nature of control covariance bound.

Figure 8.15(a) shows the decreasing variation in the prestress required for all strings as we increase the output covariance bound while maintaining the same control input $\bar{U}$. Basically, less prestress is required for relaxed performance constraints. The result shows that strings 1 and 3 have the same prestress values and variations. This can be understood from the symmetry of the structure. Similarly, strings 4, 5, 6, and 7 follow the same trend. Notice that the optimization requires strings 4, 5, 6, and 7 to have high prestress value as these strings are directly connected

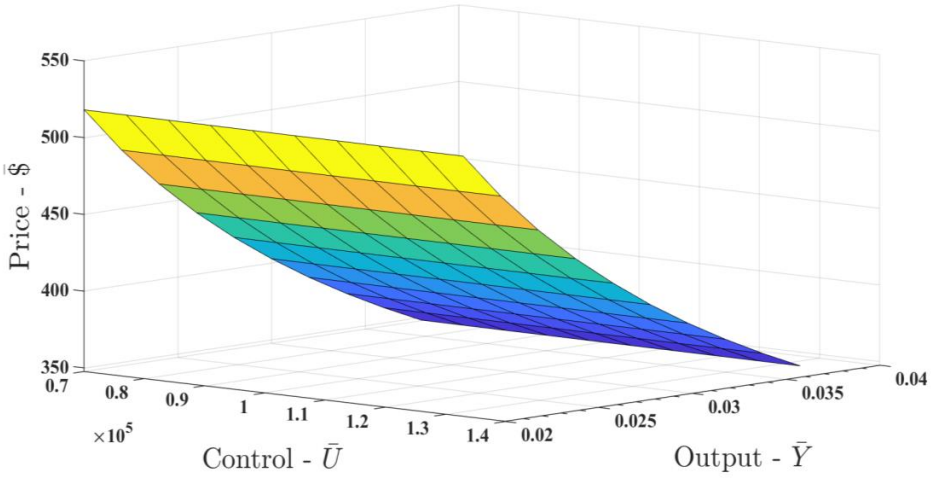

Figure 8.14: A surface plot of the variation in budget with input-$\bar{U}$ and output-$\bar{Y}$.

to the payload. Figure 8.15(b) shows the effectiveness of the algorithm as the price converges in about 20 to 30 iterations. The 10 different lines in the plot represent different values of performance constraints $\bar{Y}$ = (0.02 m^2 to 0.04 m^2).

The variation in required sensor precision with varying output bound $\bar{Y}$ is shown in Figure 8.16(a). The sensors corresponding to $\dot{n}_{2x}$ and $\dot{n}_{3x}$ overlaps because of symmetry. Similarly, $\dot{n}_{2y}$ and $\dot{n}_{3y}$ overlaps. As the output to be bounded is the displacement of node 5 in x and y-direction, higher precision is required for $\dot{n}_{5x}$ and $\dot{n}_{5y}$. The figure shows that less precision on sensors and actuators is required for relaxed performance requirements. Figure 8.16(b) shows that more precision is required on strings 4, 5, 6, and 7 as these strings are directly connected to the payload.

8.9.3 Tensegrity Beam Example

For a given 2D tensegrity structure shown in Figure 8.17, this section optimizes the optimal prestresses in each string, precisions of sensors and actuators, and matrices corresponding to the dynamic controller for covariance control. The bars are shown in black, and the strings are shown in red. The mass for both the bars are assumed to be $m_b = 1$Kg and the mass for point mass is assumed to be $m_s = 0.5$Kg. The tensegrity dynamics is linearized about the equilibrium

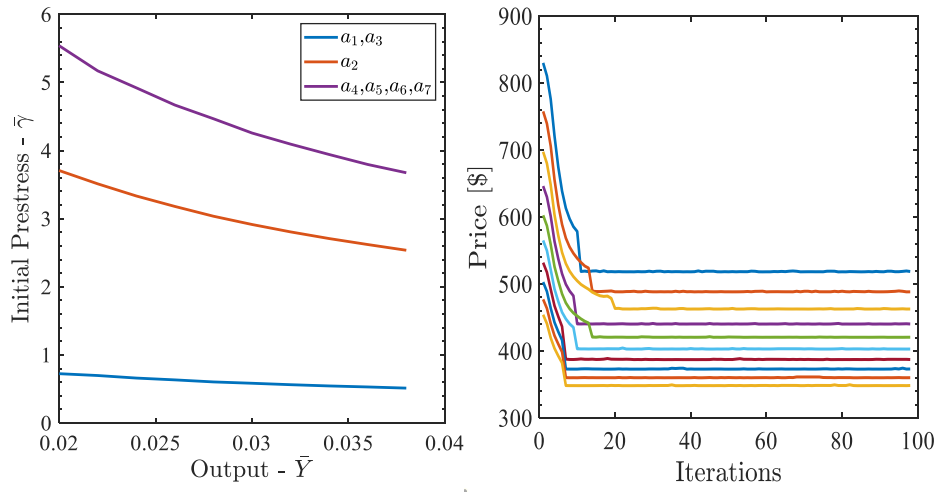

Figure 8.15: (a)Variation in the optimal prestress with $\bar{Y}$. (b) Convergence of minimum price required. $\bar{U} = 10^4$ N^2/m^2 for all 7 strings.

configuration (corresponding to Figure 8.17) with minimum prestress values of $\bar{\gamma} = 100$ and no external force. The disturbances come from the external force which is modeled as a zero-mean white noise with intensity $W_p = 1\text{N}^2$. The disturbances are present on all the nodes with all strings as potential actuators. The output to be bound is the top node at the far right of the beam (node 10) in x and y-direction.

$$y = \begin{bmatrix} n_{10x} \\ n_{10y} \end{bmatrix} = C_y \begin{bmatrix} \eta_{2_\phi} \\ \dot{\eta}_{2_\phi} \end{bmatrix}, \; C_y = \begin{bmatrix} 0 & I \end{bmatrix} \Phi_2 V_{2_\phi} \begin{bmatrix} I & 0 \end{bmatrix}, \tag{8.156}$$

and the measurements are the positions and velocity of all the nodes except nodes 1 and 2 as these nodes are fixed to ground.

$$z = C_z \begin{bmatrix} \eta_{2_\phi} \\ \dot{\eta}_{2_\phi} \end{bmatrix} + I w_s, \; C_z = \begin{bmatrix} \Phi_2 V_{2_\phi} & 0 \\ 0 & \Phi_2 V_{2_\phi} \end{bmatrix}. \tag{8.157}$$

Some values assumed for this example are $\bar{\alpha}_L = 0.1\alpha_0$, $\bar{\alpha}_U = 10\alpha_0, \bar{\gamma}_a = \bar{\gamma}_s = 1e3, p_a = p_s = 1$, and $p_\alpha = 10$.

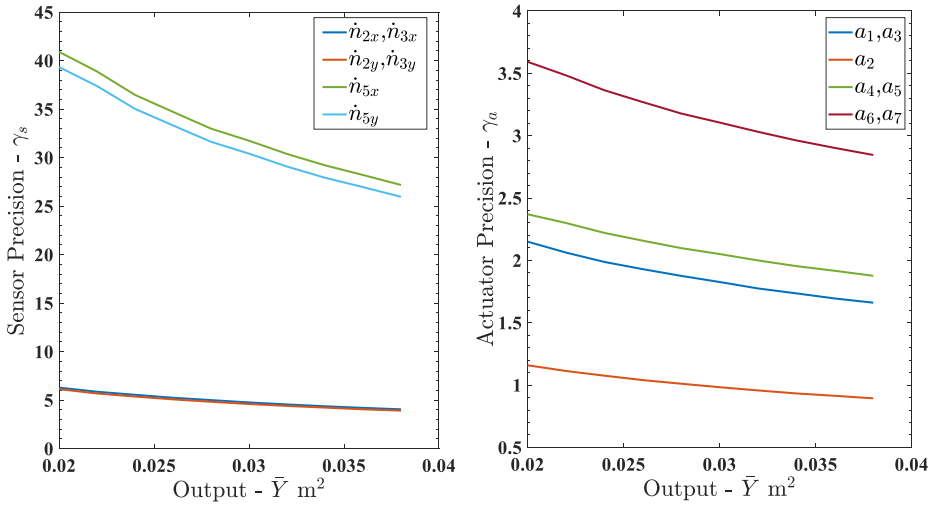

Figure 8.16: (a)Variation in the required sensor precision. (b) Variation in the required actuator precision.

The surface plot in Figure 8.18 shows the variation in budget requirement $\bar{\$}$ as we change the input covariance bound $\bar{U}$ and output covariance bound $\bar{Y}$. The required budget monotonically decreases with a more relaxed performance constraint for all values of control input bounds. The same decreasing trend in budget follows as we increase the control input bound. This variation is small showing the relatively less strict nature of control covariance bound.

Figure 8.19 shows the contour curve for the variation in input-$\bar{U}$ and output-$\bar{Y}$. The figure shows the decreasing values of the prestress required for all strings as we increase the output covariance bound while maintaining the same control input $\bar{U}$, or to reduce the output covariance more prestress is required in the structure. Basically, less prestress is required for relaxed performance constraints. The increase in prestress with relaxed input covariance can be understood due to less precision required on actuator and sensor, hence more money can be spent on pre-stress.

Figure 8.20 shows the total sensor precision and actuator precision with variation in input-$\bar{U}$ and output-$\bar{Y}$. It can be observed that less precision on sensors and actuators is required for relaxed performance requirements along both the axes for output $\bar{Y}$ and input $\bar{U}$. This can be simply related to less budget requirement for the relaxed performance and control energy requirement from Fig. 8.18.

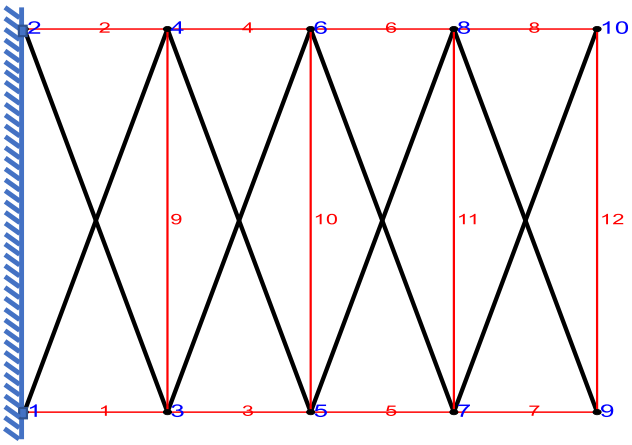

Figure 8.17: 2D Tensegrity Beam

Table 8.3: Sensor Precision for the measurement of velocity of x and y coordinates of all the nodes (refer to Fig.8.17).

	n1	n2	n3	n4	n5	n6	n7	n8	n9	n10
x	0.00	0.00	5.49	12.75	8.75	17.47	12.31	46.59	13.61	164.17
y	0.00	0.00	0.00	0.00	0.00	0.00	0.00	0.00	73.24	155.39

The required sensor precision for output bound $\bar{Y} = 0.02$ and input bound $\bar{U} = 1.2$ is given in Tables (8.4 and 8.3). The position sensors needs measurement only for the node that have output performance specified n_{10x}, n_{10y}. However, for the velocity measurement, considerable precision is required to measure x-axis of all the nodes except the right most nodes and both x and y axis for the right most nodes, $\dot{n}_{9x}, \dot{n}_{9y}, \dot{n}_{10x}, \dot{n}_{10y}$.

Table 8.5 gives the required precision values for all the actuators to achieve the performance bound of $\bar{Y} = 0.02$ with input constraint of $\bar{U} = 1.2$. The table shows higher precision is required on strings 8, and 12 as these strings are directly connected to the output node and least precision is required for strings 9,10, and 11 as these strings do not directly affect the motion of the node n_{10}.

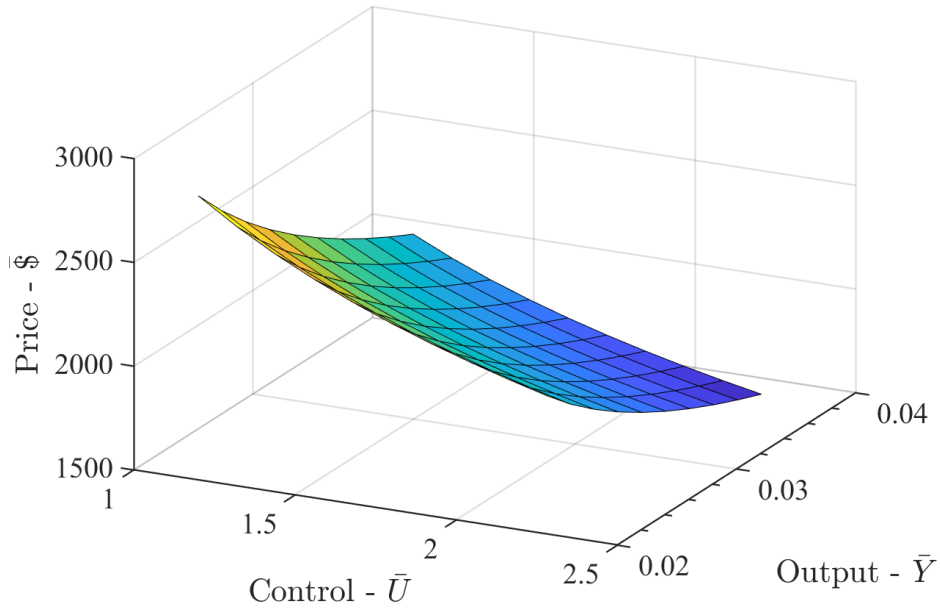

Figure 8.18: The surface plot of the variation in budget with input-$\bar{U}$ and output-$\bar{Y}$.

Table 8.4: Sensor Precision for the measurement of position of x and y coordinates of all the nodes (refer to Fig.8.17).

	n1	n2	n3	n4	n5	n6	n7	n8	n9	n10
x	0.00	0.00	0.00	0.00	0.00	0.00	0.00	0.00	0.00	144.92
y	0.00	0.00	0.00	0.00	0.00	0.00	0.00	0.00	0.00	76.06

8.10 Conclusion

In the first part of this chapter, the nonlinear dynamics for the tensegrity system is linearized about an equilibrium position, and the modes corresponding to bar length change are removed to make the system physically realizable. The robust linear control theory was used to actively reject the noises and disturbances using the standard $\mathcal{H}_\infty$, generalized $\mathcal{H}_2$ formulation. Moreover, the precision of the actuators and sensors (information architecture) along with the controller is also solved for the covariance control problem. All the examples are shown on a T_1D_1 tensegrity robotic arm system. With the fixed structural parameters, the above-mentioned problem was proved to be

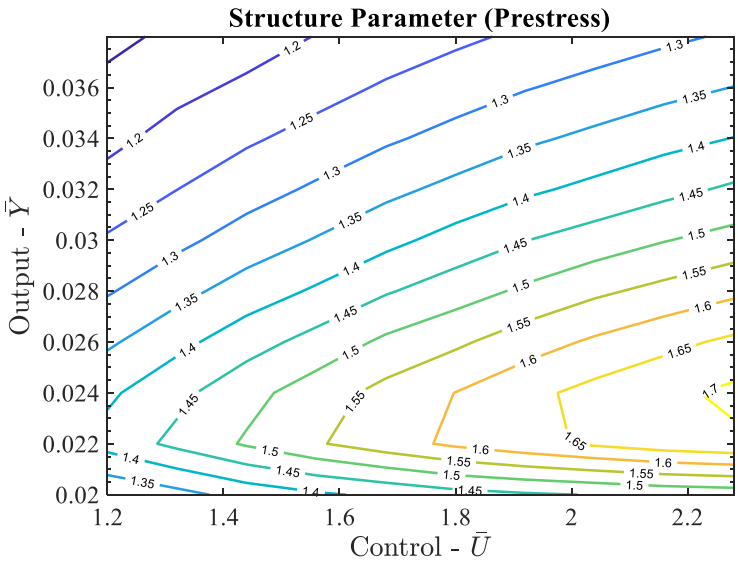

Figure 8.19: The contour plot for the prestress value with variation in input-$\bar{U}$ and output-$\bar{Y}$.

Table 8.5: Actuator Precision for all the strings (refer to Fig.8.17).

Str No.	1	2	3	4	5	6
γ_a	168.22	173.29	113.03	203.72	182.25	240.43
Str No.	7	8	9	10	11	12
γ_a	104.17	597.00	24.46	43.92	74.53	200.21

convex having a globally optimal solution.

In the last half of this chapter, a novel system-level design approach by the simultaneous selection of control law, instrument precision, and structure parameters is developed. The system dynamics is assumed to be linear along with the free structural parameters. A dynamic controller is generated to bound the covariance of inputs and outputs with the precision of the sensors and actuators as the optimization variable. The problem is set as a feasibility problem, where matrix upper bounds are specified for the covariance of selected outputs and the covariance of the control signals. Specified upper bounds on the available precision of sensors/actuators and structural parameters are also given. The covariance control problem is formulated in the LMI framework where the combined optimization for structure parameter, sensor/actuator precision,

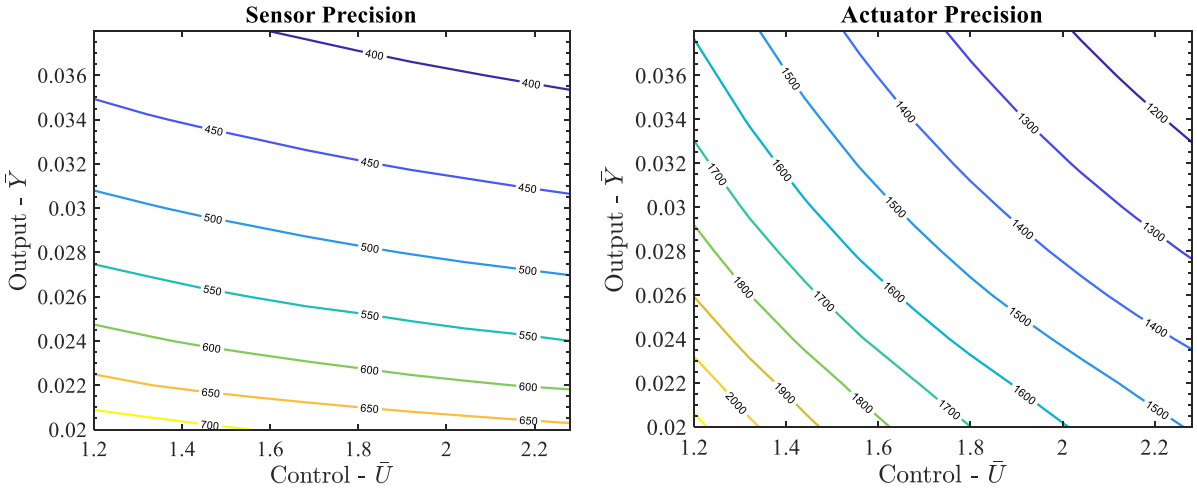

Figure 8.20: The contour plot for the total sensor precision and actuator precision with variation in input-$\bar{U}$ and output-$\bar{Y}$.

and control law was found to be a non-convex problem. The nonlinear matrix inequalities constraints were approximated as linear matrix inequalities by adding a convexifying potential function. A sub-optimal solution was achieved by iterating over the approximated convex problem. Results are provided for both dynamic compensation and full state feedback controller design. The tensegrity paradigm was used to integrate the structure and control design along with the information architecture. The linearized tensegrity dynamics model was used with initial prestress in the strings as a free structure parameter which appears linearly in the system matrices. The force density in the strings is used as the control input. This chapter may be used to design passive structures by reducing the level set of control covariance (to zero) while holding the output covariance constraint as shown in the example. Trade-off analysis provided between cost vs. control energy and performance requirement showed that as performance and control energy constraints are relaxed, tighter budget constraints are achievable. Tensegrity examples were used to show the effectiveness of the developed results. The example results provide the knowledge on price estimate, what initial prestress to choose, where to put more precise sensors/actuators and the controller parameters.

9. CONCLUSIONS AND CONTRIBUTIONS OF THE DISSERTATION

Tensegrity was chosen to be the paradigm to connect the structure and control because of its several advantages explained earlier. The approach here is to make little progress in individual domains and then finally integrate the domains to yield a system design formulation.

The first contribution the proposed research is to design minimum mass tensegrity structures for compressive loading conditions. First, we design the structure according to a given application. The design requirement can be to minimize the mass of the structure or store mechanical energy while minimizing the mass of the structure. A detailed study of the minimum mass tensegrity structures designed to take compressive loads was done. The optimal configuration for tensegrity T-bar and D-bar structures were studied considering both local and global failures. The calculation for the optimal configuration includes optimal complexity, angle, and cross-sectional area for each member of the structure. Tensegrity D-bar structure was also studied as a lightweight impact structure where most of the impact energy was stored in the elastic strings to reduce the high impulse of the collision. The proposed research provides a general approach to design a structure based on optimizing mass, stiffness or mechanical energy stored in a tensegrity structure.

The second contribution of the proposed research is to develop the dynamics of any tensegrity structure. After designing the structure to optimize some mechanical properties based on static calculation, one needs to perform the dynamic simulation to understand the behaviour of the structure in the presence of dynamic loading. This research provides a second-order matrix differential equation that simulates the dynamics of any tensegrity structure. A reduced-order model was also developed for class-k tensegrity structures making the model more accurate and computationally efficient. The formulation also considers massive strings and opens an avenue to study tensegrity membrane structures. An extra degree of freedom was also added to the control of

the tensegrity structure by adding wheels to the rigid bars. The dynamics for this novel gyroscopic tensegrity system was developed with proof of concept using a small bench top experimental setup. A Matlab based tensegrity software is also developed as part of the proposed research.

The third contribution is to develop the control algorithm to change the shape of the structure. In this chapter, a control algorithm is written that allows us to change the shape of any class of tensegrity structure. The reduced-order model of tensegrity dynamics is used to control the node position of any class-k tensegrity structure. The algorithm also allows to control the positions, velocity and acceleration of any number of nodes and in any particular direction. A T_nD_1 tensegrity robotic arm was used to provide all the results. The shape control of gyroscopic tensegrity system is further discussed to shows the rotation of D-bar about its own axis which was not possible with the standard tensegrity system control. A Linear Matrix Inequality (LMI) framework is then used to calculate control gains to bound errors for five different types of control problems for given disturbance statistics.

The final objective is to integrate structure, control and information architecture. To integrate the disciplines, we start by realizing a minimal-order linear system with no modes corresponding to the change in bar length. The robust liner control theory is further applied to reject the disturbances using $\mathcal{H}_\infty$, generalized $\mathcal{H}_2$ and covariance bound controller. The results are provided for the tensegrity robotic arm. Finally, the covariance control formulation is used to integrate structure and control design where free structure parameters, information architecture (sensor/actuator precision) and control law are simultaneously optimized to meet some given performance criteria in the presence of some budget constraint. The Linear Matrix Inequalities (LMIs) are used to bound the covariance of output and covariance of control inputs. The prestress in the strings is assumed as the free structure parameter that appears linearly in the characteristic matrices of the linearized tensegrity dynamics. An algorithm to find the location and precision of the sensor/actuator is also one of the outcomes of the proposed research.

REFERENCES

[1] N. Veuve, S. D. Safaei], and I. F. Smith, "Active control for mid-span connection of a deployable tensegrity footbridge," *Engineering Structures*, vol. 112, pp. 245 – 255, 2016.

[2] V. SunSpiral, G. Gorospe, J. Bruce, A. Iscen, G. Korbel, S. Milam, A. Agogino, and D. Atkinson, "Tensegrity based probes for planetary exploration: Entry, descent and landing (EDL) and surface mobility analysis," *International Journal of Planetary Probes*, vol. 7, 2013.

[3] R. Fuller, E. Applewhite, and A. Loeb, *Synergetics; explorations in the geometry of thinking*. Macmillan, 1975. [Online]. Available: https://books.google.com/books?id=iXBQAAAAMAAJ

[4] H. Lalvani, "Origins of tensegrity: Views of emmerich, fuller and snelson," *International Journal of Space Structures*, vol. 11, no. 1-2, p. 27, 1996. [Online]. Available: http://sps.sagepub.com/content/11/1-2/27.short

[5] R. B. Fuller, "Tensile integrity structures," 1959, uS Patent 3.063.521.

[6] R. E. Skelton and M. C. de Oliveira, *Tensegrity Systems*. Springer US, 2009.

[7] C. R. Calladine, "Buckminster Fuller's "tensegrity" structures and Clerk Maxwell's rules for the construction of stiff frames," *International Journal of Solids and Structures*, vol. 14, no. 2, pp. 161–172, 1978.

[8] R. Motro, "Tensegrity systems: the state of the art," *International Journal of Space Structures*, vol. 7, no. 2, pp. 75–83, 1992.

[9] R. Connelly and W. Whiteley, "The stability of tensegrity frameworks," *International Journal of Space Structures*, vol. 7, no. 2, pp. 153–163, 1992.

[10] M. Masic, R. E. Skelton, and P. E. Gill, "Optimization of tensegrity structures," *International Journal of Solids and Structures*, vol. 43, no. 16, pp. 4687–4703, 2006.

[11] C. Paul, H. Lipson, and F. J. Valero Cuevas, "Evolutionary form-finding of tensegrity structures," in *Proceedings of the 7th Annual Conference on Genetic and Evolutionary Computation*. ACM, 2005, pp. 3–10.

[12] A. G. Tibert and S. Pellegrino, "Review of form-finding methods for tensegrity structures," *International Journal of Space Structures*, vol. 26, no. 3, pp. 241–255, 2011.

[13] J. Zhang and M. Ohsaki, "Self-equilibrium and stability of regular truncated tetrahedral tensegrity structures," *Journal of the Mechanics and Physics of Solids*, vol. 60, no. 10, pp. 1757 – 1770, 2012.

[14] J. Cheong and R. E. Skelton, "Nonminimal dynamics of general class k tensegrity systems," *International Journal of Structural Stability and Dynamics*, vol. 15, no. 2, p. 1450042 (22 pages), 2015.

[15] R. Goyal and R. E. Skelton, "Dynamics of class 1 tensegrity systems including cable mass," in *16th Biennial ASCE Conference - Earth and Space 2018*, 2018, pp. 868 – 876. [Online]. Available: https://ascelibrary.org/doi/abs/10.1061/9780784481899.082

[16] R. Goyal and R. Skelton, "Tensegrity system dynamics with rigid bars and massive strings," *Multibody System Dynamics*, vol. 46(3), pp. 203–228, 2019.

[17] S. Jiang, R. E. Skelton, and E. A. P. Hernandez, "Analytical equations for the connectivity matrices and node positions of minimal and extended tensegrity plates," *International Journal of Space Structures*, p. 0956059920902375, 2020.

[18] H. Karnan, R. Goyal, M. Majji, R. E. Skelton, and P. Singla, "Visual feedback control of tensegrity robotic systems," *2017 IEEE/RSJ International Conference on Intelligent Robots and Systems (IROS)*, pp. 2048–2053, Sept 2017.

[19] R. E. Skelton and M. C. de Oliveira, "Optimal tensegrity structures in bending: the discrete Michell truss," *Journal of the Franklin Institute*, vol. 347, no. 1, pp. 257–283, 2010.

[20] K. Nagase and R. E. Skelton, "Minimal mass design of tensegrity structures," in *Sensors and Smart Structures Technologies for Civil, Mechanical, and Aerospace Systems 2014*, vol. 9061. International Society for Optics and Photonics, 2014, p. 90610W.

[21] R. Goyal, E. A. Peraza Hernandez, and R. Skelton, "Analytical study of tensegrity lattices for mass-efficient mechanical energy absorption," *International Journal of Space Structures*, vol. 34, no. 1-2, pp. 3–21, 2019.

[22] U. Boz, R. Goyal, and R. E. Skelton, "Actuators and sensors based on tensegrity d-bar structures," *Frontiers in Astronomy and Space Sciences | Space Robotics*, vol. 5, no. 41, 2018.

[23] G. Carpentieri, R. E. Skelton, and F. Fraternali, "Minimum mass and optimal complexity of planar tensegrity bridges," *International Journal of Space Structures*, vol. 30, no. 3-4, pp. 221–243, 2015.

[24] G. Carpentieri, R. Skelton, and F. Fraternali, "A minimal mass deployable structure for solar energy harvesting on water canals," *Structural and Multidisciplinary Optimization*, pp. 1–10, 2016. [Online]. Available: http://dx.doi.org/10.1007/s00158-016-1503-5

[25] K. Nagase and R. E. Skelton, "Double-helix tensegrity structures," *AIAA Journal*, vol. 53, no. 4, pp. 847–862, 2014. [Online]. Available: http://dx.doi.org/10.2514/1.J053264

[26] G. Carpentieri and R. E. Skelton, "On the minimal mass design of composite membranes," *Composites Part B: Engineering*, 2016. [Online]. Available: http://www.sciencedirect.com/science/article/pii/S1359836816321382

[27] J. J. Rimoli, "A reduced-order model for the dynamic and post-buckling behavior of tensegrity structures," *Mechanics of Materials*, vol. 116, pp. 146 – 157, 2018, iUTAM Symposium on Dynamic Instabilities in Solids.

[28] S. I. Bel Hadj Ali, N., "Dynamic behavior and vibration control of a tensegrity structure," *International Journal of Solids and Structures*, vol. 47, pp. 1285–1296, 2010.

[29] K. Caluwaerts, J. Despraz, A. Işçen, A. P. Sabelhaus, J. Bruce, B. Schrauwen, and V. SunSpiral, "Design and control of compliant tensegrity robots through simulation and hardware validation," *Journal of The Royal Society Interface*, vol. 11, no. 98, 2014. [Online]. Available: http://rsif.royalsocietypublishing.org/content/11/98/20140520.abstract

[30] S. Djouadi, R. Motro, J. C. Pons, and B. Crosnier, "Active control of tensegrity systems," *Journal of Aerospace Engineering*, vol. 11, no. 2, pp. 37–44, 1998. [Online]. Available: http://ascelibrary.org/doi/abs/10.1061/%28ASCE%290893-1321%281998%2911%3A2%2837%29

[31] C. Paul, F. J. Valero-Cuevas, and H. Lipson, "Design and control of tensegrity robots for locomotion," *IEEE Transactions on Robotics*, vol. 22, no. 5, pp. 944–957, 2006.

[32] A. G. Tibert and S. Pellegrino, "Deployable tensegrity mast," *In: 44th AIAA/ASME/ASCE/AHS/ASC, Structures, Structural Dynamics and Materials Conference and Exhibit, Norfolk , VA, USA.*, p. 1978, 2003.

[33] A. Amendola, G. Carpentieri, M. de Oliveira, R. Skelton, and F. Fraternali, "Experimental investigation of the softening/stiffening response of tensegrity prisms under compressive loading," *Composite Structures*, vol. 117, pp. 234 – 243, 2014.

[34] R. Goyal, T. Bryant, M. Majji, R. E. Skelton, and A. Longman, "Design and control of growth adaptable artificial gravity space habitat," in *AIAA SPACE and Astronautics Forum and Exposition*, 2017, p. 5141.

[35] M. Chen, Y. Shen, R. Goyal, M. Majji, and R. E. Skelton, "Energy analysis of growth adaptable artificial gravity space habitat," in *AIAA SPACE and Astronautics Forum and Exposition*, 2018, p. 5109.

[36] D. E. Ingber, "The architecture of life," *Scientific America*, vol. 278, no. 1, pp. 48–57, 1998.

[37] P. V. Y. S. R. S. Mauricio De Oliveira, Carlos Vera and L. A. Sung, "Nanomechanics of multiple units in the erythrocyte membrane skeletal network," *Annals of Biomedical Engineering*, vol. 38-9, pp. 2956–2967, 2010.

[38] F. B. Carlos Vera, Robert Skelton and L. A. Sung, "3-d nanomechanics of an erythrocyte junctional complex in equibiaxial and anisotropic deformations," *Annals of Biomedical Engineering*, vol. 33-10, pp. 1387–1404, 2005.

[39] F. Vishala, "Non-linear trajectory control of tensegrity prosthetic (protense) leg," *Master's Thesis*, 2018.

[40] R. Skelton and C. Sultan, "Controllable tensegrity: A new class of smart structures," in *Smart Structures and Materials 1997: Mathematics and Control in Smart Structures*, vol. 3039. International Society for Optics and Photonics, 1997, pp. 166–178.

[41] F. Fraternali, G. Carpentieri, and A. Amendola, "On the mechanical modeling of the extreme softening/stiffening response of axially loaded tensegrity prisms," *Journal of the Mechanics and Physics of Solids*, vol. 74, pp. 136 – 157, 2015.

[42] D. D. Tommasi, G. Marano, G. Puglisi, and F. Trentadue, "Morphological optimization of tensegrity-type metamaterials," *Composites Part B: Engineering*, vol. 115, pp. 182 – 187, 2017, composite lattices and multiscale innovative materials and structures.

[43] J. M. Gere and S. P. Timoshenko, *Theory of Elastic Stability*. McGraw-Hill, 1961.

[44] J. M. Gere and B. J. Goodno, *Mechanics of Materials*. Cengage Learning, 2011.

[45] R. Goyal, R. Skelton, and E. A. Peraza Hernandez, "Design of minimal mass load-bearing tensegrity lattices," *Mechanics Research Communications*, vol. 103, p. 103477, 2020.

[46] R. E. Skelton, R. Montuori, and V. Pecoraro, "Globally stable minimal mass compressive tensegrity structures," *Composite Structures*, vol. 141, pp. 346 – 354, 2016. [Online]. Available: http://www.sciencedirect.com/science/article/pii/S0263822316300174

[47] R. Montuori and R. E. Skelton, "Globally stable tensegrity compressive structures for arbitrary complexity," *Composite Structures*, vol. 179, pp. 682 – 694, 2017. [Online]. Available: http://www.sciencedirect.com/science/article/pii/S0263822317323206

[48] D. De Tommasi, G. C. Marano, G. Puglisi, and F. Trentadue, "Optimal complexity and fractal limits of self-similar tensegrities," *Proceedings of the Royal Society of London A: Mathematical, Physical and Engineering Sciences*, vol. 471, no. 2184, 2015.

[49] F. Fraternali and A. Amendola, "Mechanical modeling of innovative metamaterials alternating pentamode lattices and confinement plates," *Journal of the Mechanics and Physics of Solids*, vol. 99, pp. 259–271, 2017.

[50] A. Amendola, G. Carpentieri, L. Feo, and F. Fraternali, "Bending dominated response of layered mechanical metamaterials alternating pentamode lattices and confinement plates," *Composite Structures*, vol. 157, pp. 71–77, 2016.

[51] A. P. Sabelhaus, J. Bruce, K. Caluwaerts, P. Manovi, R. F. Firoozi, S. Dobi, A. M. Agogino, and V. SunSpiral, "System design and locomotion of SUPERball, an untethered tensegrity robot," in *2015 IEEE international conference on robotics and automation (ICRA)*. IEEE, 2015, pp. 2867–2873.

[52] L.-H. Chen, K. Kim, E. Tang, K. Li, R. House, E. L. Zhu, K. Fountain, A. M. Agogino, A. Agogino, V. Sunspiral, and E. Yung, "Soft spherical tensegrity robot design using rod-centered actuation and control," *Journal of Mechanisms and Robotics*, vol. 9, no. 2, p. 025001, 2017.

[53] C. P. Johnson and K. M. Will, "Beam buckling by finite element procedure," *Journal of the Structural Division*, vol. 100, no. Proc Paper 10432, 1974.

[54] M. Mukhopadhyay and A. Mukherjee, "Finite element buckling analysis of stiffened plates," *Computers & Structures*, vol. 34, no. 6, pp. 795–803, 1990.

[55] L. Zhao and E. A. Peraza Hernandez, "Theoretical study of tensegrity systems with tunable energy dissipation," *Extreme Mechanics Letters*, vol. 32, p. 100567, 2019.

[56] R. J. V. R. P. Singh and P. Likins, "Dynamics of flexible bodies in tree topology - a computer oriented approach," *AIAA Journal of Guidance, Control, and Dynamics*, vol. 8, pp. 584–590, 1985.

[57] H. Murakami, "Static and dynamic analyses of tensegrity structures. part 1. nonlinear equations of motion," *International Journal of Solids and Structures*, vol. 38(20), pp. 3599–3613, 2001.

[58] C. Sultan, M. Corless, and R. E. Skelton, "Linear dynamics of tensegrity structures," *Engineering Structures*, vol. 24(6), pp. 671–685, 2002.

[59] M. Masic and R. E. Skelton, "Selection of prestress for optimal dynamic/control performance of tensegrity structures," *International Journal of Solids and Structures*, vol. 43, no. 7, pp. 2110 – 2125, 2006. [Online]. Available: http://www.sciencedirect.com/science/article/pii/S0020768305003641

[60] G. Tan and S. Pellegrino, "Nonlinear vibration of cable-stiffened pantographic deployable structures," *Journal of Sound and Vibration*, vol. 314, no. 3, pp. 783 – 802, 2008. [Online]. Available: http://www.sciencedirect.com/science/article/pii/S0022460X08000552

[61] R. E. Skelton, "Dynamics and control of tensegrity systems," *IUTAM Symposium on Vibration Control of Nonlinear Mechanisms and Structures*, pp. 309–318, 2005. [Online]. Available: http://dx.doi.org/10.1007/1-4020-4161-6_28

[62] K. Nagase and R. E. Skelton, "Network and vector forms of tensegrity system dynamics," *Mechanics Research Communications*, vol. 59, pp. 14–25, 2014.

[63] J. W. Gibbs, "Elements of vector analysis," 1884, p. 67.

[64] P. Hughes, *Spacecraft Attitude Dynamics*. Wiley & Sons, New York, 1986.

[65] R. Goyal, M. Chen, M. Majji, and R. E. Skelton, "Motes: Modeling of tensegrity structures," *Journal of Open Source Software*, vol. 4(42), p. 1613, 2019.

[66] R. Goyal, M. Chen, M. Majji, and R. Skelton, "Gyroscopic tensegrity robots," *IEEE Robotics and Automation Letters*, vol. 5(2), pp. 1239–1246, 2020.

[67] B. Wie, *Space vehicle dynamics and control*. American Institute of Aeronautics and Astronautics, 2008.

[68] A. M. Giordano, C. Ott, and A. Albu-Schäffer, "Coordinated control of spacecraft's attitude and end-effector for space robots," *IEEE Robotics and Automation Letters*, vol. 4, no. 2, pp. 2108–2115, 2019.

[69] C. M. Roithmayer, "International space station attitude control and energy storage experiment: Effects of flywheel torque," *NASA Technical Report*, 1999.

[70] S. R. Vadali and H.-S. Oh, "Space station attitude control and momentum management: A nonlinear look," *Journal of Guidance, Control and Dynamics*, vol. 15, no. 3, 1992.

[71] R. Wang, R. Goyal, S. Chakravorty, and R. E. Skelton, "Model and data based approaches to the control of tensegrity robots," *IEEE Robotics and Automation Letters*, vol. 5(3), pp. 3846 – 3853, 2020.

[72] D. Rus, "Design, fabrication and control of soft robots," *Nature*, vol. 521, no. 5, pp. 467–475, 2015.

[73] C. Majidi, "Soft robotics: a perspective — current trends and prospects for the future," *Soft Robotics*, vol. 1, pp. 5–11, 2014.

[74] B. Adam and I. F. Smith, "Active tensegrity: A control framework for an adaptive civil-engineering structure," *Computers & Structures*, vol. 86, no. 23, pp. 2215 – 2223, 2008.

[75] B. A. and I. Smith, "Tensegrity active control: Multiobjective approach," *Journal of Computing in Civil Engineering*, vol. 21, no. 1, pp. 3–10, 2007.

[76] A. P. Sabelhaus, A. K. Akella, Z. A. Ahmad, and V. SunSpiral, "Model-predictive control of a flexible spine robot," in *2017 American Control Conference (ACC)*, May 2017, pp. 5051–5057.

[77] M. Zhang, X. Geng, J. Bruce, K. Caluwaerts, M. Vespignani, V. SunSpiral, P. Abbeel, and S. Levine, "Deep reinforcement learning for tensegrity robot locomotion," in *2017 IEEE International Conference on Robotics and Automation (ICRA)*, May 2017, pp. 634–641.

[78] T. Bliss, T. Iwasaki, and H. Bart-Smith, "Central pattern generator control of a tensegrity swimmer," *IEEE/ASME Transactions on Mechatronics*, vol. 18, no. 2, pp. 586–597, 2012.

[79] T. Bliss, J. Werly, T. Iwasaki, and H. Bart-Smith, "Experimental validation of robust resonance entrainment for cpg-controlled tensegrity structures," *IEEE Transactions On Control Systems Technology*, vol. 21, no. 3, pp. 666–678, 2012.

[80] B. Nurimbetov, M. Issa, and H. A. Varol, "Robotic assembly planning of tensegrity structures," in *2019 IEEE/SICE International Symposium on System Integration (SII)*, 2019, pp. 73–78.

[81] A. Kuzdeuov, M. Rubagotti, and H. A. Varol, "Neural network augmented sensor fusion for pose estimation of tensegrity manipulators," *IEEE Sensors Journal*, vol. 20, no. 7, pp. 3655–3666, 2020.

[82] P. R. Kumar and P. Varaiya, *Stochastic systems: Estimation, identification, and adaptive control*. SIAM, 2015, vol. 75.

[83] P. A. Ioannou and J. Sun, *Robust adaptive control*. Courier Corporation, 2012.

[84] R. Goyal, M. Majji, and R. E. Skelton, "A vector approach for analytical dynamics of multiple rigid rods," *International Journal of Structural Stability and Dynamics*, vol. 19, no. 7, pp. 1–25, 2019.

[85] R. E. Skelton, T. Iwasaki, and K. Grigoriadis, *A Unified Algebraic Approach to Control Design.* Taylor & Francis, London, UK, 1998.

[86] M. A. Rotea, "The generalized $\mathcal{H}_2$ control problem," *Automatica*, vol. 29, no. 2, pp. 373 – 385, 1993. [Online]. Available: http://www.sciencedirect.com/science/article/pii/000510989390130L

[87] C. Scherer, P. Gahinet, and M. Chilali, "Multiobjective output-feedback control via lmi optimization," *IEEE Transactions on Automatic Control*, vol. 42, no. 7, pp. 896–911, 1997.

[88] T. Iwasaki and R. Skelton, "All controllers for the general $\mathcal{H}_\infty$ control problem: Lmi existence conditions and state space formulas," *Automatica*, vol. 30, no. 8, pp. 1307 – 1317, 1994. [Online]. Available: http://www.sciencedirect.com/science/article/pii/0005109894901104

[89] P. P. Khargonekar and M. A. Rotea, "Mixed $\mathcal{H}_2/\mathcal{H}_\infty$ control: a convex optimization approach," *IEEE Transactions on Automatic Control*, vol. 36, no. 7, pp. 824–837, 1991.

[90] P. Gahinet and P. Apkarian, "A linear matrix inequality approach to $\mathcal{H}_\infty$ control," *International Journal of Robust and Nonlinear Control*, vol. 4, no. 4, pp. 421–448, 1994.

[91] S. Boyd, S. P. Boyd, and L. Vandenberghe, *Convex optimization*. Cambridge university press, 2004.

[92] I. Pólik and T. Terlaky, "A survey of the s-lemma," *SIAM Review*, vol. 49, no. 3, pp. 371–418, 2007.

[93] R. Goyal and R. E. Skelton, "Joint optimization of plant, controller, and sensor/actuator design," in *2019 American Control Conference (ACC)*, July 2019, pp. 1507–1512.

[94] F. Li, M. C. de Oliveira, and R. E. Skelton, "Integrating Information Architecture and Control or Estimation Design," *SICE Journal of Control, Measurement, and System Integration*, vol. Vol.1, no. No.2, March 2008.

[95] R. Saraf, R. Bhattacharya, and R. Skelton, "H2 optimal sensing architecture with model uncertainty," in *2017 American Control Conference (ACC)*, May 2017, pp. 2429–2434.

[96] M. C. D. Oliveira and J. C. Geromei, "Linear output feedback controller design with joint selection of sensors and actuators," *IEEE Transactions on Automatic Control*, vol. 45, no. 12, pp. 2412–2419, Dec 2000.

[97] S. Joshi and S. Boyd, "Sensor selection via convex optimization," *IEEE Transactions on Signal Processing*, vol. 57, no. 2, pp. 451–462, 2009.

[98] J. Lu and R. E. Skelton, "Instrument and control design in linear systems," *International Journal of Control*, vol. 72, no. 9, p. 799–814, 1999.

[99] J. Lu and R. Skelton, "Integrating structure and control design to achieve mixed $H2/H\infty$ performance," *International Journal of Control*, vol. 73, no. 16, p. 1449–1462, 2000.

[100] R. V. Grandhi, "Structural and control optimization of space structures," *Computers & Structures*, vol. 31, no. 2, pp. 139 – 150, 1989.

[101] K. M. Grigoriadis and R. E. Skelton, "Integrated structural and control design for vector second-order systems via lmis," in *Proceedings of the 1998 American Control Conference. ACC (IEEE Cat. No.98CH36207)*, vol. 3, June 1998, pp. 1625–1629 vol.3.

[102] M. C. de Oliveira, J. F. Camino, and R. E. Skelton, "A convexifying algorithm for the design of structured linear controllers," in *Proceedings of the 39th IEEE Conference on Decision and Control (Cat. No.00CH37187)*, vol. 3, Dec 2000, pp. 2781–2786.

[103] J. F. Camino, M. de Oliveira, and R. Skelton, ""Convexifying" Linear Matrix Inequality Methods for Integrating Structure and Control Design," *Journal of Structural Engineering*, vol. Vol.129, no. No.7, July 2003.

APPENDIX A

BAR LENGTH CORRECTION

In order to compensate the error accumulated during the integration of dynamics equations, the vector of each rod b, centre of mass vector r and their time derivatives $\dot{b}$ and $\dot{r}$ have to be modified. In this document, first we will correct the bar vector b and its derivative $\dot{b}$ in such a way that the resulting rod vector preserves its length and its velocity vector is orthogonal to it. After correcting b and $\dot{b}$, we find r and $\dot{r}$ such that the Class-K constraints are satisfied.

A.1 Class 1 Bar length Correction

Let us denote the corrupted value of bar vector and its derivative after integration as $\bar{b}$ and $\dot{\bar{b}}$, respectively. Let the additive vectors p and r be added to $\bar{b}$ and $\dot{\bar{b}}$ in such a way that the resulting rod vector preserves its length and its velocity vector is orthogonal to it. Among infinite pairs satisfying the constraints above, one reasonable choice can be selected by the following statement.

Theorem A.1.1. *For any given $\bar{b}$ and $\dot{\bar{b}}$, the corrective vectors p and r minimizing*

$$J(p, r) = q\|p\|^2 + \|r\|^2, \tag{A.1}$$

subject to constraints $\|\bar{b} + p\| = l$ and $(\bar{b} + p)^{\mathsf{T}}(\dot{\bar{b}} + r) = 0$ are calculated as

$$p = lv - \bar{b}, r = -vv^{\mathsf{T}}\dot{\bar{b}}, \tag{A.2}$$

where $v = [xI + \dot{\bar{b}}\dot{\bar{b}}^{\mathsf{T}}]^{-1}ql\bar{b}$, and x is a real root of the following polynomial:

$$x^4 + a_3x^3 + a_2x^2 + a_1x + a_0 = 0, \quad \textit{where} \tag{A.3}$$

$$a_3 = 2\|\dot{\bar{b}}\|^2,\ \ a_2 = \|\dot{\bar{b}}\|^4 - (ql)^2\|\bar{b}\|^2,\ \ a_1 = 2(ql)^2\Big((\bar{b}^{\mathsf{T}}\dot{\bar{b}})^2 - \|\dot{\bar{b}}\|^2\|\bar{b}\|^2\Big),$$

$$a_0 = (ql)^2\|\dot{\bar{b}}\|^2\Big((\bar{b}^{\mathsf{T}}\dot{\bar{b}})^2 - \|\dot{\bar{b}}\|^2\|\bar{b}\|^2\Big). \tag{A.4}$$

Proof: The corrected rod vector and its corrected time derivative satisfy

$$(\bar{b}+p)^{\mathsf{T}}(\bar{b}+p) = b^{\mathsf{T}}b = l^2, \tag{A.5}$$

$$(\bar{b}+p)^{\mathsf{T}}(\dot{\bar{b}}+r) = b^{\mathsf{T}}\dot{b} = 0. \tag{A.6}$$

Note that (A.5) implied that

$$\bar{b}+p = lv \Rightarrow p = lv - \bar{b}, \;\; \forall v^{\mathsf{T}}v = 1. \tag{A.7}$$

Besides, (A.6) yields

$$v^{\mathsf{T}}(\dot{\bar{b}}+r) = 0 \Rightarrow r = -vv^{\mathsf{T}}\dot{\bar{b}} + V_v z, \tag{A.8}$$

for any arbitrary z, since $(v^{\mathsf{T}})^{+} = v$ and $v^{\mathsf{T}}V_v = 0$, where V_v is the left null space of v. Now, one can solve the minimization problem of (A.1), with p and r given by (A.7) and (A.8), subject to constraint $v^{\mathsf{T}}v = 1$, i.e.,

$$\begin{aligned} J(p,r) &= q\|p\|^2 + \|r\|^2 + \lambda(v^{\mathsf{T}}v - 1) \\ &= q\|lv - \bar{b}\|^2 + \| - vv^{\mathsf{T}}\dot{\bar{b}} + V_v z\|^2 + \lambda(v^{\mathsf{T}}v - 1) \\ &= ql^2 v^{\mathsf{T}}v + q\|\bar{b}\|^2 - 2ql\bar{b}^{\mathsf{T}}v + (v^{\mathsf{T}}\dot{\bar{b}})^2 + \|z\|^2 + \lambda(v^{\mathsf{T}}v - 1), \end{aligned} \tag{A.9}$$

since $V_v^{\mathsf{T}}V_v = I$. Note that (A.9) is minimized with respect to z when $z = 0$. Moreover, in order to minimize (A.9) with respect to v, one can write

$$\frac{\partial J}{\partial v} = 0 \Rightarrow 2ql^2v - 2ql\bar{b} + 2\dot{\bar{b}}\dot{\bar{b}}^{\mathsf{T}}v + 2\lambda v = 0 \tag{A.10}$$

$$\Rightarrow v = \Big((ql^2 + \lambda)I + \dot{\bar{b}}\dot{\bar{b}}^{\mathsf{T}}\Big)^{-1} ql\bar{b} = (xI + \dot{\bar{b}}\dot{\bar{b}}^{\mathsf{T}})^{-1} ql\bar{b}, \tag{A.11}$$

where $x = ql^2 + \lambda$. Using the matrix equivalence $(A + BCD)^{-1} = A^{-1} - A^{-1}B(C^{-1} + DA^{-1}B)^{-1}DA^{-1}$ to express v in terms of x yields

$$\begin{aligned}(xI + \dot{\bar{b}}\dot{\bar{b}}^{\mathsf{T}})^{-1} &= x^{-1}I - x^{-1}(x + \|\dot{\bar{b}}\|^2)^{-1}\dot{\bar{b}}\dot{\bar{b}}^{\mathsf{T}} \\ &= \Big(x(x + \|\dot{\bar{b}}\|^2)\Big)^{-1}\Big((x + \|\dot{\bar{b}}\|^2)I - \dot{\bar{b}}\dot{\bar{b}}^{\mathsf{T}}\Big) \\ \Rightarrow v &= ql\Big(x(x + \|\dot{\bar{b}}\|^2)\Big)^{-1}\Big((x + \|\dot{\bar{b}}\|^2)\bar{b} - \dot{\bar{b}}\dot{\bar{b}}^{\mathsf{T}}\bar{b}\Big). \end{aligned} \tag{A.12}$$

Finally, substituting (A.12) in $v^{\mathsf{T}}v = 1$ and after some algebraic manipulations, one can obtain polynomial (A.3) with coefficients presented in (A.4). Therefore, each real root of this polynomial is substituted in (A.12) to generate v which in turn gives the pair p and r using (A.2). We choose the root that gives the smallest value for $J(p, r)$. □

A.2 Class K Bar length Correction

From the above polynomial algorithm, we get b and $\dot{b}$ which can be arranged in matrix form to give B and $\dot{B}$. Now, we update R and $\dot{R}$ such that the Class K constraints are satisfied.

Theorem A.2.1. *For any given B, $\dot{B}$ and corrupted matrix (not satisfying constraints because of numerical errors in integration) of centre of mass vectors and its derivatives, $\bar{R}$ and $\dot{\bar{R}}$, we can find corrected R and $\dot{R}$ using*

$$R = (\frac{1}{2}D - \frac{1}{4}BC_bP)V_1\Sigma^{-1}U_1^{\mathsf{T}} + \bar{R}U_2U_2^{\mathsf{T}} \tag{A.13}$$

$$\dot{R} = -\frac{1}{4}\dot{B}C_bPV_1\Sigma^{-1}U_1^{\mathsf{T}} + \dot{\bar{R}}U_2U_2^{\mathsf{T}} \tag{A.14}$$

where $NP = D$ comes from Class K constraints and U_1, U_2, Σ, V_1 and V_2 come from the SVD of

matrix $C_r P$ as

$$C_r P = \begin{bmatrix} U_1 & U_2 \end{bmatrix} \begin{bmatrix} \Sigma & 0 \\ 0 & 0 \end{bmatrix} \begin{bmatrix} V_1^\mathsf{T} \\ V_2^\mathsf{T} \end{bmatrix}$$

.

Proof: From our dynamics derivation, we define

$$\begin{bmatrix} B & R \end{bmatrix} = N \begin{bmatrix} C_b^\mathsf{T} & C_r^\mathsf{T} \end{bmatrix}$$

Recognizing that $\begin{bmatrix} \frac{1}{2}C_b^\mathsf{T} & 2C_r^\mathsf{T} \end{bmatrix}^{-1} = \begin{bmatrix} C_b^\mathsf{T} & C_r^\mathsf{T} \end{bmatrix}^\mathsf{T}$ [14], we can write

$$N = \begin{bmatrix} B & R \end{bmatrix} \begin{bmatrix} \frac{1}{2}C_b \\ 2C_r \end{bmatrix}.$$

Now, using the Class K constraint equation

$$\begin{aligned} NP &= D \\ \begin{bmatrix} B & R \end{bmatrix} \begin{bmatrix} \frac{1}{2}C_b \\ 2C_r \end{bmatrix} P &= D \\ RC_r P &= \frac{1}{2}D - \frac{1}{4}BC_b P. \end{aligned}$$

Calling $C_r P = A$ and $\frac{1}{2}D - \frac{1}{4}BC_b P = C$, the above equation becomes

$$RA = C. \tag{A.15}$$

The existence condition for the solution of above equation to exist is

$$C(I - A^{+}A) = 0$$

and all the solutions of the equation are given by

$$R = CA^{+} + Z(I - AA^{+}).$$

The Singular Value Decomposition of matrix A can be written as

$$A = \begin{bmatrix} U_1 & U_2 \end{bmatrix} \begin{bmatrix} \Sigma & 0 \\ 0 & 0 \end{bmatrix} \begin{bmatrix} V_1^{\mathsf{T}} \\ V_2^{\mathsf{T}} \end{bmatrix}$$

$$A = U_1 \Sigma V_1^{\mathsf{T}}$$

Using the SVD of matrix A, the existence condition can be written as

$$CV_2 = 0$$

where V_2 represents the right null space of matrix A. Moreover, all the solutions can be written as

$$R = CA^{+} + Z_2 U_2^{\mathsf{T}}$$

where U_2 represents the left null space of matrix A and Z_2 is an arbitrary matrix. Finally, the existence condition and all the solution can respectively be written as

$$(\frac{1}{2}D - \frac{1}{4}BC_bP)V_2 = 0 \tag{A.16}$$

$$R = (\frac{1}{2}D - \frac{1}{4}BC_bP)V_1\Sigma^{-1}U_1^{\mathsf{T}} + Z_2U_2^{\mathsf{T}} \tag{A.17}$$

We minimize the 2 norm of difference between previous center of position matrix ($\bar{R}$) and updated

center of position matrix(R) i.e. $||R - \bar{R}||_2$, to find the arbitrary matrix Z_2.

$$\min_{z_2} \ ||(\frac{1}{2}D - \frac{1}{4}BC_bP)V_1\Sigma^{-1}U_1^\mathsf{T} + Z_2U_2^\mathsf{T} - \bar{R}||_2$$

Theroem: $X = A^+CB^+$ minimizes the $||AXB - C||$.

Hence, the arbitrary matrix Z_2 can be found out as

$$Z_2 = \left[\bar{R} - (\frac{1}{2}D - \frac{1}{4}BC_bP)V_1\Sigma^{-1}U_1^\mathsf{T}\right]U_2$$
$$Z_2 = \bar{R}U_2$$

as $U_1^\mathsf{T}U_2 = 0$.

Substituting this result in Equation A.17, we obtain Equation A.13. A similar procedure can be used to get equation A.14 using $\dot{N}P = 0$. □

Finally, with updated B and $\dot{B}$ from section 1 and updated R and $\dot{R}$ from above section, we get

$$N = \begin{bmatrix} B & R \end{bmatrix} \begin{bmatrix} \frac{1}{2}C_b \\ 2C_r \end{bmatrix}$$
$$\dot{N} = \begin{bmatrix} \dot{B} & \dot{R} \end{bmatrix} \begin{bmatrix} \frac{1}{2}C_b \\ 2C_r \end{bmatrix}.$$

APPENDIX B

ANALYTICAL SOLUTION FOR LAGRANGE MULTIPLIER

The aim here is to write an analytical solution for the Lagrange multiplier Ω. Notice that Ω appears linearly in two terms in Equation 5.109. We solve this by substituting K_s and $\hat{\lambda}$ to write the equation in terms of Ω and known variables only. Then we combine all the coefficients of Ω to left hand side and all the known variables on right hand side to write it in a simple linear algebra problem.

B.1 Lagrange Multiplier for General Tensegrity systems

Lemma B.1.1. *The Lagrange Multiplier that satisfies Equation 5.109 can be computed as*

$$\begin{bmatrix} \omega_1 \\ \omega_2 \\ \vdots \\ \omega_c \end{bmatrix} = \left(\sum_{i=1}^{\beta} \frac{1}{2l_i^2} \mathcal{C}_{:,i}^{\mathsf{T}} \otimes (b_i \otimes (b_i \mathcal{D}_{i,:})^{\mathsf{T}}) - \begin{bmatrix} \mathcal{E} \otimes e_1^{\mathsf{T}} \\ \mathcal{E} \otimes e_2^{\mathsf{T}} \\ \mathcal{E} \otimes e_3^{\mathsf{T}} \end{bmatrix} \right)^{-1} \begin{bmatrix} \mathcal{A}_{1,:}^{\mathsf{T}} \\ \mathcal{A}_{2,:}^{\mathsf{T}} \\ \mathcal{A}_{3,:}^{\mathsf{T}} \end{bmatrix}, \tag{B.1}$$

where ω_i is the i^{th} column of Ω, $\mathcal{C} = P^{\mathsf{T}} C_{nb}^{\mathsf{T}} C_b^{\mathsf{T}}$, $\mathcal{D} = C_b C_{nb} M_s^{-1} U_1$, $\mathcal{E} = P^{\mathsf{T}} M_s^{-1} U_1$, and $\mathcal{A} = -S\hat{\gamma} C_s M_s^{-1} U_1 + B \lfloor \frac{1}{2} \hat{l}^{-2} B^{\mathsf{T}} (S\hat{\gamma} C_s - W) C_{nb}^{\mathsf{T}} C_b^{\mathsf{T}} - \hat{l}^{-2} \hat{J} \dot{B}^{\mathsf{T}} \dot{B} \rfloor C_b C_{nb} M_s^{-1} U_1 + W M_s^{-1} U_1 \in \mathbb{R}^{3 \times c}$.

Proof: Let us start by substituting for K_s from Equation 5.98 in Equation 5.109:

$$N \begin{bmatrix} C_s^{\mathsf{T}} \hat{\gamma} C_{sb} - C_{nb}^{\mathsf{T}} C_b^{\mathsf{T}} \hat{\lambda} C_b & C_s^{\mathsf{T}} \hat{\gamma} C_{ss} \end{bmatrix} M_s^{-1} U_1 - \Omega P^{\mathsf{T}} M_s^{-1} U_1 = W M_s^{-1} U_1 \tag{B.2}$$

$$N \left(\begin{bmatrix} C_s^{\mathsf{T}} \hat{\gamma} C_{sb} & C_s^{\mathsf{T}} \hat{\gamma} C_{ss} \end{bmatrix} - \begin{bmatrix} C_{nb}^{\mathsf{T}} C_b^{\mathsf{T}} \hat{\lambda} C_b & 0 \end{bmatrix} \right) M_s^{-1} U_1 - \Omega P^{\mathsf{T}} M_s^{-1} U_1 = W M_s^{-1} U_1 \tag{B.3}$$

$$N \left(C_s^{\mathsf{T}} \hat{\gamma} \begin{bmatrix} C_{sb} & C_{ss} \end{bmatrix} - C_{nb}^{\mathsf{T}} C_b^{\mathsf{T}} \hat{\lambda} C_b \begin{bmatrix} I & 0 \end{bmatrix} \right) M_s^{-1} U_1 - \Omega P^{\mathsf{T}} M_s^{-1} U_1 = W M_s^{-1} U_1 \tag{B.4}$$

Now, we substitute for $C_{nb} = [I \;\; 0]$ and $C_s = [C_{sb} \;\; C_{ss}]$ from Equation 5.61 and Equation 5.66 respectively:

$$N(C_s^{\mathsf{T}}\hat{\gamma}C_s - C_{nb}^{\mathsf{T}}C_b^{\mathsf{T}}\hat{\lambda}C_bC_{nb})M_s^{-1}U_1 - \Omega P^{\mathsf{T}}M_s^{-1}U_1 = WM_s^{-1}U_1 \tag{B.5}$$

$$S\hat{\gamma}C_sM_s^{-1}U_1 - B\hat{\lambda}C_bC_{nb}M_s^{-1}U_1 - \Omega P^{\mathsf{T}}M_s^{-1}U_1 = WM_s^{-1}U_1. \tag{B.6}$$

Further substituting $\hat{\lambda}$ from Equation 5.99 here gives:

$$S\hat{\gamma}C_sM_s^{-1}U_1 - B\lfloor\frac{1}{2}\hat{l}^{-2}B^{\mathsf{T}}(S\hat{\gamma}C_s - W - \Omega P^{\mathsf{T}})C_{nb}^{\mathsf{T}}C_b^{\mathsf{T}} - \hat{l}^{-2}\hat{J}\dot{B}^{\mathsf{T}}\dot{B}\rfloor C_bC_{nb}M_s^{-1}U_1 - \Omega P^{\mathsf{T}}M_s^{-1}U_1 = WM_s^{-1}U_1 \tag{B.7}$$

$$\frac{1}{2}B\lfloor\hat{l}^{-2}B^{\mathsf{T}}\Omega P^{\mathsf{T}}C_{nb}^{\mathsf{T}}C_b^{\mathsf{T}}\rfloor C_bC_{nb}M_s^{-1}U_1 - \Omega P^{\mathsf{T}}M_s^{-1}U_1 = -S\hat{\gamma}C_sM_s^{-1}U_1 + B\lfloor\frac{1}{2}\hat{l}^{-2}B^{\mathsf{T}}(S\hat{\gamma}C_s - W)C_{nb}^{\mathsf{T}}C_b^{\mathsf{T}} - \hat{l}^{-2}\hat{J}\dot{B}^{\mathsf{T}}\dot{B}\rfloor C_bC_{nb}M_s^{-1}U_1 + WM_s^{-1}U_1 = \mathcal{A} \tag{B.8}$$

$$\frac{1}{2}B\lfloor\hat{l}^{-2}B^{\mathsf{T}}\Omega\mathcal{C}\rfloor\mathcal{D} - \Omega\mathcal{E} = \mathcal{A} \tag{B.9}$$

where $\mathcal{C} = P^{\mathsf{T}}C_{nb}^{\mathsf{T}}C_b^{\mathsf{T}}$, $\mathcal{D} = C_bC_{nb}M_s^{-1}U_1$, $\mathcal{E} = P^{\mathsf{T}}M_s^{-1}U_1$, and $B = [b_1 \;\; b_2 \;\; \cdots b_\beta] \in \mathbb{R}^{3\times\beta}$. Notice that Equation B.9 is only written in terms of Ω and known variables. Now, we combine the coefficients of Ω by first breaking it as $\Omega = [\omega_1 \;\; \omega_2 \;\; \cdots \omega_c] \in \mathbb{R}^{3\times c}$ and then combining all the

coefficients together.

$$\hat{l}^{-2}B^{\mathsf{T}}\Omega\mathcal{C} = \hat{l}^{-2}\begin{bmatrix} b_1^{\mathsf{T}}\omega_1 & b_1^{\mathsf{T}}\omega_2 & \cdots & b_1^{\mathsf{T}}\omega_c \\ b_2^{\mathsf{T}}\omega_1 & b_2^{\mathsf{T}}\omega_2 & \cdots & b_2^{\mathsf{T}}\omega_c \\ \vdots & & \ddots & \vdots \\ b_\beta^{\mathsf{T}}\omega_1 & b_\beta^{\mathsf{T}}\omega_2 & \cdots & b_\beta^{\mathsf{T}}\omega_c \end{bmatrix}\begin{bmatrix} \mathcal{C}_{1,1} & \cdots & \mathcal{C}_{1,\beta} \\ \vdots & \ddots & \vdots \\ \mathcal{C}_{c,1} & \cdots & \mathcal{C}_{c,\beta} \end{bmatrix} \tag{B.10}$$

$$\Rightarrow \mathcal{F} = \frac{1}{2}\lfloor \hat{l}^{-2}B^{\mathsf{T}}\Omega\mathcal{C}\rfloor = \begin{bmatrix} \ddots & 0 & 0 \\ 0 & \sum_{j=1}^{c}\frac{\mathcal{C}_{j,i}}{2l_i^2}b_i^{\mathsf{T}}\omega_j & 0 \\ 0 & 0 & \ddots \end{bmatrix}. \tag{B.11}$$

Therefore, the element on the mth row and nth column of the matrix $\mathcal{G} = \frac{1}{2}B\lfloor\hat{l}^{-2}B^{\mathsf{T}}\Omega\mathcal{C}\rfloor\mathcal{D}$, for $m \in \{1,2,3\}$ and $n \in \{1,2,\cdots,c\}$, is equal to

$$\mathcal{G}_{m,n} = b_{m,1}\mathcal{F}_{1,1}\mathcal{D}_{1,n} + b_{m,2}\mathcal{F}_{2,2}\mathcal{D}_{2,n} + \cdots + b_{m,\beta}\mathcal{F}_{\beta,\beta}\mathcal{D}_{\beta,n} = \sum_{j=1}^{c}\sum_{i=1}^{\beta} b_{m,i}\mathcal{D}_{i,n}\frac{\mathcal{C}_{j,i}}{2l_i^2}b_i^{\mathsf{T}}\omega_j. \tag{B.12}$$

The second term in Equation B.9 is also written in terms of the Lagrange multiplier as:

$$\Omega\mathcal{E} = [\omega_1 \;\; \omega_2 \;\; \cdots \;\; \omega_c]\mathcal{E} = \omega_1\mathcal{E}_{1,:} + \omega_2\mathcal{E}_{2,:} + \cdots + \omega_c\mathcal{E}_{c,:} = \sum_{j=1}^{c}\omega_j\mathcal{E}_{j,:}. \tag{B.13}$$

Similarly, the element on the mth row and nth column of this matrix is equal to:

$$(\Omega\mathcal{E})_{m,n} = \sum_{j=1}^{c} e_m^{\mathsf{T}}\omega_j\mathcal{E}_{j,n} = \sum_{j=1}^{c}\mathcal{E}_{j,n}e_m^{\mathsf{T}}\omega_j. \tag{B.14}$$

Substituting the m, n^{th} element from Equation B.12 and Equation B.14 into Equation B.9 gives:

$$\sum_{j=1}^{c}\sum_{i=1}^{\beta} b_{m,i}\mathcal{D}_{i,n}\frac{\mathcal{C}_{j,i}}{2l_i^2}b_i^{\mathsf{T}}\omega_j - \sum_{j=1}^{c}\mathcal{E}_{j,n}e_m^{\mathsf{T}}\omega_j = \mathcal{A}_{m,n} \tag{B.15}$$

$$\Rightarrow \sum_{j=1}^{c}\Big(\sum_{i=1}^{\beta}\frac{b_{m,i}\mathcal{D}_{i,n}\mathcal{C}_{j,i}}{2l_i^2}b_i^{\mathsf{T}} - \mathcal{E}_{j,n}e_m^{\mathsf{T}}\Big)\omega_j = \mathcal{A}_{m,n}. \tag{B.16}$$

This can be rearranged to shape a matrix equation:

$$\Theta^{3c\times 3c}\begin{bmatrix}\omega_1\\ \omega_2\\ \vdots\\ \omega_{n_c}\end{bmatrix} = \begin{bmatrix}\mathcal{A}_{1,1}\\ \mathcal{A}_{1,2}\\ \vdots\\ \mathcal{A}_{1,c}\\ \vdots\\ \mathcal{A}_{2,1}\\ \mathcal{A}_{2,2}\\ \vdots\\ \mathcal{A}_{2,c}\\ \vdots\\ \mathcal{A}_{3,1}\\ \mathcal{A}_{3,2}\\ \vdots\\ \mathcal{A}_{3,c}\end{bmatrix} \tag{B.17}$$

$$
\begin{bmatrix}
\mathcal{A}_{1,1} \\ \mathcal{A}_{1,2} \\ \vdots \\ \mathcal{A}_{1,c} \\ \vdots \\ \mathcal{A}_{2,1} \\ \mathcal{A}_{2,2} \\ \vdots \\ \mathcal{A}_{2,c} \\ \vdots \\ \mathcal{A}_{3,1} \\ \mathcal{A}_{3,2} \\ \vdots \\ \mathcal{A}_{3,c}
\end{bmatrix}
=
\begin{bmatrix}
\sum_{i=1}^{\beta} \frac{b_{1,i}\mathcal{D}_{i,1}\mathcal{C}_{1,i}}{2l_i^2} b_i^{\mathsf{T}} - \mathcal{E}_{1,1} e_1^{\mathsf{T}} & \cdots & \sum_{i=1}^{\beta} \frac{b_{1,i}\mathcal{D}_{i,1}\mathcal{C}_{c,i}}{2l_i^2} b_i^{\mathsf{T}} - \mathcal{E}_{c,1} e_1^{\mathsf{T}} \\
\sum_{i=1}^{\beta} \frac{b_{1,i}\mathcal{D}_{i,2}\mathcal{C}_{1,i}}{2l_i^2} b_i^{\mathsf{T}} - \mathcal{E}_{1,2} e_1^{\mathsf{T}} & \cdots & \sum_{i=1}^{\beta} \frac{b_{1,i}\mathcal{D}_{i,2}\mathcal{C}_{c,i}}{2l_i^2} b_i^{\mathsf{T}} - \mathcal{E}_{c,2} e_1^{\mathsf{T}} \\
\vdots & \ddots & \vdots \\
\sum_{i=1}^{\beta} \frac{b_{1,i}\mathcal{D}_{i,c}\mathcal{C}_{1,i}}{2l_i^2} b_i^{\mathsf{T}} - \mathcal{E}_{1,c} e_1^{\mathsf{T}} & \cdots & \sum_{i=1}^{\beta} \frac{b_{1,i}\mathcal{D}_{i,c}\mathcal{C}_{c,i}}{2l_i^2} b_i^{\mathsf{T}} - \mathcal{E}_{c,c} e_1^{\mathsf{T}} \\
\sum_{i=1}^{\beta} \frac{b_{2,i}\mathcal{D}_{i,1}\mathcal{C}_{1,i}}{2l_i^2} b_i^{\mathsf{T}} - \mathcal{E}_{1,1} e_2^{\mathsf{T}} & \cdots & \sum_{i=1}^{\beta} \frac{b_{2,i}\mathcal{D}_{i,1}\mathcal{C}_{c,i}}{2l_i^2} b_i^{\mathsf{T}} - \mathcal{E}_{c,1} e_2^{\mathsf{T}} \\
\sum_{i=1}^{\beta} \frac{b_{2,i}\mathcal{D}_{i,2}\mathcal{C}_{1,i}}{2l_i^2} b_i^{\mathsf{T}} - \mathcal{E}_{1,2} e_2^{\mathsf{T}} & \cdots & \sum_{i=1}^{\beta} \frac{b_{2,i}\mathcal{D}_{i,2}\mathcal{C}_{c,i}}{2l_i^2} b_i^{\mathsf{T}} - \mathcal{E}_{c,2} e_2^{\mathsf{T}} \\
\vdots & \ddots & \vdots \\
\sum_{i=1}^{\beta} \frac{b_{2,i}\mathcal{D}_{i,c}\mathcal{C}_{1,i}}{2l_i^2} b_i^{\mathsf{T}} - \mathcal{E}_{1,c} e_2^{\mathsf{T}} & \cdots & \sum_{i=1}^{\beta} \frac{b_{2,i}\mathcal{D}_{i,c}\mathcal{C}_{c,i}}{2l_i^2} b_i^{\mathsf{T}} - \mathcal{E}_{c,c} e_2^{\mathsf{T}} \\
\sum_{i=1}^{\beta} \frac{b_{3,i}\mathcal{D}_{i,1}\mathcal{C}_{1,i}}{2l_i^2} b_i^{\mathsf{T}} - \mathcal{E}_{1,1} e_3^{\mathsf{T}} & \cdots & \sum_{i=1}^{\beta} \frac{b_{3,i}\mathcal{D}_{i,1}\mathcal{C}_{c,i}}{2l_i^2} b_i^{\mathsf{T}} - \mathcal{E}_{c,1} e_3^{\mathsf{T}} \\
\sum_{i=1}^{\beta} \frac{b_{3,i}\mathcal{D}_{i,2}\mathcal{C}_{1,i}}{2l_i^2} b_i^{\mathsf{T}} - \mathcal{E}_{1,2} e_3^{\mathsf{T}} & \cdots & \sum_{i=1}^{\beta} \frac{b_{3,i}\mathcal{D}_{i,2}\mathcal{C}_{c,i}}{2l_i^2} b_i^{\mathsf{T}} - \mathcal{E}_{c,2} e_3^{\mathsf{T}} \\
\vdots & \ddots & \vdots \\
\sum_{i=1}^{\beta} \frac{b_{3,i}\mathcal{D}_{i,c}\mathcal{C}_{1,i}}{2l_i^2} b_i^{\mathsf{T}} - \mathcal{E}_{1,c} e_3^{\mathsf{T}} & \cdots & \sum_{i=1}^{\beta} \frac{b_{3,i}\mathcal{D}_{i,c}\mathcal{C}_{c,i}}{2l_i^2} b_i^{\mathsf{T}} - \mathcal{E}_{c,c} e_3^{\mathsf{T}}
\end{bmatrix}
\begin{bmatrix}
\omega_1 \\ \omega_2 \\ \vdots \\ \omega_c
\end{bmatrix}
\tag{B.18}
$$

$$
\begin{bmatrix}
\mathcal{A}_{1,:}^{\mathsf{T}} \\ \mathcal{A}_{2,:}^{\mathsf{T}} \\ \mathcal{A}_{3,:}^{\mathsf{T}}
\end{bmatrix}
=
\begin{bmatrix}
\sum_{i=1}^{\beta} \frac{b_{1,i}\mathcal{C}_{1,i}}{2l_i^2} \mathcal{D}_{i,:}^{\mathsf{T}} b_i^{\mathsf{T}} & \cdots & \sum_{i=1}^{\beta} \frac{b_{1,i}\mathcal{C}_{c,i}}{2l_i^2} \mathcal{D}_{i,:}^{\mathsf{T}} b_i^{\mathsf{T}} \\
\sum_{i=1}^{\beta} \frac{b_{2,i}\mathcal{C}_{1,i}}{2l_i^2} \mathcal{D}_{i,:}^{\mathsf{T}} b_i^{\mathsf{T}} & \cdots & \sum_{i=1}^{\beta} \frac{b_{2,i}\mathcal{C}_{c,i}}{2l_i^2} \mathcal{D}_{i,:}^{\mathsf{T}} b_i^{\mathsf{T}} \\
\sum_{i=1}^{\beta} \frac{b_{3,i}\mathcal{C}_{1,i}}{2l_i^2} \mathcal{D}_{i,:}^{\mathsf{T}} b_i^{\mathsf{T}} & \cdots & \sum_{i=1}^{\beta} \frac{b_{3,i}\mathcal{C}_{c,i}}{2l_i^2} \mathcal{D}_{i,:}^{\mathsf{T}} b_i^{\mathsf{T}}
\end{bmatrix}
\begin{bmatrix}
\omega_1 \\ \omega_2 \\ \vdots \\ \omega_c
\end{bmatrix}
-
\begin{bmatrix}
\mathcal{E}_{1,:}^{\mathsf{T}} e_1^{\mathsf{T}} & \mathcal{E}_{2,:}^{\mathsf{T}} e_1^{\mathsf{T}} & \cdots & \mathcal{E}_{c,:}^{\mathsf{T}} e_1^{\mathsf{T}} \\
\mathcal{E}_{1,:}^{\mathsf{T}} e_2^{\mathsf{T}} & \mathcal{E}_{2,:}^{\mathsf{T}} e_2^{\mathsf{T}} & \cdots & \mathcal{E}_{c,:}^{\mathsf{T}} e_2^{\mathsf{T}} \\
\mathcal{E}_{1,:}^{\mathsf{T}} e_3^{\mathsf{T}} & \mathcal{E}_{2,:}^{\mathsf{T}} e_3^{\mathsf{T}} & \cdots & \mathcal{E}_{c,:}^{\mathsf{T}} e_3^{\mathsf{T}}
\end{bmatrix}
\begin{bmatrix}
\omega_1 \\ \omega_2 \\ \vdots \\ \omega_c
\end{bmatrix}
\tag{B.19}
$$

$$\begin{bmatrix} \mathcal{A}_{1,:}^{\mathsf{T}} \\ \mathcal{A}_{2,:}^{\mathsf{T}} \\ \mathcal{A}_{3,:}^{\mathsf{T}} \end{bmatrix} = \left(\begin{bmatrix} \sum_{i=1}^{\beta} \frac{\mathcal{C}_{1,i}}{2l_i^2} b_i \otimes (b_i \mathcal{D}_{i,:})^{\mathsf{T}} & \cdots & \sum_{i=1}^{\beta} \frac{\mathcal{C}_{c,i}}{2l_i^2} b_i \otimes (b_i \mathcal{D}_{i,:})^{\mathsf{T}} \end{bmatrix} - \begin{bmatrix} \mathcal{E} \otimes e_1^{\mathsf{T}} \\ \mathcal{E} \otimes e_2^{\mathsf{T}} \\ \mathcal{E} \otimes e_3^{\mathsf{T}} \end{bmatrix} \right) \begin{bmatrix} \omega_1 \\ \omega_2 \\ \vdots \\ \omega_c \end{bmatrix} \tag{B.20}$$

$$\begin{bmatrix} \mathcal{A}_{1,:}^{\mathsf{T}} \\ \mathcal{A}_{2,:}^{\mathsf{T}} \\ \mathcal{A}_{3,:}^{\mathsf{T}} \end{bmatrix} = \left(\sum_{i=1}^{\beta} \frac{1}{2l_i^2} \mathcal{C}_{:,i}^{\mathsf{T}} \otimes (b_i \otimes (b_i \mathcal{D}_{i,:})^{\mathsf{T}}) - \begin{bmatrix} \mathcal{E} \otimes e_1^{\mathsf{T}} \\ \mathcal{E} \otimes e_2^{\mathsf{T}} \\ \mathcal{E} \otimes e_3^{\mathsf{T}} \end{bmatrix} \right) \begin{bmatrix} \omega_1 \\ \omega_2 \\ \vdots \\ \omega_c \end{bmatrix} \tag{B.21}$$

The above equation represents $3c$ equations for $3c$ unknowns and taking the inverse will give us Equation B.1.

B.2 Lagrange Multiplier for Gyroscopic Tensegrity systems

The aim here is to write an analytical solution for the Lagrange multiplier Ω in Equation 6.64.

Lemma B.2.1. *The Lagrange Multiplier that satisfies Equation 6.64 can be computed as*

$$\begin{bmatrix} \omega_1 \\ \omega_2 \\ \vdots \\ \omega_c \end{bmatrix} = \left(\sum_{i=1}^{\beta} \frac{1}{2l_i^2} \mathcal{C}_{:,i}^{\mathsf{T}} \otimes (b_i \otimes (b_i \mathcal{D}_{i,:})^{\mathsf{T}}) - \begin{bmatrix} \mathcal{E} \otimes e_1^{\mathsf{T}} \\ \mathcal{E} \otimes e_2^{\mathsf{T}} \\ \mathcal{E} \otimes e_3^{\mathsf{T}} \end{bmatrix} \right)^{-1} \begin{bmatrix} \mathcal{A}_{1,:}^{\mathsf{T}} \\ \mathcal{A}_{2,:}^{\mathsf{T}} \\ \mathcal{A}_{3,:}^{\mathsf{T}} \end{bmatrix}, \tag{B.22}$$

where ω_i is the i^{th} column of Ω, $\mathcal{C} = P^{\mathsf{T}} C_{nb}^{\mathsf{T}} C_b^{\mathsf{T}}$, $\mathcal{D} = C_b C_{nb} M_s^{-1} U_1$, $\mathcal{E} = P^{\mathsf{T}} M_s^{-1} U_1$, and $\mathcal{A} = -S\hat{\gamma} C_s M_s^{-1} U_1 + B \lfloor \frac{1}{2} \hat{l}^{-2} B^{\mathsf{T}} (S\hat{\gamma} C_s - W) C_{nb}^{\mathsf{T}} C_b^{\mathsf{T}} - \hat{l}^{-2} \hat{J} \dot{B}^{\mathsf{T}} \dot{B} \rfloor C_b C_{nb} M_s^{-1} U_1 + W_T M_s^{-1} U_1 \in \mathbb{R}^{3 \times c}$.

B.3 Lagrange Multiplier for Vectorized Equations

The aim here is to write an analytical solution for the Lagrange multiplier ω. Notice that ω appears linearly in two terms in Equation (7.110). We solve this by substituting K_s and $\hat{\lambda}$ to write the equation in terms of ω and known variables only. Then we combine all the coefficients of ω to left hand side and all the known variables on right hand side to write it in a simple linear algebra problem.

Lemma B.3.1. *The Lagrange Multiplier that satisfies Equation (7.110) can be computed as*

$$\begin{aligned} w = &(V_{11}\mathcal{D}\widehat{\mathcal{F}_x}\mathcal{H} + V_{12}\mathcal{D}\widehat{\mathcal{F}_y}\mathcal{H} + V_{13}\mathcal{D}\widehat{\mathcal{F}_z}\mathcal{H} - V_1^{\mathsf{T}}\mathcal{M}^{-1}A^{\mathsf{T}})^{-1}V_1^{\mathsf{T}}\mathcal{M}^{-1}W_{vec} \\ &- (V_{11}\mathcal{D}\widehat{\mathcal{F}_x}\mathcal{H} + V_{12}\mathcal{D}\widehat{\mathcal{F}_y}\mathcal{H} + V_{13}\mathcal{D}\widehat{\mathcal{F}_z}\mathcal{H} - V_1^{\mathsf{T}}\mathcal{M}^{-1}A^{\mathsf{T}})^{-1}(V_{11}\mathcal{C}n_x + V_{12}\mathcal{C}n_y + V_{13}\mathcal{C}n_z), \end{aligned} \tag{B.23}$$

where $V_1^{\mathsf{T}} = [V_{11}\ V_{12}\ V_{13}]$, $\mathcal{D} = \frac{1}{2}M_s^{-1}C_{nb}^{\mathsf{T}}C_b^{\mathsf{T}}\hat{l}^{-2}$, $\mathcal{E} = C_{nb}^{\mathsf{T}}C_b^{\mathsf{T}}$, $\mathcal{F}_x = C_bC_{nb}n_x$, $\mathcal{F}_y = C_bC_{nb}n_y$, $\mathcal{F}_z = C_bC_{nb}n_z$.

$$\begin{aligned} \mathcal{C} = M_s^{-1}C_s^{\mathsf{T}}\hat{\gamma}C_s + M_s^{-1}C_{nb}^{\mathsf{T}}C_b^{\mathsf{T}}\hat{J}\hat{l}^{-2}\lfloor\dot{B}^{\mathsf{T}}\dot{B}\rfloor C_bC_{nb} \\ + \frac{1}{2}M_s^{-1}C_{nb}^{\mathsf{T}}C_b^{\mathsf{T}}\hat{l}^{-2}\lfloor B^{\mathsf{T}}(W - S\hat{\gamma}C_s)C_{nb}^{\mathsf{T}}C_b^{\mathsf{T}}\rfloor C_bC_{nb}, \end{aligned}$$

$$\textit{and } \mathcal{H} = \begin{bmatrix} e_1^{\mathsf{T}}(b_{11}A_1^{\mathsf{T}} + b_{12}A_2^{\mathsf{T}} + b_{13}A_3^{\mathsf{T}}) \\ \\ e_2^{\mathsf{T}}(b_{21}A_1^{\mathsf{T}} + b_{22}A_2^{\mathsf{T}} + b_{23}A_3^{\mathsf{T}}) \\ \\ \vdots \\ \\ e_\beta^{\mathsf{T}}(b_{\beta 1}A_1^{\mathsf{T}} + b_{\beta 2}A_2^{\mathsf{T}} + b_{\beta 3}A_3^{\mathsf{T}}) \end{bmatrix}.$$

Proof: Let us write $V_1^\mathsf{T} = [V_{11}\ V_{12}\ V_{13}]$ and replace for $\mathcal{M} = (I_3 \otimes M_s)$, $\mathcal{K} = (I_3 \otimes K_s)$ and $n = [n_{1x}\ n_{2x} \cdots n_{Nx}\ n_{1y}\ n_{2y} \cdots n_{Ny}\ n_{1z}\ n_{2z} \cdots n_{Nz}]^\mathsf{T} = [n_x^\mathsf{T}\ n_y^\mathsf{T}\ n_z^\mathsf{T}]^\mathsf{T}$:

$$[V_{11}\ V_{12}\ V_{13}] \begin{bmatrix} M_s^{-1} & 0 & 0 \\ 0 & M_s^{-1} & 0 \\ 0 & 0 & M_s^{-1} \end{bmatrix} \begin{bmatrix} K_s & 0 & 0 \\ 0 & K_s & 0 \\ 0 & 0 & K_s \end{bmatrix} \begin{bmatrix} n_x \\ n_y \\ n_z \end{bmatrix} - V_1^\mathsf{T}\mathcal{M}^{-1}A^\mathsf{T}\omega = V_1^\mathsf{T}\mathcal{M}^{-1}W_{vec} \tag{B.24}$$

$$V_{11}M_s^{-1}K_s n_x + V_{12}M_s^{-1}K_s n_y + V_{13}M_s^{-1}K_s n_z - V_1^\mathsf{T}\mathcal{M}^{-1}A^\mathsf{T}\omega = V_1^\mathsf{T}\mathcal{M}^{-1}W_{vec} \tag{B.25}$$

Let us start by taking first term and substituting for K_s from Equation (5.98):

$$\begin{aligned} V_{11}M_s^{-1}K_s n_x =& V_{11}M_s^{-1}\begin{bmatrix} C_s^\mathsf{T}\hat{\gamma}C_{sb} - C_{nb}^\mathsf{T}C_b^\mathsf{T}\hat{\lambda}C_b & C_s^\mathsf{T}\hat{\gamma}C_{ss} \end{bmatrix} n_x & \text{(B.26)} \\ =& V_{11}M_s^{-1}\left(\begin{bmatrix} C_s^\mathsf{T}\hat{\gamma}C_{sb} & C_s^\mathsf{T}\hat{\gamma}C_{ss} \end{bmatrix} - \begin{bmatrix} C_{nb}^\mathsf{T}C_b^\mathsf{T}\hat{\lambda}C_b & 0 \end{bmatrix}\right) n_x & \text{(B.27)} \\ =& V_{11}M_s^{-1}\left(C_s^\mathsf{T}\hat{\gamma}\begin{bmatrix} C_{sb} & C_{ss} \end{bmatrix} - C_{nb}^\mathsf{T}C_b^\mathsf{T}\hat{\lambda}C_b\begin{bmatrix} I & 0 \end{bmatrix}\right) n_x & \text{(B.28)} \end{aligned}$$

Now, we substitute for $C_{nb} = [I\ \ 0]$ and $C_s = [C_{sb}\ \ C_{ss}]$ from dynamics derivation :

$$\begin{aligned} V_{11}M_s^{-1}K_s n_x =& V_{11}M_s^{-1}(C_s^\mathsf{T}\hat{\gamma}C_s - C_{nb}^\mathsf{T}C_b^\mathsf{T}\hat{\lambda}C_bC_{nb})n_x & \text{(B.29)} \\ =& V_{11}M_s^{-1}C_s^\mathsf{T}\hat{\gamma}C_s n_x - V_{11}M_s^{-1}C_{nb}^\mathsf{T}C_b^\mathsf{T}\hat{\lambda}C_bC_{nb}n_x & \text{(B.30)} \end{aligned}$$

Further substituting $\hat{\lambda}$ from Equation (7.99) here gives:

$$\begin{aligned} V_{11}M_s^{-1}K_s n_x =& V_{11}M_s^{-1}C_s^\mathsf{T}\hat{\gamma}C_s n_x + V_{11}M_s^{-1}C_{nb}^\mathsf{T}C_b^\mathsf{T}\hat{J}\hat{l}^{-2}\lfloor\dot{B}^\mathsf{T}\dot{B}\rfloor C_bC_{nb}n_x \\ &+ \frac{1}{2}V_{11}M_s^{-1}C_{nb}^\mathsf{T}C_b^\mathsf{T}\hat{l}^{-2}\lfloor B^\mathsf{T}(W + [A_1^\mathsf{T}\omega\ A_2^\mathsf{T}\omega\ A_3^\mathsf{T}\omega]^\mathsf{T} - S\hat{\gamma}C_s)C_{nb}^\mathsf{T}C_b^\mathsf{T}\rfloor C_bC_{nb}n_x \end{aligned} \tag{B.31}$$

$$V_{11}M_s^{-1}K_s n_x = V_{11}M_s^{-1}C_s^{\mathsf{T}}\hat{\gamma}C_s n_x + V_{11}M_s^{-1}C_{nb}^{\mathsf{T}}C_b^{\mathsf{T}}\hat{J}\hat{l}^{-2}\lfloor \dot{B}^{\mathsf{T}}\dot{B}\rfloor C_b C_{nb} n_x$$
$$+ \frac{1}{2}V_{11}M_s^{-1}C_{nb}^{\mathsf{T}}C_b^{\mathsf{T}}\hat{l}^{-2}\lfloor B^{\mathsf{T}}(W - S\hat{\gamma}C_s)C_{nb}^{\mathsf{T}}C_b^{\mathsf{T}}\rfloor C_b C_{nb} n_x$$
$$+ \frac{1}{2}V_{11}M_s^{-1}C_{nb}^{\mathsf{T}}C_b^{\mathsf{T}}\hat{l}^{-2}\lfloor B^{\mathsf{T}}[A_1^{\mathsf{T}}\omega\ A_2^{\mathsf{T}}\omega\ A_3^{\mathsf{T}}\omega]^{\mathsf{T}}C_{nb}^{\mathsf{T}}C_b^{\mathsf{T}}\rfloor C_b C_{nb} n_x \quad \text{(B.32)}$$

$$V_{11}M_s^{-1}K_s n_x = V_{11}\mathcal{C}n_x + V_{11}\mathcal{D}\lfloor B^{\mathsf{T}}[A_1^{\mathsf{T}}\omega\ A_2^{\mathsf{T}}\omega\ A_3^{\mathsf{T}}\omega]^{\mathsf{T}}\mathcal{E}\rfloor \mathcal{F}_x \quad \text{(B.33)}$$

where

$$\mathcal{C} = M_s^{-1}C_s^{\mathsf{T}}\hat{\gamma}C_s + M_s^{-1}C_{nb}^{\mathsf{T}}C_b^{\mathsf{T}}\hat{J}\hat{l}^{-2}\lfloor \dot{B}^{\mathsf{T}}\dot{B}\rfloor C_b C_{nb}$$
$$+ \frac{1}{2}M_s^{-1}C_{nb}^{\mathsf{T}}C_b^{\mathsf{T}}\hat{l}^{-2}\lfloor B^{\mathsf{T}}(W - S\hat{\gamma}C_s)C_{nb}^{\mathsf{T}}C_b^{\mathsf{T}}\rfloor C_b C_{nb} \quad \text{(B.34)}$$

$\mathcal{D} = \frac{1}{2}M_s^{-1}C_{nb}^{\mathsf{T}}C_b^{\mathsf{T}}\hat{l}^{-2}$, $\mathcal{E} = C_{nb}^{\mathsf{T}}C_b^{\mathsf{T}}$, and $\mathcal{F}_x = C_b C_{nb} n_x$.

Let us take the right side of the equation (B.33)

$$\mathcal{D}\lfloor B^{\mathsf{T}}[A_1^{\mathsf{T}}\omega\ A_2^{\mathsf{T}}\omega\ A_3^{\mathsf{T}}\omega]^{\mathsf{T}}\mathcal{E}\rfloor\mathcal{F}_x = \mathcal{D}\lfloor\mathcal{E}^{\mathsf{T}}[A_1^{\mathsf{T}}\omega\ A_2^{\mathsf{T}}\omega\ A_3^{\mathsf{T}}\omega]B\rfloor\mathcal{F}_x \tag{B.35}$$

$$= \mathcal{D}\lfloor\begin{bmatrix} e_1^{\mathsf{T}} \\ e_2^{\mathsf{T}} \\ \vdots \\ e_\beta^{\mathsf{T}} \end{bmatrix}[A_1^{\mathsf{T}}\omega\ A_2^{\mathsf{T}}\omega\ A_3^{\mathsf{T}}\omega]\begin{bmatrix} b_1 & b_2 & \cdots & b_\beta \end{bmatrix}\rfloor\mathcal{F}_x = \mathcal{D}\widehat{\begin{bmatrix} e_1^{\mathsf{T}}\mathcal{G}b_1 \\ e_2^{\mathsf{T}}\mathcal{G}b_2 \\ \vdots \\ e_\beta^{\mathsf{T}}\mathcal{G}b_\beta \end{bmatrix}}\mathcal{F}_x \tag{B.36}$$

$$= \mathcal{D}\widehat{\mathcal{F}_x}\begin{bmatrix} e_1^{\mathsf{T}}[A_1^{\mathsf{T}}\omega\ A_2^{\mathsf{T}}\omega\ A_3^{\mathsf{T}}\omega]b_1 \\ e_2^{\mathsf{T}}[A_1^{\mathsf{T}}\omega\ A_2^{\mathsf{T}}\omega\ A_3^{\mathsf{T}}\omega]b_2 \\ \vdots \\ e_\beta^{\mathsf{T}}[A_1^{\mathsf{T}}\omega\ A_2^{\mathsf{T}}\omega\ A_3^{\mathsf{T}}\omega]b_\beta \end{bmatrix} = \mathcal{D}\widehat{\mathcal{F}_x}\begin{bmatrix} e_1^{\mathsf{T}}(b_{11}A_1^{\mathsf{T}}\omega + b_{12}A_2^{\mathsf{T}}\omega + b_{13}A_3^{\mathsf{T}}\omega) \\ e_2^{\mathsf{T}}(b_{21}A_1^{\mathsf{T}}\omega + b_{22}A_2^{\mathsf{T}}\omega + b_{23}A_3^{\mathsf{T}}\omega) \\ \vdots \\ e_\beta^{\mathsf{T}}(b_{\beta1}A_1^{\mathsf{T}}\omega + b_{\beta2}A_2^{\mathsf{T}}\omega + b_{\beta3}A_3^{\mathsf{T}}\omega) \end{bmatrix} \tag{B.37}$$

$$= \mathcal{D}\widehat{\mathcal{F}_x}\begin{bmatrix} e_1^{\mathsf{T}}(b_{11}A_1^{\mathsf{T}} + b_{12}A_2^{\mathsf{T}} + b_{13}A_3^{\mathsf{T}})\omega \\ e_2^{\mathsf{T}}(b_{21}A_1^{\mathsf{T}} + b_{22}A_2^{\mathsf{T}} + b_{23}A_3^{\mathsf{T}})\omega \\ \vdots \\ e_\beta^{\mathsf{T}}(b_{\beta1}A_1^{\mathsf{T}} + b_{\beta2}A_2^{\mathsf{T}} + b_{\beta3}A_3^{\mathsf{T}})\omega \end{bmatrix} = \mathcal{D}\widehat{\mathcal{F}_x}\begin{bmatrix} e_1^{\mathsf{T}}(b_{11}A_1^{\mathsf{T}} + b_{12}A_2^{\mathsf{T}} + b_{13}A_3^{\mathsf{T}}) \\ e_2^{\mathsf{T}}(b_{21}A_1^{\mathsf{T}} + b_{22}A_2^{\mathsf{T}} + b_{23}A_3^{\mathsf{T}}) \\ \vdots \\ e_\beta^{\mathsf{T}}(b_{\beta1}A_1^{\mathsf{T}} + b_{\beta2}A_2^{\mathsf{T}} + b_{\beta3}A_3^{\mathsf{T}}) \end{bmatrix}\omega \tag{B.38}$$

$$\mathcal{D}\lfloor B^{\mathsf{T}}[A_1^{\mathsf{T}}\omega\ A_2^{\mathsf{T}}\omega\ A_3^{\mathsf{T}}\omega]^{\mathsf{T}}\mathcal{E}\rfloor\mathcal{F}_x = \mathcal{D}\widehat{\mathcal{F}_x}\mathcal{H}\omega \tag{B.39}$$

where $\mathcal{H} = \begin{bmatrix} e_1^{\mathsf{T}}(b_{11}A_1^{\mathsf{T}} + b_{12}A_2^{\mathsf{T}} + b_{13}A_3^{\mathsf{T}}) \\ \\ e_2^{\mathsf{T}}(b_{21}A_1^{\mathsf{T}} + b_{22}A_2^{\mathsf{T}} + b_{23}A_3^{\mathsf{T}}) \\ \\ \vdots \\ \\ e_\beta^{\mathsf{T}}(b_{\beta 1}A_1^{\mathsf{T}} + b_{\beta 2}A_2^{\mathsf{T}} + b_{\beta 3}A_3^{\mathsf{T}}) \end{bmatrix}$.

Substituting from equation (B.39) into equation (B.33), we get

$$V_{11}M_s^{-1}K_s n_x = V_{11}\mathcal{C}n_x + V_{11}\mathcal{D}\widehat{\mathcal{F}_x}\mathcal{H}\omega \tag{B.40}$$

Similarly,

$$V_{12}M_s^{-1}K_s n_y = V_{12}\mathcal{C}n_y + V_{12}\mathcal{D}\widehat{\mathcal{F}_y}\mathcal{H}\omega \tag{B.41}$$

$$V_{13}M_s^{-1}K_s n_z = V_{13}\mathcal{C}n_z + V_{13}\mathcal{D}\widehat{\mathcal{F}_z}\mathcal{H}\omega \tag{B.42}$$

Substituting from equation (B.40-B.42) into equation (B.25), we get

$$V_{11}\mathcal{C}n_x + V_{11}\mathcal{D}\widehat{\mathcal{F}_x}\mathcal{H}\omega + V_{12}\mathcal{C}n_y + V_{12}\mathcal{D}\widehat{\mathcal{F}_y}\mathcal{H}\omega + V_{13}\mathcal{C}n_z + V_{13}\mathcal{D}\widehat{\mathcal{F}_z}\mathcal{H}\omega - V_1^{\mathsf{T}}\mathcal{M}^{-1}A^{\mathsf{T}}\omega = V_1^{\mathsf{T}}\mathcal{M}^{-1}W_{vec} \tag{B.43}$$

$$(V_{11}\mathcal{D}\widehat{\mathcal{F}_x}\mathcal{H} + V_{12}\mathcal{D}\widehat{\mathcal{F}_y}\mathcal{H} + V_{13}\mathcal{D}\widehat{\mathcal{F}_z}\mathcal{H} - V_1^{\mathsf{T}}\mathcal{M}^{-1}A^{\mathsf{T}})\omega = V_1^{\mathsf{T}}\mathcal{M}^{-1}W_{vec} - V_{11}\mathcal{C}n_x - V_{12}\mathcal{C}n_y - V_{13}\mathcal{C}n_z \tag{B.44}$$

Taking the inverse of square coefficient matrix of ω will give back the required equation (B.23).

APPENDIX C

PROOF OF LEMMA AND THEOREMS

C.1 Proof of Lemma 2.3.1

Let us consider a section of a beam such as that illustrated in Fig. C.1. The axial strain ε at any location in the beam is given as follows:

$$\varepsilon \;=\; \varepsilon_0 - y\kappa \;=\; \varepsilon_0 - y\frac{\mathrm{d}^2 w}{\mathrm{d}x^2}. \tag{C.1}$$

where $-r \leq y \leq r$ and ε_0 is the strain at $y = 0$. Here, we assume that $\varepsilon_0 = 0$ (i.e., that the bar is undergoing bending deformation only). By making this assumption, ε is given as:

$$\varepsilon = -y\frac{\mathrm{d}^2 w}{\mathrm{d}x^2}. \tag{C.2}$$

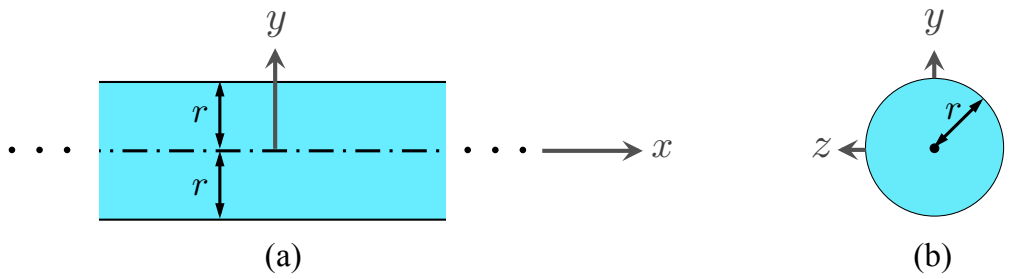

Figure C.1: (a) Section of a beam aligned with the x-axis. (b) Circular beam cross-section of radius r.

The first and second derivatives of deflection w from Eq. (2.2) with respect to the axial coordinate x are given as follows:

$$\frac{\mathrm{d}w}{\mathrm{d}x} = w_{max}\frac{n\pi}{l}\cos\left(\tfrac{n\pi x}{l}\right), \qquad \frac{\mathrm{d}^2 w}{\mathrm{d}x^2} = -w_{max}\left(\frac{n\pi}{l}\right)^2 \sin\left(\tfrac{n\pi x}{l}\right). \tag{C.3}$$

By substitution of Eq. (C.3) into Eq. (C.2), the following expression of the axial strain ε is obtained:

$$\varepsilon = y w_{max} \left(\frac{n\pi}{l}\right)^2 \sin\left(\tfrac{n\pi x}{l}\right). \tag{C.4}$$

For the linear elastic material comprising the beam, ε is related to the axial stress σ via Hooke's law:

$$\varepsilon = \frac{\sigma}{E_b}. \tag{C.5}$$

As stated in Section 2.3, at post-buckling it is assumed that failure of the beam to support the applied force occurs when material yielding starts. This failure condition is met when the stress at *any* point in the beam reaches the material yield stress, denoted by σ_b. At such a stress, the strain of the material at failure ε_b is determined via Eq. (C.5):

$$\varepsilon_b = \frac{\sigma_b}{E_b}. \tag{C.6}$$

From Eq. (C.4), the maximum absolute value of strain in the beam occurs at:

$$y = y_{max}, \qquad \sin\left(\tfrac{n\pi x}{l}\right) = \pm 1, \tag{C.7}$$

where y_{max} is the largest value (in magnitude) of the off-axis coordinate y in the cross-section of the beam. Assuming that the beam has a circular cross-section of radius r, then $y_{max} = \pm r$. At post-buckling failure due to material yield, the maximum absolute value of strain corresponds to ε_b. By substituting Eqs. (C.6) and (C.7) into Eq. (C.4), the following expression is obtained:

$$\varepsilon_b \;=\; \frac{\sigma_b}{E_b} \;=\; r w_{max} \left(\frac{n\pi}{l}\right)^2. \tag{C.8}$$

The previous equation is rearranged to obtain the expression for w_{max} as a function of the material yield stress σ_b provided in Eq. (2.3).

The expression for w_{max} from Eq. (2.3) is substituted in Eq. (C.4) to obtain the maximum allowable strain field in the bent beam:

$$\varepsilon \;=\; y\frac{\sigma_b}{rE_b}\left(\frac{n\pi}{l}\right)^{-2}\left(\frac{n\pi}{l}\right)^{2}\sin\left(\tfrac{n\pi x}{l}\right) \;=\; y\frac{\sigma_b}{rE_b}\sin\left(\tfrac{n\pi x}{l}\right). \tag{C.9}$$

cf. Eq. (2.4). This concludes the proof. □

C.2 Proof of Theorem 2.4.2

Let us consider a D-bar system of length l, complexity q, angle parameter α, and p strings per D-bar unit subject to a compressive force of magnitude f. The material comprising the bars has Young's modulus E_b and mass density ρ_b while the material comprising the strings has yield stress σ_s and mass density ρ_s. The mass of each bar, denoted by m_q, is given as:

$$m_q = \pi\rho_b l_q r_q^2. \tag{C.10}$$

From Eqs. (2.26) and (C.10), it follows that:

$$m_q = 2\rho_b l_q^2\left(\frac{f_q}{\pi E_b}\right)^{\frac{1}{2}}. \tag{C.11}$$

By substitution of the expressions for f_q and l_q from Eqs. (2.21) and (2.15), respectively, the following equation for the mass of each bar is obtained:

$$m_q = \frac{\rho_b l^2}{2^{2q-1}p^{\frac{q}{2}}\cos^{\frac{5q}{2}}(\alpha)}\left(\frac{f}{\pi E_b}\right)^{\frac{1}{2}}. \tag{C.12}$$

It can also be verified from Eqs. (C.10) and (C.12) that the radius r_q of each bar is given as:

$$r_q = \left(\frac{l}{2^{q-1}p^{\frac{q}{2}}\cos^{\frac{3q}{2}}(\alpha)}\right)^{\frac{1}{2}}\left(\frac{f}{\pi^3 E_b}\right)^{\frac{1}{4}}. \tag{C.13}$$

We now add the mass of each bar in the D-bar system to obtain the total mass of the bars, denoted by m_b:

$$m_b \;=\; n_b m_q \;=\; (2p)^q \frac{\rho_b l^2}{2^{2q-1} p^{\frac{q}{2}} \cos^{\frac{5q}{2}}(\alpha)} \left(\frac{f}{\pi E_b}\right)^{\frac{1}{2}} \;=\; \frac{p^{\frac{q}{2}} \rho_b l^2}{2^{q-1} \cos^{\frac{5q}{2}}(\alpha)} \left(\frac{f}{\pi E_b}\right)^{\frac{1}{2}}. \qquad \text{(C.14)}$$

The mass of each string introduced at the i^{th} self-similar iteration is denoted by m_{si}, $i = 1, \ldots, q$, and is determined as follows:

$$m_{si} = \rho_s l_{si} A_{si} \qquad\qquad i = 1, \ldots, q. \qquad \text{(C.15)}$$

An expression for A_{si} determined by assuming failure due to material yielding at the strings is provided in Eq. (2.36). We substitute such an expression into Eq. (C.15) and obtain the following function for m_{si}:

$$m_{si} = \frac{\rho_s l_{si} t_i}{\sigma_s} \qquad\qquad i = 1, \ldots, q. \qquad \text{(C.16)}$$

The expressions for t_i and l_{si} from Eqs. (2.22) and (2.19), respectively, are then substituted into the previous equation:

$$m_{si} = \frac{l f \rho_s \tan^2(\alpha)}{2^{i-1} p^i \sigma_s \cos^{2i-2}(\alpha)} \qquad\qquad i = 1, \ldots, q. \qquad \text{(C.17)}$$

It can also be verified that the radius r_{si} of each string introduced at the i^{th} self-similar iteration is given as:

$$r_{si} = \left(\frac{f \tan(\alpha)}{\pi p^i \sin\left(\frac{\pi}{p}\right) \sigma_s \cos^{i-1}(\alpha)}\right)^{\frac{1}{2}} \qquad\qquad i = 1, \ldots, q. \qquad \text{(C.18)}$$

We now add the mass of all the strings in the D-bar system to obtain the total mass of the strings, denoted by m_s:

$$m_s \;=\; \sum_{i=1}^{q} n_{si} m_{si} \;=\; \sum_{i=1}^{q} 2^{i-1} p^i \frac{l f \rho_s \tan^2(\alpha)}{2^{i-1} p^i \sigma_s \cos^{2i-2}(\alpha)}, \tag{C.19}$$

$$m_s \;=\; \frac{l f \rho_s \tan^2(\alpha)}{\sigma_s} \sum_{i=1}^{q} \frac{1}{\cos^{2i-2}(\alpha)}. \tag{C.20}$$

Using the identity in Eq. (2.45), the following expression for the total mass of the strings in a D-bar system is determined:

$$m_s = \frac{l f \rho_s (\sec^{2q}(\alpha) - 1)}{\sigma_s}. \tag{C.21}$$

The total mass of the D-bar system, m_D, is obtained by adding the total mass of the bars and the total mass of the strings:

$$m_D = m_b + m_s. \tag{C.22}$$

The final expression for m_D stated in Eq. (2.48) is obtained by substituting m_b and m_s from Eqs. (C.14) and (C.21), respectively, into Eq. (C.22). This concludes the proof. □